Imaging of Large Offset Ocean Bottom Seismic Data

by

Edmund C. Reiter

B.S. Geophysics
Boston College (1985)

Submitted to the Department of Earth, Atmospheric, and Planetary Sciences
in partial fulfillment of the requirements for the degree of

Doctor of Philosophy

at the

MASSACHUSETTS INSTITUTE OF TECHNOLOGY

February 1991

Signature of Author ..
Department of Earth, Atmospheric, and Planetary Sciences

Certified by.....
M. Nafi Toksöz
Director, Earth Resources Laboratory
Thesis Advisor

Certified by.....
G. M. Purdy
Woods Hole Oceanographic Institution
Thesis Co-Advisor

Accepted by.....
Thomas H. Jordan
Chairman, Department of Earth, Atmospheric and Planetary Sciences

Imaging of Large Offset Ocean Bottom Seismic Data

by

Edmund C. Reiter

Submitted to the Department of Earth, Atmospheric, and Planetary Sciences
on February 8, 1991, in partial fulfillment of the
requirements for the degree of
Doctor of Philosophy

Abstract

This thesis describes techniques to image deep crustal velocity and reflectivity structure from large offset Ocean Bottom Hydrophone (OBH) data. We choose to emphasize methods which image the data, rather than methods which forward model the data, to better utilize the increased data volumes associated with modern large offset marine seismic experiments.

We first describe a method for determining a two-dimensional (2-D) velocity field from refraction data that has been decomposed into some function of slowness. The most common decomposition, intercept time - slowness or $\tau - p$, is used as an intermediate step in an iterative wavefield continuation procedure previously applied to one-dimensional (1-D) velocity inversions. We extend the 1-D approach to 2-D by performing the downward continuation along numerically computed raypaths. Synthetic data are used to demonstrate how this approach can compensate for the effects of known lateral inhomogeneities while determining an underlying 1-D velocity field. We also use synthetic data to show how multiple refraction lines may be used to determine a general 2-D velocity model. Large offset field data collected with an OBH are used to illustrate this technique in an area of significant lateral heterogeneity caused by a sloping seafloor. At present, limitations of this 2-D approach are caused primarily by the sparseness of typical refraction surveys, but hopefully may be overcome in the future with more appropriate acquisition geometries.

Next, we show that data from an on-bottom hydrophone recording a near-surface source provide an opportunity to treat water column multiples as useful signal. A ray-equation based Kirchhoff pre-stack depth migration is used to image primary reflections and deep water multiples recorded on an Ocean Bottom Hydrophone (OBH). We use synthetic data to examine the difficulties in identifying the true path of the water column multiple. For flat-layered media there are two different multiple paths which have identical travel times: one that reflects beneath the source, and one that reflects over the receiver. However, they do not have the same amplitude, and it can be shown that their amplitudes differ sufficiently to allow a reliable image to be

extracted from the energy that reflects over the receiver. As a final step, the image obtained from the multiple is corrected for the π phase shift from the free surface and then added to the image from the primary reflection. Application of the technique allows the utilization of coherent deep water multiples as signal, and this results in an increased signal-to-noise ratio in the final image.

Finally, we discuss the application of both the 2-D velocity inversion/imaging method and the deep water multiple migration method to field data collected across the Carolina Trough off the East Coast of the U.S. Migration of large offset Moho reflections result in an image of the Moho over approximately 80 km of offset which clearly shows the Moho shallowing from approximately 37 km to approximately 25 km. Comparison of a velocity image from the 2-D velocity inversion/imaging method with a reflectivity image from Kirchhoff migration shows that first order velocity discontinuities in the velocity image correspond well with highly reflective depths in the reflectivity image.

Thesis Advisor: M. Nafi Toksöz
Title: Director, Earth Resources Laboratory

Thesis Co-Advisor: G. M. Purdy
Title: Woods Hole Oceanographic Institution

dedicated to James Michael Dolloway

1963 - 1977

Acknowledgments

I would first like to thank my advisor M. Nafi Toksoz for his tireless efforts on behalf of the Earth Resources Laboratory (ERL) which have allowed me complete freedom to pursue my graduate studies with access to the best of facilities. Greg Duckworth, M. Nafi Toksoz and G. M. Purdy deserve thanks on behalf of their efforts as research advisors over the past 5 years. I would like to thank Paul Stoffa, Dale Sawyer and Debbie Hutchinson for many helpful discussions pertaining to the material in this thesis. Initial stages of this work were supported by a National Science Foundation grant no. 1818120 at the Woods Hole Oceanographic Institution. Additional support was provided by the Air Force Geophysical Laboratory, Founding Members and Full Waveform Acoustic Logging Consortia of ERL and an AMOCO Fellowship.

Arthur Cheng, Roy Wilkens, Robert Reilinger, Anton Dainty, Roger Turpening and the rest of the scientific staff at ERL have helped in providing an interesting and stimulating research environment. Ottar Sandvin deserves special thanks for suggesting seismic imaging as a dissertation topic so many years ago. Tim Keho was very helpful in introducing me to Kirchhoff migration and physical conditioning although not at the same time. Steve Holbrook showed considerable patience in teaching me the fundamentals of refraction data interpretation and skill in providing a much needed velocity model. I thank Alan Kafka and John Ebel for their advice and encouragement during my undergraduate education at Boston College.

I thank Sara Brydges for her efforts which result in the remarkably smooth day to day operation of ERL. Sue Turbak's kind, friendly and caring attitude was a refreshing change from the day to day drudgery of life at MIT. Liz Henderson's Latex skills coupled with the daily combat of working with and around Nafi's schedule make her cool calm demeanor that much more impressive. I thank Jane Maloof and Al Taylor for their work in keeping an ever expanding computer system functioning and putting up with all of the attendant grief (especially Jane) from people like myself. Naida Buckingham's pleasant smile, kind Christmas cards and occasional history lesson were a needed diversion from graduate school.

Jack Foley and Bob Cicerone, my third floor pals from day one, made MIT (a bit) more enjoyable and I am lucky to have been so fortunate. I also thank Jumpin Jeff Meredith, Jim Mendelson, Joe Matarese, Sadi Kuleli and a long list of past and present students.

Lastly I would like to thank Delaine and my Mom and Dad for their never ending support and encouragement.

Contents

Chapter 1

Introduction

Objectives

In this thesis we develop and apply methods to image large offset Ocean Bottom Hydrophone (OBH) seismic data. Stationary OBHs deployed in advance along a traditional marine seismic reflection line provide an inexpensive and convenient method of acquiring high quality, densely sampled large offset seismic data. Seismic surveys which employ OBHs in addition to traditional reflection profiling are increasingly being recognized as an important part of deep crustal seismic programs. One such survey, conducted in June of 1988 off the southeastern U.S. Atlantic coast, is presented in this thesis; it provides the motivation for development of a variety of imaging methods. Figure 1 illustrates the geometry and simplified ray paths involved in a marine reflection/refraction survey of the type presented in this thesis. The fixed OBHs record primarily refracted and post-critically reflected arrivals while the seismic profiling vessel records primarily pre-critically reflected energy. Surveys of this type allow an order of magnitude increase in the spatial sampling of the large offset wavefield over traditional refraction methods. As a result, traditional methods of large offset data analysis, primarily ray theory-based two-dimensional forward modeling, become difficult to perform due to the attendant increase in data volume. Techniques which

directly "image" or project the seismic observations onto an interpretable model space are far more efficient at handling the increased large offset data volumes than traditional forward modeling methods. In this thesis we address the increased volumes of modern large offset data by focusing on techniques to directly image the large offset wavefield, in the hope of making interpretation of modern large offset seismic data a more exact and efficient process.

Large offset seismic surveys record energy which has propagated at low angles of incidence throughout the crustal column. Post-critical reflections and refractions make up the majority of the large offset wavefield and constrain crustal properties in a fundamentally different manner than near-vertical incidence reflection surveys. Traditional reflection surveys primarily record near-vertical incidence, pre-critical reflections, and provide a high resolution image of the reflectivity of the upper regions of the crust. In contrast, by recording energy which has a significant horizontal component to its travel path, large offset refraction surveys have traditionally provided control primarily on velocities. The inverse relationship between the observed ray parameter of post-critical and refracted energy, and the interval velocity at the turning point of the corresponding ray paths, has been widely exploited for estimating velocity profiles. Without large offset acquisition, these arrivals are not recorded, forcing less accurate velocity models to be derived from the moveout of pre-critical reflections. An additional advantage of large offset acquisition may be seen by comparing the vertically incident reflection coefficient to the wide-angle or critical reflection coefficient. The critical reflection coefficient is by definition unity, while deep crustal reflectors commonly have a normal incidence reflection coefficient an order of magnitude less. This typically results in higher signal-to-noise ratios in large offset data than in near-vertical reflection data for deep crustal reflectors. In this study we concentrate on taking advantage of the information contained in the large offset wavefield, and show how detailed images of the earth's crust may be obtained from such data.

Background

Active seismic investigations of the earth's crust generally fall into two categories: short offset near-vertical incidence reflection surveys, and large offset refraction surveys. Reflection surveys have historically been used to image the shallow crust (< 10 km deep), most commonly for purposes of petroleum prospecting (Sheriff and Geldart, 1982). Refraction surveys have been used primarily for deeper investigations of the earth's crust and upper mantle (Steinhart, 1964; Roller and Jackson, 1966; Hales, 1972), although their first widespread use was for the detection of shallow salt domes in the Southwest U.S. (Gardner, 1939; Musgrave, 1967). Traditional refraction and reflection surveys differ in two important aspects. First, the spatial sampling of receiver groups in reflection surveying is typically 25-50 m, while receiver spacing in refraction work is commonly 1,000-5,000 m. Secondly, the ratio of the source-receiver offset to the depth of study (offset/depth) is commonly less than 1.5 for reflection surveying, while for refraction surveying it is usually greater than 3. The difference in spatial sampling between reflection and refraction surveys has in recent years been increasingly reduced. For example, the 1986 PASSCAL Ouachita experiment (Chang and McMechan, 1989) involved receiver spacings of approximately 250 m and the data we address in this thesis has an effective receiver spacing of 50 m. Effective shot spacings remain quite different between reflection (50 m) and refraction geometries (5,000-10,000 m). However, modern refraction acquisition is tending more toward the finer spatial sampling of traditional reflection surveys (Talwani et al., 1990). Therefore, although the difference in spatial sampling between reflection and refraction has historically been significant, it is increasingly blurred by modern refraction acquisition.

The more important distinction between reflection and refraction surveying is the ratio of the source-receiver offset to the depth of study. This ratio determines the type of seismic energy (e.g., pre-critical reflection, refraction or post-critical reflection) and consequently the type of information which may be most robustly inferred

from the seismic observations. Source-receiver offset to depth ratios of less than 1.5 generally result in observations of pre-critically reflected and scattered energy. These observations permit the construction of an impedance contrast map with the traditional seismic section dimensions of offset and two-way travel time. Source-receiver offset to depth ratios of greater than 3 allow the recording of refracted and post-critically reflected arrivals. We use the term "refracted" to include the classic head wave as well as the more common turning ray which bottoms without reflection in a vertical velocity gradient. Refracted and post-critically reflected arrivals allow the robust determination of velocity structures; relative to reflection data, they provide a low resolution one- or two-dimensional estimate of the earth's structure. Because the velocity structure is determined, interpretations of refraction data are commonly displayed using a depth axis rather than the two-way travel time axis of the standard seismic section. The terms "large offset", "refraction" and "wide-angle reflection" are all used to describe acquisition geometries with large (> 3) source-receiver offset to depth ratios, in which few if any pre-critical reflections are observed.

Current techniques of interpreting large offset data have revolved around two-dimensional forward modeling of observed travel times and amplitudes. Two-dimensional modeling is commonly performed with asymptotic ray theory, while one-dimensional media may be modeled by more complete synthetic seismogram algorithms such as the reflectivity method. The net result of the forward modeling effort is generally a line drawing of a 2-D model which includes distinct layers of either constant velocities or velocity gradients. As greater volumes of data are accurately modeled, the final model becomes increasingly well-constrained. A major drawback of the forward modeling approach is the difficulty in expressing which portions of the model are well-constrained and which portions are not. Boundaries which have reversed coverage may be highlighted in an effort to illustrate some measure of goodness of fit, but forward modeling alone does not generally lend itself to quantitative representations of model quality. An additional difficulty in forward modeling has been exposed with

the increase in data volume that modern large offset experiments have provided. The relatively high amount of human effort involved in forward modeling has proved to be a significant impediment for processing large volumes of data. The more detailed models required to adequately represent the dense spatial sampling of modern surveys further strain the capacity of the forward modeling technique. As a result of this strain, imaging techniques more amenable to the large volumes of modern large offset data are necessary.

One such technique, originally developed for near-vertical reflection profiling, is called "migration". Depth migration, one of several types of migration, is a process by which an image of the earth's reflectivity is produced from observations of reflected, or scattered seismic energy. An advantage of migrating the large offset reflected wavefield is the ability to produce an image of the subsurface which immediately makes clear which portions of the model are well-constrained. A difficulty is that the quality of the input velocity model which directly determines the correctness of the final image is not directly addressed by migration. Aside from this consideration, migration of large offset reflected wavefields is quite attractive for large volumes of data and has recently been applied to several data sets. The ability to project data observations to a convenient compact form such as a 2-D image of reflectivity, is a necessary characteristic of new large offset data interpretation algorithms.

Contributions of this Thesis

A new technique to directly image the refracted and post-critically reflected wavefield in two dimensions is presented and developed in this thesis. Just as migration produces a 2-D image of the reflectivity, our approach allows direct imaging of a 2-D velocity structure from refracted and post-critically reflected energy. In addition to providing an image of the velocity structure, this new approach iteratively determines a best-fitting velocity model. The final best-fitting velocity model is displayed as a three dimensional (3-D) data volume with axes of offset, depth, velocity. A slowness-

decomposed representation of the large offset data (e.g., tau-p) is imaged into the 3-D data volume. The velocity model is defined as a surface of maxima in this data volume, clearly illustrating which portions of the velocity model are well-constrained. Effects of limited bandwidth and source strength are easily observed in the final image, because the entire wavefield is present throughout the imaging process. Avoidance of travel time picking and the direct imaging of a 2-D velocity model give this new approach significant potential for conveniently processing increased volumes of large offset data. We apply this technique to synthetic and field data, demonstrating its ability to iteratively determine velocity structure as well as provide a direct image of a 2-D velocity field.

We also present a method that treats water column multiples as useful signal, which allows these arrivals to be used to enhance the image of the subsurface. Coherent first order water column multiples are a major component of deep water ocean bottom hydrophone data. Observation of such arrivals motivated an effort to treat the multiples as useful signal rather than as the noise which traditional methods attempt to suppress. We show that, for the geometry of an on-bottom receiver recording a near-surface source, the first order water column multiple may be treated as signal useful for enhancing images of the subsurface. The on-bottom geometry allows the unique identification of the dominant first order water column multiple's travel path; this allows the use of this arrival in 2-D imaging problems. We demonstrate our approach to treating the first order water column multiple as useful signal with both synthetic and field data. A 2-D pre-stack Kirchhoff depth migration is used to image wide-angle reflected arrivals along both primary and water column multiple paths. The necessary Green's functions are computed with asymptotic ray theory, allowing convenient imaging of the water column multiple arrivals as well as the more traditional primary reflections. Field data examples image the crust/mantle interface with both primary and water column multiple arrivals. Strong constructive interference is observed when the primary and multiple image are summed, resulting in a final

composite image of increased signal strength.

Finally, a semblance-guided median filter is presented which may be used to enhance large offset arrivals and suppress background noise. This filter consists of an initial velocity estimation step followed by a traditional median filter. We demonstrate the advantages of the semblance-guided median filter on both OBH and Vertical Seismic Profile (VSP) data. We use this approach as a robust background noise suppression tool for enhancing large offset reflected and refracted arrivals in our OBH data. We also use this method as a velocity filter on VSP data to separate upgoing and downgoing wavefields and to suppress large amplitude tube waves.

Outline

In this thesis we present techniques which allow the imaging of large offset ocean bottom hydrophone data. In Chapter 2 we present a 2-D velocity inversion/imaging method. This approach allows a 2-D velocity field to be iteratively determined and imaged from slowness-decomposed large offset data. Development of this approach represents a new and potentially powerful method for 2-D velocity estimation from large offset seismic data.

In Chapter 3 we present a method for treating deep water column multiples recorded by an OBH as useful signal. We show that for an on-bottom recording geometry, the first order water column multiple may be assumed to be dominated a single multiple path which can be used in 2-D imaging schemes such as pre-stack Kirchhoff depth migration.

Results of applying both imaging techniques to large offset field data are presented in Chapter 4. We successfully image the Moho shallowing from 37 to 25 km across the oceanic-continental crust transition zone with a 2-D pre-stack Kirchhoff migration. We also present results of imaging both the velocity field (2-D velocity inversion/imaging) and the reflectivity (Kirchhoff) with the same large offset data.

A summary of this work and comments on the utility of large offset data in general

are found in Chapter 5.

In Appendix A a review of the one-dimensional velocity inversion/imaging approach of (Clayton and McMechan, 1981) is given. This material provides the necessary background for the extension of this method to two dimensions presented in Chapter 2.

A derivation of the non-planar Kirchhoff operator is reviewed in Appendix B. Results of this derivation provide the framework for the 2-D Kirchhoff ray-based pre-stack depth migration used in Chapter 3.

Appendix C describes a semblance-guided median filter and illustrates the success of this approach on a variety of seismic data. This method represents an extension of the traditional median filter which significantly expands the usefulness of this proven and robust non-linear digital filter.

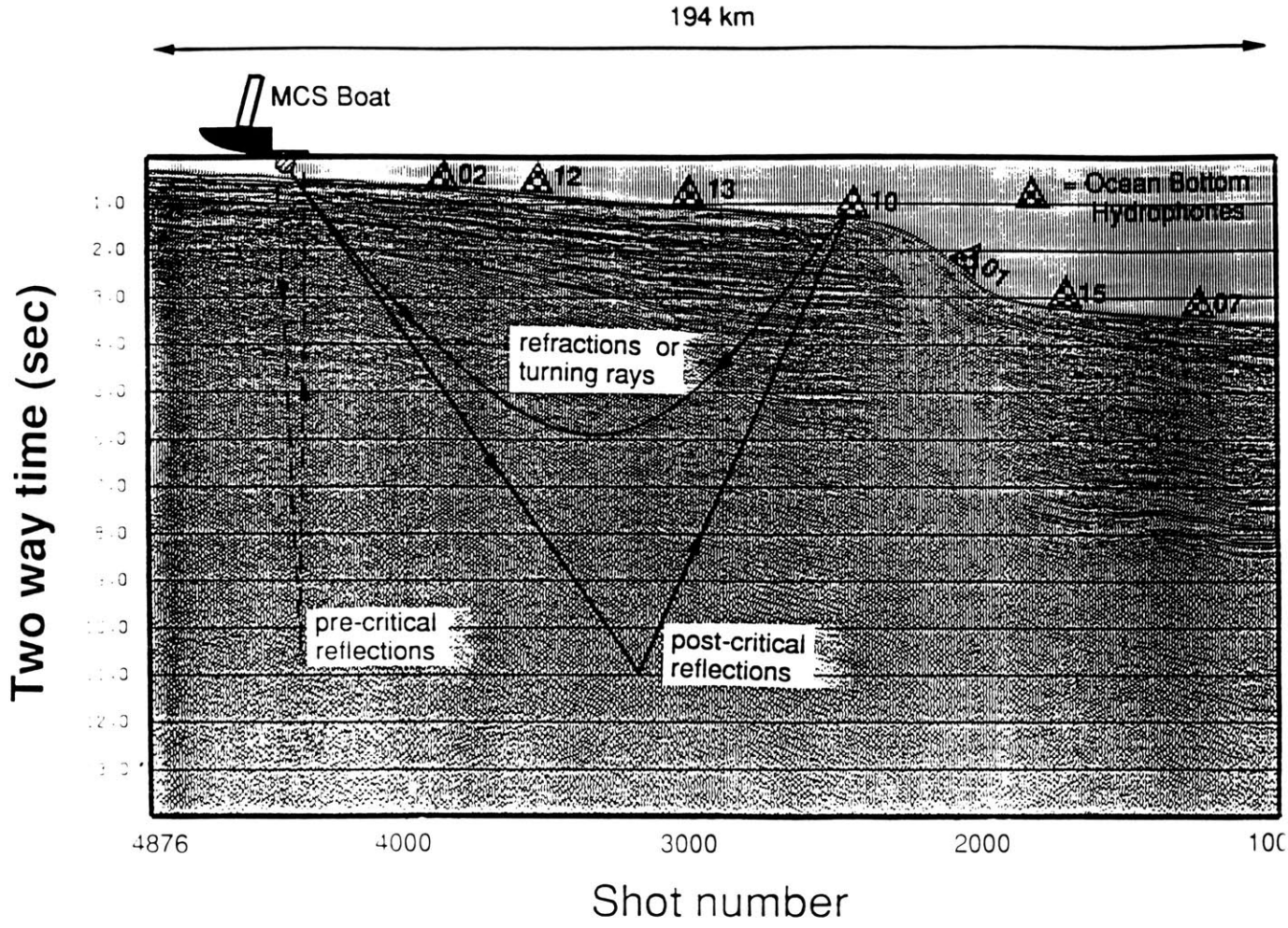

Figure 1. Diagram of marine "piggyback" reflection/refraction experiment. Fixed Ocean Bottom Hydrophones (OBH) are deployed prior to commencement of a standard marine reflection survey. The OBH's record a densely sampled (50 m in this case) large offset wavefield with signal observed at offsets up to 200 km. This thesis is concerned with techniques to directly image large-offset OBH data from this acquisition geometry.

Chapter 2

Two-Dimensional Velocity Inversion/Imaging of Large Offset Seismic Data

Introduction

Refraction profiles may be analyzed by a variety of methods which use either the intercept time - ray parameter ($\tau - p$) plane or the offset - ray parameter ($X - p$) plane as an intermediate step in the determination of a one-dimensional (1-D) velocity-depth function. We describe a method here which follows the general wavefield continuation approach of Clayton and McMechan (1981) and McMechan (1983b), but removes their 1-D restriction on the velocity function to allow velocities to vary in both depth (Z) and offset (X). In their method the original data, recorded in the offset time ($X - T$) domain, are transformed to either the $\tau - p$ or $X - p$ domains. From either of these slowness-decomposed data spaces, the data are downward continued to the depth-slowness ($Z - p$) plane assuming a 1-D trial velocity function. In the 1-D case, analytic forms of the downward continuation operators are available for both $\tau - p$ and $X - p$ data.

For imaging two-dimensional (2-D) velocity structures, we use rays to perform the downward continuation from a slowness-decomposed data space to the slowness-offset-depth $s(p, x, z)$ model space. This permits the proper treatment of more complex velocity fields than the the laterally homogeneous (1-D) case. We use the term "velocity inversion/imaging" because a best fitting 2-D velocity field is iteratively determined (inversion) *and* imaged by the downward continued data. The final model is represented by the three-dimensional data volume $s(p, x, z)$ with the maxima of this image defining the velocity field. Our 2-D approach is iterative with the updated velocity field being picked directly from the image in $s(p, x, z)$ space. Convergence is assumed when the downward continued data image the input velocity field.

Previous techniques for determining 1-D velocity profiles from $\tau - p$ data may be classified into two distinct categories; methods that use discrete $\tau - p$ points (picks), and methods which involve complete wavefield transformations. The former classification encompasses a wide variety of approaches in which workers including Johnson and Gilbert (1972), Bessanova et al. (1974), Garmany et al. (1979), Diebold and Stoffa (1981), Stark and Parker (1987) seek to derive 1-D velocity profiles and estimates of their goodness from discrete $\tau - p$ points. The methods in which discrete $\tau - p$ values are defined vary significantly but have increasingly tended toward the approaches of McMechan and Ottolini (1980), Stoffa et al. (1981), Chapman (1981), Phinney et al. (1981) and Treitel et al. (1982) which involve some version of the slant stack. When discrete points of the classic $\tau - p$ curve are required, a locus of monotonically decreasing maxima is identified and picked from the $\tau - p$ image. The $\tau - p$ data may be deconvolved (e.g., Treitel et al., 1982; Stoffa et al., 1981) to decrease uncertainty in the picking procedure.

A competing approach to the inversion of $\tau - p$ data was first presented by Clayton and McMechan (1981). This approach involves complete transformation of the $\tau - p$ wavefield to the domain of depth and slowness $(z - p)$, as opposed to inversion of discrete data points. At convergence, the best fitting model is defined by a locus of

maxima in the $z - p$ plane representing the desired depth - slowness profile. Carrion and Kuo (1985) present an approach similar to Clayton and McMechan (1981), but they formalize the model update procedure.

The main advantages of this approach are twofold. First, the entire wavefield is present throughout the inversion, which eliminates the subjectivity of travel time picking. Next, transformation of the observed wavefield onto a model space allows decisions about the reliability of the data to be made directly in the model space. Confidence in the final model may be derived from the quality of the final velocity image. A review of the 1-D approach of is given in Appendix A. We have chosen to follow the wavefield transformation approach of Clayton and McMechan (1981) to retain the benefits of this method while extending it to laterally varying media.

We examine two types of 2-D velocity structures and acquisition geometries. First, we investigate the case of a single refraction survey acquired in a region of known 2-D lateral heterogeneity which is surrounded by an unknown 1-D velocity structure. Synthetic data illustrate how the known 2-D component of structure may be fixed while the 1-D component of velocity structure is iteratively determined. Common examples of this type of structure are found in sparse offshore refraction surveys where the water depth does not remain constant. Secondly, we address the more general case of determining a complete 2-D velocity field from multiple refraction surveys. Synthetic data show that the correct 2-D velocity field may be determined by simultaneously downward continuing multiple receiver gathers and iteratively updating a 2-D model.

A 53 km long refraction line recorded by an Ocean Bottom Hydrophone (OBH) is used to demonstrate the ability of this approach to properly account for 2-D sea floor topography. The shape of the seafloor is assumed to be known and an underlying 1-D velocity function is imaged.

Two-dimensional velocity imaging

Velocity imaging of large offset data involves two transformations. First, the data are transformed from the original observation plane of offset and time $(X-T)$, to any of the slowness-decomposed data spaces of intercept time - ray parameter $(\tau-p_0)$, offset - ray parameter $(X-p_0)$ or total travel time - ray parameter $(T-p_0)$. Secondly, the slowness-decomposed data are repeatedly downward continued to slowness-offset-depth space $(s(p_b,x_b,z))$ along numerically computed ray paths. We first discuss the basic ideas of the 2-D downward continuation step and then elaborate on the implementation of this procedure.

Figure 1 illustrates the geometry used to describe our 2-D velocity inversion/imaging process. The seismic survey is assumed to consist of a single receiver recording a moving source which fires at closely spaced intervals. By reciprocity this geometry is equivalent to traditional land refraction surveys which employ many receivers with a single source. Slant stacking (e.g., Stoffa et al., 1981; Phinney et al., 1981; McMechan and Ottolini, 1980) a receiver gather acquired from the geometry in Figure 1 decomposes the data into the ray parameter p_0 located directly beneath the line of sources and intercept time. In the 2-D case, it is necessary to specify the position of the measured ray parameter because this quantity is not constant along the ray path. For 1-D media the ray parameter measured by the slant stack (p_0) is the same as the ray parameter at the bottoming point (p_b). However, in 2-D media this is no longer the case and the ray parameter measured by the slant stack is not generally equal to the ray parameter at the bottoming point. We must therefore specify at what spatial location a ray parameter is measured for this quantity to be physically meaningful. The lateral position of the ray bottoming point is denoted x_b and the ray parameter at the bottoming point as p_b. Given the correct velocity model, the raypath which properly models a slowness p_0 may be found by searching for a ray which begins at the receiver position and emerges with an angle $\theta = \arcsin(p_0 \cdot v_0)$. Figure 1 shows how θ is measured, and v_0 refers to the velocity directly beneath the source array

which is assumed to be known. This ray may be found by varying the takeoff angle until a ray emerges within an acceptable tolerance of θ. We see that this a variation of two-point ray tracing where an angle of emergence (θ) is modeled instead of a source or receiver position. This ray path which fits the angle θ is the path along which each slowness observation p_0 is downward continued. Each slowness observation p_0 requires a new ray path to be found which emerges with the proper θ.

Once a ray is found, the quantities of velocity $v(x,z)$ and ray parameter $p(x,z)$ are stored along the entire ray path as well as x_b and p_b from the bottoming point (Figure 1). At this point the necessary information to downward continue a given slowness vector has been computed, and the slowness observation p_0 may be imaged to $s(p_b, x_b, z)$ space. We first give expressions for the downward continuation of $\tau - p_0$ data and subsequently treat $X - p$ and $T - p$ data.

Equations 2.1-2.4 describe the downward continuation of $\tau - p$ data for the 2-D case.

$$s(p_b, x_b, z) = Q_{\tau 2d}[\Psi_{\tau 2d}(p_0, z), p_0] \tag{2.1}$$

$$warp(p_0) = (T_{total} - p_0 \cdot X)/\tau_{2D}(p_0) \tag{2.2}$$

$$\tau_{2D}(p_0) = \left[\int_{z_{rec}}^{z_{bottom}} + \int_{z_{bottom}}^{z_{src}}\right] [|(v(x,z))^{-2} - p(x,z)^2|]^{1/2} dz \tag{2.3}$$

$$\Psi_{\tau 2d}(p_0, z) = \left\{\left[\int_{z_{rec}}^{z} + \int_{z}^{z_{src}}\right] [|(v(x,z))^{-2} - p(x,z)^2|]^{1/2} dz\right\} \cdot warp(p_0) \tag{2.4}$$

where, x_b = lateral position of bottoming point;

p_b = ray parameter at bottoming point;

p_0 = observed slowness being downward continued;

$p(x,z)$ = spatially varying ray parameter (stored along ray path);

$v(x,z)$ = spatially varying velocity (stored along ray path);

z_{rec} = depth of the receiver;

z_{bottom} = bottoming depth of ray;

z_{src} = depth of source;

$s(p, x, z)$ = the slowness-offset-depth image of the velocity field;

$warp(p_0)$ = the correction term for the 1-D nature of the $\tau - p$ data;

T_{total} = total travel time along ray;

τ_{2D} = true 2-D vertical travel time along ray;

$Q_{\tau 2d}(\tau, p_0) = \tau - p$ image of $X - T$ data from 2-D earth;

$\Psi_{\tau 2d}$ = 2-D downward continuation operator for $\tau - p$

Equation 1 mathematically describes the process which images the two-dimensional data plane $Q_{\tau 2d}$ onto the three-dimensional model volume of $s(p, x, z)$. Each observed slowness vector of $Q_{\tau 2d}(\tau, p_0)$ is positioned at slowness p_b and offset x_b in the new model space $s(p, x, z)$. Next, the downward continuation operator of Equation 4 is evaluated for all depths z under consideration. Figure 2 shows the relationship between the ray paths found for several slowness vectors p_0 and the location of those vectors after downward continuation to $s(p, x, z)$ space. Each slowness observation p_0 maps to a single line in the model volume $s(p, x, z)$. In Figure 2 the position of this line in the slowness-offset plane is determined by the p_b and x_b at the bottoming point of numerically computed ray path. Projection of the slowness observation in the depth domain is determined by evaluating the downward continuation operator (Equation 4) for the depths of interest. Equation 4 is the 2-D analog to the 1-D time domain operator of Clayton and McMechan (1981). The 2-D velocity field is defined by the location of energy corresponding to the classic τ curve in $s(p, x, z)$ space.

For the case of $\tau - p$ data an additional slowness-dependent term referred to as $warp(p_0)$ is incorporated to account for the 1-D assumption of the forward transform itself. When the $\tau - p$ data is constructed by stacking over straight lines, the τ actually measured is the vertical delay time assuming a 1-D medium (Stoffa et al., 1981). The true 2-D vertical delay time is impossible to measure from a set of surface measurements; this discrepancy must be taken into account. Equation 3 is

an expression for the true vertical delay time $\tau_{2D}(p_0)$ along the raypath. The term $warp(p_0$ (Equation 2) is simply the ratio of the measured one-dimensional τ from the slant stack to the true τ_{2D} calculated along the ray path using Equation 3. The term $warp(p_0)$ is multiplied into the downward continuation operator given by Equation 4 to make the expression exact at the bottoming point of the ray path.

The other two slowness-decomposed data spaces, $X-p$ and $T-p$, while not as convenient to extract from $X-T$ data, do not suffer the inherent 1-D complications of the forward $\tau-p$ transform. Creation of $X-p$ data is discussed by McMechan (1983a) who suggests the use of short overlapping slant stacks. Tang et al. (1984) suggest an alternative approach called "cross stacking" which yields comparable results to McMechan (1983a). Equations 5-6 describe the process of downward continuing a $X-p$ wavefield in 2-D.

$$s(p_b, x_b, z) = Q_{X2d}[\Psi_{X2d}(p_0, z), p_0] \tag{2.5}$$

$$\Psi_{X2d}(p_0, z) = [\int_{z_{rec}}^{z} + \int_{z}^{z_{src}}]p(x,z)[|v^{-2}(x,z) - p^2(x,z)|]^{-1/2}dz \tag{2.6}$$

$Q_{X2d}(X, p_0) = X-p$ image of $X-T$ data from 2-D earth;
$\Psi_{X2d} =$ 2-D downward continuation operator for $X-p$;

The $X-p$ downward continuation operator does not require a slowness dependent correction term $warp(p_0)$. Since there was no assumption of one-dimensionality in the medium in the forward transform other than that of a locally planar wavefront, there is no need for a correction term.

Decomposition of recorded data into $T-p$ (total travel time-slowness) is not a common procedure. A possible approach is to compute N closely spaced (in offset) overlapping slant stacks decomposed into slowness and T. The classic $T-p$ image is defined by the maxima of all N slant stacks. We have found, for simple synthetic examples, that computing multiple semblance slant stacks and letting the final $T-p$ image be defined by the maximum of N of such stacks yields accurate results.

Equations 7 and 8 describe the 2-D downward continuation process for $T-p$ decomposed data.

$$s(p_b, x_b, z) = Q_{T2d}[\Psi_{T2d}(p_0, z), p_0] \tag{2.7}$$

$$\Psi_{T2d}(p_0, z) = [\int_{z_{rec}}^{z} + \int_{z}^{z_{src}}](v(x,z))^{-2}[|(v(x,z))^{-2} - p(x,z)^2|]^{-1/2}dz \tag{2.8}$$

$Q_{T2d}(X, p_0) = T-p$ image of $X-T$ data from 2-D earth;

$\Psi_{T2d} =$ 2-D downward continuation operator for $T-p$;

As in the $X-p$ case, no correction term $warp(p_0)$ is needed for $T-p$ data. We include Equations 7-8 for completeness in the presentation of the most obvious slowness decompositions. Although this is not a commonly used data space, it is possible to extract it from large offset dense refraction surveys.

Implementation

An initial model is chosen which represents the best estimate of the velocity structure. This model may include layers and velocity gradients within those layers. To begin the downward continuation procedure a ray is sought which terminates at the surface with slowness p_0. To find such a ray, we search for a ray which emerges with an angle $\theta = arcsin(p_0 \cdot v_0)$, which assumes the velocity (v_0) directly beneath the source or receiver array is known. For the geometry in Figure 1 this raypath is found by adjusting the takeoff angle of rays which begin at the receiver position and terminate at the free surface until a ray which emerges with an angle θ is found.

Beginning with the smallest slowness p_0 (fastest apparent velocity), rays are traced through the deepest available portion of the starting model. When a ray is found which emerges with the desired slowness p_0 the quantities $p(x,z)$ and $v(x,z)$ are stored for this ray path and the p_0 observation is downward continued using (for example) Equation 4. It is possible that a ray which emerges with an angle θ does not exist for raypaths which travel in the deepest portion of the model due to simple

effects of velocity gradients and boundaries. If p_0 is a slowness that is too large (velocity too slow) for the given raypath to model, a raypath corresponding to next shallower layer is used. In the model shown in Figure 4, a slowness of $p_0 = (1/5.7)$ can be modeled by a ray which bottoms in layer 4, but it is not possible to model a slowness of $p_0 = (1/4.0)$ with energy bottoming in layer 4. In this case the next shallower ray must be used, i.e., a ray bottoming in layer 3. This procedure of imaging the smallest p_0 with the deepest rays and using increasingly shallower rays is repeated until rays are traced through the uppermost layer being imaged. If the p_0 searching is done in this manner, the post-critically reflected and refracted wavefield will be downward continued along the correct ray paths for a multi-layered increasing velocity model. For velocity fields with significant low velocity regions, the ray search cannot be simplified in this manner. In this case, no refracted arrivals bottom in the low velocity regions and other information such as pre-critical reflections must be used (Clayton and McMechan, 1981). When too little information about the velocity exists to specify layers, a simple gradient may be used for the initial model and layers may be added when the $s(p, x, z)$ image indicates. In practice this approach of beginning with a simple gradient and adding layers when necessary has proved successful with both synthetic and field data.

This procedure is iterative because an initial trial velocity field must be chosen to perform the first downward continuation step. The data are imaged into $s(p, x, z)$ space, and the velocity surface defined by the imaged data is compared to the velocity surface used in the downward continuation (trial velocity model). If the data image onto the input velocity surface, the convergence condition is satisfied and the correct velocity field is assumed to be found. If the data do not image onto the input velocity function, an updated 2-D velocity field is picked directly from the data in $s(p, x, z)$ space. This procedure is repeated until the input velocity field is imaged and convergence is achieved. Figure 3a shows schematically the effect of using a velocity field that is too slow in a downward continuation step. The shaded surface represents the

velocity used in the downward continuation and the data have imaged to a surface above the input velocity. A new input velocity field would be picked from the positions of the pulses in Figure 3a. Figure 3b illustrates the image obtained when the correct velocity function is used. In this case the data image onto the velocity field (shaded area) used in the downward continuation. In the following section we show that the procedure converges to the correct velocity model using two synthetic data sets.

Synthetic Examples

Dipping layer model

The first 2-D model examined consists of a constant velocity dipping layer overlying a 1-D velocity structure consisting of gradients and first order velocity discontinuities (Figure 4). The 2-D overburden has a velocity of 1.5 km/sec; the second layer contains a gradient from 2.5 to 3.0 km/sec, the third layer a gradient from 3.5 to 4.5 km/sec and the last layer a gradient from 5.25 to 6.36 km/sec. The purpose of this example is to show that in the presence of a well-known 2-D overburden (such as a water layer), that a single, densely shot refraction line is capable of retrieving the underlying 1-D velocity structure. Ray-synthetic data (Cerveny et al., 1977) from the model are shown in Figure 5; they simulate a source at zero offset and receivers spaced every 0.2 km for 60 km of total coverage. All primary ray theoretical arrivals are computed including turning rays (refractions) and pre- and post-critical reflections. The data are chosen so the peak amplitude of the wavelet coincides with the ray-theoretical arrival time. The $\tau - p$ representation of the data is shown in Figure 6 and is generated by simple slant stack described by Equation 9.

$$Q_{\tau 2d}(\tau, p_0) = \int_0^{xmax} P(\tau + p_0 x, x) dx \tag{2.9}$$

where $Q_{\tau 2d}(\tau, p_0) = \tau - p$ representation of the X-T wavefield;
$P(t, x) =$ observed wavefield;

τ = effective 1-D vertical travel time;

p_0 = horizontal slowness at the receiver level;

x = receiver offset;

Figure 7a is a $s(p_b, x_b, z)$ image of the downward continued $\tau - p$ data in Figure 6 using a trial 1-D underlying simple gradient velocity function represented by the dashed line. The offset variable x is not shown on Figure 7 because the velocity structure beneath the dipping layer is invariant with respect to x. The 2-D overburden is assumed to be known in this case and the 1-D underlying velocity profile is sought. The solid line in Figure 7a shows the true underlying velocity function, and it is evident that the data have not been imaged onto the correct velocity function. The trial velocity function (dotted line in Figure 7a) contained no layers, other than the fixed surficial dipping layer, and thus the ray search was carried out in the gradient layer only. The updated velocity function needed for the 2nd iteration is picked directly from maxima of the slowness vectors in Figure 7a. The new velocity function is still chosen to contain only gradients with no layers yet specified. The 2nd iteration is shown in Figure 7b and it is apparent that the correct velocity function is being approached. Again, the updated velocity profile is chosen to contain only gradients and the imaged data are shown in Figure 7c. At this point the velocity discontinuity at 5 km depth is sufficiently clear to justify the inclusion of a layer in the updated velocity velocity model. The velocity model picked from the image in Figure 7c consists of a gradient in the second layer which extends to 5 km depth. The third layer extends from 5 to 16 km in depth and includes only the gradients shown as the dashed line in Figure 7d. As described in the previous section, ray tracing should start with the smallest slowness and search along the deepest region of the model. For the case of the trial velocity function used for iteration 4, the velocity contrast between layers 2 and 3 is approximately 2.5 km/sec - 3.4 km/sec. It is not possible to find a ray that emerges with a slowness $p_0 = 1/3.0$ and bottoms in layer 3 of the model.

This slowness may only be modeled by a ray which bottoms (in this case reflects) in layer 2 and so the ray search is carried out along this path. Iterations 5 and 6 are shown in Figures 7e and 7f and use velocity models restricted to a single layer beneath the 5 km discontinuity which consists of updated gradients picked from the image. At iteration 8 (Figure 7h), a new layer is added at 10 km depth based on the discontinuity observed in the image of iteration 7 (Figure 7g). Finally, Figure 8 shows the image obtained when the correct velocity model is used for the downward continuation. Comparing Figure 8 with Figure 7h verifies that the condition of convergence (the velocity profile being imaged by the downward continued data) is met for the case of a 2-D overburden. Figures 7a-h illustrate that a realistic underlying 1-D velocity profile may be extracted from a model in which a significant known 2-D overburden exists. The data consisted of an unreversed refraction profile of sufficient offset to record rays which bottom at the depths of interest. The basic pattern of convergence observed in the 1-D case is generally repeated for this 2-D approach. The starting model was simple and far from the true model. The updated velocity models picked from the image quickly drove the problem to convergence. A more detailed discussion of the convergence and uniqueness properties is found in a subsequent section.

The introduction of first order velocity discontinuities or layers during the convergence process involves an additional degree of subjectivity on the part of the user. This issue is not present in the 1-D case because the analytic downward continuation expressions integrate over the discontinuities with no special treatment. The ray field however is less robust, and in order for the correct ray paths to be found the velocity discontinuities must be explicitly modeled.

Laterally Varying Gradient Model

We now consider a more general application of our approach to a model where velocity varies with both depth and offset. Figure 9 illustrates both the velocity structure and the acquisition geometry used in this example. Receivers are positioned at coordinates

0, 30, and 60 km along the line and each receiver recorded sources with offsets to 90 km. The velocity structure consists of a gradient at 0 km offset which ranges between 2.5 km/sec at the surface to 4.5 km/sec at 20 km depth. The gradient changes laterally as well and at 200 km offset increases from 4.75 km/sec at the surface to 6.75 km/sec at depth. This example demonstrates the ability of our technique to extract a true 2-D velocity model from the slowness-decomposed wavefields of a multiple receiver (or source) refraction survey.

A velocity model consisting of a laterally homogeneous gradient ranging from 1.5 km/sec at the surface to 5.5 km/sec at 20 km depth is used as an initial model. A three-dimensional representation of the initial model is displayed as the shaded surface in Figure 10a. The nearly horizontal axis represents the offset dimension of the model and the nearly vertical axis represents depth. The remaining axis represents slowness and appears to be oriented approximately perpendicular to the page. An increase in velocity with depth is illustrated by the trend of the shaded surface from large p values at shallow depths to smaller p values at larger depths. We see no variation in the shaded surface as a function of offset in Figure 10a because the initial model is chosen to be laterally homogeneous. The vertical lines in Figure 10a correspond to $\tau - p$ vectors which have been imaged onto the initial model using Equations 1-4. The $\tau - p$ representation of the refracted arrivals are connected by the dashed lines in Figure 10a and have clearly imaged to a depth shallower than the shaded trial velocity field. The data have imaged above the trial velocity field because the trial field was slower than the true velocity model. The $\tau - p$ arrivals appear very compressed in Figure 10a because of a strong gradient with respect to depth of the downward continuation operator at depths far from that at which velocity equals slowness. An updated velocity model is picked from those points connected by dashed lines in Figure 10a. In this case we linearly interpolate (in velocity) between the discrete points at which the updated velocity model is defined. Figure 10b illustrates the result of imaging the data when using the correct velocity model. In this case the data have imaged onto the

shaded surface which is the true velocity model used to compute the synthetic data. This graphical representation of the data imaging onto itself contrasts with Figure 10a. In Figure 10a the incorrect velocity field is used in the downward continuation and the data image to a surface which lies well above the shaded region. We have shown every 10th slowness for the sake of clarity in Figures 10a and 10b.

Figures 11a, 11b and 11c show the misfit between the input model (solid line) and the updated model (dashed line) as a function of depth only. The comparison is made by evaluating the input and updated model at offsets and depths corresponding to bottoming points of turning rays. When the updated model is the same as the input model, the data have imaged onto themselves and convergence is achieved. Figure 11 shows that after 3 iterations the simple laterally-varying gradient model has nearly been retrieved. This demonstrates that the method of model updates is both stable and convergent. All updated models were calculated by linearly interpolating in velocity between those discrete points at which the updated models were defined.

This example shows the ability of our method to determine and image a true 2-D velocity field from multiple large offset gathers. Figure 10a shows the imaged data which used an incorrect trial velocity function in the downward continuation. The data have obviously not met the condition of convergence, which we define as imaging onto the trial velocity function. Figure 10b shows the result of using the correct trial velocity model in the downward continuation; the data image onto the velocity model. Figure 11 shows the convergence properties of this simple model demonstrating that our method of updating the 2-D model may be stable and convergent.

Resolution and Convergence

The resolution of our 2-D velocity inversion/imaging approach is best estimated by inspection of the final 2-D velocity image. We use the 2-D laterally-varying gradient model presented in the previous section to examine the issue of resolution and illustrate how the velocity image may be interpreted to estimate some measure of model

goodness. Figure 12 shows the final velocity image; the points which define the model are shown by the positions of the imaged $\tau - p$ wavelets. Unresolved portions of the velocity model are indicated by the lack of imaged bottoming points in these areas. The velocity in the region of the model from 0 to 10 km of offset and 10 to 20 km of depth (region A) is completely unconstrained by the three-receiver gather geometry of this example. The upper right corner of the model from 90 to 100 km of offset and 0 to 10 km of depth (region B) is also poorly constrained. There are no bottoming points in either of these regions; as a result, our approach has no way of directly updating the velocity field. Well-constrained portions of the model are those regions which contain many bottoming points. The central portion of the velocity model in Figure 12 is fairly well resolved and this is evident by the volume of bottoming points in this region of the model. In the well-resolved central portion of the model, the issue of resolution may be examined on a smaller scale. The bottoming points between receiver gathers are approximately 30 km apart. This is due to the original 30 km receiver spacing, and thus the model updates are performed by interpolating over 30 km of offset where no rays actually bottom. In this example we used a linear velocity interpolation, which was appropriate because the correct model contained lateral linear velocity gradients. For the simple laterally linear velocity trend, a minimum of two bottoming points at the same depth but at different offsets are required. In general, the wavelength of the lateral velocity variation must be sampled sufficiently in terms of the lateral density of bottoming points to allow accurate estimation of the velocity structure. The interpolation step inevitably smooths over lateral velocity variations occurring between bottoming points which are thus not adequately sampled.

Another aspect of resolution has to do with the bandwidth of the original seismic experiment. Our approach maps the entire wavefield to the model space allowing decisions regarding the quality and resolving power of the data to be made directly in this space. Low-frequency narrow-band data will manifest itself as a wide, relatively ambiguous pulse when mapped to the model space. Poor data quality and the

resulting poor model resolution may also be observed when mapping the complete wavefield directly to the model space. Portions of the model defined by noisy arrivals are obvious by inspection of the final velocity image and may be treated accordingly.

We address the issue of convergence by examples and discuss the effect of a non-constant ray parameter in 2-D media on convergence. The synthetic dipping layer example is a fairly restrictive test of the convergence behavior. In this example the 2-D overburden is fixed and the velocity updates are one-dimensional. The additional degrees of freedom compared to the 1-D case are due to the changing ray parameter along the 2-D ray path. Unlike the 1-D approach where a given slowness vector $\tau - p_0$ is imaged directly to $z - p_0$, the 2-D approach allows $\tau - p_0$ to be imaged to $z - p_b$ (p_0 being the observed ray parameter and p_b being the bottoming ray parameter). When an incorrect velocity structure is used in the downward continuation, the p_b computed via ray tracing is incorrect and the data are not "p shifted" properly. For instance, in the dipping layer example the 2-D nature of the model caused an observed ray parameter $p_0 = 0.248 sec/km$ ($v = 4.028 km/sec$) to be shifted to $p_b = .221 sec/km$ ($v = 4.511 km/sec$) when using the correct velocity model. When using the incorrect model in iteration 1 (Figure 7a), the observed ray parameter $p_0 = .248 sec/km$ was shifted to $p_b = .230 sec/km$ ($v = 4.337$). Thus, the incorrect velocity model positioned the slowness vectors inaccurately not only in depth (z) but also in p. However, this example shows that the additional degree of freedom allowed by the "p shifting" does not prevent convergence. The image based model updates are sufficiently robust enough to overcome this issue and drive the model to convergence.

The 2nd synthetic example is a more general test of the convergence properties for the 2-D problem. Unlike the previous example where the 2-D overburden was fixed, the entire model is updated at each iteration. The proper (using the correct model) "p shifting" computed for a $p_0 = .223 sec/km$ ($v = 4.47 km/sec$) for instrument 1 (0 km offset) is $p_b = 0.204 sec/km$ ($v = 4.90 km/sec$). The starting model was laterally constant for this example and therefore there was no "p shifting" in the 1st

iteration. The updated velocity models however were laterally varying, and eventually introduced the appropriate "p shifting" which drove the solution to convergence.

As more complex velocity models are imaged, the path to convergence will be significantly more complicated than for the case of a laterally-varying smooth gradient. For such models, the large density of bottoming points that are required to adequately sample the wavelength of velocity variations will aid both in guiding the model updates and in pushing the solution to convergence. Since the p_0 to p_b shift is only a function of velocity structure, as the velocity structure moves closer to the correct model, the "p shifting" becomes more accurate as well.

Field Data

We demonstrate the velocity inversion/imaging technique on field data using a 53 km long refraction line acquired with an Ocean Bottom Hydrophone (OBH) recording a 10,800 cubic inch airgun array. The data were collected during a joint reflection/refraction survey conducted by the University of Texas at Austin and the Woods Hole Oceanographic Institution across the continental margin of the East Coast of the U.S. (Stoffa et al., 1988; Reiter et al., 1988). The reflection data were recorded using a 6000 m streamer with a 25 m group interval; they show significant 2-D structure along the 53 km of line used in this example. Figure 13 shows the stacked section as well as the location of the OBH approximately halfway up the topographic shelf. The most obvious 2-D component of structure is the seafloor which shallows from 2600 m at 53 km offset to 1885 m at the OBH location. In this example, we consider only a single refraction line to demonstrate that the major 2-D structures may be correctly accounted for, and the surrounding 1-D velocity structure imaged using the method detailed in this paper. The OBH data are shown in Figure 14 with a reduction velocity of 6 km/sec. Figure 15 shows the $\tau - p$ representation of the data obtained with short overlapping semblance weighted slant stacks (Stoffa et al., 1981). The data are slant stacked over 5 km apertures with a 2.5 km shift between stacks and weighted by a

low-pass filtered estimate of the semblance. Seventy five slownesses between 1./(2.5 km/sec) and 1./(20.0 km/sec) are used in the $\tau - p$ decomposition. Larger slownesses corresponding to velocities in the near-bottom sediments were excluded for the sake of clarity. These near-bottom velocities were constrained by forward modeling (Holbrook et al., 1990) and held constant during the inversion.

A starting model is chosen, with the seafloor and the structure of the upper 2.0 km sediment assumed to be known. These structures remain fixed throughout the inversion, and an underlying 1-D velocity structure is sought. An initial model consisting of a simple gradient (solid line) is used for the 1st downward continuation; the resulting image is shown in Figure 16. The updated model may be represented by a simple slowness vs. depth plot (e.g., Figure 16), because the updated model is 1-D. Figure 16 shows that the downward continued data do not image the input velocity structure, and an updated model is picked from the image. In this example we chose smooth model updates in the initial stages of the inversion. After the fourth iteration, distinct layers were added as indicated by the images similar to the synthetic example shown in Figure 7. After 9 iterations, three layers had been added and convergence was achieved. Figure 17 shows the final velocity model (solid line) together with the imaged data. The data have correctly imaged the input velocity function and show several distinct features. A mid-crustal velocity discontinuity, most likely the termination of the sedimentary column, is clearly seen near 9 km depth. This is marked by reflection labeled "9 km" in the raw data of Figure 14 and in the $\tau - p$ representation in Figure 15. The velocities increase from approximately 4 km/sec to over 5 km/sec at this interface. The next deeper reflection labeled "15 km" images to a depth of roughly 15 km, and although weaker than "9 km", clearly indicates the presence of significantly higher velocities at this depth. The region between "9 km" and "15 km" is imaged as a gradient with velocities increasing to over 6 km/sec at 15 km depth. Velocity increases at boundary "15 km" to over 7 km/sec with the next constraint being a prominent wide-angle reflection labeled "23 km" in Figures

14 and 15. This reflection is assumed to come from the Moho and is observed at offsets from 48-53 km. At these offsets this event emerges as a first arrival and has an apparent velocity of approximately 8 km/sec. The velocity image in Figure 17 places this event at around 22-23 km deep; this is consistent with the interpretation that this is transitional crust Moho (Holbrook et al., 1990; Austin et al., 1990).

In this example we have shown that our ray-based 2-D approach to velocity imaging can properly account for known, large-scale lateral heterogeneities and extract an underlying 1-D velocity function. A sea floor which shallows from 2.6 to 1.8 km is properly accounted for and velocities are imaged to depths of 25 km. Laterally-varying seafloor depth is an example of a common 2-D overburden that can be effectively removed with this technique. Other near-surface 2-D structures, such as highly deformed sedimentary sequences, are more difficult to constrain than the water column; errors made in these structures will result in errors in the underlying 1-D structure. With a single refraction line, additional information is almost always necessary if a 2-D structure is to be adequately resolved. In this case this information was provided by a coincident reflection survey. If 2-D structure is to be determined with refraction data alone, multiple large offset lines are required as discussed earlier.

Discussion

Our 2-D velocity inversion/imaging approach follows the wavefield transformation idea of Clayton and McMechan (1981). The best fitting model is defined by the bottoming points of rays corresponding to observed ray parameters. This model is displayed as a surface embedded in the three-dimensional data volume of offset-slowness-depth. This provides a convenient and compact way to display both the velocity model and the data from which the model was derived. The data themselves indicate which portions of the model are well constrained and which portions were obtained through excessive interpolation (or extrapolation) of the discretely defined velocity surface. Figure 12 illustrates how a 2-D velocity surface is defined at the

point of convergence by multiple refraction gathers. We feel that this approach is a promising one as large offset data acquisition increases in volume and forward modeling grows increasingly cumbersome. Increased volumes of data present two major difficulties for traditional methods of forward modeling. The first is simply the increased amount of time required to model the additional volume and detail present in the observed wavefield. The second is the need for some quantitative measure of certainty to be associated with the final or best fitting model. Our approach is both amenable to large data volumes and provides a measure of model goodness by inspection of the final velocity image.

There have been several other attempts to remove the 1-D limitation in $\tau - p$ inversions. Milkereit et al. (1985) describe a method for inversion of $\tau - p$ data for planar dipping layers. In their approach, the '$\tau - sum$' of Diebold and Stoffa (1981) is extended to allow for constant dip iso-velocity interfaces. They give expressions for roll along, split spread and reversed- profile geometries. Discrete $\tau - p$ picks from multiple gathers are used to solve for the necessary dips and velocities. It is noted that their approach is automatic and stable for dips up to 8 degrees. Bisset and Durrant (1990) propose a method to remove the effect of layers with known dip in the $\tau - p$ domain, thus allowing 1-D operators extended regions of applicability. This method involves transformation of the original $\tau - p$ data to simulate data acquired on a surface parallel to the dipping boundary.

Our method is less restrictive than the planar dipping layer approach of Milkereit et al. (1985). We assume no formal restrictions on the dip or curvature of the velocity field being imaged. The requirement that the data image onto the velocity surface when the correct velocity field is used in the downward continuation is valid for planar as well as non-planar dipping boundaries. An important practical consideration however, is the difficulty in converging to a complicated velocity velocity model with realistic sparse data sets. The updated velocity fields are defined only at those offsets and depths at which turning rays are found to bottom. The smallest lateral veloc-

ity wavelength that can be resolved is restricted by the lateral density of bottoming points.

Conclusions

A technique for determining 2-D velocity structures from large offset slowness-decomposed data has been presented. The fundamental idea of iterative wavefield continuation first presented by Clayton and McMechan (1981) has been extended to allow velocity to vary with both offset and depth. We use numerically computed raypaths to downward continue the slowness-decomposed data to a model space with dimensions of offset-slowness-depth. By using rays to perform the downward continuation, realistic laterally varying velocity structures may be inverted for and imaged. Our procedure is iterative with updated velocity models being picked directly from the imaged data. Our approach is valid for offset-slowness (X-p), total travel time-slowness (T-p) and vertical travel time-slowness $\tau - p$ wavefield decompositions. An additional step is required in the $\tau - p$ case to account for the one-dimensional assumption in the $\tau - p$ transform itself.

We have used synthetic data to examine geometries with a single large offset profile and a known 2-D structure such as a sloping seafloor. In this case we have shown that an underlying one-dimensional (1-D) velocity profile may be accurately determined. The other geometry examined is the more general case of an unknown 2-D velocity field with multiple large offset lines. We show that, provided the velocity structure changes sufficiently slowly with respect to the lateral density of ray bottoming points, the correct 2-D velocity field may be determined. The technique is successfully applied to a 53 km long refraction line consisting of an Ocean Bottom Hydrophone (OBH) recording a near-surface airgun array. A strict requirement of this general type of wavefield continuation is the recording of post-critical reflections and refractions which require large offset acquisition.

Our approach represents an important extension of the now commonly used 1-

D wavefield continuation approach of Clayton and McMechan (1981) to laterally varying media. Dense spatial sampling in large offset experiments is now common, allowing high quality estimates of local slowness from post-critically reflected and refracted arrivals. As a result, the 1-D wavefield continuation approach of Clayton and McMechan (1981) is currently used as a primary tool for velocity analysis (e.g., Hawman et al., 1990; Lyslo and Nowack, 1990). A limiting factor in the use of this technique has been the need for lateral homogeneity. We have eliminated the 1-D restriction on velocity structure; this greatly expands the applicability of this commonly used technique.

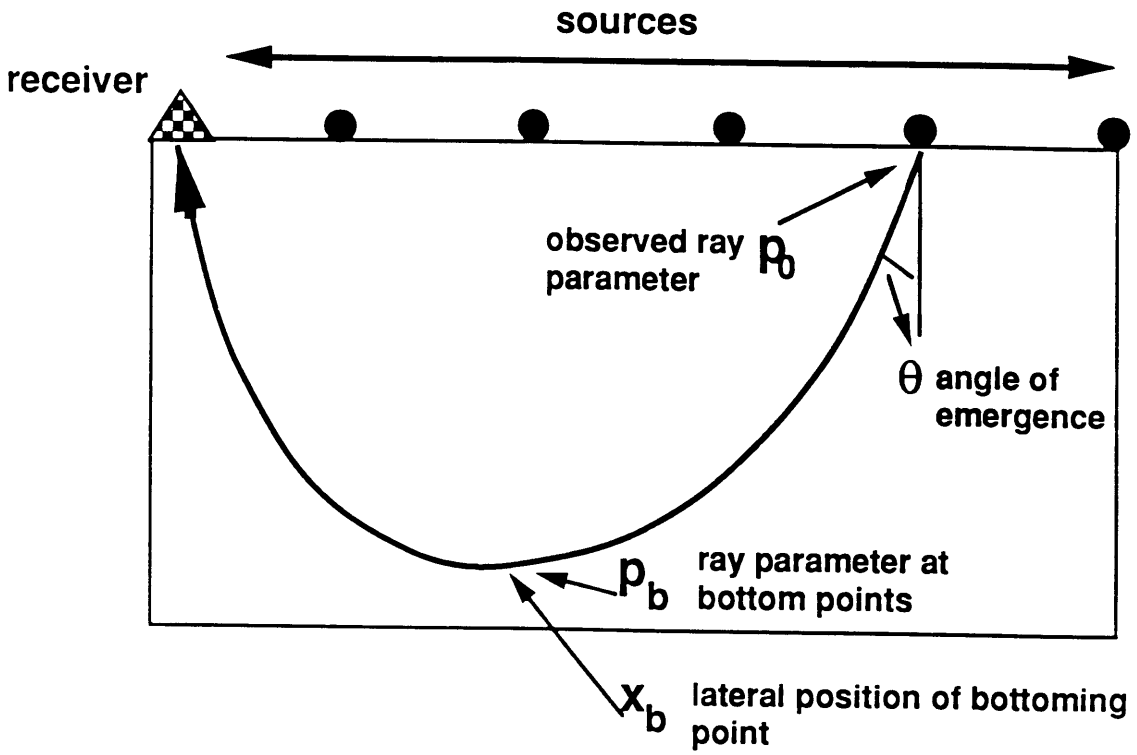

Figure 1. Schematic diagram of a ray path for a receiver gather in a medium where velocity varies in both depth and offset. Slant stacking decomposes a receiver gather into intercept time τ and slowness p_0. In two-dimensional media it is necessary to determine at what position the ray parameter is being measured because the ray parameter is not constant along the ray path. p_b and x_b denote the ray parameter and offset respectively at the bottoming point of the ray path.

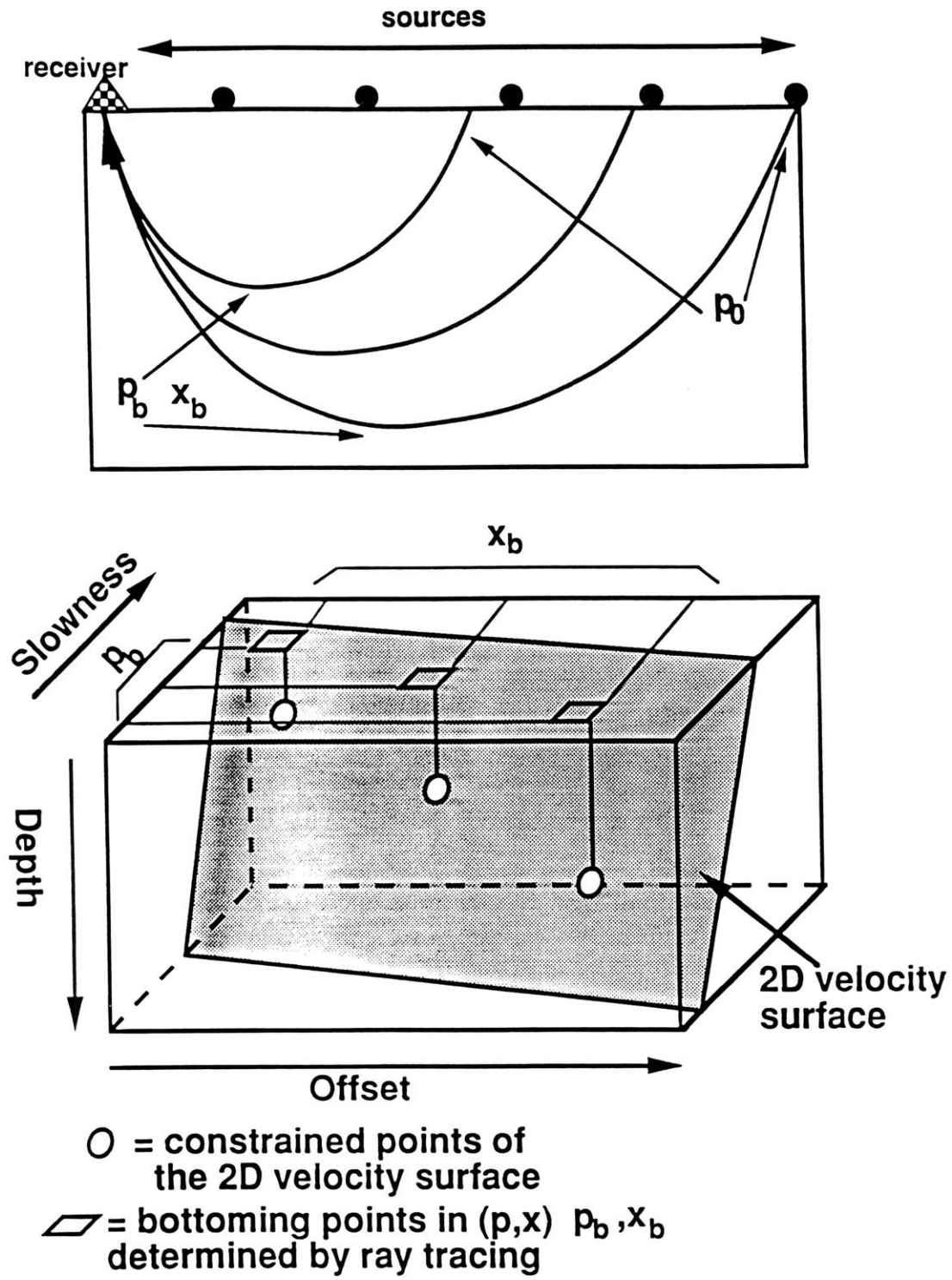

Figure 2. Imaging of a two-dimensional velocity field from slowness decomposed data. a) A ray which emerges with a slowness p_0 is found and the quantities p_b and x_b are saved. b) The slowness decomposed data are then imaged onto the three-dimensional model space $s(p_b, x_b, z)$.

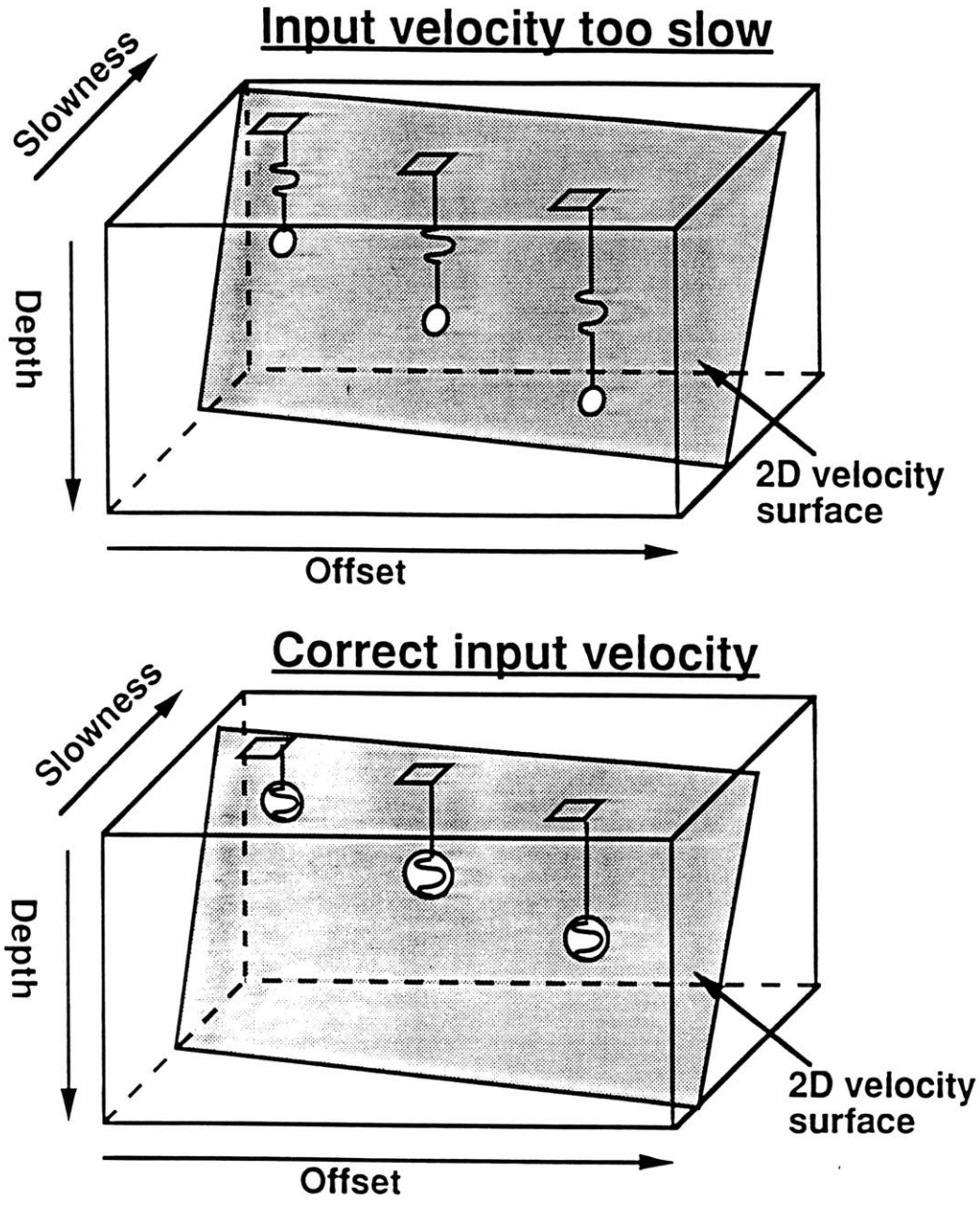

Figure 3. a) The slowness decomposed data are downward continued with a trial velocity field that is too slow. The data do not image the velocity field used in the downward continuation. b) A correct trial velocity model causes the data to image onto this model used in the downward continuation.

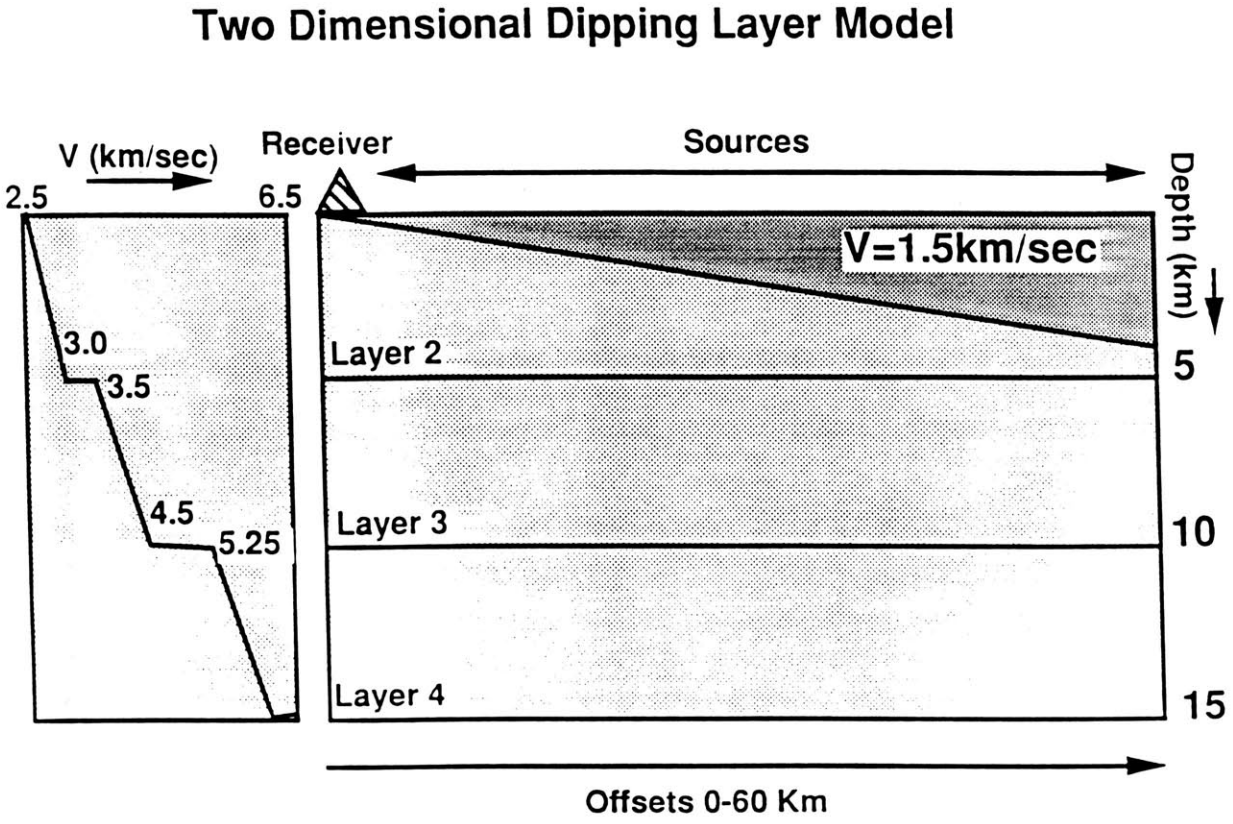

Figure 4. Model used for the dipping layer synthetic example. The dipping layer is assumed known (e.g. sloping seafloor) and the underlying 1-D velocity structure determined.

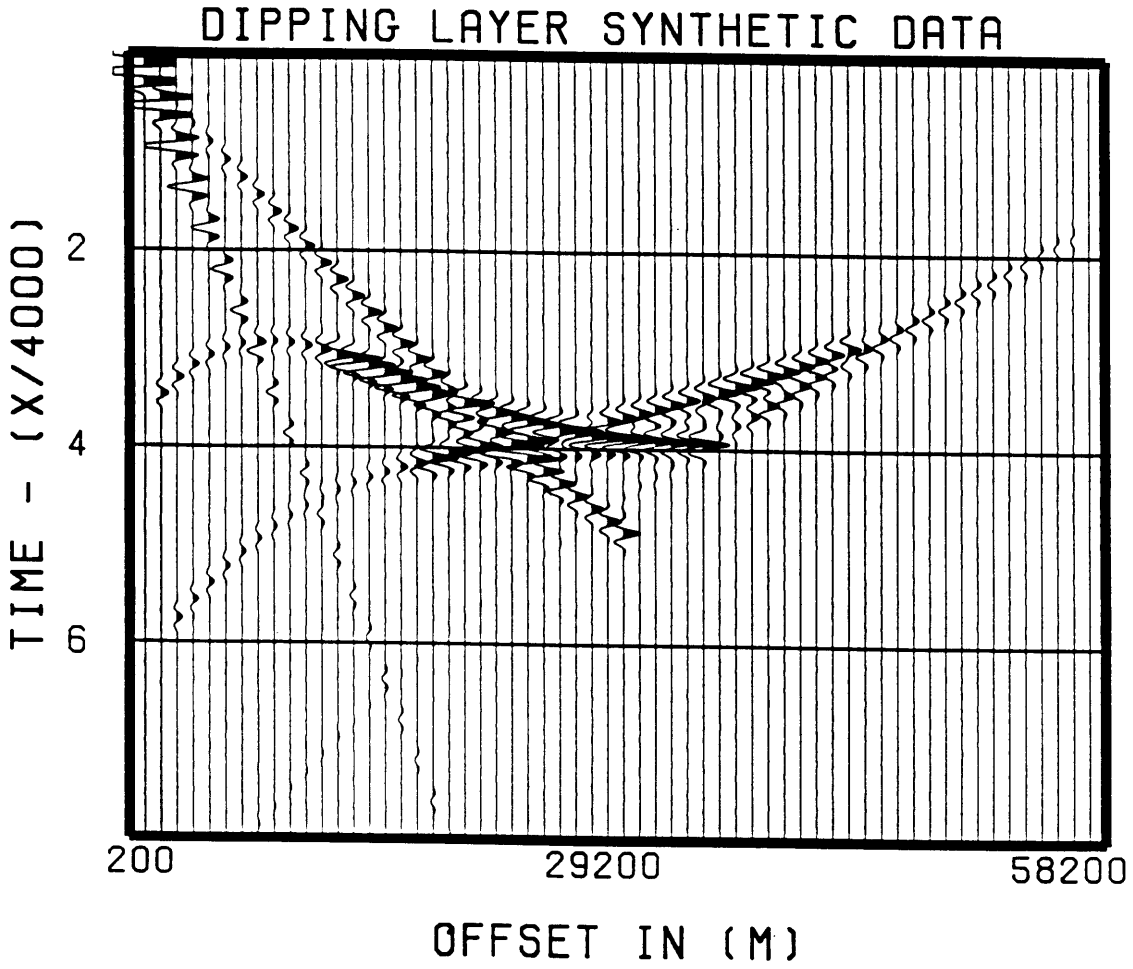

Figure 5. Ray based synthetic data for the model of Figure 4. All possible primary ray theoretical arrivals including refractions and post-critical reflections are present in the data.

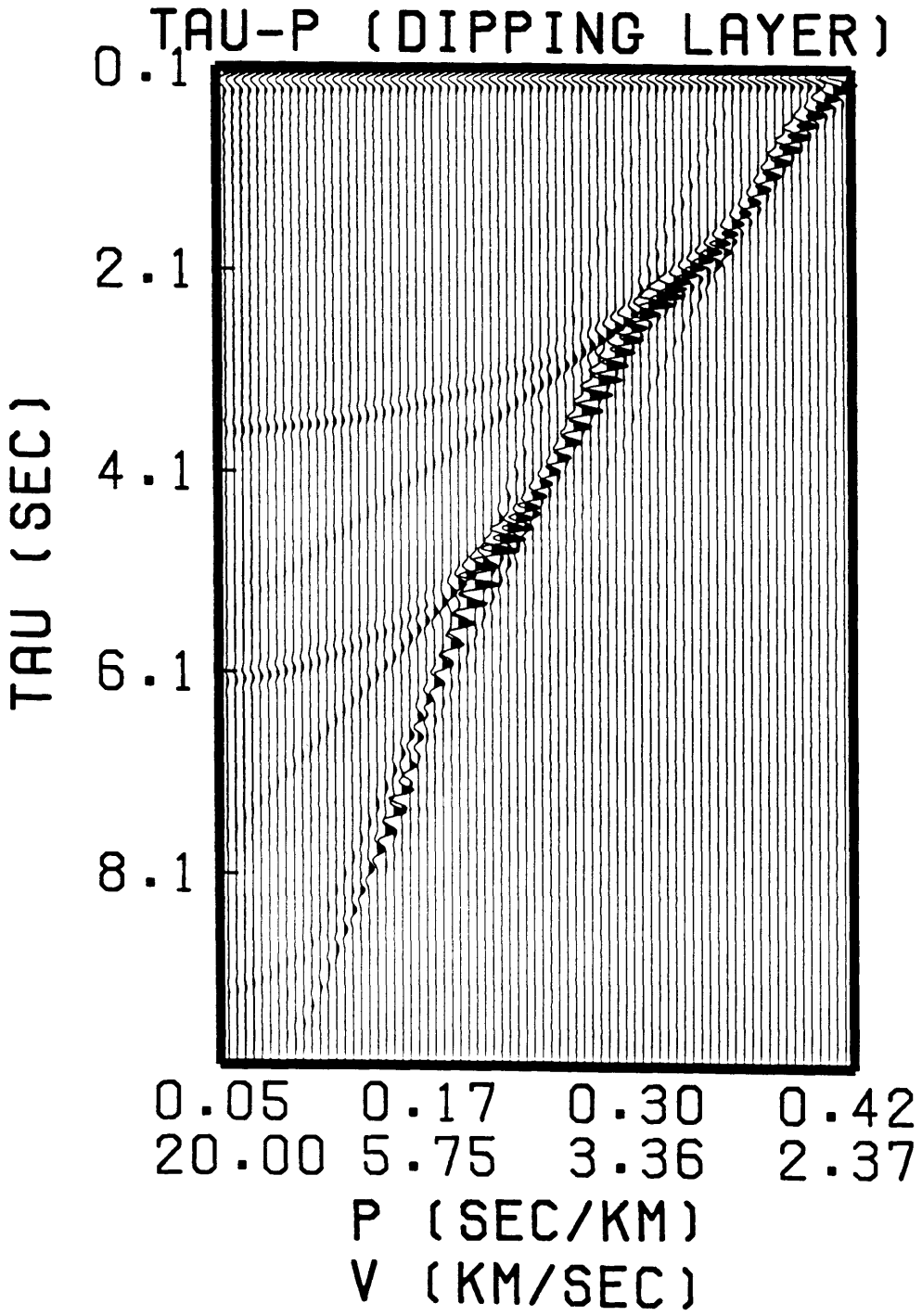

Figure 6. Simple slant stack of the synthetic data in Figure 5. Seventy five slownesses between 1/2.37 and 1/20.0 sec/km are used in the forward transform.

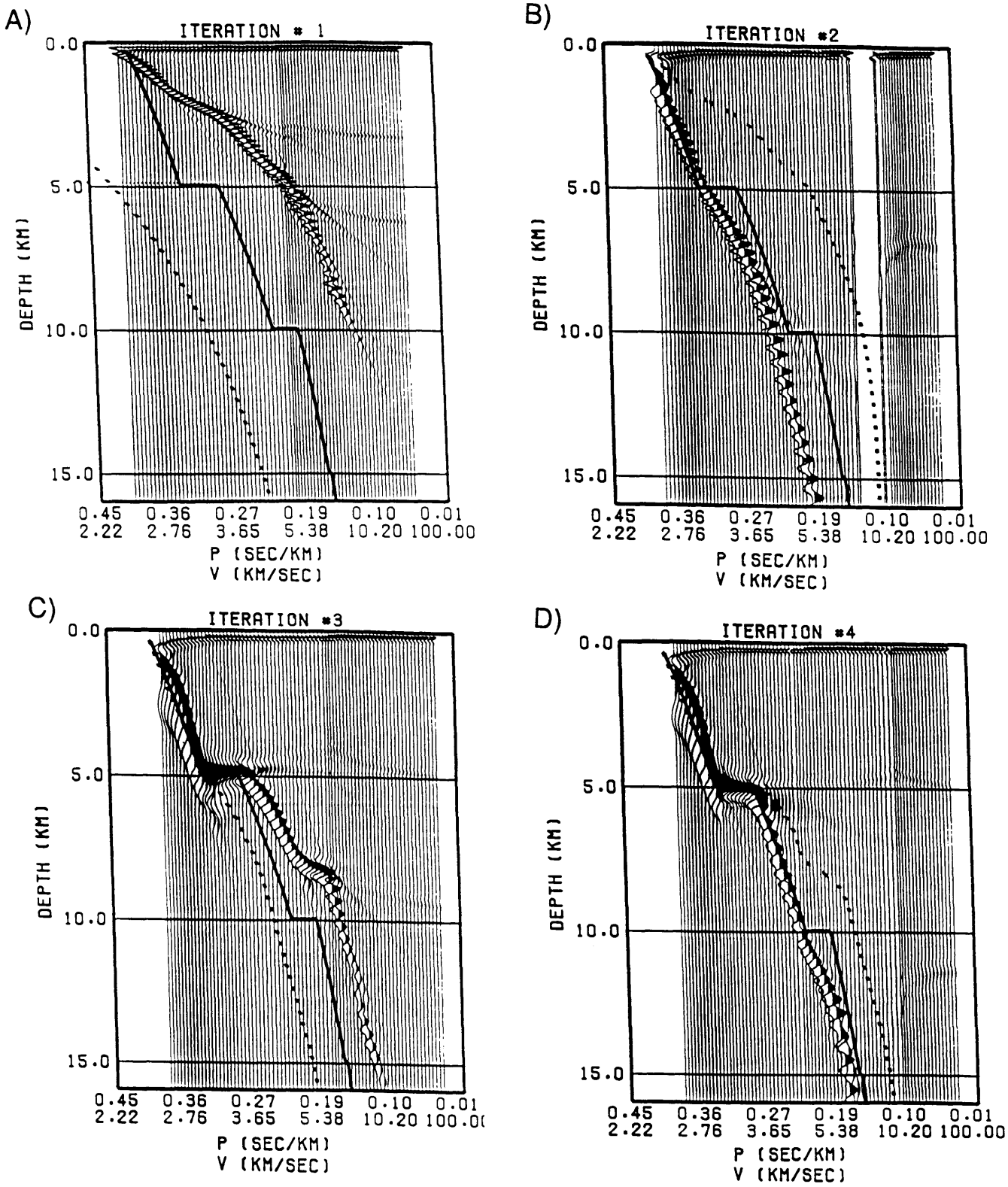

Figure 7a-d. Slowness - depth images from iterations 1-4 showing the convergence to the correct velocity profile obtained with our 2-D velocity inversion/imaging approach. The dashed line represents the velocity profile used in the downward continuation and the solid line represents the correct model. A distinct layer is added at iteration 4.

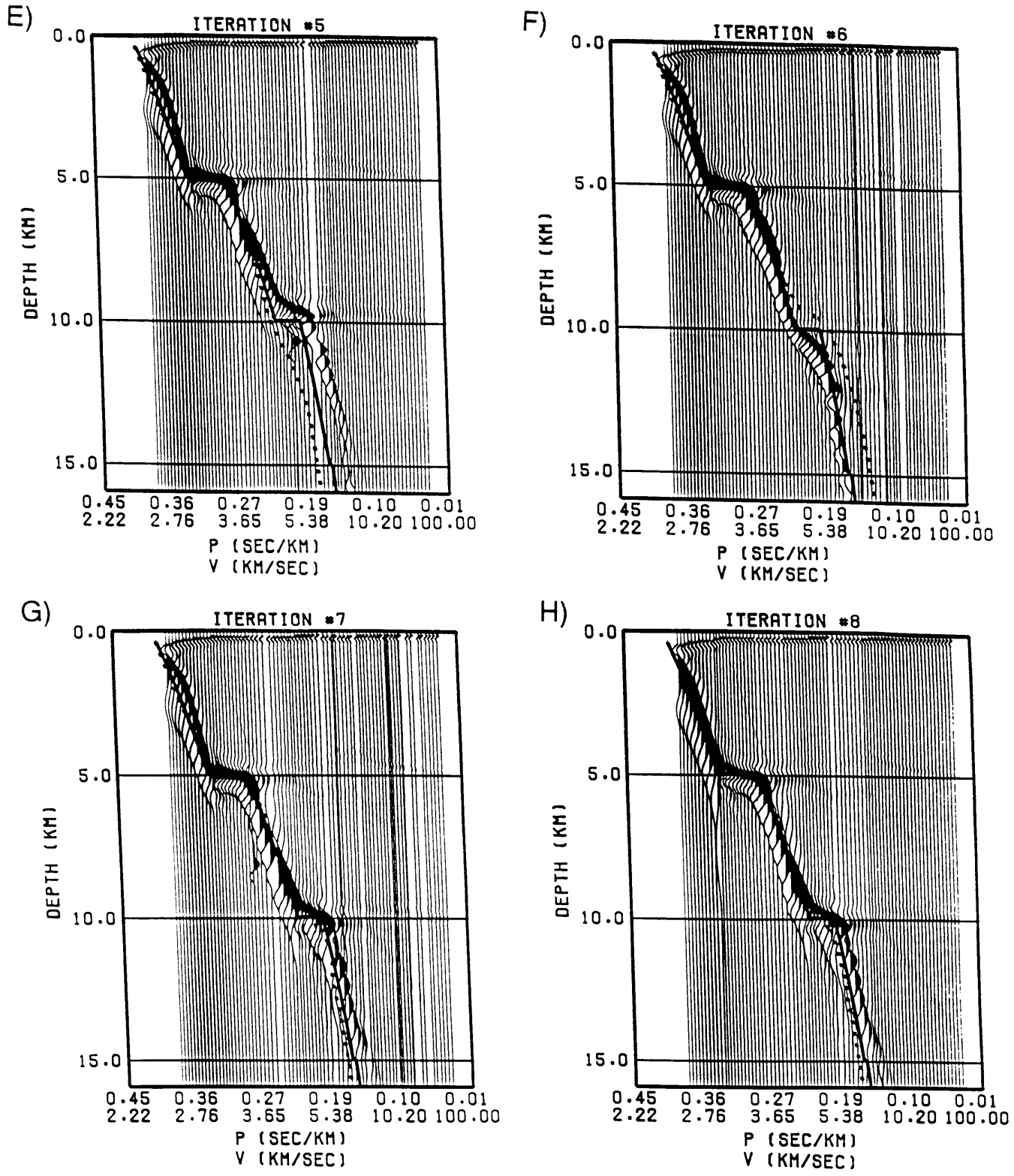

Figure 7e-h. Slowness - depth images from iterations 5-8 showing the convergence to the correct velocity profile obtained with our ray based downward continuation approach. The dashed line represents the velocity profile used in the downward continuation and the solid line represents the true model. A distinct layer is added at iteration 7.

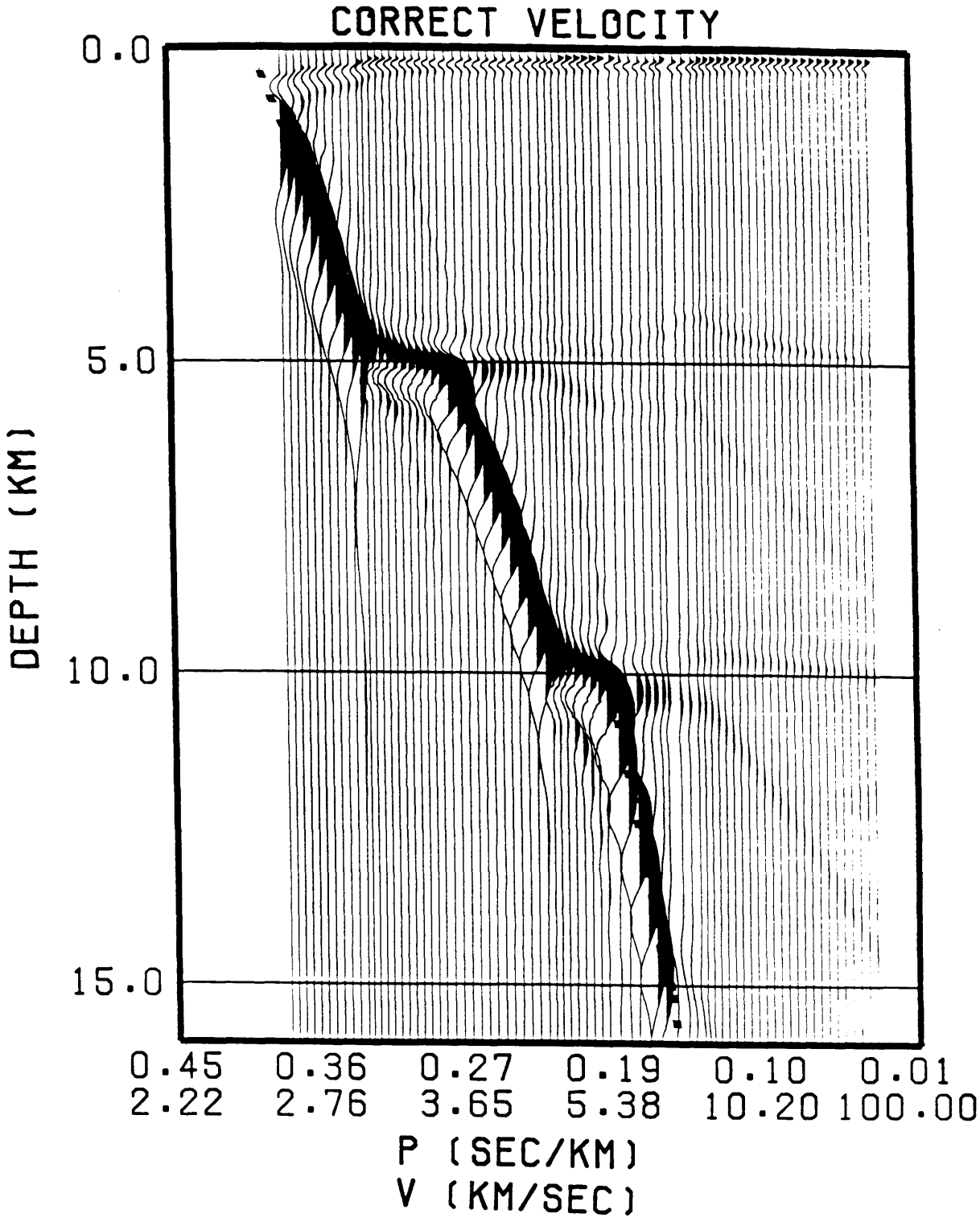

Figure 8. Slowness - depth image obtained when using the correct velocity model in our 2-D approach. The data have imaged the velocity profile used in the downward continuation indicating convergence.

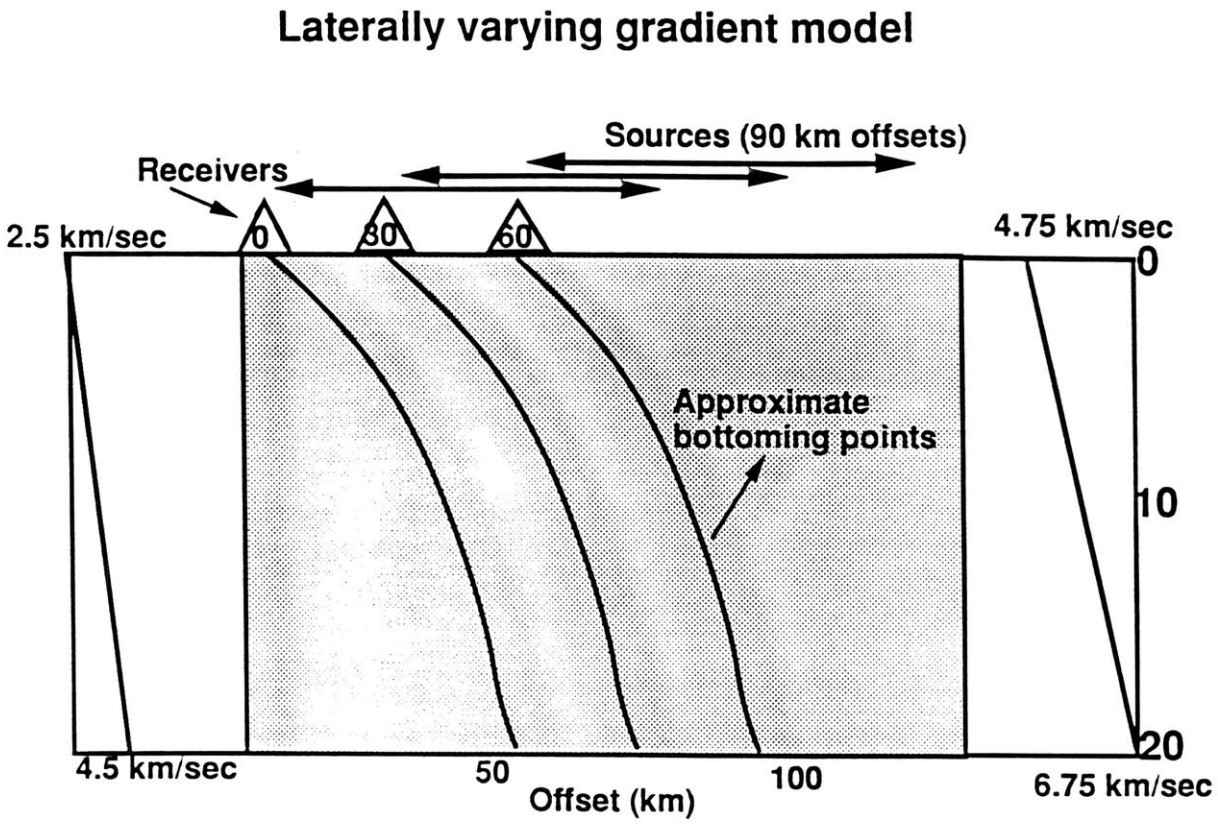

Figure 9. Laterally varying velocity model and acquisition geometry. The data consist of three receiver gathers each recording source offsets from 0 to 90 km. This model is used to demonstrate the success of the 2-D velocity inversion/imaging approach at extracting a true 2-D model from multiple refraction surveys (receiver gathers).

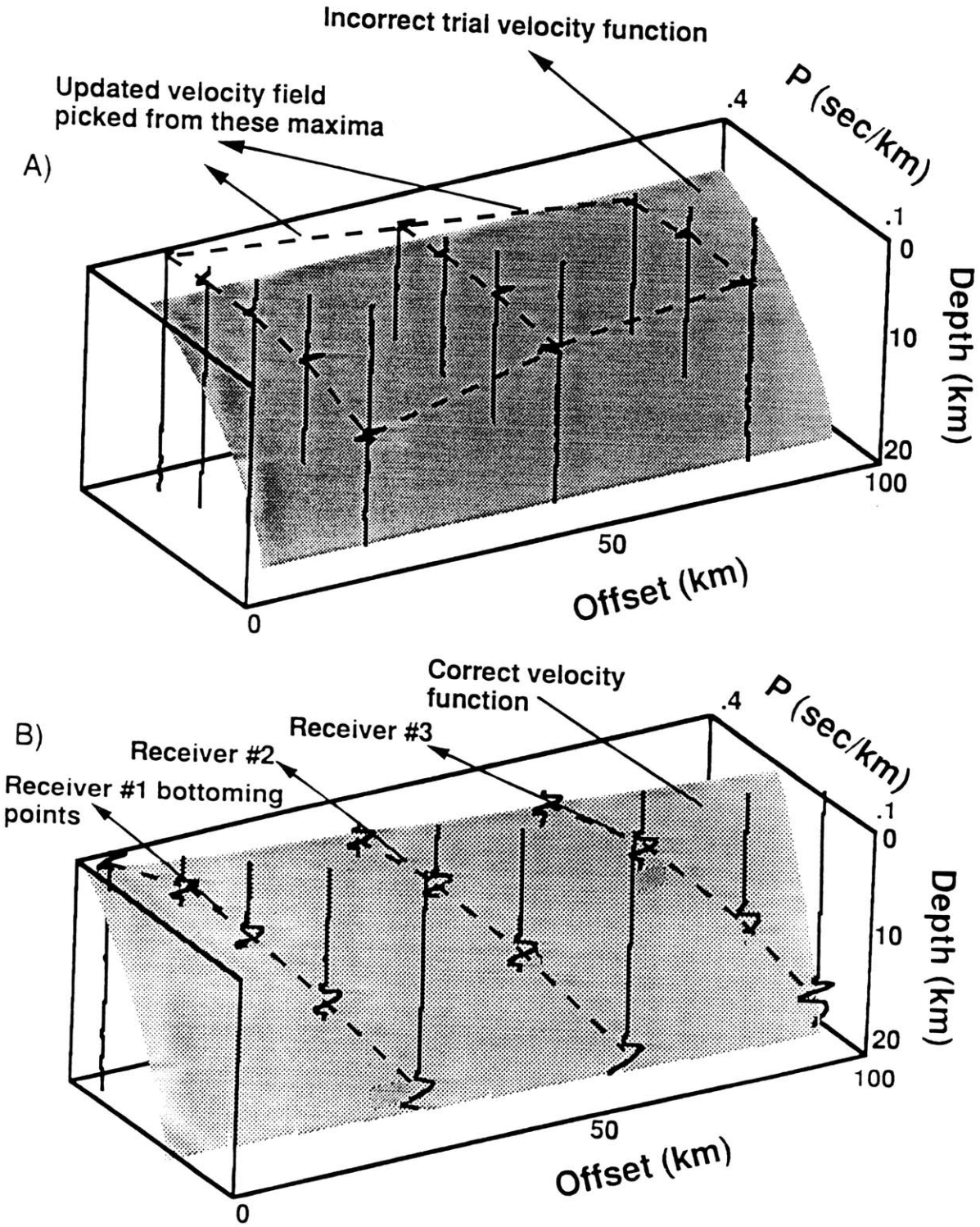

Figure 10. a) Three-dimensional data volume of offset, slowness and depth. The shaded region represents the velocity field used in the downward continuation. The velocity field is incorrect (too slow) and thus the data do not image onto the shaded region. An updated trial velocity field is picked from the image data and is shown by the dashed lines. b) The correct velocity model is used in the downward continuation and the data image onto the shaded region indicating convergence.

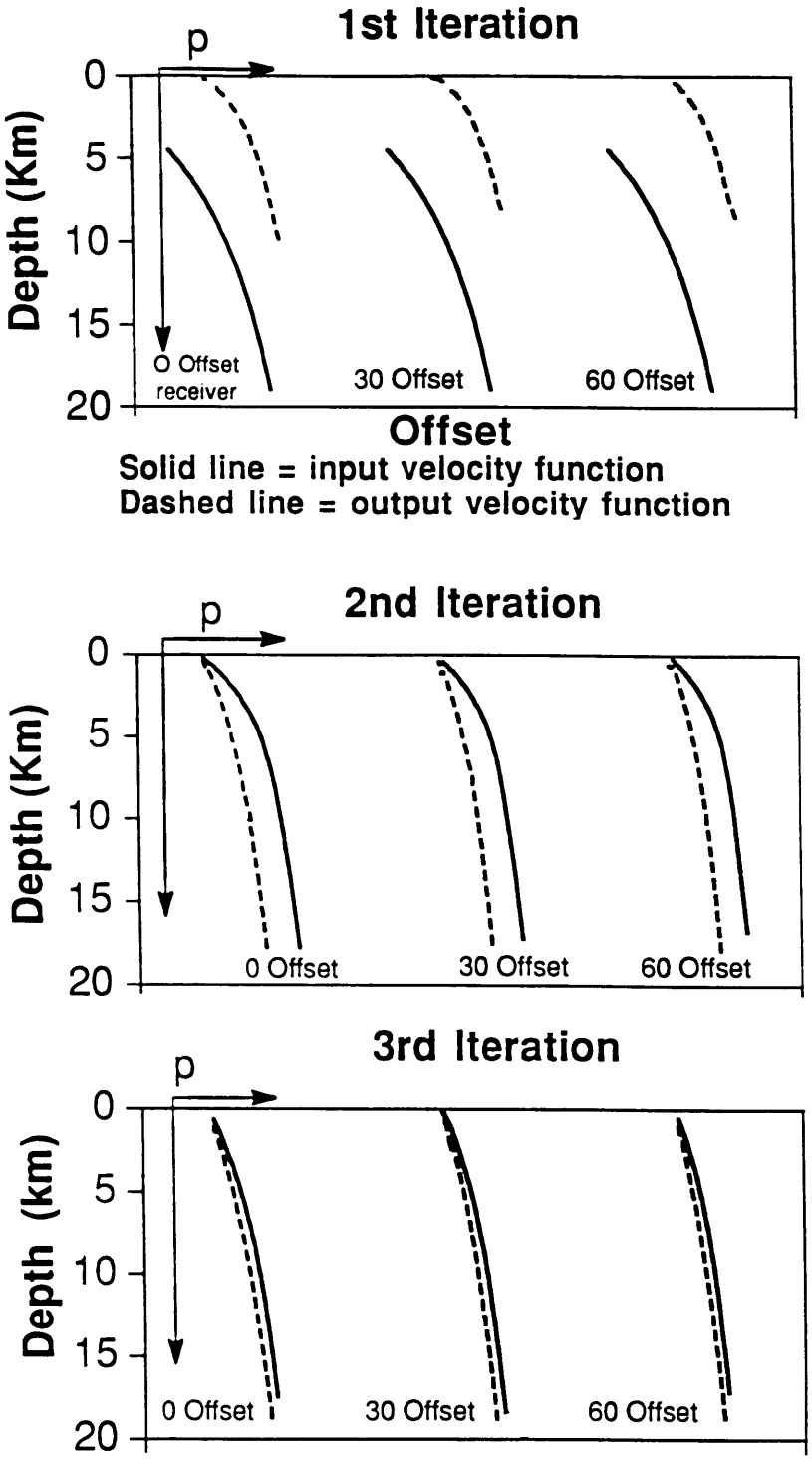

Figure 11. a) The misfit between the updated velocities (dashed lines) and velocity used in the downward continuation (solid) line after the first iteration. b) Second iteration. c) Third iteration. After three iterations the updated model is very close to the input model indicating convergence is occurring.

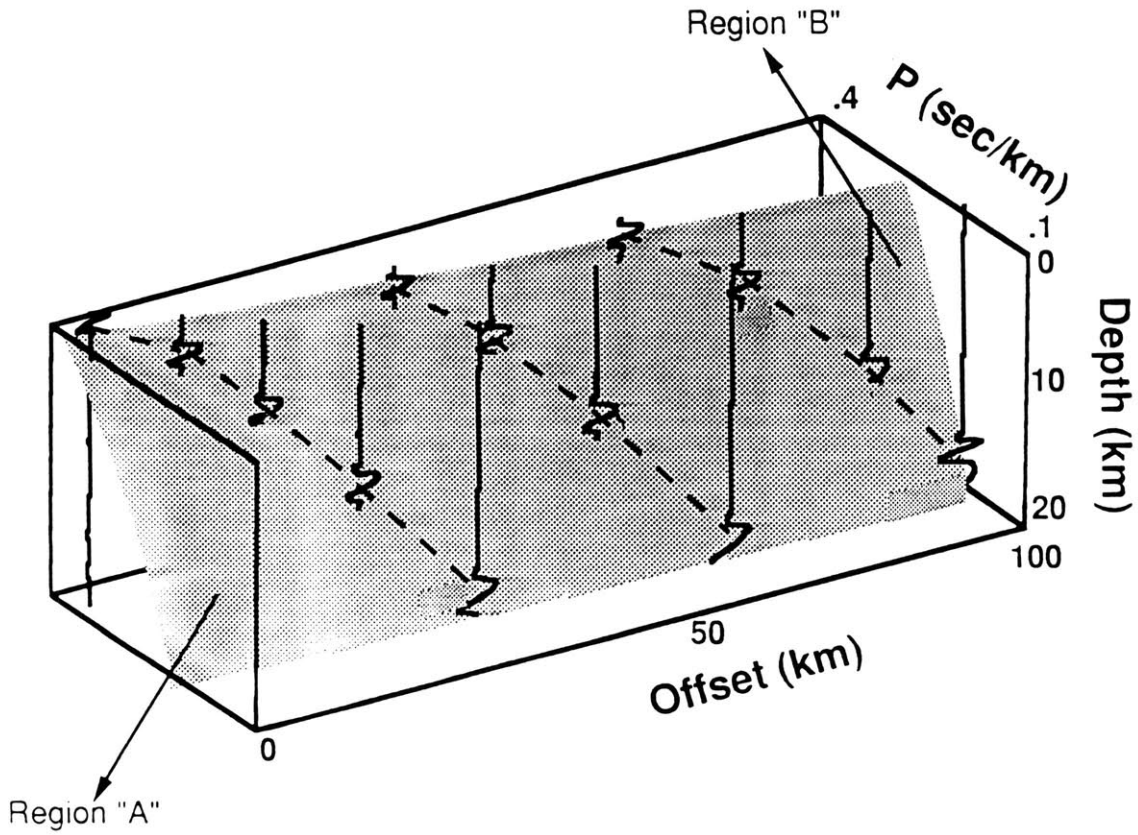

Figure 12. Those portions of the model which contain bottoming points of turning rays are best resolved by our method. The corners of the model do not contain bottoming points and as a result are poorly resolved. The central portion of the model is well defined due to the density of bottoming points.

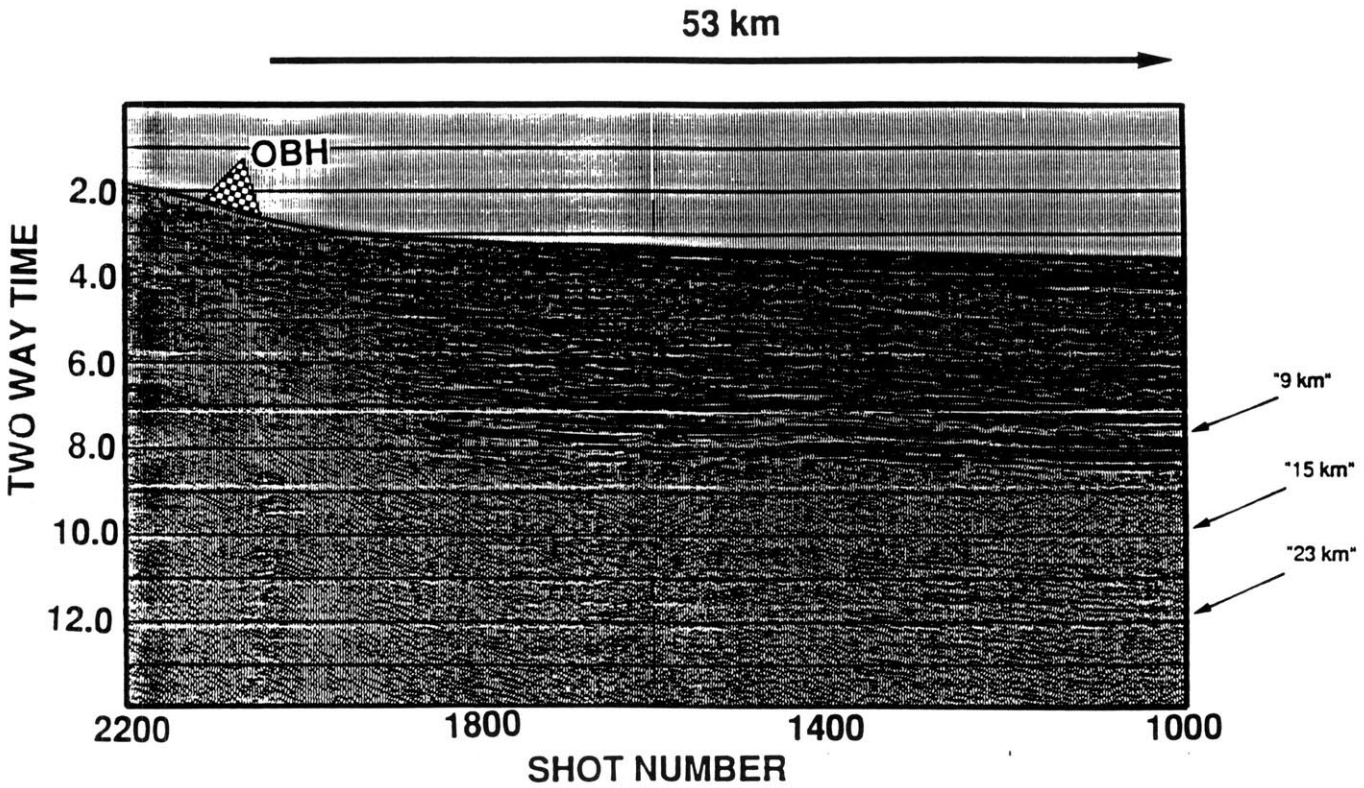

Figure 13. Stacked MCS data from region just east of the Carolina Trough. The OBH recorded the airgun from the MCS survey and is shown in Figure 14. The water bottom shallows from 2600 m to 300 m along the reflection line.

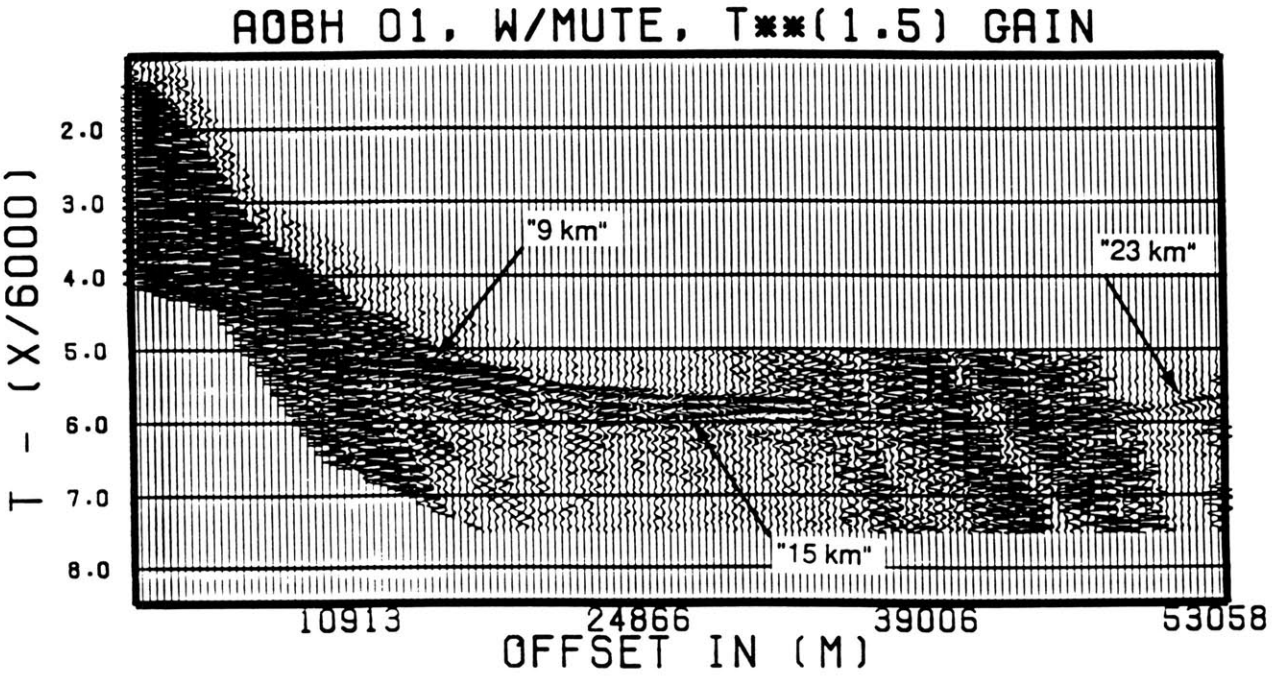

Figure 14. OBH refraction data acquired during the a MCS survey. The data are scaled with a $T^{1.5}$ factor.

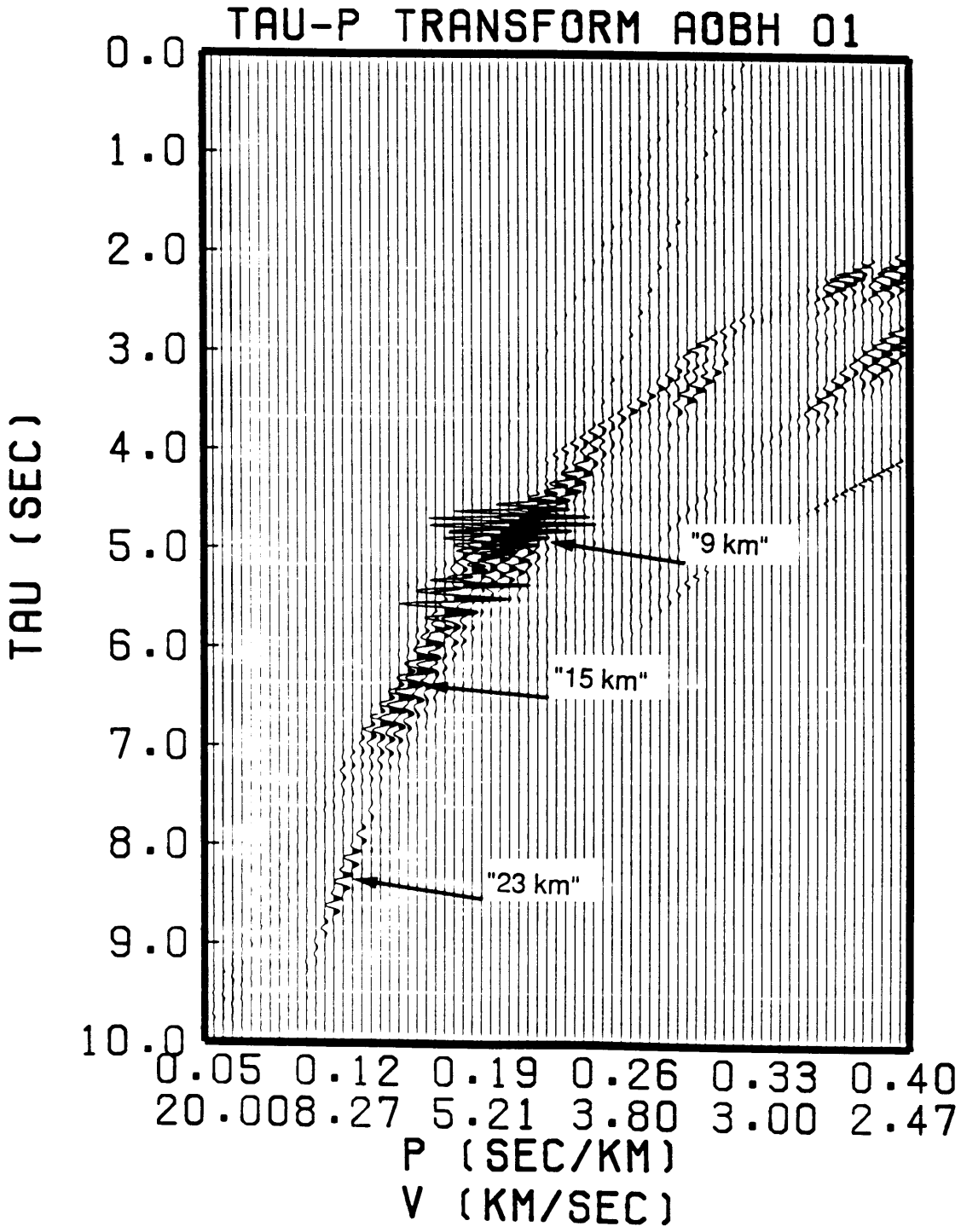

Figure 15. Slant stack obtained from OBH data in Figure 14. The data are stacked in 5 km sub-arrays and weighted by a low passed estimate of the semblance. A shift of 2.5 km between sub-arrays is used.

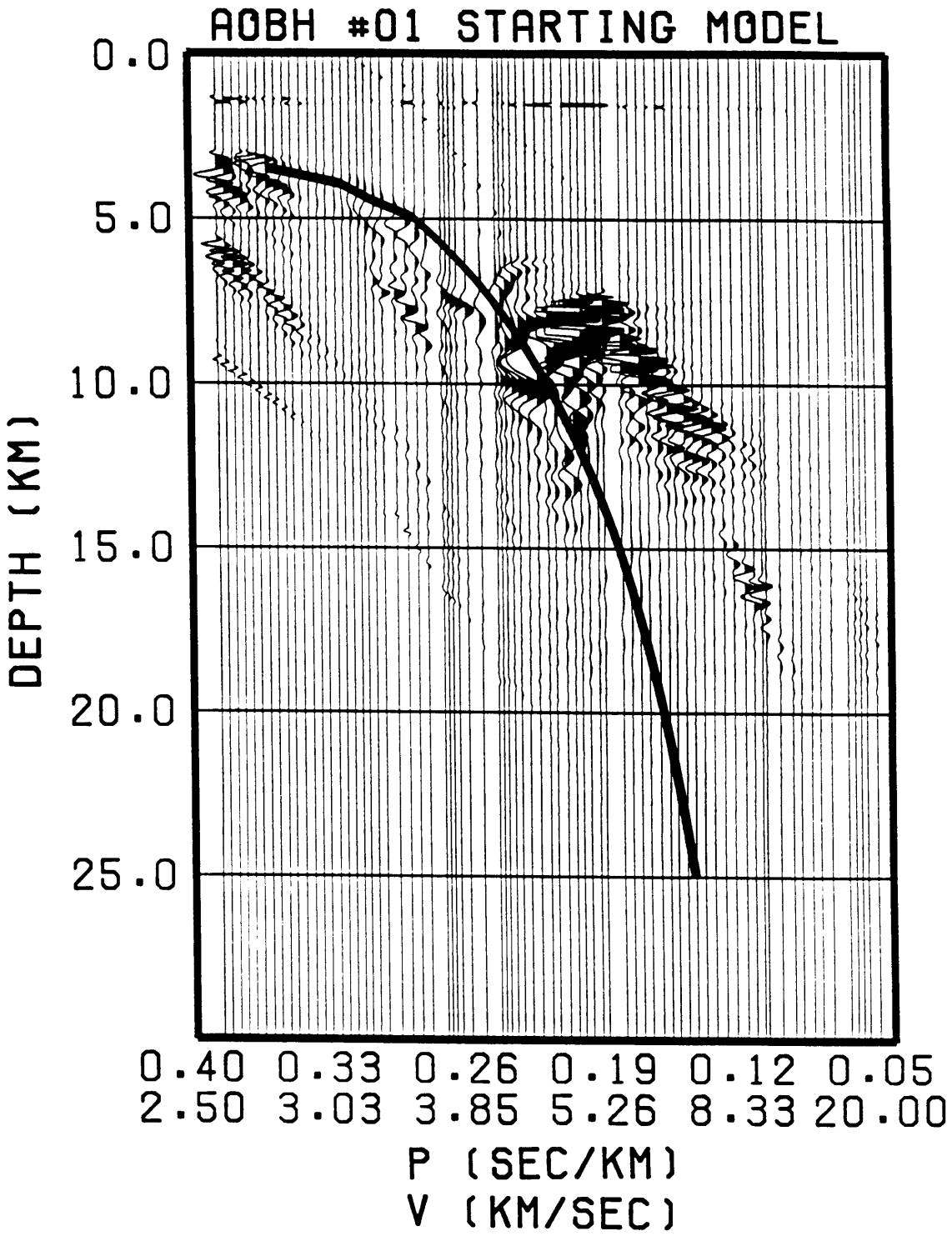

Figure 16. Depth - slowness image from the first iteration from downward continuation of the slant stacked data in Figure 15. The solid line represents a simple single layer velocity gradient used in the downward continuation. The data do not image onto the solid line indicating an incorrect velocity model.

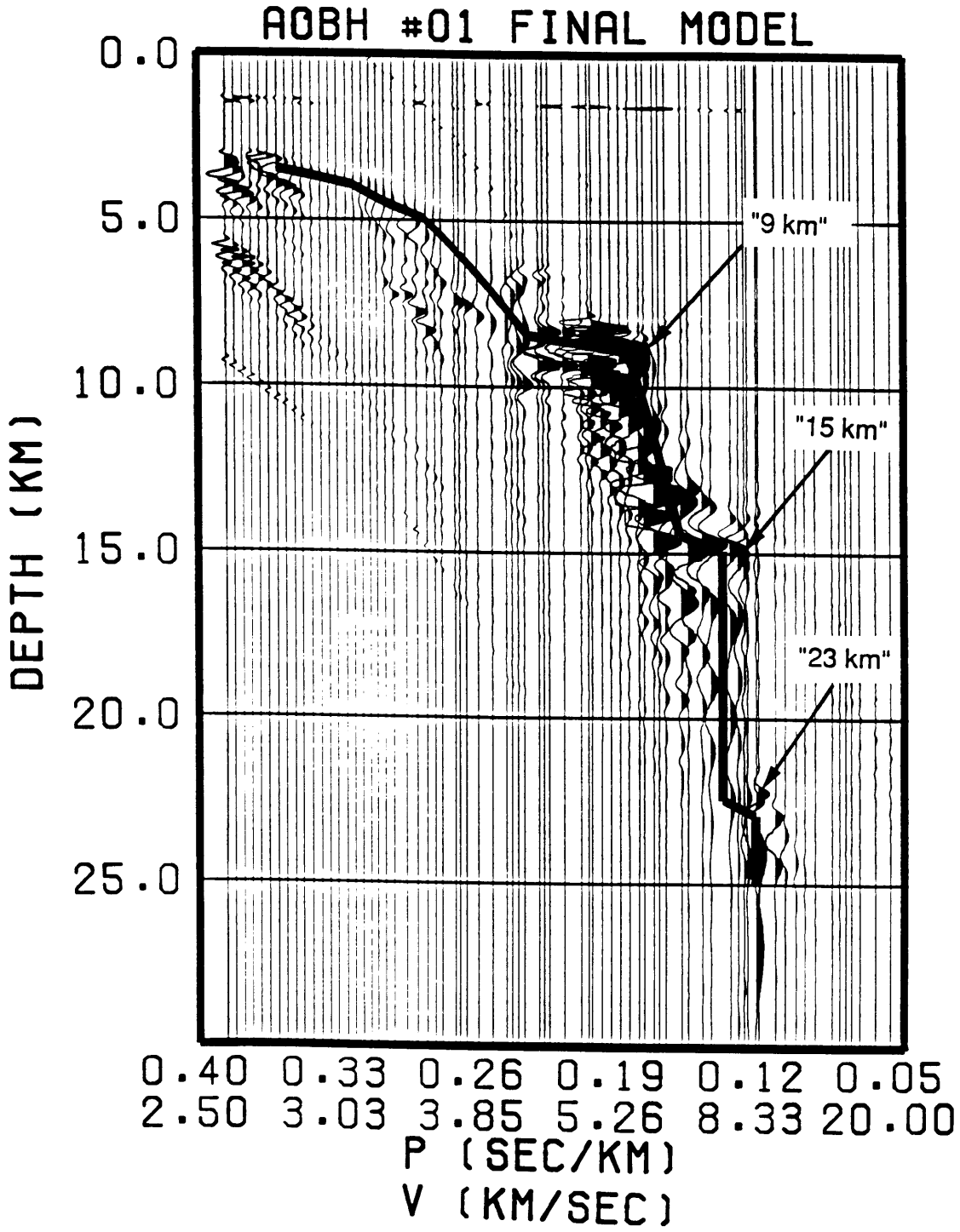

Figure 17. Depth - slowness image obtained with best fitting velocity model. The data have imaged either onto or very near to the solid line representing the velocity profile used in the downward continuation.

Chapter 3

Joint Imaging With Primary Reflections and Deep Water Multiples

Introduction

Large offset seismic data acquired with a fixed Ocean Bottom Hydrophone (OBH) and a large repeatable airgun array provide an ideal opportunity to image deep crustal reflectors. Such data may be conveniently collected by deploying OBHs in advance along the predicted path of a conventional marine Multi Channel Seismic (MCS) survey. Stationary OBHs record the airgun source of the MCS vessel from near zero offset as the vessel steams overhead, to offsets of 100 km or more depending on the length of the MCS line and power of the airgun array. Large offset receiver gathers, with a typical shot interval of 50 m, constructed from the OBH recordings have an order of magnitude greater spatial sampling of the large offset wavefield than do similar experiments conducted with explosive sources (Trehu et al., 1989). These relatively inexpensive "piggyback" experiments, in which fixed receivers record an MCS source, are increasingly being recognized as an important method of constraining

deep structure.

Migration of wide-angle reflections (WAR) recorded on large offset seismic surveys is recognized to be an effective means of directly imaging deep crustal structure (e.g., McMechan and Fuis, 1987; Milkereit, 1987; Chang et al., 1989). The goal of migration is to map the reflected (or scattered) wavefield to the spatial location at which scattering occurred. Ideally, this process produces an image of the earth's reflectivity with the correct spatial relationships between the various reflecting and diffracting surfaces. Migration has been extensively applied to conventional MCS data; the dense spatial sampling of the wavefield has resulted in high quality images of mid- to shallow crustal structure.

A fundamental difficulty encountered in migration of large offset data is the sparsity and low signal-to-noise ratio of the data. Unlike MCS data, where the redundancy in the recorded data allows the imaging of weak reflectors, large offset data are commonly single fold and only the strongest reflectors are visible in the migrated image. These limitations of large offset data motivated an effort to more fully utilize the recorded wavefield in an ocean bottom recording environment. A prominent feature of deep water OBH data is the presence of a strong water column multiple delayed from the primary arrival by the two-way transit time of the water column (e.g., Nakamura et al., 1987; Ebeniro et al., 1988; Reiter and Toksoz, 1990). In this paper we demonstrate the feasibility of incorporating the first order water column multiple in a two-dimensional (2-D) imaging scheme. We show that provided the water depth is great enough to allow temporal separation of the primary reflection from the water column multiple, the multiple may be treated as additional signal and used to enhance the subsurface image. Field data (OBH) collected in 1100 m of water are used to illustrate the success of our approach. At this depth the primary and multiple arrivals are separate in time from each other and no specific processing is required to distinguish one arrival from the other.

Several approaches to migration of wide-angle reflection data have recently been

presented. McMechan and Fuis (1987) describe a ray-based pre-stack Kirchhoff depth migration and apply this approach to field data from a land refraction survey in Alaska. Chang and McMechan (1989) present an alternative wide-angle imaging scheme using a reverse time finite difference approach and also apply their method to large offset land data. We choose a variation of the Kirchhoff pre-stack depth migration approach of McMechan and Fuis (1987) which adopts the algorithm of Hu and McMechan (1986), originally developed for vertical seismic profile imaging, to the large offset regime appropriate to wide-angle reflection imaging. In this approach, rays are traced through a 2-D velocity model and the necessary Green's functions are computed numerically. Each trace is migrated or summed into the image space along approximately ellipsoidal trajectories. Constructive interference between migrated traces produces an image of subsurface reflectivity. Ray-based migration schemes are attractive for both wide-angle imaging and imaging of water column multiples. Wide-angle imaging problems typically involve source-receiver offsets of up to 100 km and ray-based schemes avoid much of the computer memory requirements of finite difference extrapolations. In order to properly image non-primary reflected energy such as a water column multiple, a Green's function describing the multiple's path must be computed. An advantage of a ray-based migration approach is the ease with which ray theory may be used to compute these functions. Multiples are migrated by ray tracing along the appropriate travel path and imaged just as primary reflections are. Individual images are obtained from the primary reflections and water column multiples and may be combined in a separate step.

Outline

We first present observations concerning the amplitude characteristics of first order water column multiples and then use synthetic data to show that this phase is dominated by one of two possible travel paths for the on-bottom recording geometry. Synthetic data simulating an OBH recording a near-surface source are migrated us-

ing 2-D pre-stack Kirchhoff approach along this dominant path to demonstrate that the multiple may be treated as useful signal.

Next, our implementation of a 2-D pre-stack Kirchhoff depth migration is presented and the extension to imaging multiples is discussed. We show that only minor modifications are required to incorporate the water column multiple in the migrated image.

Lastly, field observations of wide-angle reflections recorded by an OBH at offsets between 88-100 km are migrated along both primary and water column multiple paths. We examine the validity and success of our approach by showing the sum and difference of the two images. An increase in reflector strength is clearly observed when the images are summed, demonstrating the advantage realized by utilizing the water column multiple arrival.

Amplitudes of Water Column Multiples

A fundamental difficulty with treating water column multiples as useful signal arises from an uncertainty as to which path the multiple energy actually travels. In general, for a water column multiple of order N, there are N+1 ray paths which contribute to the arrival. Figure 1 shows the two possible paths along which a first order water column multiple may travel. For a surface source and surface receiver geometry, the multiple may have either reflected beneath the source (Figure 1a), or reflected beneath the receiver (Figure 1b). If the medium being imaged varies in depth only (1-D), the multiple may be migrated along either of the possible paths and an accurate one-dimensional (1-D) image constructed. In the case shown in Figures 1a and 1b, both possible multiple paths will have identical travel times and amplitudes. Figures 1c and 1d illustrate the two possible multiple paths for media with a flat water bottom and a dipping reflector at depth. For two-dimensional (2-D) media of this type, the two possible multiple paths will clearly have different travel times but will result in events of comparable amplitude.

A clear 2-D image can then be obtained only if the contribution from each of the two paths may be isolated and imaged along its correct travel path. Separating these contributions in the observation data space of offset and time is difficult. A structure which varies in both depth and offset (2-D) will result in differing travel time curves for each of the possible multiple travel paths. Traditional methods of wavenumber filtering rely on events having sufficiently different moveouts to allow separation in the frequency-wavenumber domain. The difference in moveout between two possible multiple paths is determined by the degree of dip in the 2-D structure and except in extreme cases is not sufficient to allow effective separation of the phases.

The advantage of the on-bottom acquisition geometry is that one of the two possible first order water column multiples has a significantly larger amplitude than the other. Figure 2 illustrates the raypaths of the first order water column multiple for an OBH recording a near-surface source. We will refer to the multiple path in which energy reflects (peglegs) under the source as the "source multiple" and energy which reflects above the receiver as the "receiver multiple" (Figure 2). Examination of the dynamics of the receiver and source multiple raypaths reveals that for realistic seafloor properties the receiver multiple has a larger amplitude. The receiver multiple undergoes a nearly perfect reflection from the free surface, while the source multiple is reduced in amplitude by a factor proportional to the reflection coefficient at the water sediment interface. Figure 3 shows the ratio of the receiver multiple to the source multiple for a variety of seafloor velocities. We compute the ratio by averaging the ray-theoretical amplitudes of each multiple from zero offset to an offset corresponding to twice the depth of the water column. We assume a density to velocity relation of $\rho = 1.7 + .2 \cdot V_p$ with V_p being the compressional wave velocity of the sediment and ρ being the density. As the reflection coefficient of the water sediment interface grows larger, the difference in amplitude between the source and receiver multiple grows smaller. However, for realistic seafloor properties the receiver multiple remains the dominant arrival. From Figure 3 we see that for a water bottom velocity of 1750

m/sec the ratio of the receiver to source multiple is approximately 13.

We use synthetic data calculated using ray theory (Cerveny et al., 1977) to examine the amplitudes of first order water column multiples for both traditional surface seismic and on-bottom recording geometries. Figure 4 shows a simple model consisting of a water column of constant depth with a single 10^o dipping reflector embedded in a halfspace of 1750 m/sec. The reflector is defined by a +12% density contrast and is located at 6 km depth at 0 offset. Figure 5 shows a comparison of first order water column multiples recorded by an on-bottom receiver to that of a surface receiver. The receivers are located at 0 km offset and record sources at intervals of 0.25 km from 0 to 5 km (Figure 4). The event labeled "receiver multiple" is clearly the dominant arrival in the on-bottom geometry. In contrast, the surface receiver geometry shown in Figure 5b does not have a dominant arrival. In this case both possible multiples have similar amplitudes.

Figure 6 is a comparison of images obtained by migration of the synthetic on-bottom data of Figure 5a versus the surface receiver data of Figure 5b. We image the data with a ray-based Kirchhoff migration algorithm discussed in a following section. Figure 6a shows a clear interpretable image of the single dipping reflector obtained by migration of the on-bottom data along the receiver multiple path (Figure 2). A tight 10 ± 5 degree dip filter was applied during migration to the images of Figure 6 to reduce elliptical migration artifacts. The small amplitude source multiple (Figure 5a) is incorrectly migrated to a position slightly below the correct position of the reflector. The source multiple's small amplitude coupled with a lack of focussing by the migration operator reduce the amplitude of this interference to a level which is not visible at this scale. Figure 6b is an image from migration of the surface receiver data of Figure 5b along a receiver pegleg multiple path (Figure 1b). In this case the interference caused by the presence of the other multiple path or the source pegleg, (Figure 1a) is substantial. The large amplitude event lying beneath the correct reflector position is the mispositioned source multiple pegleg. The presence

of two multiple arrivals of similar amplitude, but slightly separate in time, produces an image in which it is quite difficult to distinguish the true reflector position from the artifact. Figure 6a, however, illustrates that a useful interpretable image may be obtained from the first order water column multiple for the on-bottom recording geometry.

In Figure 7 we compare images from migrating the synthetic on-bottom data along receiver multiple and source multiple paths. We scale the receiver multiple's image so that the incorrectly positioned source multiple is visible just beneath the true reflector (Figure 7a). The image from migrating the same data along the source multiple path is shown in Figure 7b. In this case although the source multiple is correctly imaged, a large amplitude receiver multiple artifact positioned above the true reflector dominates the image. When comparing the relative strength of the artifact or mispositioned multiple in Figures 6 and 7, there are two separate issues to consider. The first is simply the relative amplitudes of the two constituent multiple paths. If one of the multiple paths is dominant such as in the on-bottom case, the artifact from the smaller amplitude path will generally be manageable. Secondly, events will be best focussed when migrated along the correct travel path and will appear less focussed when migrated along the incorrect multiple path. For example, in Figure 7a the mispositioned source multiple appears weaker and less focussed than in Figure 7b where it was migrated along the correct travel path. We find the "focussing effect" to be a considerably weaker factor in determining artifact suppression than the "relative amplitude" issue.

The observation that the receiver multiple is dominant in the on-bottom geometry is the reason why we migrate on-bottom data along the receiver multiple path. Although both receiver and source multiples are present in the observed data, we have shown the dominant receiver multiple will yield a useful image (Figure 6a). This is in contrast to traditional surface seismic geometries where two nearly equal amplitude arrivals make up the first order multiple; our approach is ineffective in these cases.

Higher order multiples recorded by an on-bottom receiver suffer from the same difficulties as first order multiples do in the surface seismic geometry. Considering effects of seafloor reflections only, for an Nth order multiple there are N equal amplitude multiple paths for an on-bottom acquisition geometry and $N+1$ equal amplitude multiple paths for a surface seismic geometry. Thus we see that for the second order multiple, an on-bottom receiver records two equal amplitude multiples and suffers from the same difficulties as the surface seismic geometry does for the first order multiple.

Method: Ray-based 2-D Kirchhoff Migration

We use a ray equation-based Kirchoff pre-stack depth migration similar to one described in Hu and McMechan (1986) to image both primary reflections and water column multiples. An excellent summary of this approach in the context of wide-angle imaging is found in McMechan and Fuis (1987). Here we will summarize only our particular implementation and the extension to imaging multiples. In Appendix B we derive the 2-D Kirchhoff approximation from Green's 2nd Theorem (Morse and Feschback, 1953). This approximation allows realistic 2-D velocity models to be considered and has been widely applied in Vertical Seismic Profile imaging. The medium is considered to be acoustic and to consist of point diffractors on a dense regularly sampled grid. An arbitrary 2-D background velocity is assumed to be known and the contribution of each trace (source-receiver pair) is computed for all points on the regularly sampled image grid. The contribution of each trace is determined assuming a single scattering travel path where energy traveled from the source to a point diffractor and returned to a receiver. Travel times are calculated for paths from each image point to the source location (T_{src}) and from each image point to the receiver location (T_{rec}). The total travel time for any point in the image space is then $T = T_{src} + T_{rec}$ and the reflectivity at that point is assumed to be proportional to the strength of the observed signal at time T. We take a slightly different approach than McMechan and

Fuis (1987) in calculation of the travel times T_{src} and T_{rec}. Figure 8 illustrates our implementation of the basic 2-D Kirchhoff depth migration. We perform two-point ray tracing by tracing rays from the edges of an image space to the source and receiver locations. The travel times and ray positions of each ray are saved while that ray is contained within the image space. An integration time step (Cerveny et al., 1977) for the ray tracing is chosen such that the image space is adequately sampled. The density of ray paths and time integration step along each ray path determine the positions in the image space at which the desired travel time function is sampled, and result in a scattered 2-D set of data points defining the travel time surface. This scattered 2-D data set is then interpolated onto a regular grid of points in the offset-depth domain. In addition to the travel times, the angle of the ray equation-approximated wavefield with respect to a vertical normal is also computed and interpolated in an identical procedure. These data are used later if an angle-of-incidence weighting is desired to enhance specific reflector dips. Computational costs are approximately doubled by computing the ray-field angle, but this allows an exact dip filter to be applied during imaging. Traditional methods of dip filtering use simple trigonometric relationships which need to be extended to cover geometries with a source and receiver at different depths and do not correctly account for lateral velocity variation.

McMechan and Fuis (1987) computed travel times by shooting a dense fan of rays from a source or receiver position into the medium. A 2-D interpolation is used to resample the travel time surface onto a regular grid. Their approach is computationally more efficient as no two point ray tracing is involved. However our method ensures a dense sampling of the particular portion of the medium (image space) with the correct travel times from the ray equation. Dense sampling of the input data for the interpolation step helps reduce any inaccuracies from the bilinear interpolator.

Migrating non-primary reflections (e.g., multiples) requires a simple extension of existing ray-based wide-angle imaging schemes. A number of authors (e.g., McMechan

and Fuis, 1987; Keho, 1986) have pointed out the applicability of 2-D ray-based Kirchhoff algorithms to the imaging of internal and free surface multiples. If the ray path of a non-primary event can be determined, the arrival may be imaged in exactly the same manner as a primary reflection, except the travel times are computed by ray tracing along the non-primary path. In the case of the receiver multiple in this study, also called a free surface multiple in other geometries (e.g., Hu and McMechan, 1986; Verm et al., 1987), the ray tracing is performed along a path that includes the reflection from the free surface (Figure 8b). All subsequent computations are performed just as in the primary reflection case. Care must be taken to correct the data for any gross phase differences between the primary and multiple paths before summing the two images together. The receiver multiple undergoes a polarity reversal at the free surface and this must be corrected for before combination with the primary image.

Synthetic example

Realistic OBH acquisition conditions often involve water depths which vary along the large offsets needed to acquire deep penetration wide-angle reflection data. The model used in the previous synthetic examples (Figure 4) consisted of a horizontal seafloor with a dipping reflector at depth. In order to model more realistic structures, we now investigate the case of a 2-D water bottom with dipping reflectors at depth. The same behavior of a dominant receiver multiple is present, although in this case the difference in travel times between that and the source multiple is determined strongly by the differences in water depth between the source and receiver locations. A model is chosen to closely represent a field data set used and described in a subsequent section of this paper.

Synthetic data simulating an OBH in 1020 m of water recording sources in less than 400 m of water are used to illustrate the success of our approach in treating the receiver multiple as useful signal. A series of reflectors at depths from 20-30

km are specified by small positive density contrasts. Figure 9 shows the model used in calculation of the synthetic data. This includes the actual seafloor topography used in a subsequent field example. The synthetic data in Figure 10 are calculated with ray theory and include all primary reflections as well as contributions from both source and receiver multiples. The primary reflections are labeled "P", the receiver multiples "Mr" and the source multiples as "Ms". The receiver multiples are larger in amplitude than the source multiple as expected from our previous synthetic examples, and arrive later because the water depth at the receiver is more than twice that at the source locations. The source multiples arrive between the primary and receiver multiple arrivals, interfering with both sets of reflections (Figure 10). Their amplitude however, is small enough to allow the other arrivals to be clearly identified. We will show that the interference caused by the source multiple is sufficiently small in the migrated images to allow an interpretable structure to be determined. In this example and for most realistic wide-angle geometries, the primary reflections and the multiples have very similar apparent velocities. This precludes the use of a simple velocity filter to separate the different arrivals as is often successfully accomplished in traditional reflection processing. Instead, we rely on the water depth to separate the primary from the receiver multiple.

If it were possible to separate downgoing arrivals (receiver multiple) from upgoing arrivals (primaries), the primary could be easily separated from the receiver multiple. If both the temporal derivative (i.e., pressure) and spatial derivative (i.e.,velocity) of the wavefield were recorded, the multiple and primary arrivals could be distinguished as downgoing and upgoing wavefields respectively. Nakamura et al. (1987) point out that a hydrophone-geophone pair of sensors are necessary to acquire sufficient information to perform such a wavefield separation. A single hydrophone does not record sufficient information to allow this type of wavefield separation and instead we rely on the time separation due to deep water to isolate the receiver multiple.

Figure 11a is an image resulting from the migration of the synthetic data of

Figure 10 along the primary reflection paths. Elliptical artifacts characteristic of single source or receiver gather migrations are clearly evident in Figure 11. These can be reduced, as in Figure 6, with a dip filter if so desired. The image from migration of the synthetic data of Figure 10 along the receiver multiple path is shown in Figure 11b. Figure 11b is plotted with reverse polarity so a direct comparison may be made to the primary's image in Figure 11a. In both Figures 11a and 11b the incorrectly positioned source multiple is too small to be visible in the migrated image. The migration operator defocusses the source multiple to such a degree that it is not visible in the either the primary or receiver multiple's image in Figure 11. Figure 11c is obtained by summing the images of Figure 11a and 11b. This composite image shows the expected increase in reflector amplitude and demonstrates the advantage obtained by treating the multiple as useful signal. Comparison of Figure 11a with 11c shows that by including the multiple in the image, the reflector strength has been doubled.

Migration of the data in Figure 10 along the source multiple path results in the image in Figure 12. In this case the dipping reflectors are not imaged correctly because the larger amplitude primary and receiver multiple arrivals are incorrectly positioned and dominate the image. Unlike Figures 11a and 11b where the defocussing effects of the migration operator virtually eliminate the source multiple, the larger amplitude primary and receiver multiple are not reduced enough in amplitude to produce a useful image from the source multiple.

Field Data Application

A piggyback reflection/refraction experiment was conducted in June 1988 off the East Coast of the U.S. across a deep sedimentary basin known as the Carolina Trough (Figure 13). We present data from OBH#10 on Line 6 in Figure 13 which recorded data at offsets up to 100 km. Eight OBHs (Koelsch et al., 1982) were deployed prior to commencement of MCS shooting and are shown as circles on Line 6 in Figure

13. Water depths ranged from a depth of 2600 m at the seaward end of the line to approximately 300 m at the shot point at the landward end. A 10,800 cubic inch airgun array and a shot interval of 50 m allowed the identification of numerous wide- angle reflected phases. The OBH data have been forward modeled with 2-D ray tracing by Holbrook et al. (1990) and we use this velocity model in subsequent migration examples. A more detailed description of the experiment may be found in Austin et al. (1990) and in Chapter 4.

Figure 14 shows data from OBH # 10 recorded as the source moved away from the receiver toward land at source-receiver offsets from 85 to 101 km. The receiver was located in 1020 m of water and recorded sources in water depths ranging from 450 to 420 m. A prominent reflection thought to originate from a depth of approximately 35 km is labeled for both the primary (P) and receiver multiple (Mr) arrivals. Additional laterally coherent portions of reflected energy are visible beneath the primary and receiver multiple arrivals. The label Ms?? indicates the approximate time when the source multiple should arrive given a water depth of 450 - 420 m. For the water depths involved in this example, the receiver multiple should lag the primary by about 1.35 sec, while the source multiple should arrive about 0.56 sec after the primary arrival. Figure 14 clearly shows the expected large amplitude arrival corresponding to the receiver multiple. The source multiple, however, is not visible at 0.56 sec behind the primary as predicted from the source region water depths. This observation confirms our conclusions from forward modeling that the source multiple may be effectively ignored, because the primary and the receiver multiple account for the majority of the recorded energy for the on-bottom geometry.

The field data from Figure 14 are migrated along the primary reflection path and the resulting image is shown in Figure 15a. The image is 72 km wide and extends from 20 to 40 km in depth. Figures 15a-d were constructed with no dip filter and large amplitude high angle elliptical artifacts are prominent. The upper portion of the velocity model for the migration was derived from picking reflector boundaries from

the stacked MCS time section and ray tracing the corresponding wide-angle reflections on the OBH data. Deeper velocity control was obtained by forward modeling of large offset reflected and refracted arrivals observed on both OBH # 10 and additional on-bottom hydrophones. A smoothed version of the velocity model of Holbrook et al. (1990) (see Figure 5c, Chapter 4) is used as input for the migration procedure. The prominent ellipse bottoming at approximately 37 km depth in Figure 15a corresponds with the recorded reflection labeled "P" in the raw data of Figure 14. Figure 15b is an image from migrating the field data along the receiver multiple path. The polarity has been reversed in the plot to allow a direct comparison with the primary's image in Figure 15a. The reflector at 37 km depth is again clearly imaged; however, in this case an event at 25 km is now present. The event at 25 km in Figure 15b is the incorrectly positioned primary reflection which was properly migrated in Figure 15a to a depth of 37 km. This primary reflection is incorrectly imaged above the correct position because it has been migrated along the receiver multiple path. Likewise, careful inspection of Figure 15a reveals a steeply dipping event in the lower right portion of the image caused by the presence of the incorrectly positioned receiver multiple arrival. Figure 15c shows the result of summing the primary and receiver multiple's image. The resultant image illustrates the constructive interference and subsequent increase in reflector strength. The kinematics of the receiver multiple were correctly modeled as evidenced by the degree of constructive interference in Figure 15c. In Figure 15d we display the difference (subtraction) between Figures 15a and 15b. Most importantly, very little energy remains in the vicinity of the 37 km deep reflector. This illustrates, in the opposite manner of Figure 15c, the crucial in-phase nature of the primary and multiple's image. Figures 15a-d are displayed with identical scaling factors so true amplitude comparisons may be made among them.

Figures 16a and 16b are expanded versions of Figure 15a and 15b and include a $2.5^{\circ} \pm 5^{\circ}$ dip filter to reduce elliptical artifacts. The dip filter acts to enhance or reject portions of the equal travel time elliptical migration trajectories on the basis of

a specified dip filter. We use a simple cosine dip filter which for the case illustrated in Figure 15 is centered at 2.5°. The dip filter has a value of 1 at 2.5° and tapers to a value of 0 at −2.5° and +7.5°. Dips outside the range of −2.5° to +7.5° are not summed into the migrated image. The total lateral extent of these images is reduced to 30 km and the dipping event at 37 km is now more densely sampled in offset. Figures 16c and 16d represent the addition and subtraction respectively of Figures 16a and 16b. We present these images to demonstrate on an expanded scale the in-phase relationship of the primary and multiple's image. The suppression of elliptical artifacts makes the constructive interference between the primary and receiver multiple image more obvious and clearly demonstrates the advantage of using the water column multiple. We have also applied this method to imaging shallow structure from short offset data (Reiter et al., 1990).

Conclusions

A new approach to the treatment of deep water multiples is presented which makes use of the multiple instead of treating it as unwanted noise. This allows the first order water column multiple to be treated as additional signal to be used in a 2-D depth migration. The amount of data available for migration is effectively doubled when compared to the traditional approach of using primary reflections only. A ray-based Kirchhoff pre-stack depth migration similar to that of Hu and McMechan (1986) is used to image the water column multiple. A simple extension to existing ray-based migration schemes (involving ray tracing along the appropriate multiple travel path) is required to image the water column multiple. We show for the acquisition geometry of an OBH recording a near-surface source that one of the two possible first order water column multiple paths (the receiver multiple) has a larger amplitude than the other (source multiple). This observation justifies migrating the data along the larger amplitude multiple path, and we have shown that a reliable image may be obtained. Traditional surface source/receiver geometries do not record first order water column

multiples with differing amplitudes and thus our approach is not applicable.

The minimum water depth required for our method is determined by the temporal separation between the primary and multiply reflected wavefields. We make no effort to separate the primary arrivals from the water column multiple prior to migration. The water depth must be great enough to separate these arrivals sufficiently so that they do not interfere with one another when migrated to depth. At large offsets the apparent velocities of the multiple and primary are nearly identical and thus traditional velocity filtering is ineffective at separating the wavefields.

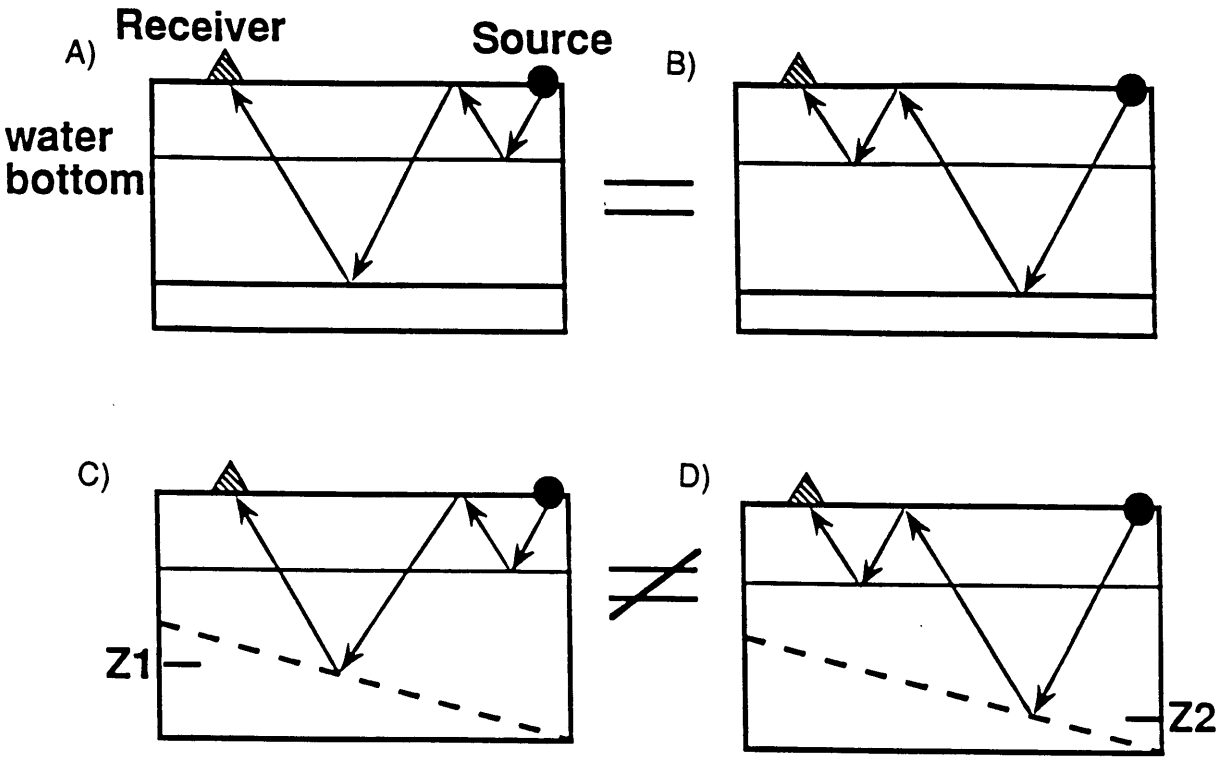

Two dimensional media cause the 1st order multiples to have slightly different travel times.

Figure 1. a) Raypath of "source pegleg", one of the two possible paths a first order water column multiple may travel in a surface source - surface receiver geometry. b) Raypath of "receiver pegleg", the other possible path for the first order water column multiple. In a one-dimensional medium both possible multiple paths have the same travel time and amplitude. c) Source multiple path in a two-dimensional medium. d) Receiver multiple in a two-dimensional medium. In two-dimensional media the two possible multiple paths have differing travel times (reflection depths).

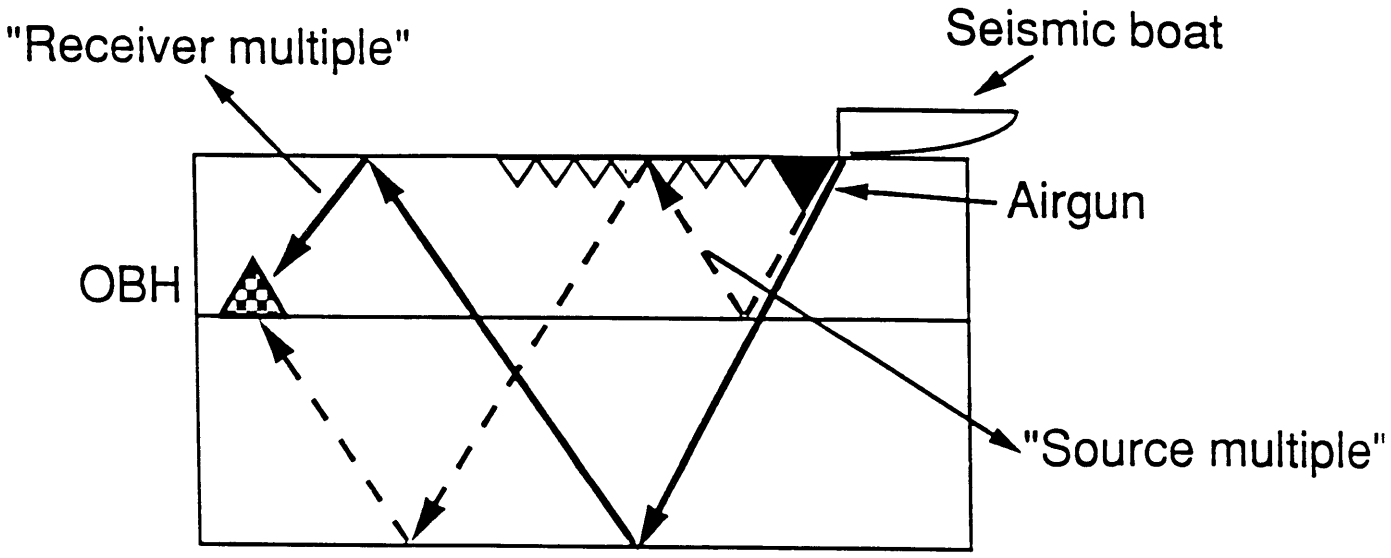

Figure 2. Schematic diagram of the two possible multiple paths for the on-bottom geometry. Unlike the surface receiver case, the on-bottom geometry records the "receiver multiple" (solid line) with a significantly larger amplitude than the "source multiple" (dashed line). The "OBH" represents an Ocean Bottom Hydrophone.

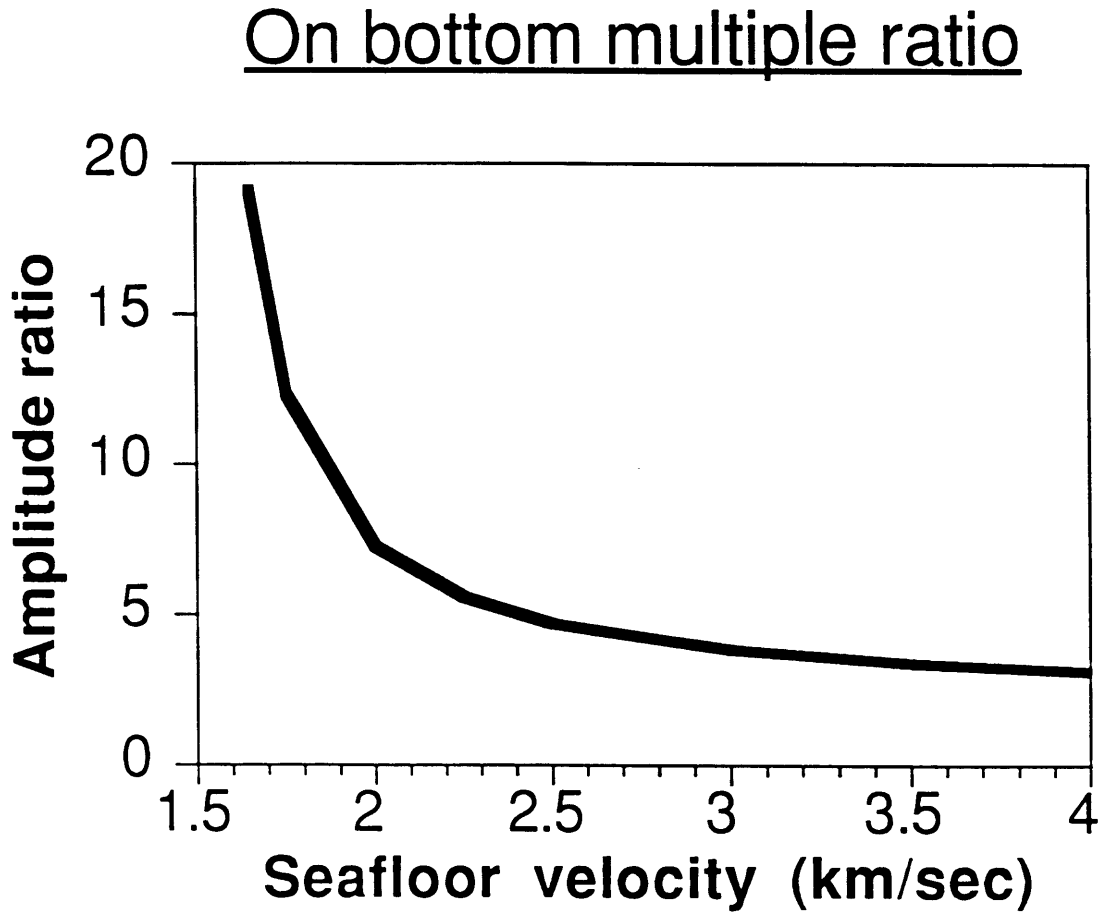

Figure 3. The ratio of the receiver multiple to the source multiple as a function of the velocity contrast at the water sediment interface. As the water bottom grows harder effectiveness of our approach decreases. For most water bottoms, the amplitude of the receiver multiple is approximately an order of magnitude greater than the amplitude of the source multiple. The curve is sampled from 1750 m/sec to 4000 m/sec every 250 m/sec resulting in a slightly jagged appearance. See text for details of amplitude calculations.

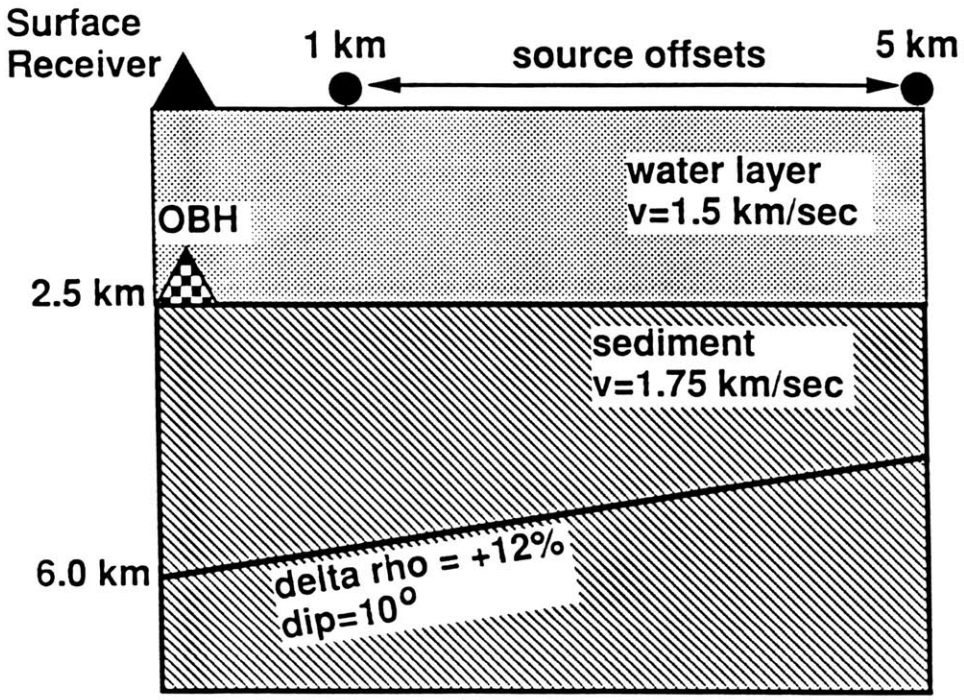

Figure 4. Model used for the synthetic data of Figure 5. The water layer is flat and a single dipping reflector is specified by a positive density contrast. The OBH is located just above the seafloor and the surface receiver just beneath the free surface.

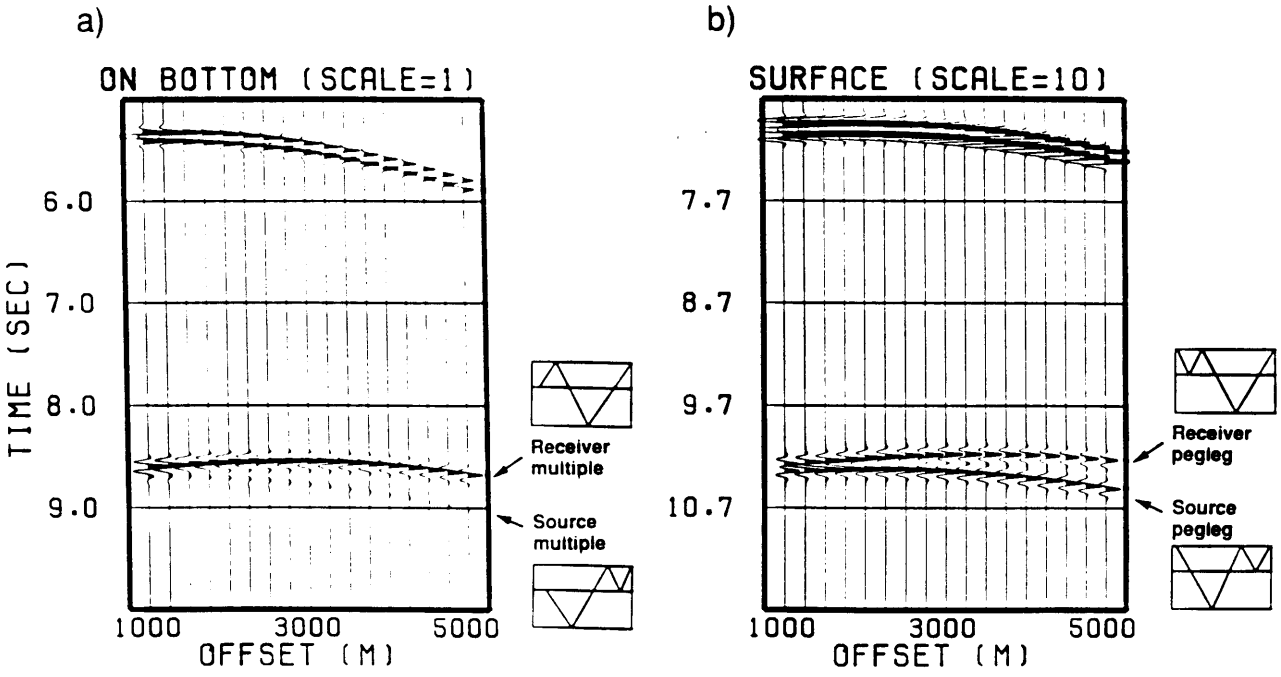

Figure 5. a) Ray based synthetic data including primary reflections as well as both possible first order water column multiples for the OBH geometry and model shown in Figure 4. The multiples arrive between 8 and 9 seconds and have differing travel times caused by the dipping reflector. b) Ray based synthetic data for the surface receiver in Figure 4. The multiples arrive between 10 and 11 seconds and have similar amplitudes as opposed to the on-bottom case (a) where the receiver multiple is the dominant arrival. The surface receiver data shown in (b) are plotted with 10 times the scaling factor as (a).

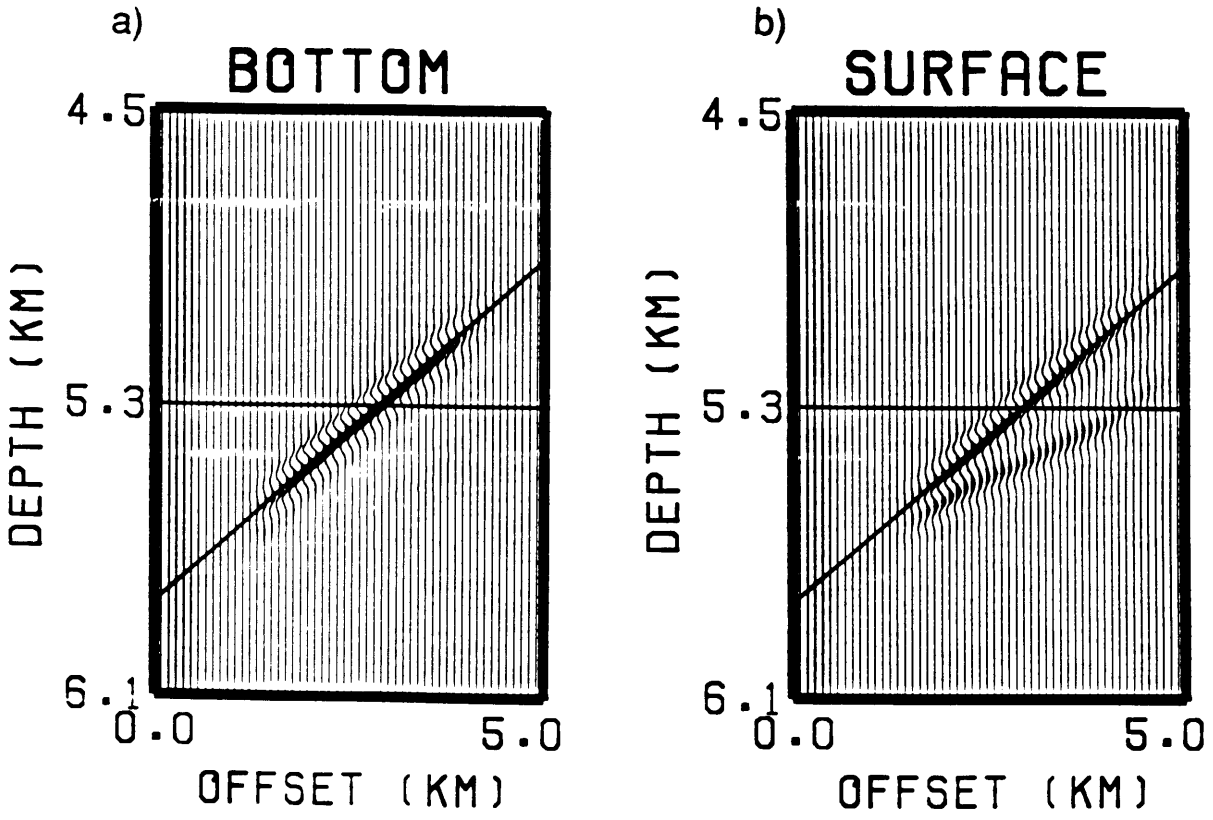

Figure 6. a) Image of the dipping reflector in Figure 4 from migration of the synthetic on-bottom data of Figure 5a along the receiver multiple raypath. b) Image of the same dipping reflector but from surface receiver data Figure 5b migrated along the receiver pegleg multiple path. Note the large amplitude mispositioned event lying beneath the true reflector location. This is caused by the presence of two equal amplitude multiples for the surface receiver case. A tight dip filter was used to reduce elliptical artifacts on both images. The surface receiver data shown in (b) are plotted with 10 times the scaling factor as (a).

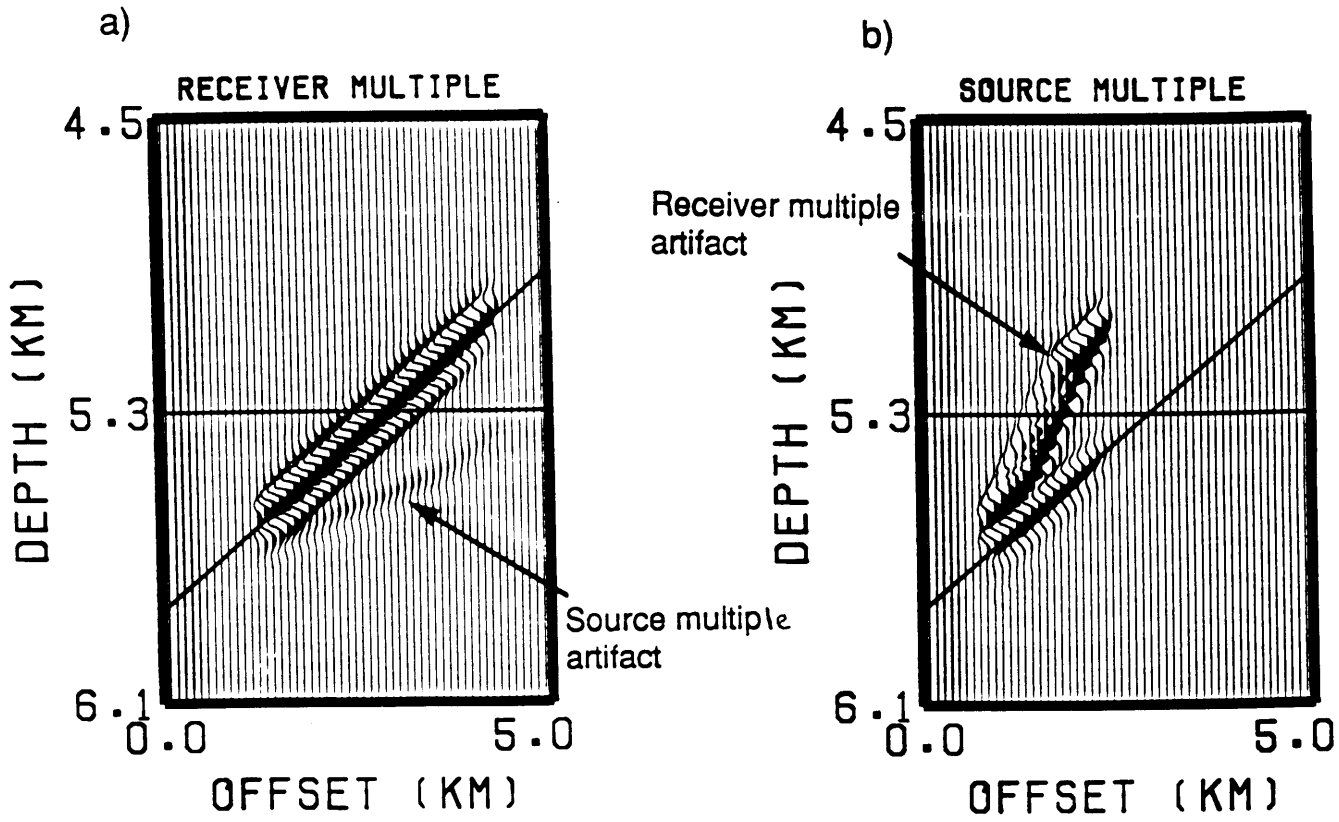

Figure 7. a) Image from migrating on-bottom data (Figure 5a) along receiver multiple path. Image is plotted at an exaggerated scale to show the source multiple artifact. b) Image from migrating on-bottom data along source multiple path. The large amplitude artifact from the receiver multiple dominates the image.

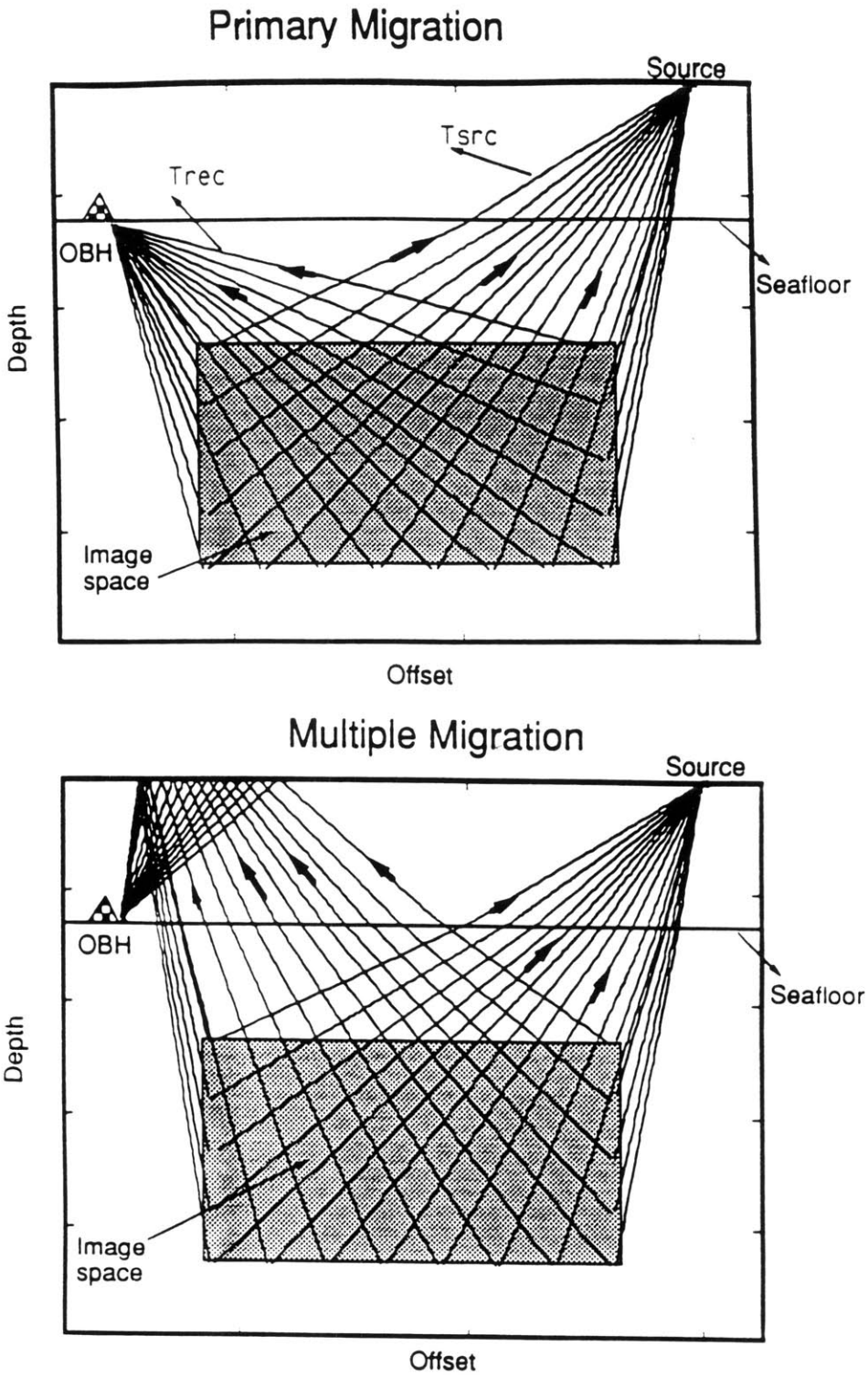

Figure 8. a) Travel times needed for migration are computed by ray tracing from the edges of an image space to the source and receiver position. The travel time and position of the ray is evaluated at discrete points within the image space and stored. This results in an unequally sampled estimate of the travel times which are then interpolated onto a dense regular grid. b) When migrating the receiver multiple arrival, T_{recv} is computed along raypaths which include a reflection from the free surface.

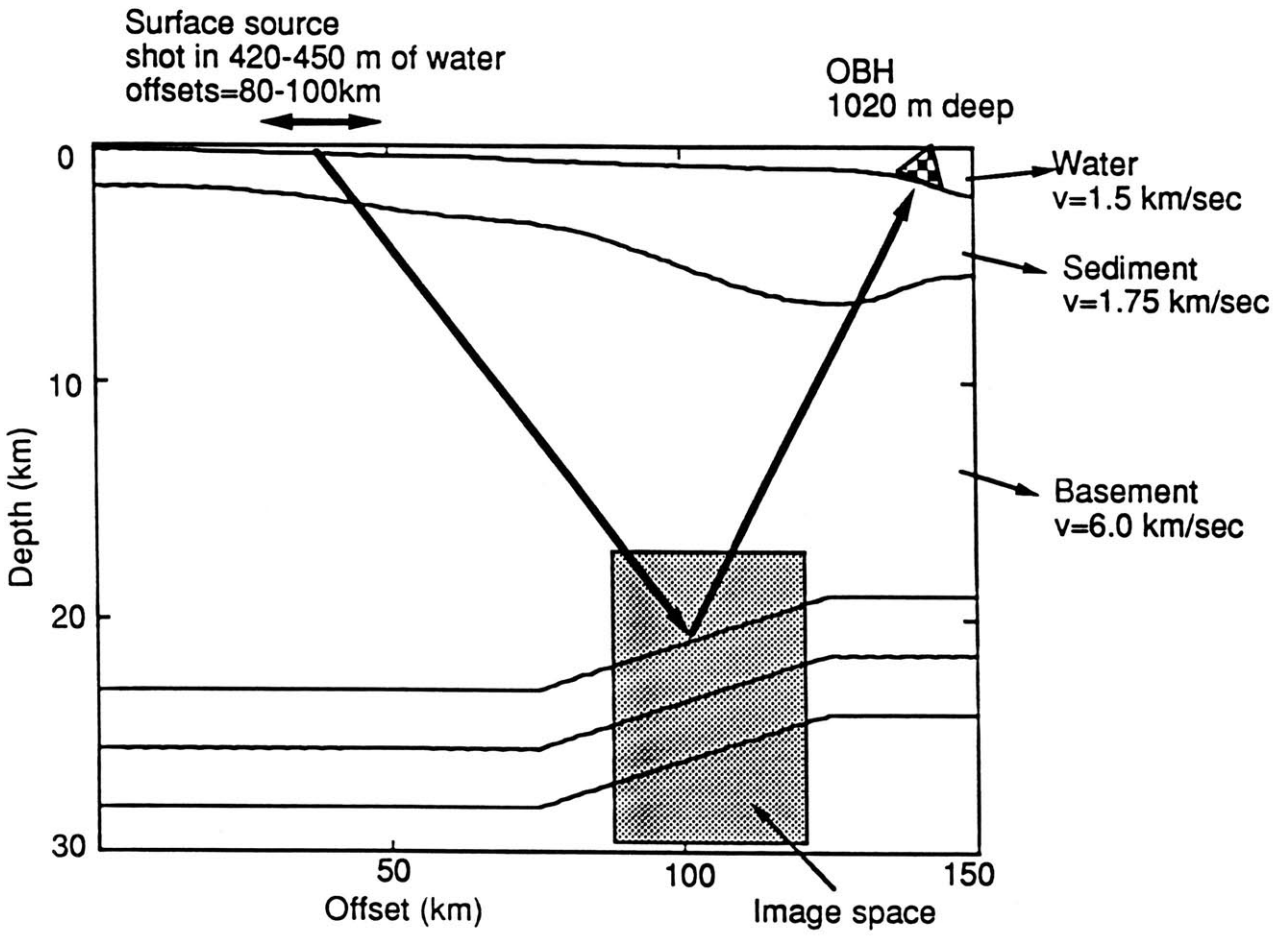

Figure 9. Model used in calculation of the synthetic data in Figure 9. The water bottom is from an actual field experiment in the Carolina Trough off the East Coast of the U.S. In this model both the water bottom and the reflectors have significant dip.

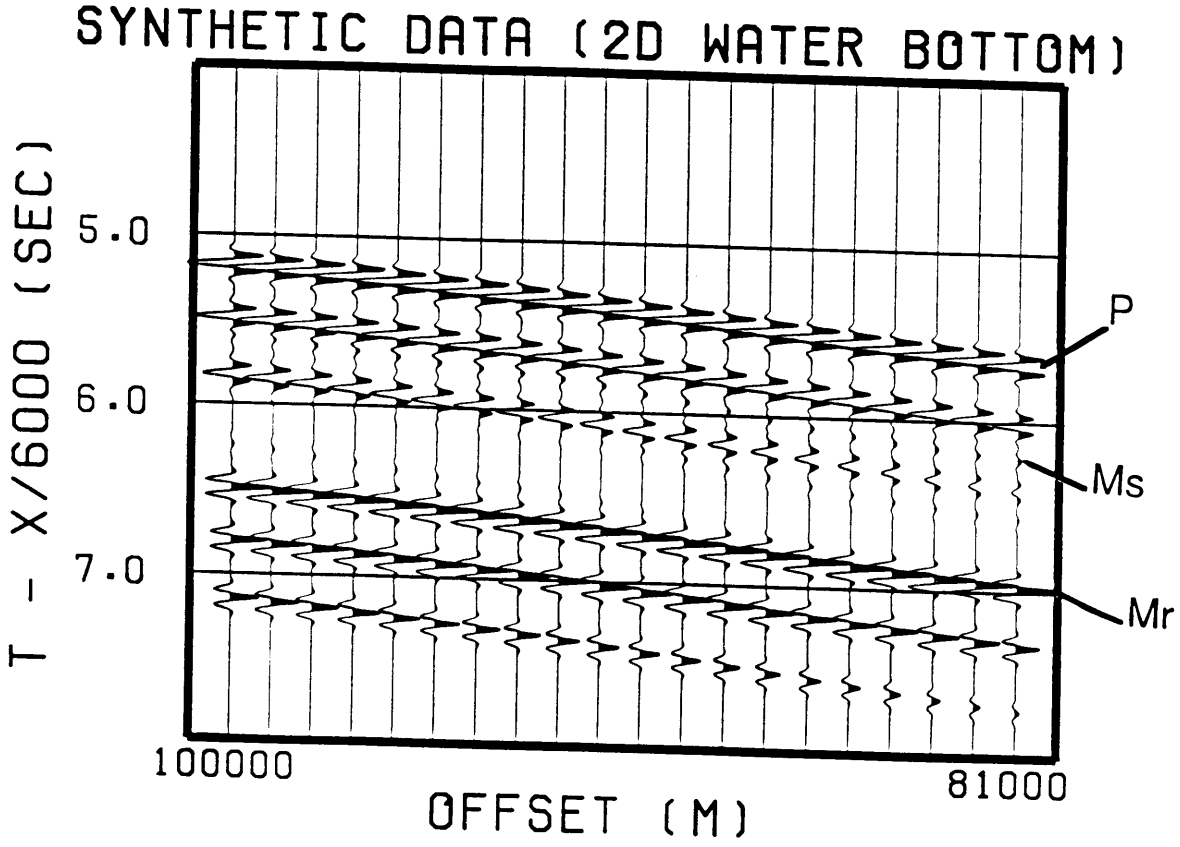

Figure 10. Ray based synthetic data from the model in Figure 9. In this case the source multiples overlap the primary and receiver multiple arrivals. The receiver multiple arrives later than the source multiple because the water depth is greater at the receiver location than at the source location.

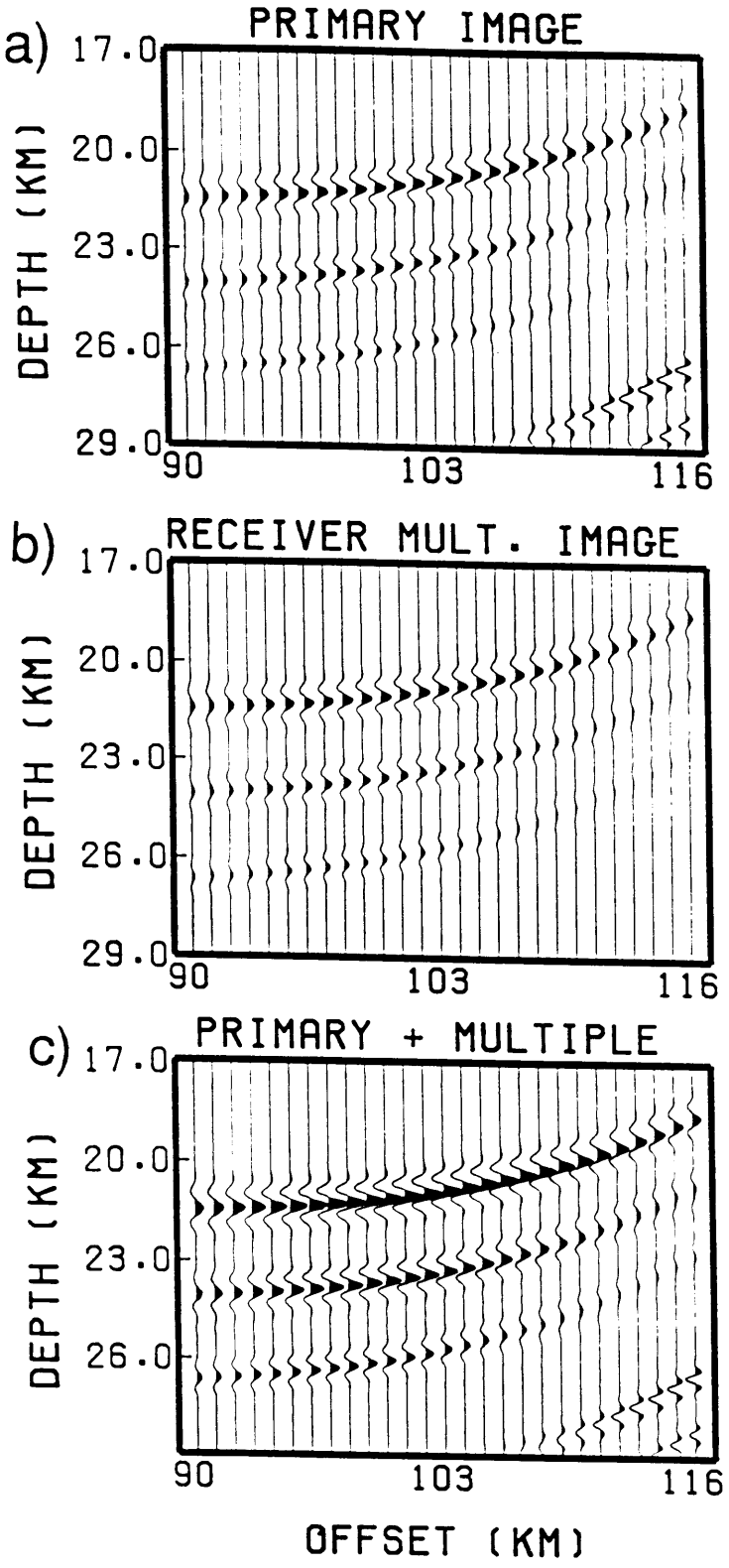

Figure 11. a) Image from migrating the synthetic data of Figure 10 along the primary reflection path. No dip filter is used and a smearing of data along elliptical trajectories is unavoidable. b) Image from migrating along the receiver multiple paths. c) Sum of (a) and (b). Note increase in signal amplitude.

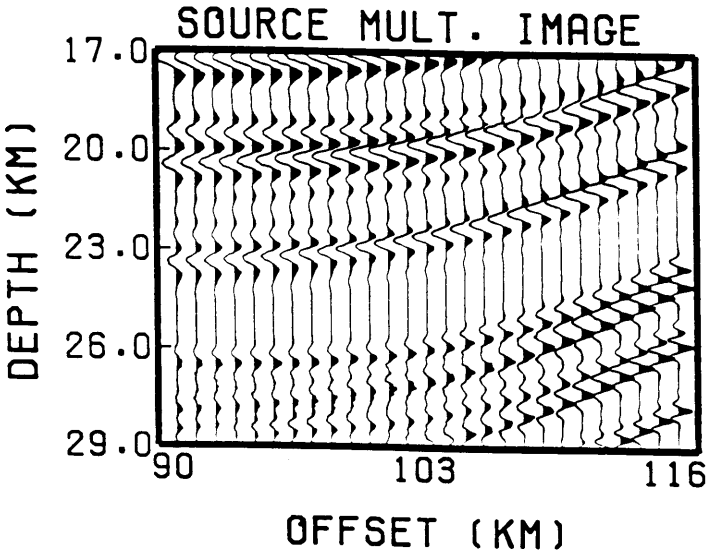

Figure 12. Image from migrating synthetic data along the source multiple ray path. In this case a useless image results due to the interference from the larger amplitude primary and receiver multiple arrivals.

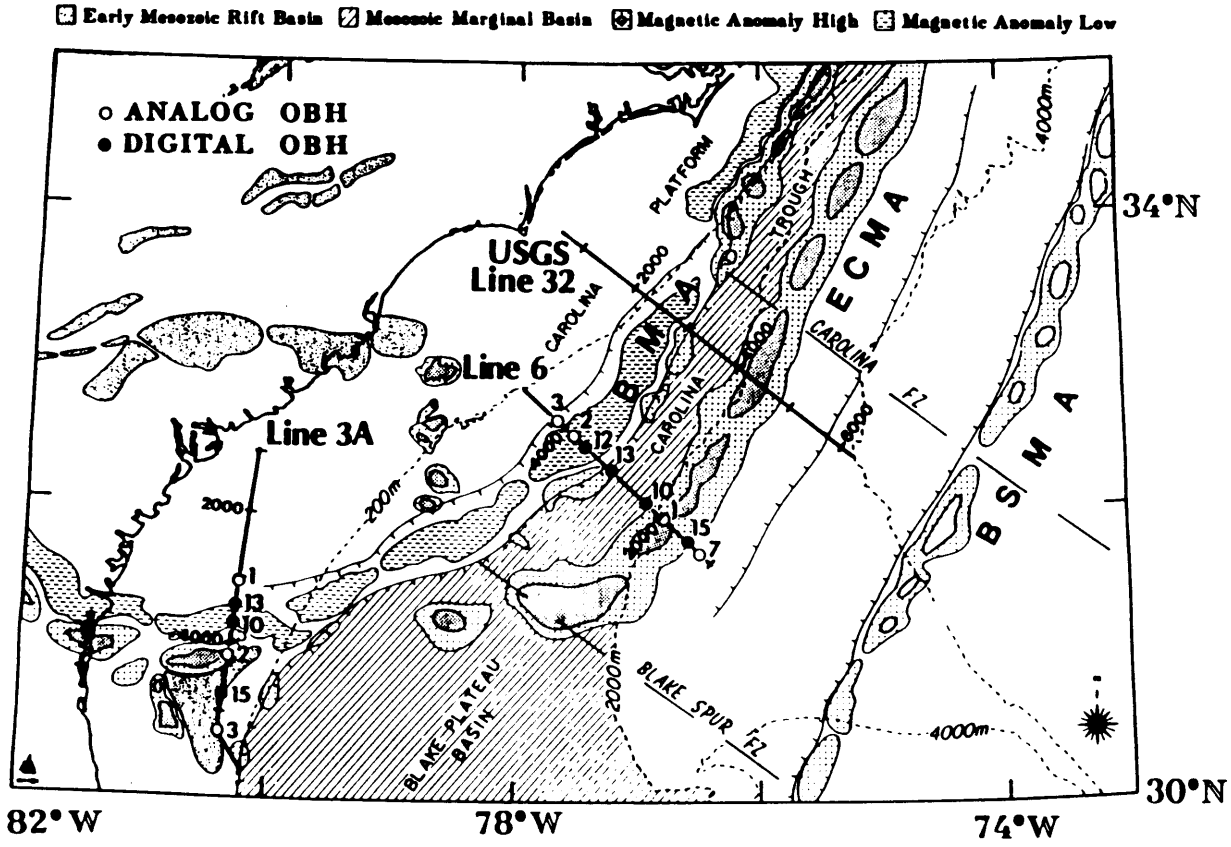

Figure 13. Plan view of piggyback refraction/reflection field experiment in the Carolina Trough. We present data from OBH 10 deployed on Line 6. Lines 3a and 6 were part of the joint University of Texas at Austin/Woods Hole Oceanographic Institution discussed in this thesis. Line 32 is part of a separate survey conducted by the United States Geological Survey.

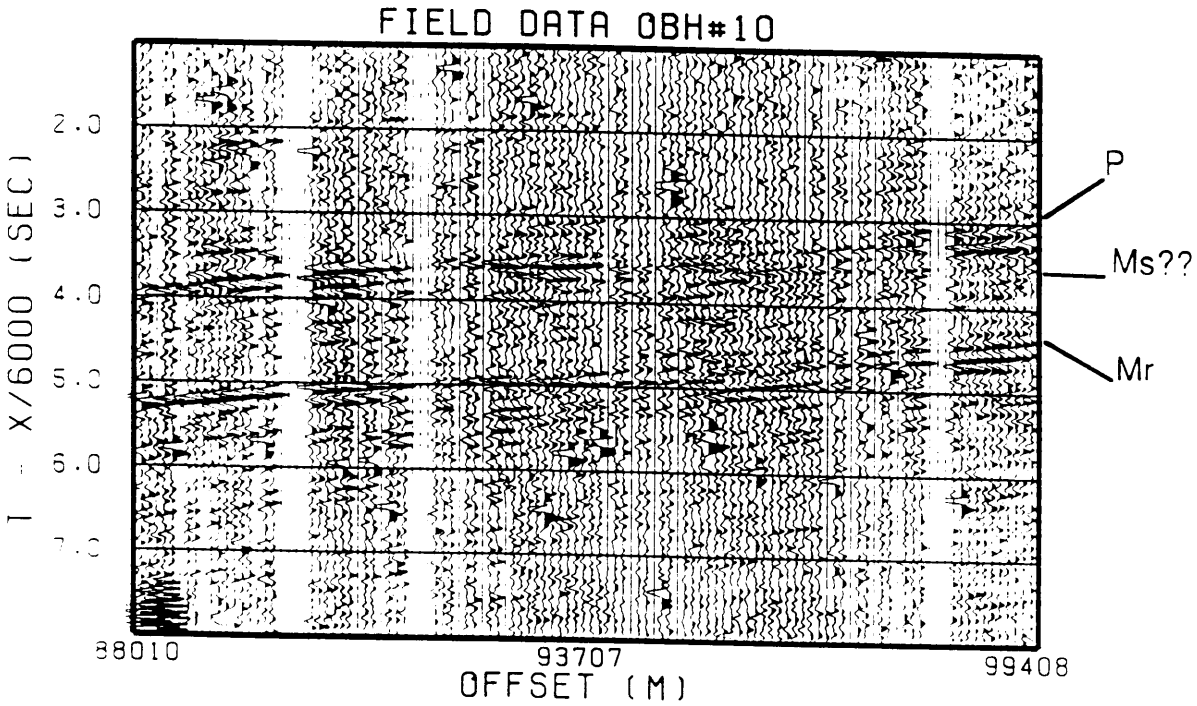

Figure 14. Wide angle Moho reflections (PmP) recorded on OBH ♯10 at offsets from 88 - 100 km. Primary reflections (P) and the receiver multiple event (Mr) are clearly visible, while the source multiple which should arrive approximately 0.55 seconds after the primary is not observed. The data have been lowpass filtered from with a smoothed trapezoid defined at 0,0,20,25 Hz.

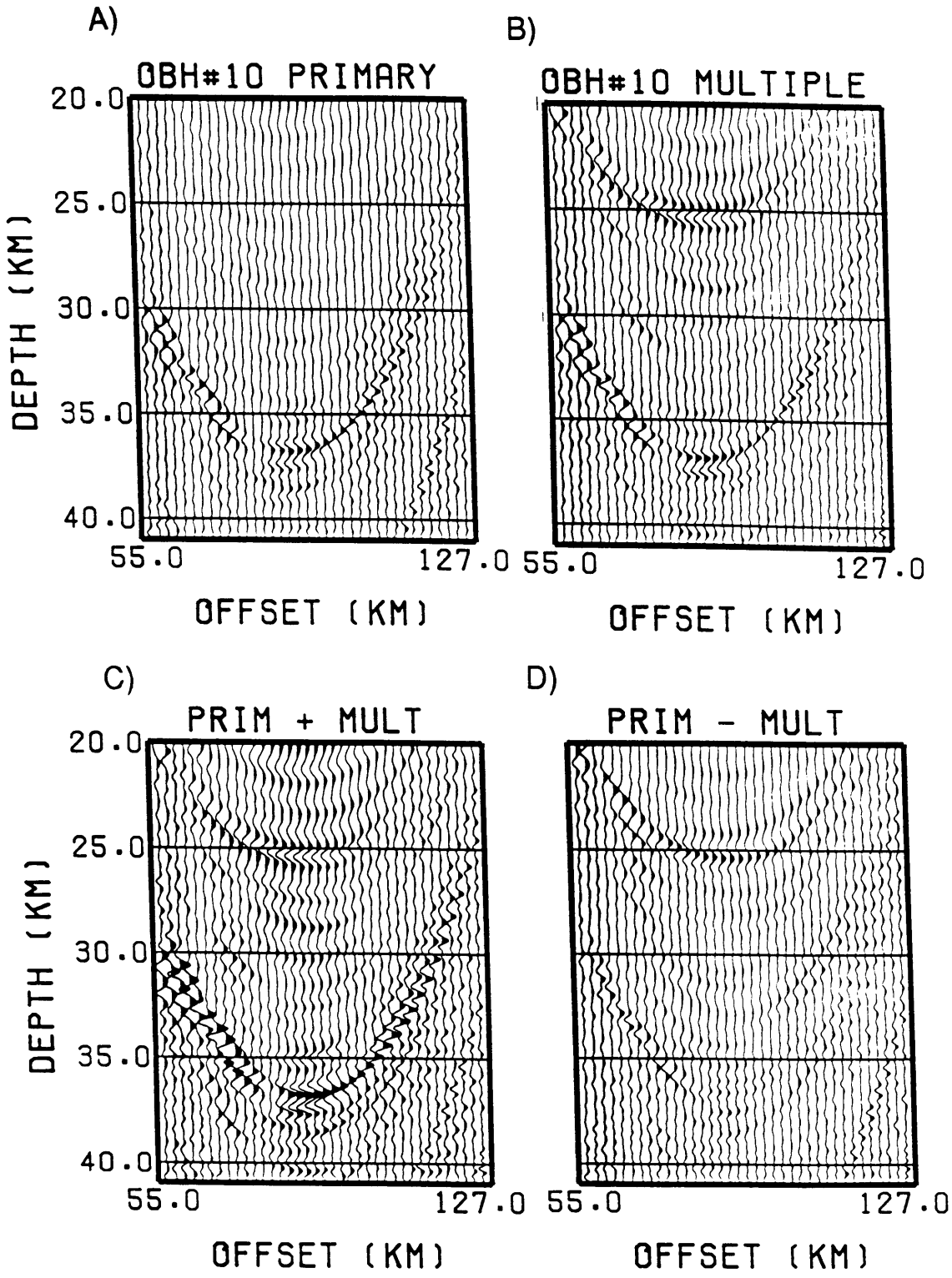

Figure 15. Raw depth images from migrating the field data of Figure 13. a) Image from migrating the data along the primary reflection path. b) Image from migrating data along the receiver multiple path. The polarity has been reversed to account for the free surface reflection allowing a direct comparison between the primary and receiver multiple's images. c) Sum of the images in (a) and (b). Note the constructive interference especially at 37 km. d) Difference (subtraction) of images in (a) and (b). Note the greatly diminished amplitudes in the vicinity of the event at 37 km.

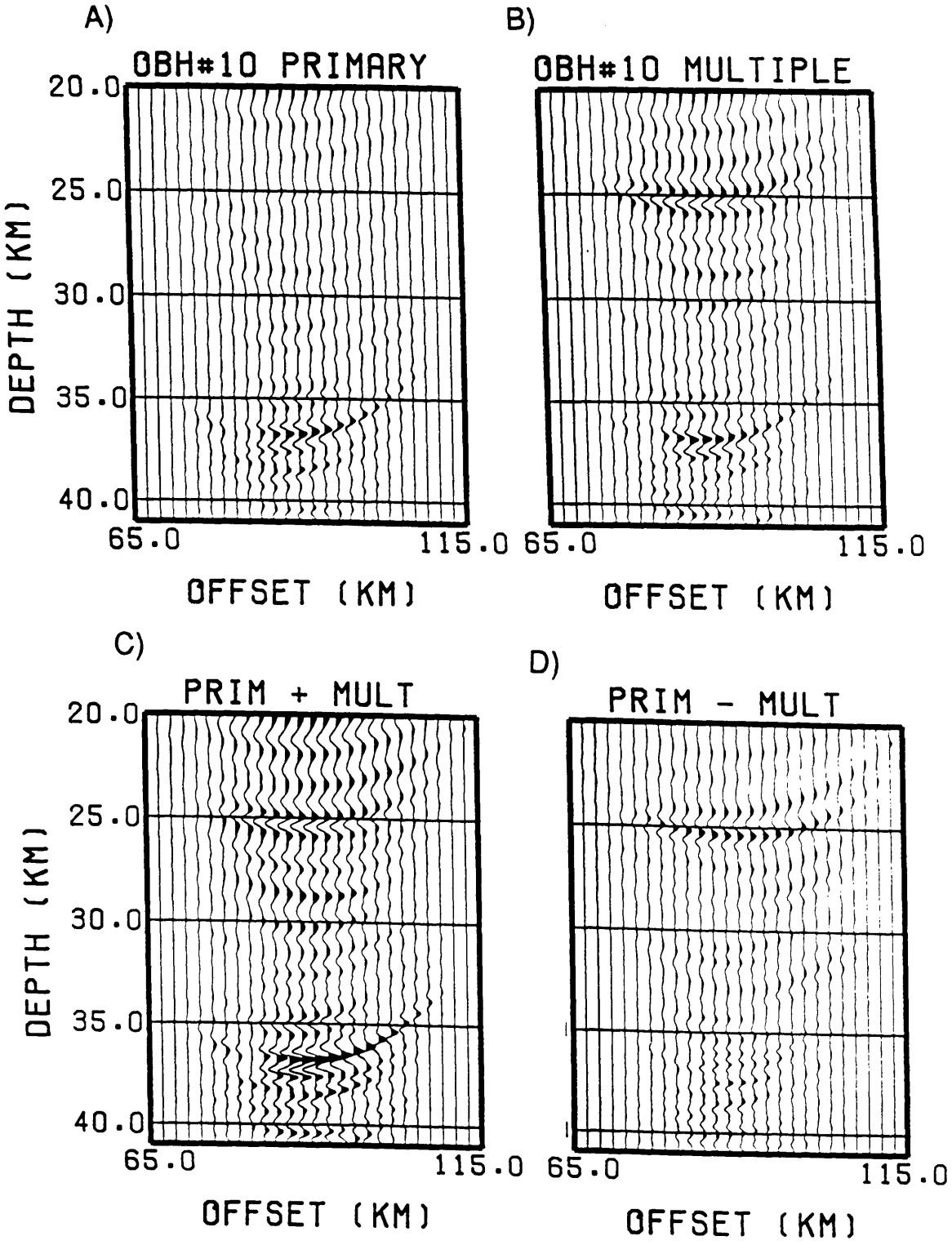

Figure 16. a) Primary image from field data in Figure 14 but with tight dip filter applied to reduce elliptical artifacts. b) Receiver multiple's image with same dip filter as (a). c) Sum of images in (a) and (b). d) Difference of images in (a) and (b).

Chapter 4

Imaging Deep Crustal Structure Beneath the Carolina Trough from Large-Offset Ocean Bottom Seismic Data

Introduction

In this thesis we have focused on techniques to either invert for or directly image deep crustal structure from large offset seismic data. We now apply both our two-dimensional (2-D) velocity inversion/imaging approach of Chapter 2 and the Kirchhoff migration method discussed in Chapter 3 in order to image some deep crustal features beneath the Carolina Trough. Our primary method of imaging is 2-D Kirchhoff pre-stack depth migration applied to wide-angle PmP (Moho reflection) phases. As discussed in Chapter 3, we utilize both primary reflections and first order water column multiples to create a 2-D depth image of the deep crust. We use images from four Ocean Bottom Hydrophones (OBH) to construct a segmented but convincing image of the Moho over an approximately 100 km transect across the Carolina Trough.

A combination of a highly repeatable source, dense trace spacing and a quiet ocean bottom recording environment result in images with excellent signal to noise ratios.

We also present results of imaging both the velocity structure and the reflectivity of a portion of transition type (intermediate between continental and oceanic) crust from a 53 km long receiver gather. The 2-D velocity inversion/imaging approach presented in Chapter 2 is used to directly image the velocity structure, with an emphasis on the deeper ($>$ 5 km) regions of the model. These results are discussed in detail in Chapter 2 and we present only the best fitting velocity model here. The Kirchhoff approach discussed in Chapter 3 is then used to image the reflectivity, or impedance contrast structure using the same raw field data. The velocity model from our 2-D velocity inversion/imaging approach is used as the input velocity for the Kirchhoff migration. We compare the velocity image to the reflectivity image from the Kirchhoff migration and see an excellent agreement between reflecting boundaries. Direct imaging of both velocity and reflectivity represents a novel approach to processing of large offset data. The ability to conveniently characterize (image) the reflectivity and velocity structure of deep crustal regimes will help to further constrain physical properties necessary to understand fundamental tectonic processes.

Carolina Trough Experiment

A joint offshore reflection/refraction seismic experiment was conducted during June of 1988 across the Carolina Trough, a deep sedimentary basin located along the U.S. East Coast. Line 6 in Figure 1 shows the location of the reflection track in relation to the Carolina Trough and prominent magnetic anomalies. Circles on Line 6 represent positions of OBHs deployed prior to MCS shooting which recorded large offset arrivals used to constrain deep crustal structure. Experiments in which stationary receivers record sources from standard reflection acquisition are called "piggyback" experiments; they provide an inexpensive means of acquiring large offset data. A limitation of large offset "piggyback" data has traditionally been inadequate signal

strength from the MCS source, which is generally weaker than large explosive sources commonly used in stand-alone refraction surveying. The Carolina Trough experiment benefitted from a large 10,800 cubic inch airgun array which provided sufficient energy to record arrivals at offsets up to 180 km. A major advantage enjoyed by large offset marine "piggyback" experiments is the repeatability of modern airgun arrays; the result of such highly repeatable sources is an enhanced ability to correlate weak arrivals across groups of traces at large offsets. This allows automatic determination of local phase velocity as well as the use of imaging techniques such as Kirchhoff migration which depend on the constructive interference between adjacent samplings of the wavefield.

One objective of the experiment was to constrain the deep structure beneath the marginal sedimentary basins whose enormous thickness have prevented prior seismic attempts from adequately imaging lower crustal structures. To address the difficulties with deep crustal imaging, a 6 km recording array was used for reflection acquisition (Austin et al., 1990), and OBHs were deployed for large offset recording of deep refracted and reflected arrivals. Originally, the OBHs were to be used for velocity control in subsequent migrations of the MCS data. However, the large offset OBH sections contained wide-angle reflections of sufficient quality to merit imaging on their own.

One of the most fundamental uncertainties regarding lower crustal structure beneath the Carolina Trough is the location of the crust/mantle boundary or Moho. The OBH data makes an important contribution in providing constraints on the Moho by recording large amplitude post-critical Moho reflections (PmP) at offsets ranging to 125 km. Another major lower crustal boundary could be the top of an "underplated" layer of high velocity (7.2 km/sec) material which has recently been postulated to be characteristic of passive margins (Trehu et al., 1989; Fowler et al., 1989). In this chapter we do not directly address the existence or location of this boundary, but 2-D forward modeling of the OBH data by Holbrook et al. (1990) indicates evidence for

its existence. Additional objectives of the experiments were to constrain the source of major magnetic anomalies. The Brunswick Magnetic Anomaly (BMA) and the East Coast Magnetic Anomaly (ECMA) are both traversed by Line 6 and contributions of this experiment regarding their origins are discussed by Austin et al. (1990). Large offset arrivals on the OBH data have not contributed significantly to interpretations of the magnetic anomalies' origins.

Reflection Acquisition

The multi-channel seismic (MCS) acquisition was carried out by a commercial seismic vessel, the GECO MY, and the data was processed by the University of Texas at Austin (UTIG). MCS data was acquired with a 6000 m, 240 channel streamer recording a 10,800 cubic inch airgun array which fired every 50 m. The data were gathered into CDPs every 12.5 m, resulting in 60 fold coverage. Subsequent processing included inside/out muting to enhance multiple discrimination and a variety of filtering operations summarized in Austin et al. (1990). F-K filtering was used to effectively suppress water column multiples, but some interbed multiples generated by high velocity carbonates persisted in the final CDP stack. The seaward end of the line began with shotpoint 1001 and extended approximately 190 km landward to shotpoint 4886. A brute stack of the data with the OBH locations superposed is shown in Figure 2. Sixteen seconds of two way time were recorded although only fourteen are displayed in Figure 2. Austin et al. (1990) present an interpretation of the reflection data, and include a detailed discussion of inferred origins of the ECMA and the BMA as well as postulated Moho reflections. Additional interpretations of the data include the work of Oh et al. (1989), Oh et al. (1990) and Austin et al. (1989).

Refraction

Eight Woods Hole Oceanographic Institution OBHs, four digitally recorded and four analog recorded, were deployed prior to the start of MCS shooting. Deployment was carried out by the contract vessel NUSC Ranger, which was used only for OBH deployment and recovery tasks. Locations of the four digital recording instruments are shown by filled circles in Figure 1. These instruments had a 16 Mb recording capacity limiting them to recording approximately 155 km of total source-receiver offset coverage. The recording windows of the digital OBHs were programmable, in theory allowing selection of which shotpoints or offsets to record. For example, the digital OBH could be programmed to record from 7:00 AM to 11:00 PM if the schedule of the MCS boat dictated optimum offset coverage between those times. In practice the schedule of the MCS vessel was subject to rapid and unpredictable change primarily due to equipment failure such as generator breakdown or streamer malfunction. Uncertainty about the MCS schedule dictated that the digital OBHs not be deployed until the latest possible time to avoid programming them to record at a time when the source was not functional. Limited support materials such as batteries and disposable anchors dictated that an instrument could not be deployed, called back to the surface, and then redeployed with a new programmed recording window. To minimize the possibility of wasting a portion of the limited 16 hour recording time, the NUSC Ranger waited until radio contact with the MCS vessel communicated a successful "run in" or start to the reflection line had begun. At this point, the NUSC Ranger, already positioned at the first deployment location, would deploy the first digital OBH and steam to the next location. Dobh # 15 was the closest position to the start of the line and therefore the first deployment. Deployment starts by positioning the ship as closely as possible to a pre-determined location, followed by dropping the OBH overboard. The NUSC Ranger could steam at roughly 3-4 times the speed of the MCS vessel; given the limited number of digital instruments, it was capable of deploying all of them with minimal loss of recording time.

Deployment of the four WHOI analog OBHs was made simple by the 10 day recording capacity of these instruments. This allowed deployment more than a day before shooting was scheduled to commence. Both digital and analog instruments were equipped with acoustic releases which allowed them to be actively retrieved. An acoustic release requires a transponder tethered to a boat (in this case the NUSC Ranger) to send acoustic signals to the release package affixed to the OBH positioned on the seafloor. The appropriate signal causes a rope connecting a disposable anchor to the OBH frame to be severed, and the positively buoyant OBH frame floats to the surface. This release method is far more convenient than pre-programmed release methods, which involve a similar anchor separating operation but at a pre-determined time. The pre-programmed release methods do not provide the flexibility needed for large scale coordinated reflection/refraction experiments.

The dynamic range of the analog instruments was limited to 40 db while the digital instruments had a dynamic range of over 100 db. The more limited dynamic range of the analog data results in distortion of seismic wave amplitudes especially at short ranges. More importantly, the analog instruments require extensive post-recovery computer processing to convert the analog signal into properly sampled digital data. This included an initial digitization stage where both the recorded analog signal is digitized along with an analog time code which had been written simultaneously to tape. The analog time code must then be checked for irregularities in tape speed which are reflected by distortion, compression or extension of the time code. These distortions are detected and removed from the seismic signal by resampling the data accordingly. The resampling of the time code is very expensive in terms of computer time, running on a VAX 11/780 at approximately a 1:1 ratio. The less variable the tape speed, the fewer the computations required to account for timing discrepancies; the previously stated computer cost is an estimate based on processing approximately 240 hours of data. The digital data require negligible computer time in post-recovery processing; only clock drift needs correcting. A limitation of the digital data is an 18

second gap occurring once every 2 minutes while the instrument was writing a data buffer to tape. This resulted in a 15% loss of data, which did not prove to be a major problem in subsequent processing. The semblance-guided median filter described in Appendix C provided an adequate interpolation approach to fill in digital data gaps. These gaps must be filled in for some types of analysis such as F-K filtering while other procedures such as migration or modeling are little affected.

Navigation on the MCS vessel was primarily STARFIX, a commercial satellite navigation system. Both the GECO MY and the NUSC Ranger were equipped with identical LORAN C receivers and satellite clocks. The LORAN C receivers were calibrated against each other during the experiment to ensure accurate navigation for the deployment phase. The shot instant was logged aboard the GECO MY on the same satellite time scale used to calibrate the OBH clocks on the NUSC Ranger. In addition to logging the shot instant, a record of the ships position as a function of time was kept to allow calculation of the shot position. A file containing shot instant and shot position was then used to reduce the raw OBH data into large offset receiver gathers. The OBH was then located relative to the shot positions by assuming the water depth at the OBH was known. The water depth was logged by the GECO MY continuously and the NUSC Ranger at the time of OBH deployment. The shortest measured travel time through the water column was assumed to indicate the closest source position. Assuming the velocity of water and the water depth are known, an offline component can be determined. No additional measurements of the water velocity as a function of depth were made at sea, so a constant velocity 1500 m/sec was used. This approach, although assuming the depth and velocity of the water, ensures the OBH position is determined relative to the shot locations, thereby eliminating any consistent biases due to differences in navigation systems.

We summarize the instrument location and shot points recorded for all of the OBHs in Table 1a. Analog instruments are referred to as Aobh and digitally recording instruments as Dobh. Of the eight OBHs deployed, only a single analog instrument,

Aobh03 returned with unuseable data. Aobh03 is not listed in Tables 1a and 1b because the time code which must be interpreted to remove variations in recorder speed was difficult to decode. Dobh12 suffered a 20% loss of data due to equipment failure but recorded useful data both before and after this temporary malfunction. Table 1b lists additional information about the OBH data including water depth at deployment location, offline component of location and unuseable portions of data. Excessive environmental noise on instruments Dobh13 and Aobh02 resulted in poor data quality as noted in Table 1b. Offline components in Table 1b refer to the distance in meters between the relocated OBHs and the track of the reflection boat. These offline components were caused by instrument drift in the ocean currents during descent to the seafloor and difficulties positioning the deployment vessel in strong currents.

A complete receiver gather from Dobh15 is shown in Figure 3a with an enhanced version of the data shown in Figure 3b. The receiver was located in 2300 m of water and the data represents one of the best quality large offset recordings from the experiment. Source offsets range from 35 km on the seaward end of the line (shotpoint 1047) to 120 km (shotpoint 4147) on the landward end of the line. The hyperbolic event with a minimum travel time at zero offset is the direct arrival through the water column. A series of sedimentary refractions and reflections are clearly seen out through 40 km. At offsets greater than 90 km, a complicated set of arrivals is observed, one of which we interpret to be a reflection from the Moho. At all offsets we observe a prominent water column multiple corresponding to a free surface reflection from above the receiver (the "receiver multiple" of Chapter 3). The large amplitude diagonal bands of energy are multiply reflected water- born energy from the previous shots. The experiment was shot every 50 m which corresponded to a shot interval of roughly 20 seconds. Slowly traveling water-born energy from up to 3 shots before is present in Figure 3. We refer to this energy as "previous shot" interference in subsequent discussions of the OBH data. Figure 3c and 3d show an expanded version

of the data in Figure 3a illustrating the high quality of deep water OBH-airgun data. Figure 4 shows an average spectrum from arrivals between 90 and 100 km offset on Dobh15. The peak frequency of about 7 hz is typical of the large offset arrivals in this experiment.

Additional Geophysical Data

The United States Geological Survey has sponsored a program of geophysical investigations along the entire U.S. Atlantic Margin. These include the seismic line labeled USGS 32 in Figure 1 as well as lines to the north and south. Grow et al. (1979) show depth sections from 6 MCS lines from south of Cape Cod to just south of Cape Hatteras. The lack of deep velocity control and good penetration prevent imaging below 15 km with these data. More recently, Hutchinson et al. (1983) interpreted Line 32 shown in Figure 1. Line 32 appears to be the highest quality line in this region other than the new Line 6 of our study. Line 32 was shot with a 3.6 km 48-channel streamer and a tuned airgun array totaling 1700 cubic inches. It has been interpreted to show a depth to basement across the Carolina Trough in all but the deepest sections of sedimentary fill. A major shortcoming of Line 32 is the lack of control on the Moho (Hutchinson et al., 1983). Trehu et al. (1989) present results of forward modeling and tau-sum inversion of three along-strike refraction profiles shot using Ocean Bottom Seismometers and explosive sources. Significantly, these results represent the best direct seismic evidence for depth to Moho for at least two points along the Carolina Trough. Deep velocities from best-fitting models also indicate a fast 7.1-7.5 km/sec region located seaward of the hinge zone with thicknesses up to 10 km. Reviews of earlier refraction work may be found in Sheridan et al. (1988) and Trehu et al. (1989). Additional deep refraction results are presented by Diebold et al. (1988) north of the Carolina Trough in the Baltimore Canyon Trough. They also document existence of a deep fast layer with velocities exceeding 7 km/sec in general agreement with the results of Trehu et al. (1989).

Potential field data exist in addition to seismic data. Sheridan et al. (1988) gives a thorough summary of gravity and magnetic observations along the U.S. Atlantic margin. Magnetic data are of particular importance in estimating depth to basement for regions with thick sedimentary deposits. Hutchinson et al. (1983) model magnetic data and estimate the depth to basement as 5-6 km in the Carolina Platform and more than 11 km in the deepest part of the trough. Gravity data (Klitgord et al., 1988; Hutchinson et al., 1983; Grow et al., 1979) have been used for estimating depth to mantle (Moho) along the entire margin. Uncertainties with modeling gravity data become significant when densities of crustal constituents are poorly known. Hutchinson et al. (1983) model gravity data with a Moho which shallows in a series of steps. They assume a Nafe/Drake density/velocity relationship in the sediment and a two layer crust beneath. Given the uncertainties of sedimentary velocities in the deep basins, gravity models are subject to corresponding uncertainties.

Wide-angle Moho imaging

Results of migrating wide-angle Moho reflections recorded by four OBHs deployed on Line 6 will now be presented. We show both raw data observations and the corresponding migrated depth images. Difficulties with presenting an interpretable image from such sparse receiver gathers will be discussed, and the use of dip filters is presented as a means to make such images more interpretable. An image approximately 100 km wide shows a strong deep reflecting horizon shallowing from 37 to 25 km. This reflector is interpreted to be Moho over a portion of the transition zone between continental and oceanic crust.

Unlike traditional MCS migrations where entire shot gathers are muted of large offset energy before imaging, wide-angle data needs to be carefully selected prior to migration. Kirchhoff migration will correctly image only that energy which satisfies the single scattering assumption, e.g diffracted and reflected arrivals. Refracted and other non-reflected arrivals compose a significant portion of the large offset wavefield.

These non-scattered arrivals may be thought of as noise; if migrated along with reflected energy, they will degrade the resulting image. "Previous shot" interference represents a major source of non-reflected noise in the OBH geometry of this experiment. Amplitudes of water-born "previous shot" energy can be up to one to two orders of magnitude greater than the sought after wide-angle reflections. If such data were to be summed into the migrated image, the constructive interference needed to produce identifiable deep reflecting horizons would be severely disrupted. Refractions or diving rays are another type of "noise" present in large offset wavefields. Refractions typically have amplitudes on the same order of magnitude as reflections. Separating the refracted wavefield from the reflected on the basis of velocity is often not possible. The reflected arrivals will generally have similar apparent velocities to the refracted arrivals. Often the difference in velocities is too small to allow effective velocity filtering, especially over relatively small apertures where such energy is laterally coherent. In cases where both reflected and refracted energy is present, the migration operator must be relied upon to defocus the refracted and focus the reflected energy.

Figure 2 shows the OBHs locations superposed on the stacked MCS section from Line 6. The data in Figure 2 are presented with a five trace running mix and every 10th trace is plotted for clarity. A higher quality presentation of the stacked section may be found in Austin et al. (1990). Three instruments, Dobh10, Dobh15 and Aobh07, recorded data of sufficient quality to migrate both primary and water column multiple PmP arrivals. Aobh01 did not record a clear water column multiple due to interference from water-born previous shot energy. Those source-receiver offsets which recorded usable Moho arrivals are listed in Table 2 and are shown in Figure 5a and 5b. We see from Figure 5 and Table 2 that landward Moho reflections tended to be observed at greater offsets than more seaward reflections. Dobh's 10 and 15 showed clear PmP arrivals from 88-100 and 94-104 km respectively. Aobh01, which recorded the most seaward PmP reflection, recorded this arrival at approximately 53-50 km

offset. This observation is in qualitative agreement with our conclusion that the Moho shallows seaward; therefore, large amplitude near critical reflections are expected to be observed at smaller offsets for receivers sampling a shallower Moho. Events were identified as PmP arrivals on the basis of arrival time, apparent velocity and forward modeling results of Holbrook et al. (1990). It is possible that some of the events we identify as PmP arrivals could be some other type of reflected or refracted energy. However, we note that our identification of PmP arrivals is consistent with reasonable velocity models for USGS Line 32 from Trehu et al. (1989).

A velocity model derived from two-dimensional ray-trace forward modeling of large offset reflected and refracted phases (Holbrook et al., 1990) is smoothed and used for subsequent migration examples. Sedimentary velocities were computed by digitizing prominent boundaries in the stacked section and locating the corresponding wide-angle reflections in the OBH data. Modeling of these wide-angle reflections allows the computation of the desired sedimentary interval velocities. Large offset phases were then modeled by holding the sedimentary velocities fixed and allowing deep velocities and reflecting boundaries to vary.

Figure 6 shows all observed arrivals which were migrated to produce our final Moho image. The data in Figure 6 are plotted on a true amplitude scale and low pass filtered with a linear roll-off from 20 to 25 hz. Figure 6a shows data from 88-100 km of offset recorded by Dobh10. A water column multiple (receiver multiple of Chapter 3) is clearly seen arriving 1.36 seconds after the primary arrival. Data from 94-104 km of offset recorded by Dobh15 are shown in Figure 6b. Dobh15 was deployed in 2380 m of water, resulting in a water column multiple arriving 3.14 seconds after the primary arrival. Figure 6c shows data from Aobh07 for offsets from 123 to 130 km. Aobh07 was the deepest water OBH deployment in 2580 m of water; it recorded a clear water column multiple delayed from the primary by 3.44 seconds. Additional data from Aobh07 from 58-70 km are shown in Figure 6d. Data from Aobh01 are shown in Figure 6e and represent the most seaward control on PmP observations. We

select the data of Figure 6 for migration because clear PmP arrivals are observed; the migrated data offsets are chosen to be free from previous shot interference. Migration of smaller source-receiver offsets would in general result in shallower crustal images, and is necessary to display the full imaging potential of large offset marine piggyback data. We chose the Moho as an imaging target because of its importance to models of passive margin evolution, and because of the strength of the observed reflection.

Figure 7a shows an image from migration of Dobh10's data in Figure 6a along a primary reflection path, and Figure 7b shows the results from migrating the data along the receiver multiple's path. Figure 7b has been plotted with reversed polarity to allow direct comparison with Figure 7a. The horizontal axis on this and all subsequent images is defined in kilometers along Line 6, as shown in Figure 2. Shotpoint 1000 is defined as kilometer 200 in this coordinate system, with shotpoint 2000 as kilometer 150 etc. The final shotpoint 4876 is defined as offset 6.2 km. Images in Figures 7a and 7b are 70 km wide and and 20 km deep; they are plotted with a vertical exaggeration of approximately 4.5. Migration of Dobh15 data (Figure 6b) along the primary reflection path is shown in Figure 7c. Figure 7d shows the same data migrated along the receiver multiple's ray path and plotted with reversed polarity. Figures 7a-d show a clear reflector at 37 and 35 km of depth respectively, which we interpret to be the crust-mantle transition. Figures 7a-d are both produced with no dip filter and thus are dominated by elliptical migration artifacts. A buildup of amplitude can be observed just slightly seaward (to the right) on the largest amplitude ellipse. Assuming the velocity model is correct or nearly so, this buildup in amplitude can be used to indicate the true position (dip) of the reflector. Both Dobh10 and Dobh15 show buildups in amplitude on the seaward side of the ellipse which is not inconsistent with a seaward shallowing of the Moho.

Figure 8a shows an image from migrating Aobh07 data recorded from 123-130 km along the primary reflection paths. The same data are migrated along the receiver multiple path and shown in Figure 8b plotted with reversed polarity. The concen-

tration of energy along the seaward side of the ellipse is more noticeable here than in Figures 7a-d. Provided the dominant ellipse in Figure 8 corresponds to the same reflector thought to be Moho in Figures 7a-d, the gross position of the ellipse agrees with the dip estimates from amplitude buildup observations in Figures 7a-d. Taking the base of the largest amplitude ellipse in Figures 7 and 8 as a reference point, the overall trend of the ellipses shallows in the seaward direction. Data from a shorter offset range, 60 to 70 km, recorded by Aobh07 is migrated and shown in Figure 8c. The same data migrated along the receiver multiple path is shown in Figure 8d. The last data group migrated is Aobh01 from 50-53 km of offset; the results is shown in Figure 8e. Figure 8e is an image from migrating along the primary reflection path, and represents the most seaward image of Moho obtained with this experiment. The amplitude buildup on the main ellipse in Figure 8e is slightly skewed to the landward side of the image. This is inconsistent with the generally shallowing Moho, although the overall position of the ellipse is not.

We now construct a final image from the individual images in Figures 7 and 8. Figure 9 shows a composite image from 60 to 190 km in offset and 15 to 40 km in depth. The image is sampled every 2 km in offset and every 0.05 km in depth. No dip filter has been applied during migration, and a confusing series of ellipses contributes to an image which is quite difficult to interpret. This image illustrates perfectly the limitations imposed by very sparse receiver sampling of the large offset wavefield. Ideally, the final summation over receivers would result in elimination by destructive (or lack of constructive) interference of elliptical artifacts present in the individual images, and enhancment of the true reflectors by constructive interference. Pre-stack migration of traditional reflection data works well because summation of densely acquired shot gathers is sufficient to reduce elliptical migration artifacts. Finite aperture of either shot or receiver gathers produces the elliptical artifacts referred to as edge effects (Stolt and Benson, 1986). These are present in individual MCS shot gather images as well as in our geometry. Regardless of the aperture limitations which

produced the elliptical artifacts in the first place, summation over receiver gathers proved entirely inadequate to produce an interpretable image.

A dip filter is one which selectively weights portions of the elliptical surface of equal travel time on the basis of dip. This may be used to enhance reflectors of a certain dip while suppressing other dips. In our case we use a cosine dip filter which is constructed by specifying some central dip and filter width. For example a dip filter centered around $+5^0$ with a width of $\pm 10^0$ would weight dips of 5^0 with a value of 1, dips of 0.0^0 and 10.0^0 with a value of 0.707, and completely reject dips outside the dip range of -5^0 to $+15^0$. Other types of filters with different roll-off characteristics may also be used for dip filtering.

Figure 10 shows the image in Figure 9, but with a $\pm 15^o$ dip filter centered around a series of dips between 2.5 and 7.5 degrees. Table 2 summarizes the dips about which the dip filters are centered in Figures 10 and 11. The most noticeable difference between Figures 9 and 10 is a reduction in the higher angle portions of the elliptical artifacts. A more interpretable image is produced at the expense of eliminating possible true reflectors outside the dip filter passband. Figure 11 is produced by migrating with a tight $\pm 7.5^o$ dip filter; it is sampled every 1 km in offset. Interpretation of this image is more obvious because of the nearly complete suppression of elliptical artifacts. It is necessary to emphasize the drawbacks with dip filtering. The choice of parameters for the dip filter emphasizes dips within the specified dip filter passband which may or may not be an accurate representation of the subsurface. To address this concern, the unfiltered, difficult to interpret images should always be presented alongside the dip-filtered images for comparison.

We present our image of the Moho along with published models based on gravity and magnetics (Hutchinson et al., 1983; Klitgord et al., 1988), and results from along-strike refraction profiles (Trehu et al., 1989). Figure 12 shows an estimate of the Moho from a combination of gravity, magnetics and reflection data as a dotted line from Hutchinson et al. (1983). The blocky nature of the Hutchinson et al. (1983)

model is required to fit magnetic and gravity observations. A modified version of the Hutchinson et al. (1983) model is presented by Klitgord et al. (1988) and shows a smoother transition from continental to oceanic crust. We show this model as a solid line in Figure 12 and observe a qualitatively better fit than with the blocky structures characteristic of potential field modeling. Both Moho estimates from Hutchinson et al. (1983) and Klitgord et al. (1988) are for Line 32 (see Figure 1) which is slightly to the north of our results.

Figure 13 shows the Moho depths from along-strike refraction profiles from Trehu et al. (1989) superimposed on our image. Circles indicate the locations at which the along strike refraction surveys were conducted; the solid line shows the interpreted Moho from Trehu et al. (1989). Our image agrees well with the along-strike refraction data. A small systematic difference indicates that our image produces a slightly shallower Moho. The misfit is well within the velocity uncertainty contained in both the migration velocity model and the model of Trehu et al. (1989). A rigorous comparison requires migrating our cross-strike OBH data with the exact velocity model of Trehu et al. (1989).

Dual Velocity/Reflectivity Imaging

We have presented two distinct approaches to imaging large offset data in this thesis. A two-dimensional velocity inversion/imaging approach was derived and presented in Chapter 2 which imaged the large offset wavefield onto a best-fitting velocity model. This approach maps post-critical reflections and refractions to their bottoming points in a three-dimensional data space of offset-depth-slowness. In Chapter 3 we use a Kirchhoff migration method to obtain a two-dimensional image of reflectivity from reflected arrivals. We now apply both methods to a single refraction line to demonstrate the potential of these techniques to fully utilize the information contained in the large offset wavefield. The paradox of migration has always been that in order to properly image the reflected wavefield, the correct velocity model must be used

in the imaging process. We address this issue by first applying our 2-D velocity inversion/imaging approach to determine an optimal velocity model, and then use this model as input to a Kirchhoff migration. Thus, we produce "dual" images, a velocity image and a reflectivity or impedance contrast image.

In Chapter 2 we presented the results of imaging a one-dimensional velocity profile beneath a fixed two-dimensional ocean bottom and upper sedimentary section. Figure 14a shows the 53 km long receiver gather from Aobh01 used in this example; we refer the reader to Chapter 2 for additional details. The resulting one-dimensional velocity image is shown in Figure 14b. It displays three prominent velocity discontinuities at around 9 km, 15 km and 22 km of depth. Reflections from these boundaries are labeled in Figure 14a as 9 km, 15 km and 22 km, respectively. Figure 14c is an image from migrating the data in Figure 14a with the imaged velocity model in Figure 14b. To avoid the large amplitude previous shot noise from about 31-50 km in Figure 14a, we do not migrate these offsets. Offsets from 53-50 km and from 31-12 km were migrated to produce the image in Figure 14c. To reduce the size of the image space and thus the computational burden, we broke the problem up into three separate migrations each with an appropriately chosen image space to encompass zero-dip specular reflections. A $0^o \pm 15^o$ dip filter was applied during migration to reduce elliptical artifacts. The three velocity discontinuities present in the velocity image in Figure 14b are now viewed in a traditional image of reflectivity in Figure 14c. The horizontal axis in Figure 14c is labeled in the coordinate system defined in Figure 2. The two images agree well in terms of the depth of the three boundaries and illustrate how these imaging techniques may be used to examine either velocity or reflectivity from large offset seismic data. In an ideal case with denser OBH spacing, the velocity image displayed in Figure 14b could be displayed as a true three-dimensional offset-depth-slowness volume. In this case the lateral bottoming points which we see in the Kirchhoff image could be directly compared to those in the velocity image. With a single receiver gather this is not justified, although we present such three-dimensional

images in Chapter 2 with synthetic data.

Discussion

The results of migrating wide-angle Moho reflections illustrate the potential of using large offset data to image deep crustal structure. An image of the crust-mantle boundary has been obtained by migration of several large offset receiver gathers; this image agrees qualitatively with previous seismic and potential field estimates. Realistic imaging of deep structure with large offset seismic data requires far greater receiver density than is currently deployed. The raw migrated image in Figure 9 shows the predominant elliptical artifacts resulting from undersampling in the receiver gather domain. A dip filter can be used to superficially improve the image, as Figure 11 shows, but a meaningful solution lies with greater receiver density. The observation of large amplitude reflections at 100 km of offset using an airgun array as a source is encouraging. Realistic velocity models make interpretation of these reflections as PmP arrivals reasonable; the data are of sufficient quality to allow constructive interference during migration. The resulting dip-filtered image of the Moho shows a signal-to-noise ratio greater than 5, which provides an image of excellent quality compared to previously published seismic images. A limitation of large offset data difficult to avoid is the lack of bandwidth. The peak energy was found around 7 hz at 100 km offset in our experiment, which translates to wavelengths of approximately 1.0 km at Moho depths.

We have also demonstrated that deep structure may be imaged in terms of both velocity and reflectivity from large offset data. This approach shows significant potential to characterize physical properties of deep crustal structure. The mid- to deep crust is not composed of the flat-lying reflective boundaries which traditional MCS surveys have been so successful at imaging. Velocity gradients make up a significant portion of the mid- to deep crust and thus are only indirectly detected with velocity analysis by MCS surveys. A technique which directly images realistic two-dimensional

velocity structures allows characterization of lower crustal velocities by defining the velocity gradients known to exist at these depths. We have shown that our velocity inversion/imaging technique may be used to derive a velocity model for standard migration techniques. Images from our velocity inversion/imaging method are shown to agree with those from a traditional migration approach.

In Figure 15 we present a composite model of crustal structure across the Carolina Trough from the sparse imaging results of our study. The location of the Moho is determined by picking the onset of the depth migrated seismic pulse in Figure 11. The model is presented with the same offset axis as Figure 2 and covers the entire reflection profile. We show those parts of the Moho which were not directly imaged by the Kirchhoff migration with a dashed line, and those portions which are well imaged by a solid line. The dashed lines represent qualitative extrapolations based on the approximate trend of the Moho from published estimates (Trehu et al., 1989; Klitgord et al., 1988; Hutchinson et al., 1983) incorporating both potential field and seismic data. The mid-crustal boundary shown at approximately 15 km at 175 km offset is imaged only by Aobh01 with source-receiver offsets of less than 30 km. We show this boundary at its imaged offsets as Aobh01, and use "??" to illustrate the uncertainty at neighboring offsets. Instruments Dobh15, Dobh10 and Aobh07 were not migrated at the relatively short offsets necessary to image this mid-crustal boundary because the primary imaging objective was the Moho, which required greater (¿ 50 km) source-receiver offsets. Figure 15 clearly shows the limited lateral coverage of the Moho enforced by the OBH locations. The Moho was imaged over slightly less than half the total length the reflection profile; geologically important regions at the beginning (seaward end) and end (landward end) of the line were not imaged. Additional OBHs would help in extending the image by increasing the effective aperture over which the large amplitude post-critical PmP arrivals are observed.

Table 1a

Instrument	Location (Shot #, Offset (km)	Shot # recorded	Offsets recorded (km)
Aobh07	# 1256, 187.25	#1001 to #4876	12.5 to -181.0
Dobh15	# 1761, 161.95	#1047 to #4153	35.6 to -115.4
Aobh01	# 2062, 146.95	#1001 to #4876	53.0 to -140.7
Dobh10	# 2373, 131.40	#1222 to #4396	57.5 to -101.1
Dobh13	# 3005, 99.80	#1512 to #4718	74.6 to -85.6
Dobh12	# 3504, 74.85	#1934 to #4827	78.5 to -66.1
Aobh02	# 3757, 62.20	#1001 to #4876	137.8 to -55.9

Table 1b

Instrument	Offline (m)	Water depth	Data quality
Aobh07	937 S	2580	good
Dobh15	816 S	2388	good
Aobh01	1200 S	1885	good
Dobh10	765 S	1020	good
Dobh13	425 S	707	noisy #1512-2400
Dobh12	????	590	no data #3440-4040
Aobh02	470	484	noisy #1001-3400

Table 2

Instrument	Offsets migrated (km)	dip filter center	Including multiple ?
Aobh01	53-50	2.5°	no
Aobh07a	53-60	5.0°	yes
Aobh07b	123-130	7.5°	yes
Dobh15	94-104	5.0°	yes
Dobh10	88-100	2.5°	no

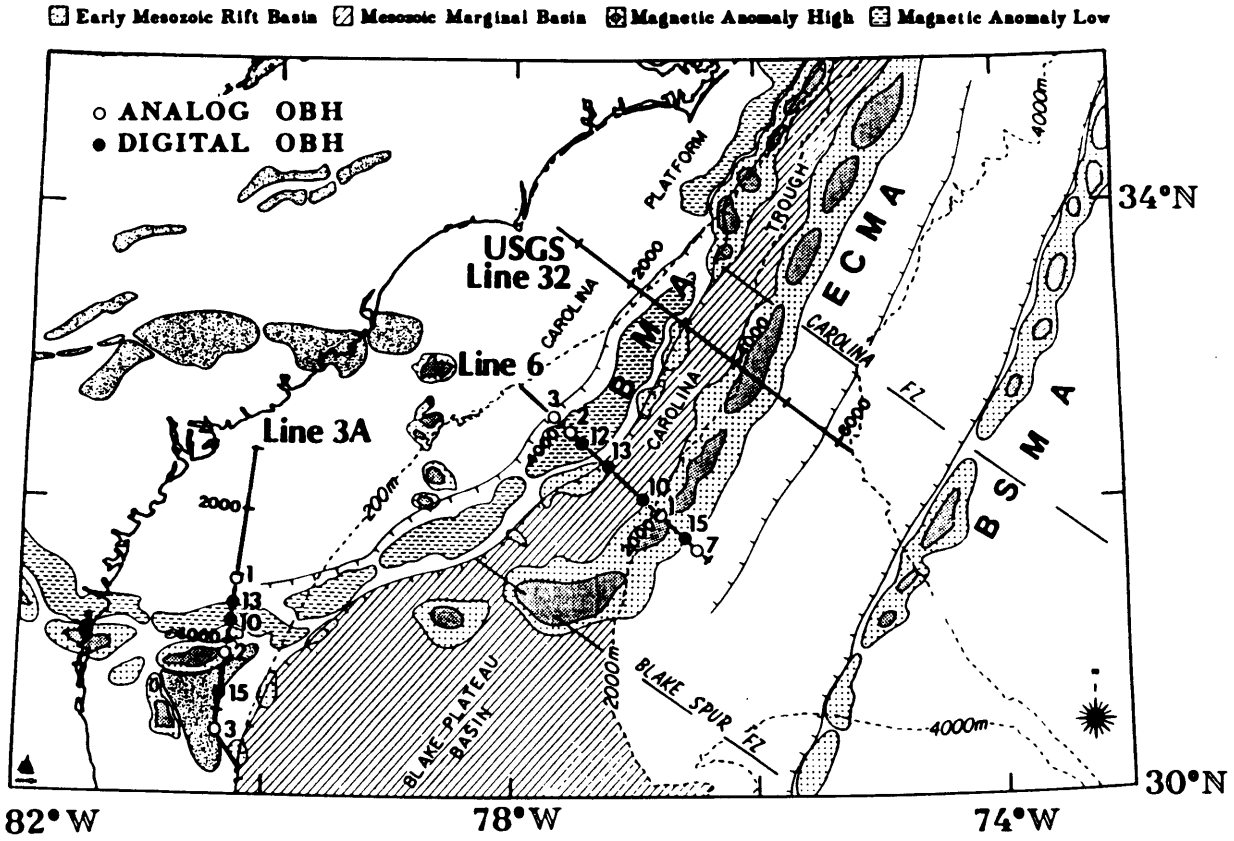

Figure 1. Plan view of the Carolina Trough reflection/refraction experiment. Lines 3A and 6 were both instrumented with fixed Ocean Bottom Hydrophones which recorded data up to 180 km of offset. Line 32 was acquired by USGS and is shown for comparison. Data from Line 6 is presented in this thesis. BMA and ECMA are Brunswick Magnetic Anomaly and East Coast Magnetic Anomaly respectively.

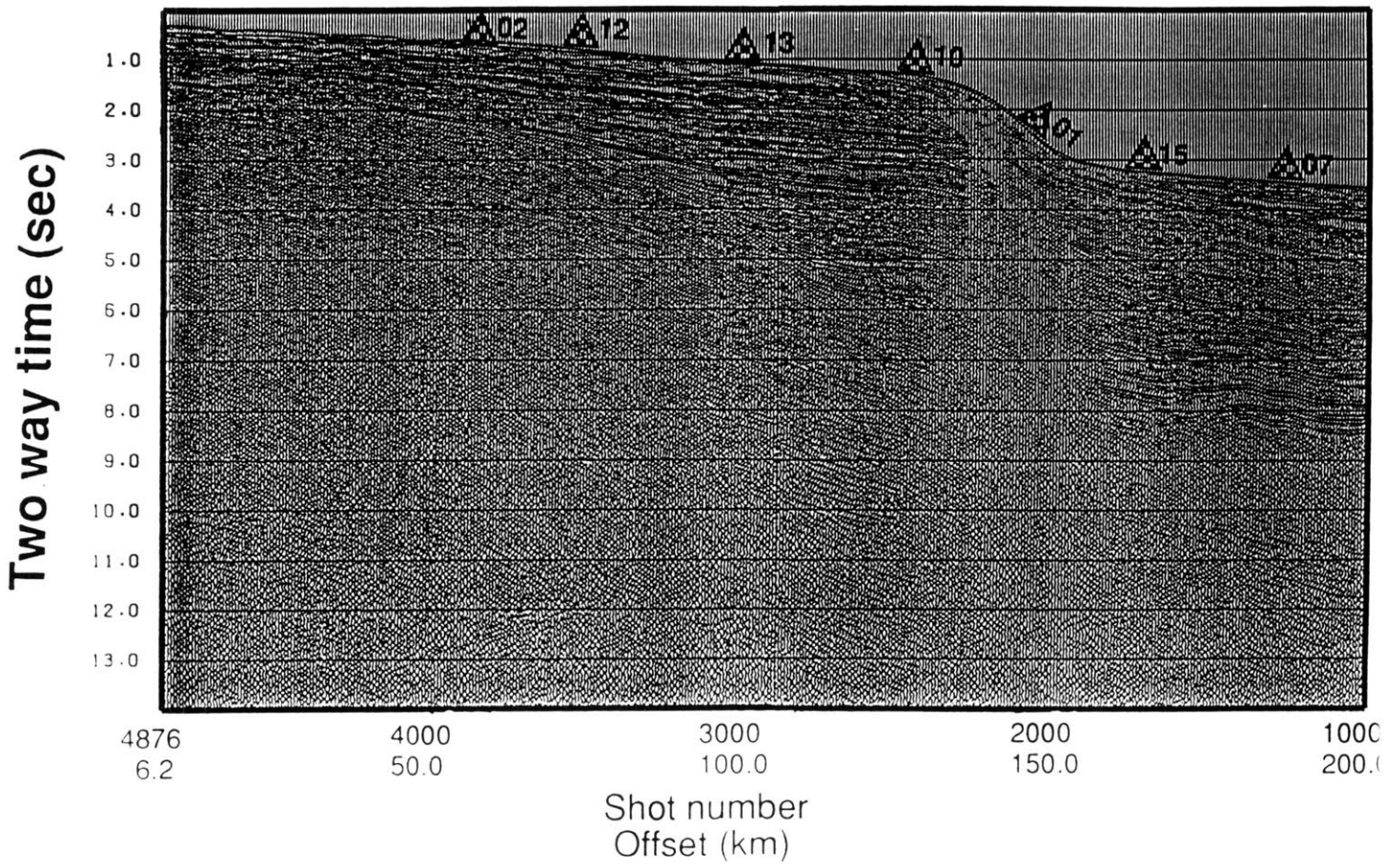

Figure 2. Stacked section from Line 6 with OBH locations shown as triangles. The stacked section was processed with a 5 trace running mix and every tenth trace plotted for clarity.

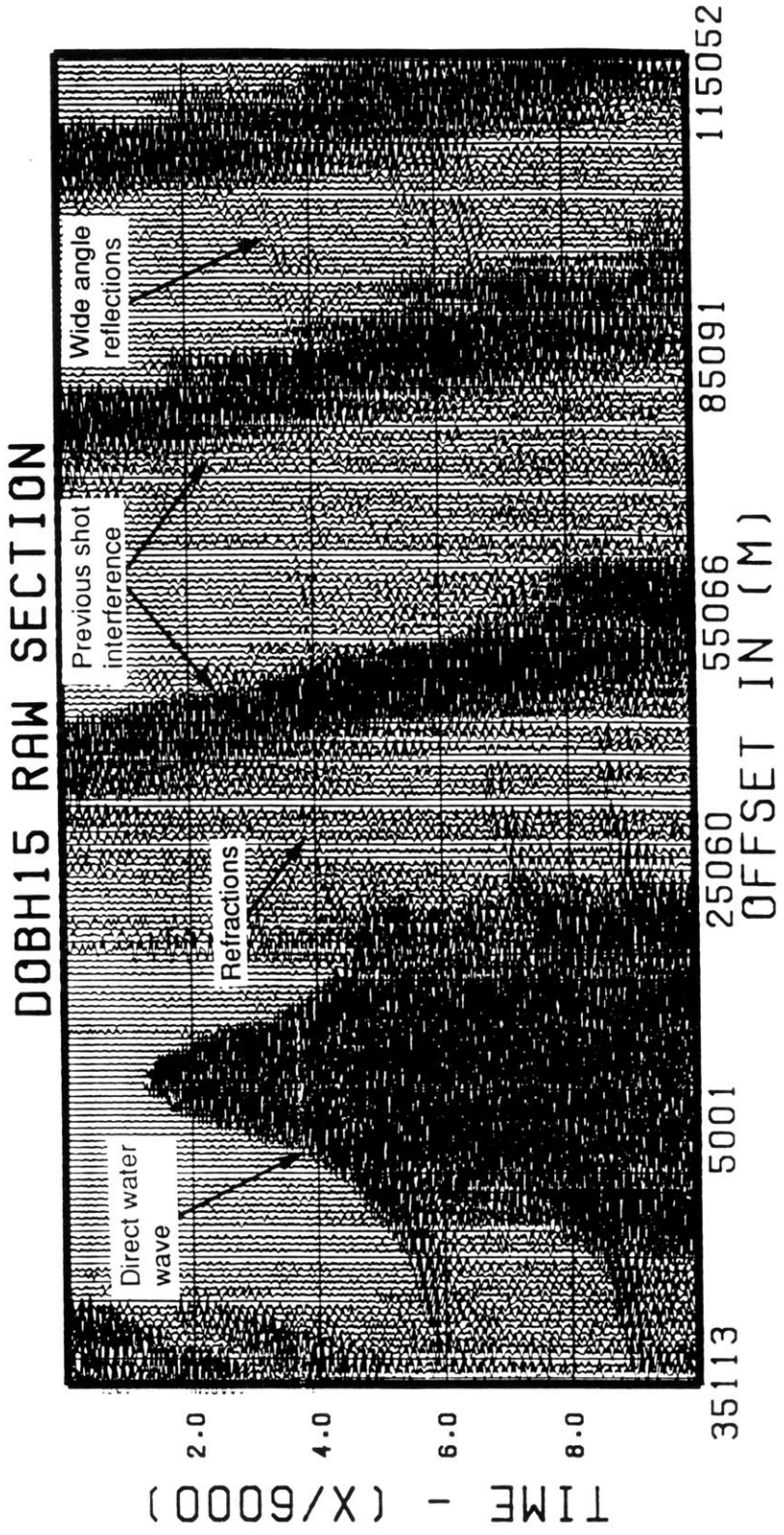

Figure 3a. Complete receiver gather from Dobh 15 (see Figure 2 for Dobh location). Offsets range from 35 km seaward (left) of the receiver to 115 km landward (right).

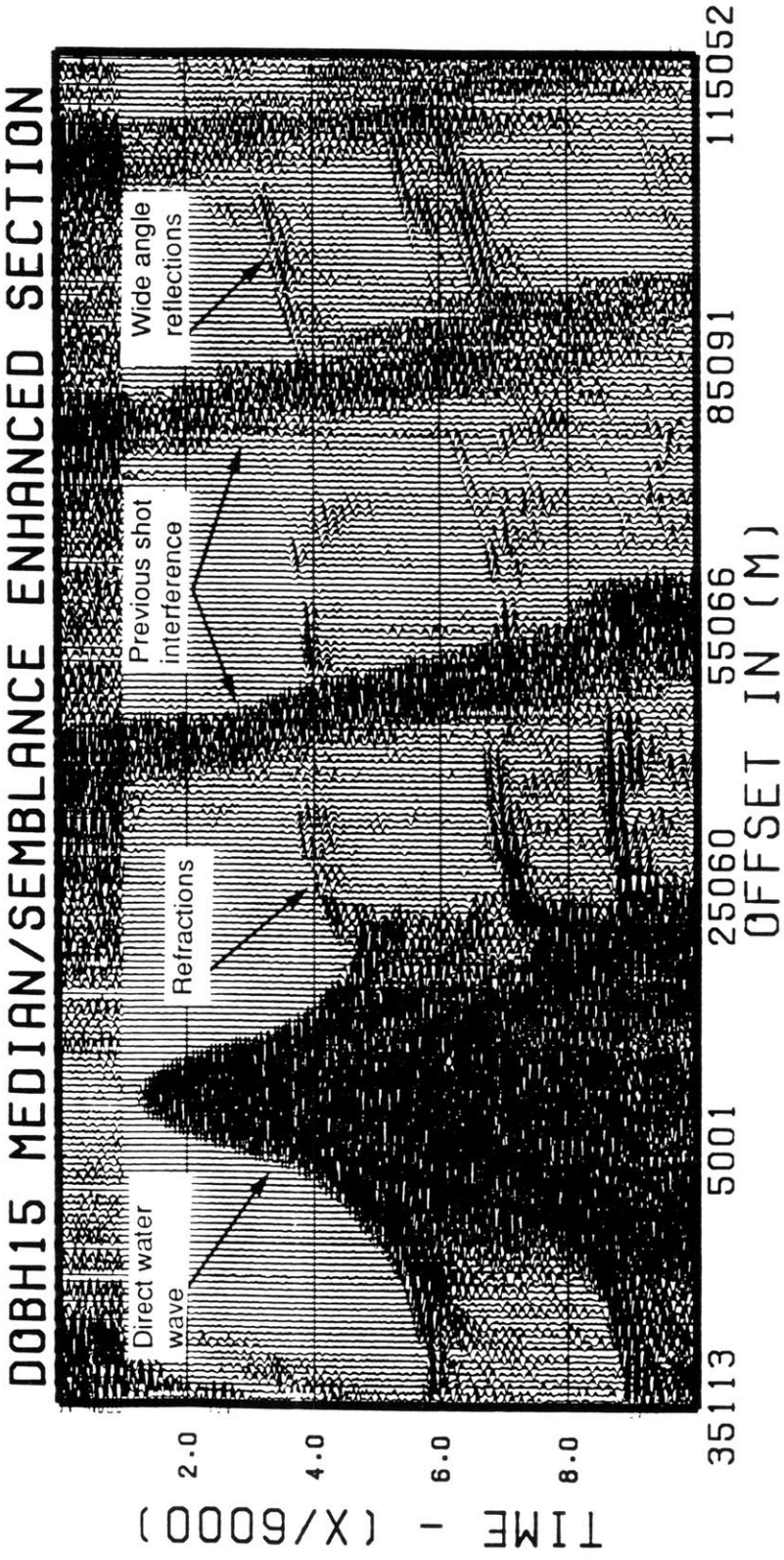

Figure 3b. Same as (3a) but after semblance-guided median filtering with a 15 trace gate and a slowness passband from 1.5-15 km/sec. The data were both median filtered and semblance weighted (see Appendix C).

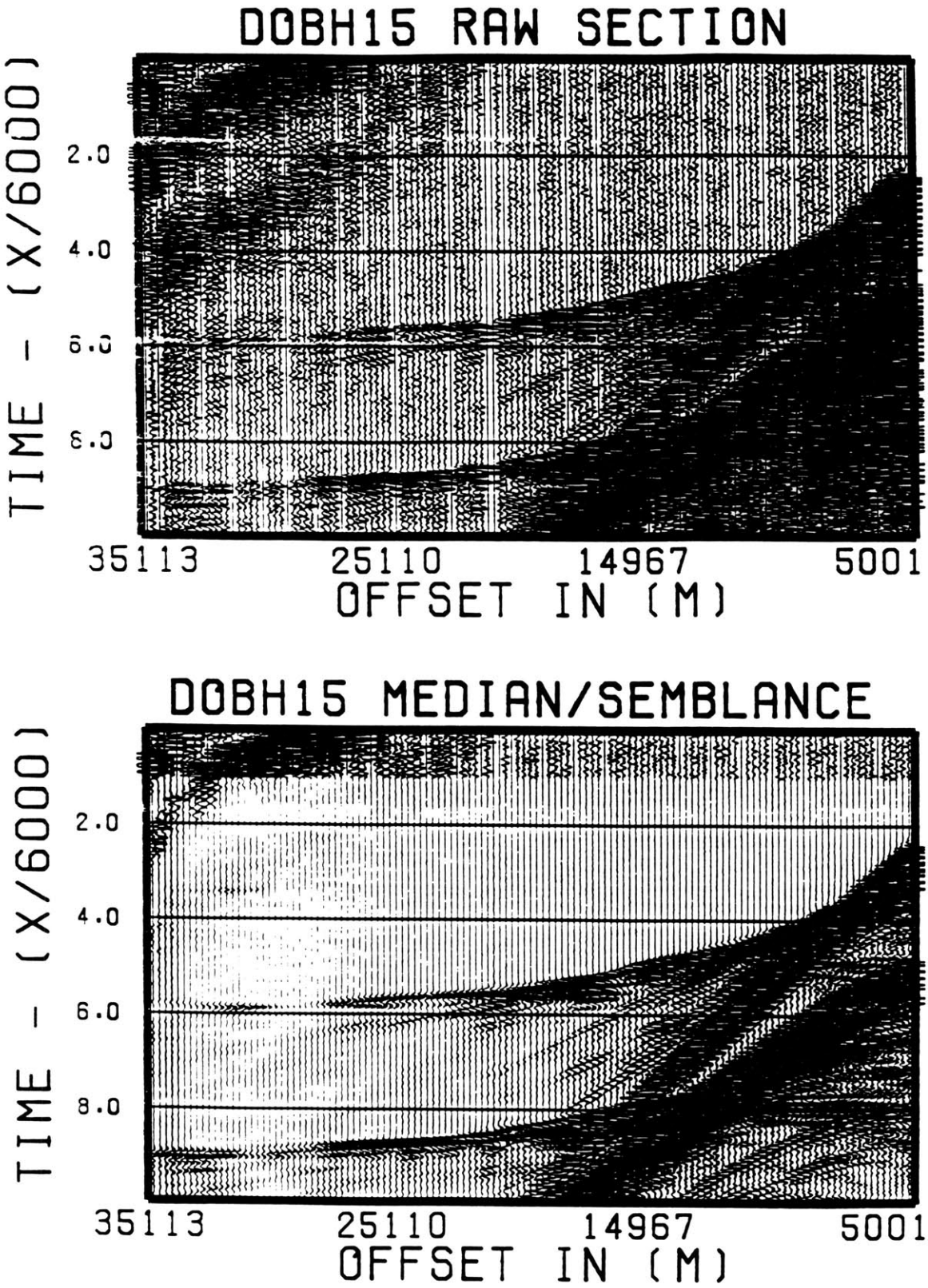

Figure 3c. Top: Expanded view of the seaward end of (3a) from 35-5 km. Data are bandpass filtered with a smoothed trapezoid defined at 1,3,20,25 Hz. Bottom: The data after semblance guided median filtering (see Appendix C). A slowness range of 1.5-15 km was passed with a 15 trace gate and semblance weighting.

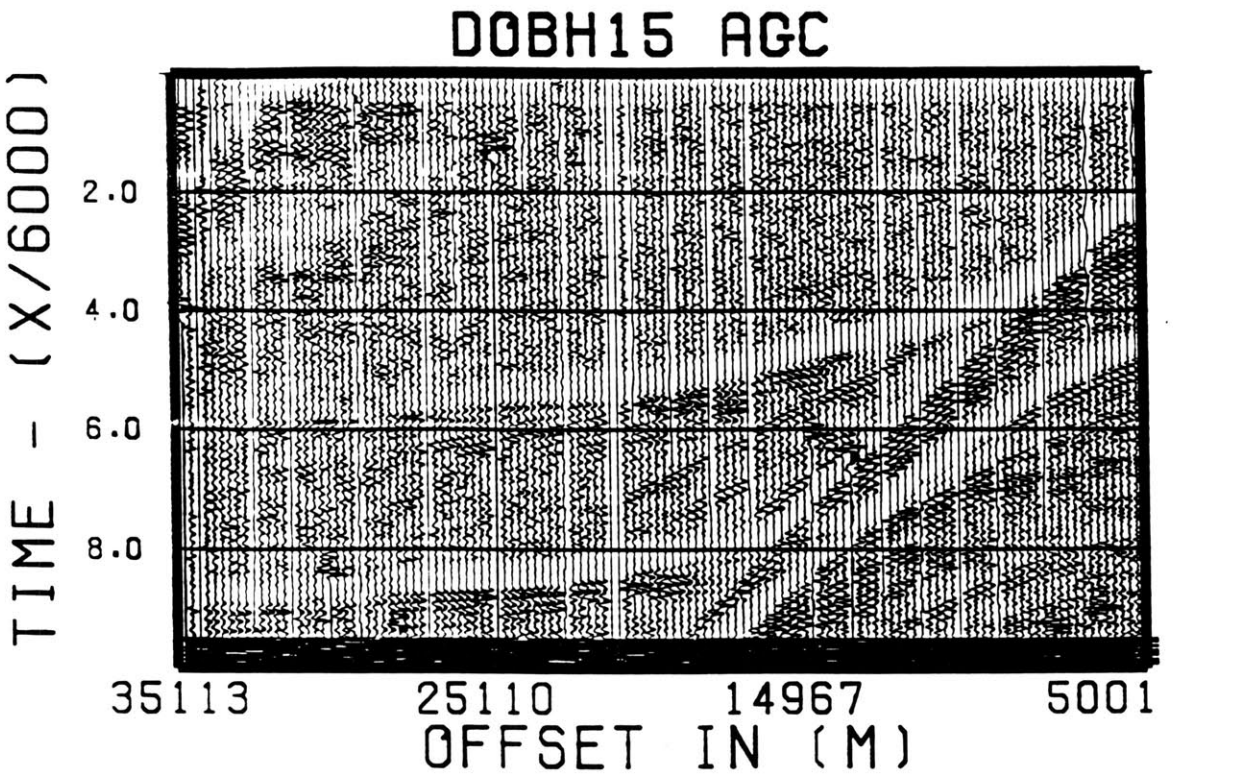

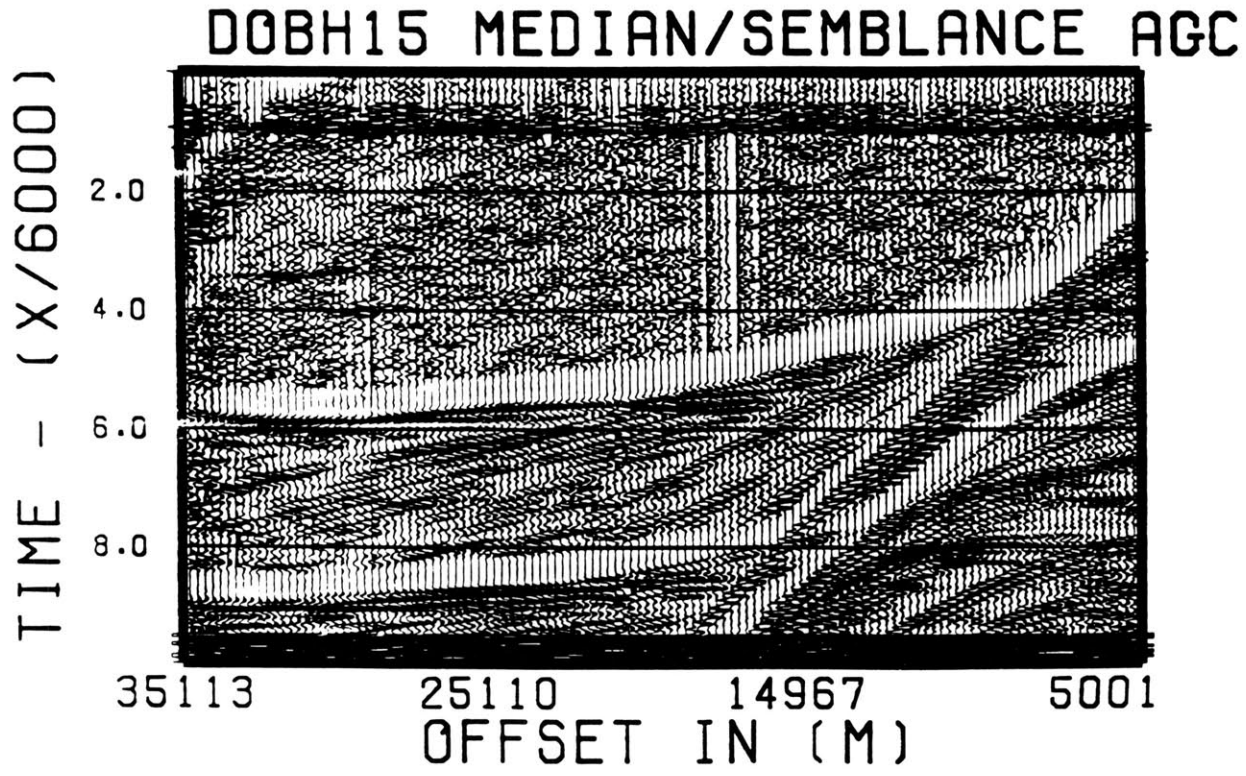

Figure 3d. Top: Automatic gain control (AGC) with a 1 second gate version of the raw data in (3c). Bottom: AGC version of the semblance guided median filtered data in (3c).

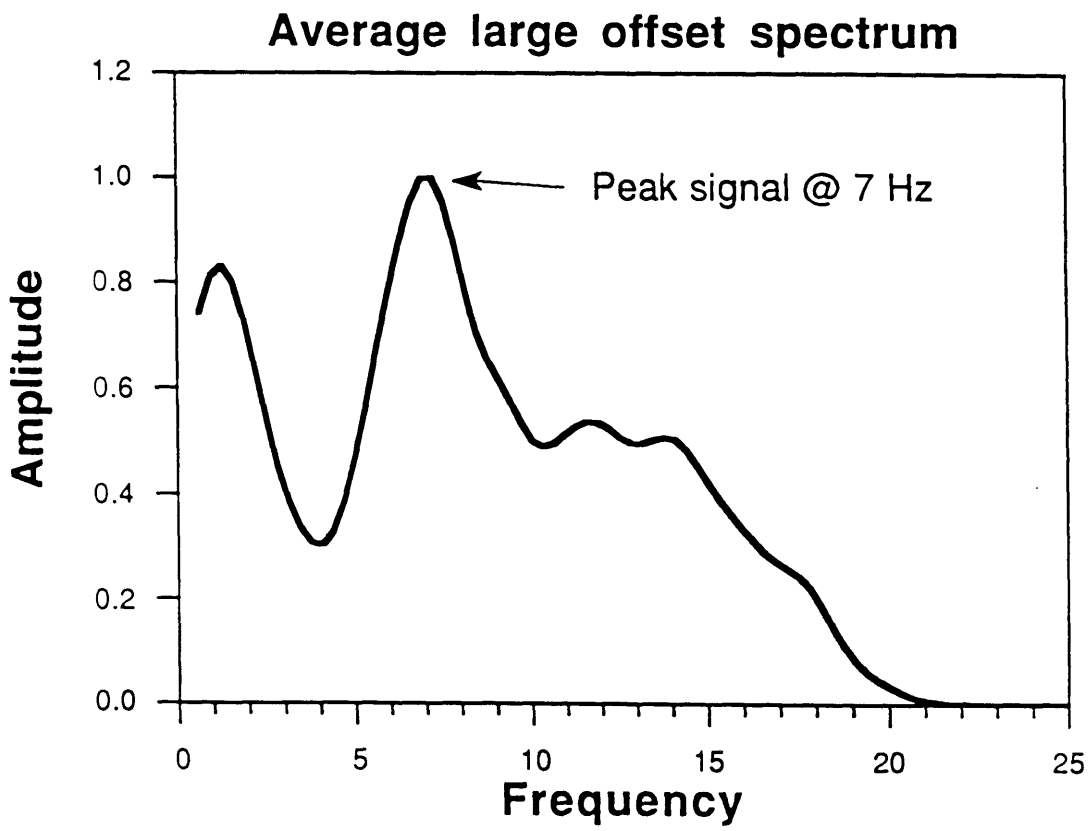

Figure 4. Average spectrum calculated from 2-8 seconds at offsets between 90 and 100 km. Prior to computation of average spectrum the data were low pass filtered with a trapezoidal filter defined at 0,0,20,25 Hz. Thus the dropoff after 20 Hz is exaggerated by lowpass filtering.

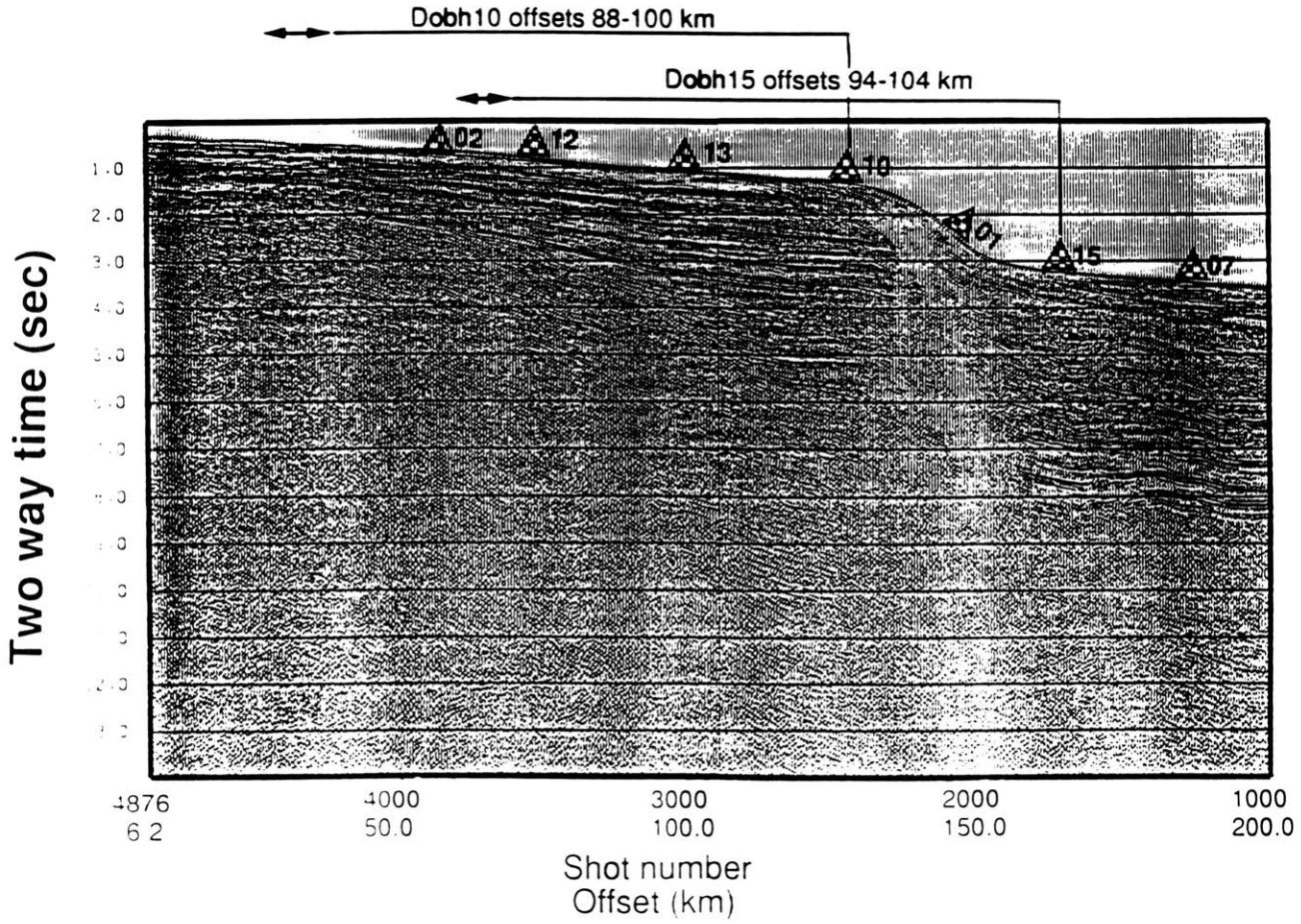

Figure 5a. a) Arrows indicate portions of receiver gathers used in migration for instruments Dobh10 and Dobh15.

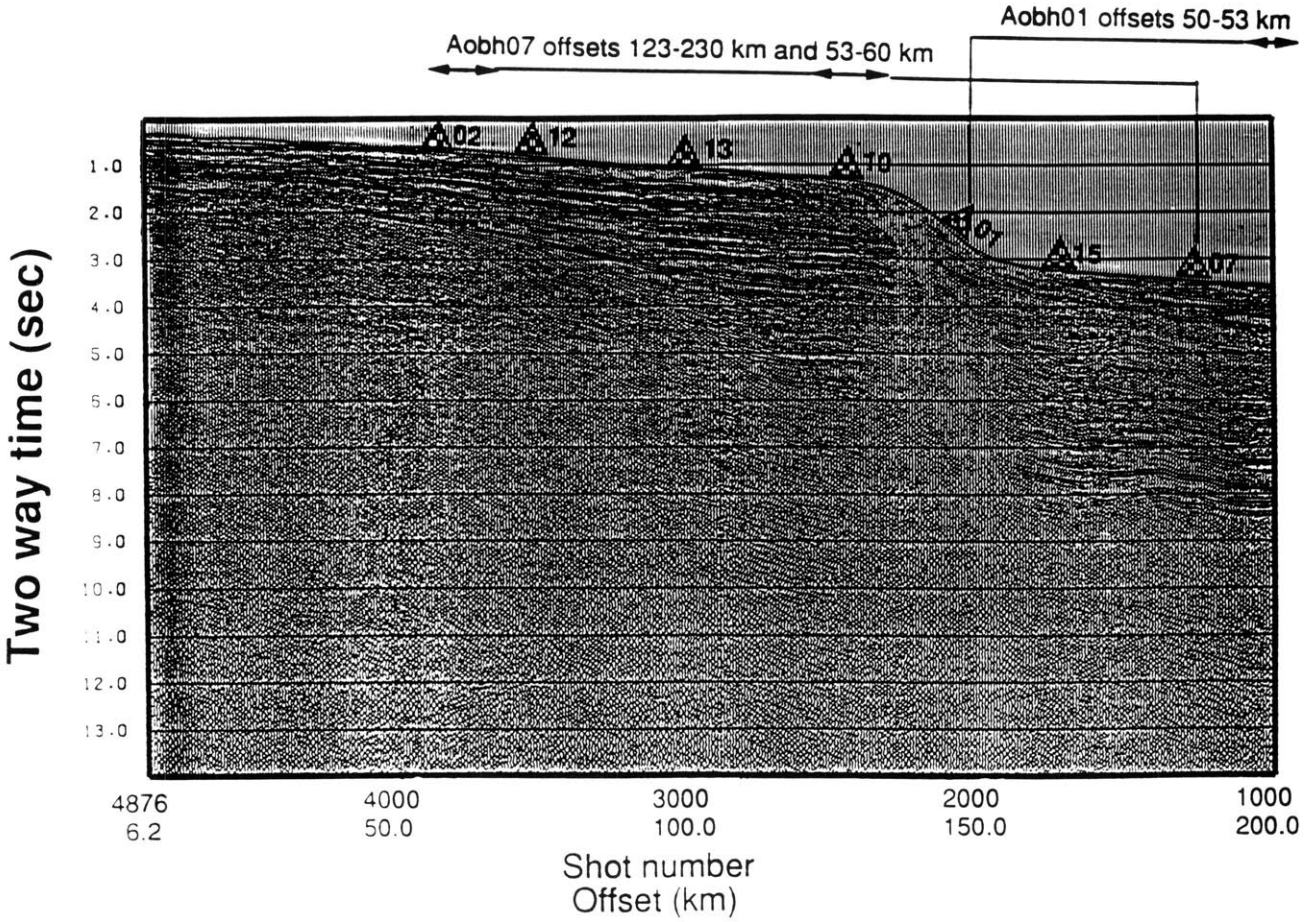

Figure 5b. b) Portions of receiver gather used for Aobh07 and Aobh01.

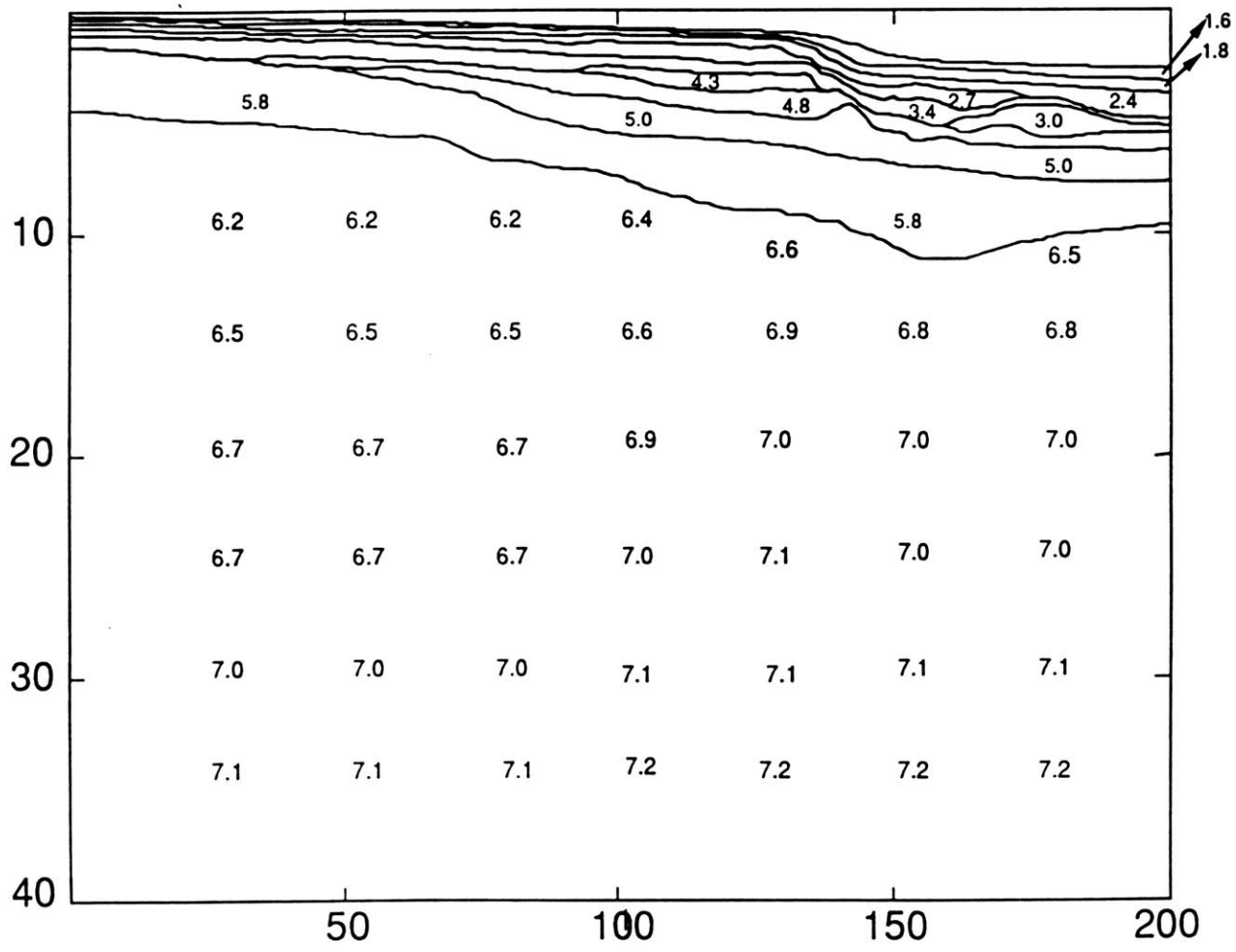

Figure 5c. c) Velocity model from (Holbrook et al., 1990) used in for migration of data in Figure 6. The model was derived from 2-D forward modeling of wide angle reflections and refractions observed on the OBH data. Detail in the sedimentary structure was obtained by digitizing sedimentary reflectors in the stacked section and finding the corresponding wide-angle reflection in the OBH data.

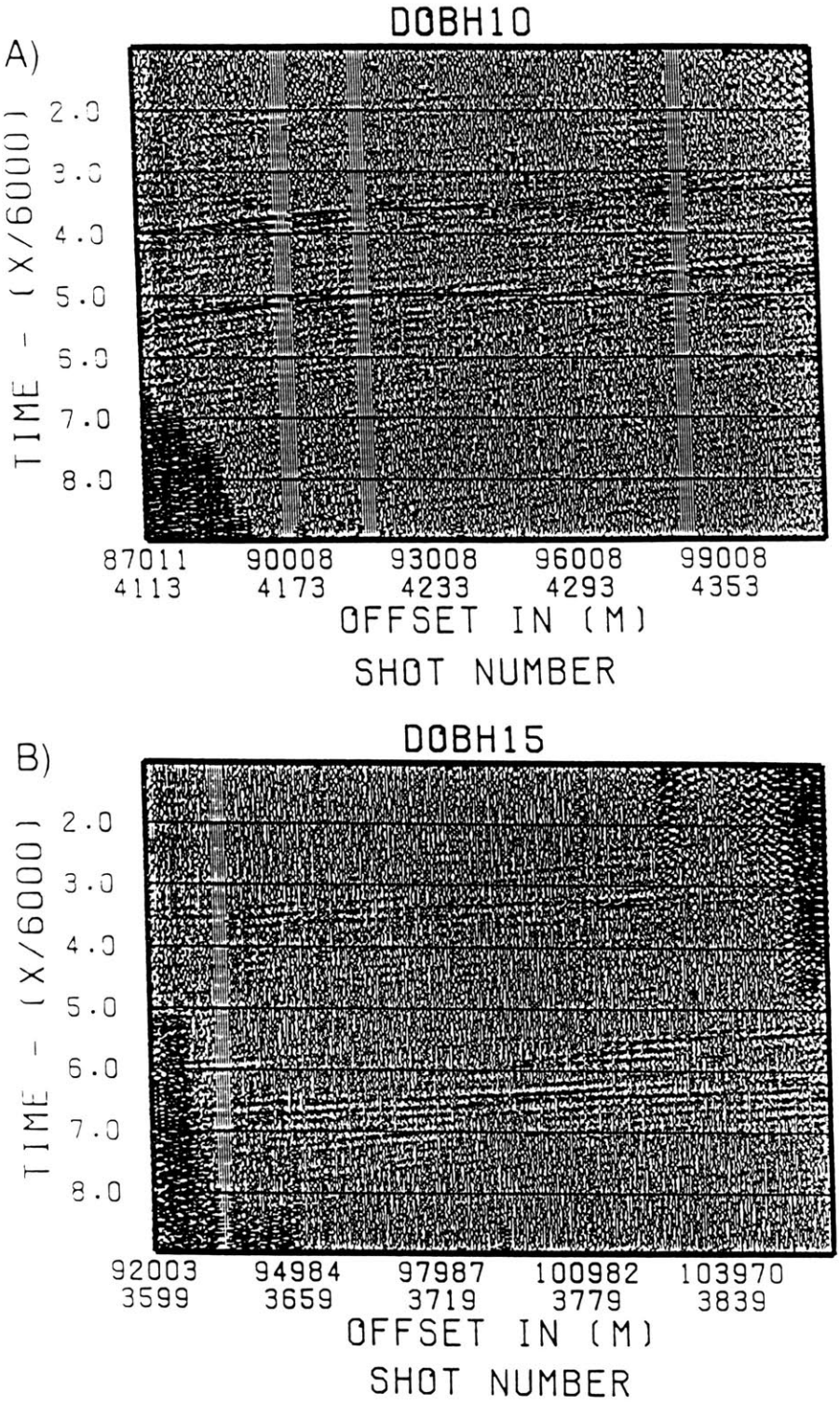

Figure 6a-b. a) Field data from Dobh10 that were migrated. b) Same for Dobh15.

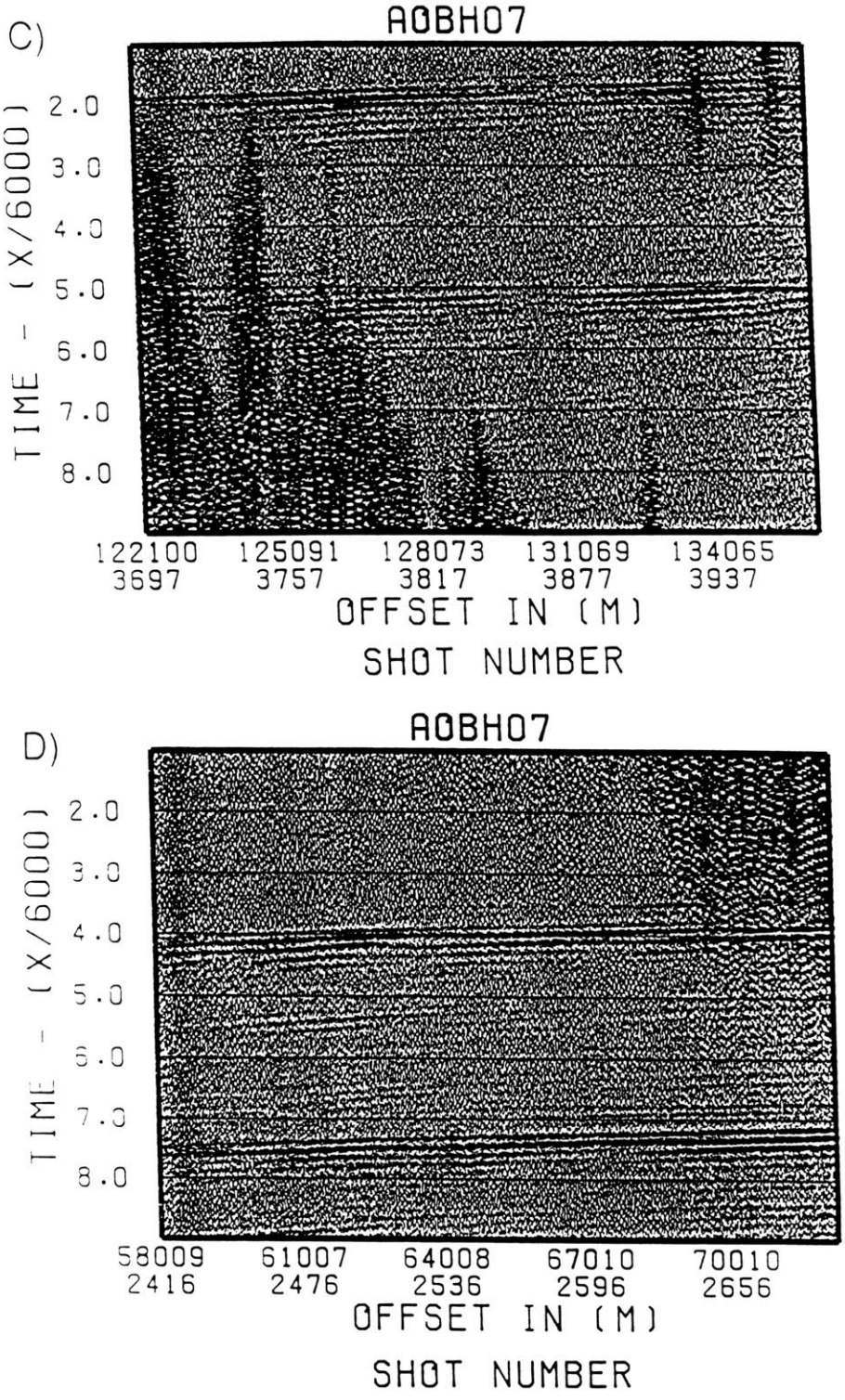

Figure 6c-d c) Field data from Aobh07 that were migrated d) Aobh07 nearer offsets.

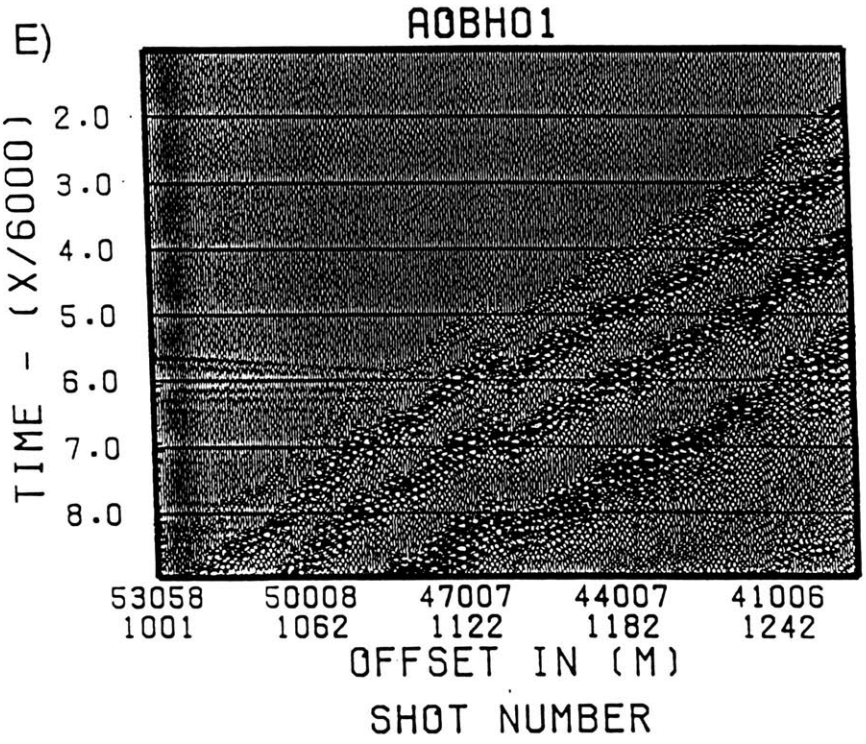

Figure 6e e) Field data from Aobh01 that were migrated.

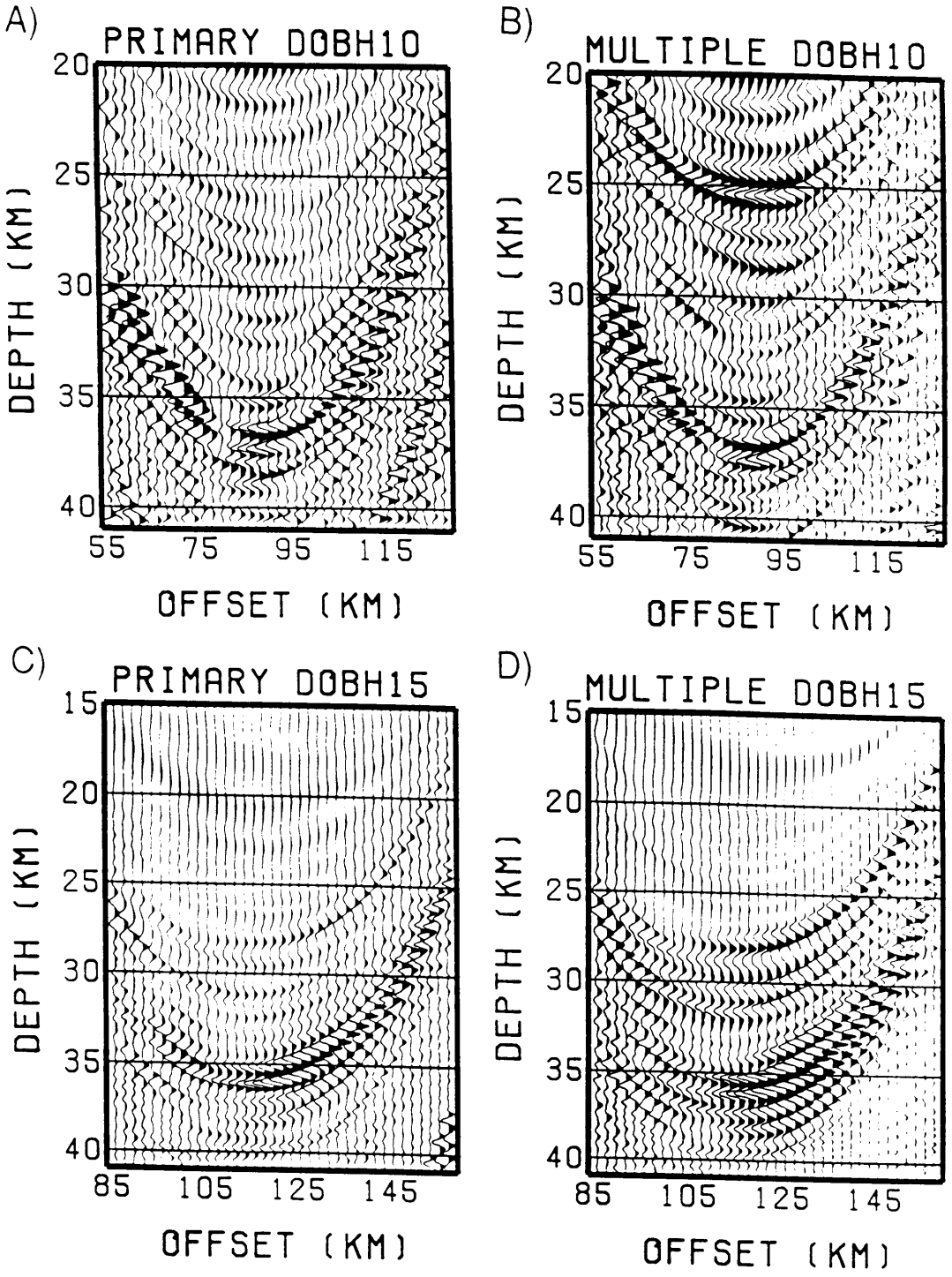

Figure 7. a) Primary image from Dobh10. b) Multiple's image from DObh10. c) Primary image from Dobh15. d) Multiple's image from Dobh15.

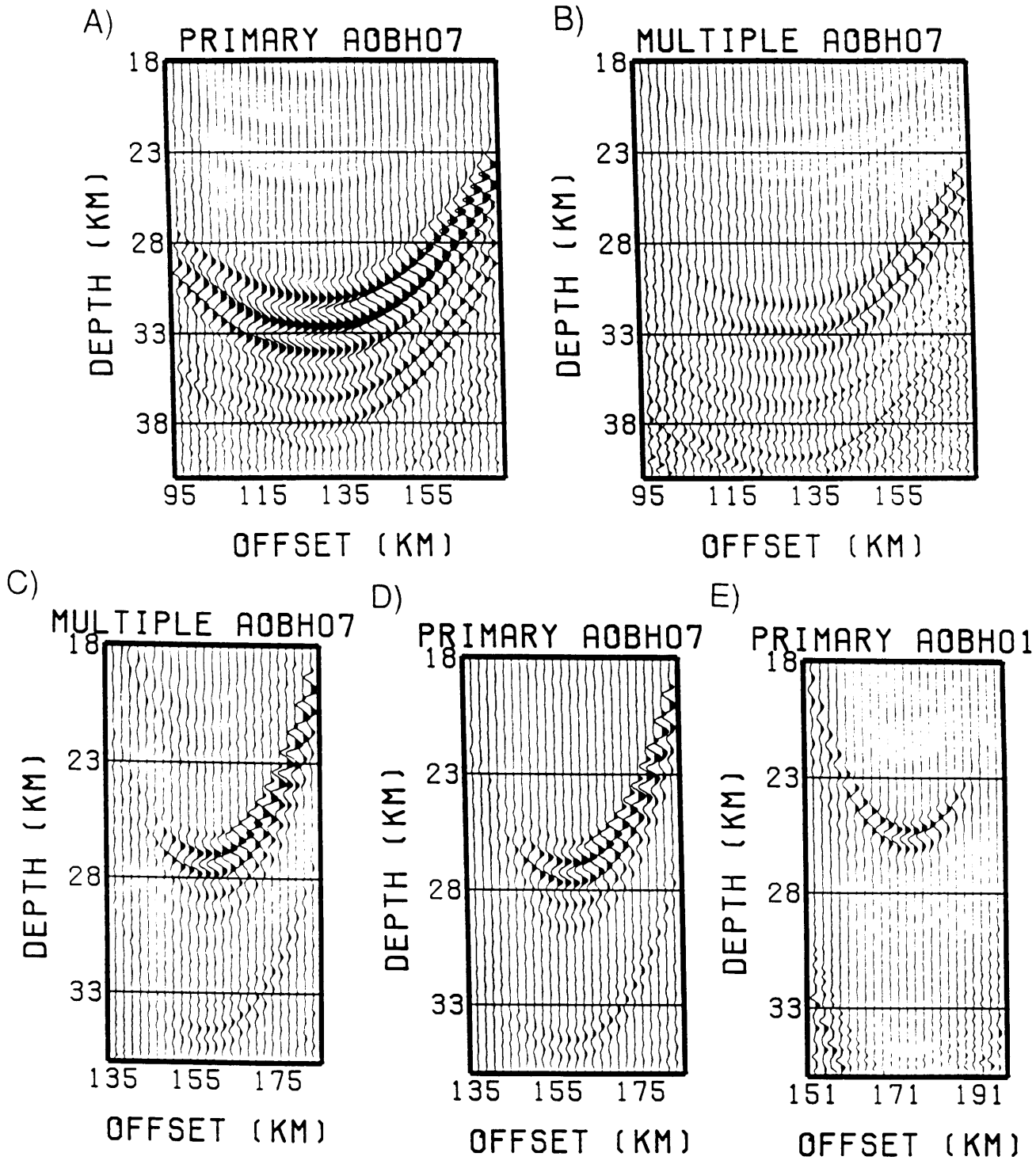

Figure 8. a) Primary image from Aobh07 (far offsets). b) Multiple's image from Aobh07 (far offsets). c) Primary image from Aobh07 (near offsets). d) Multiple's image from Aobh07 (near offsets). e) Primary image from Aobh01.

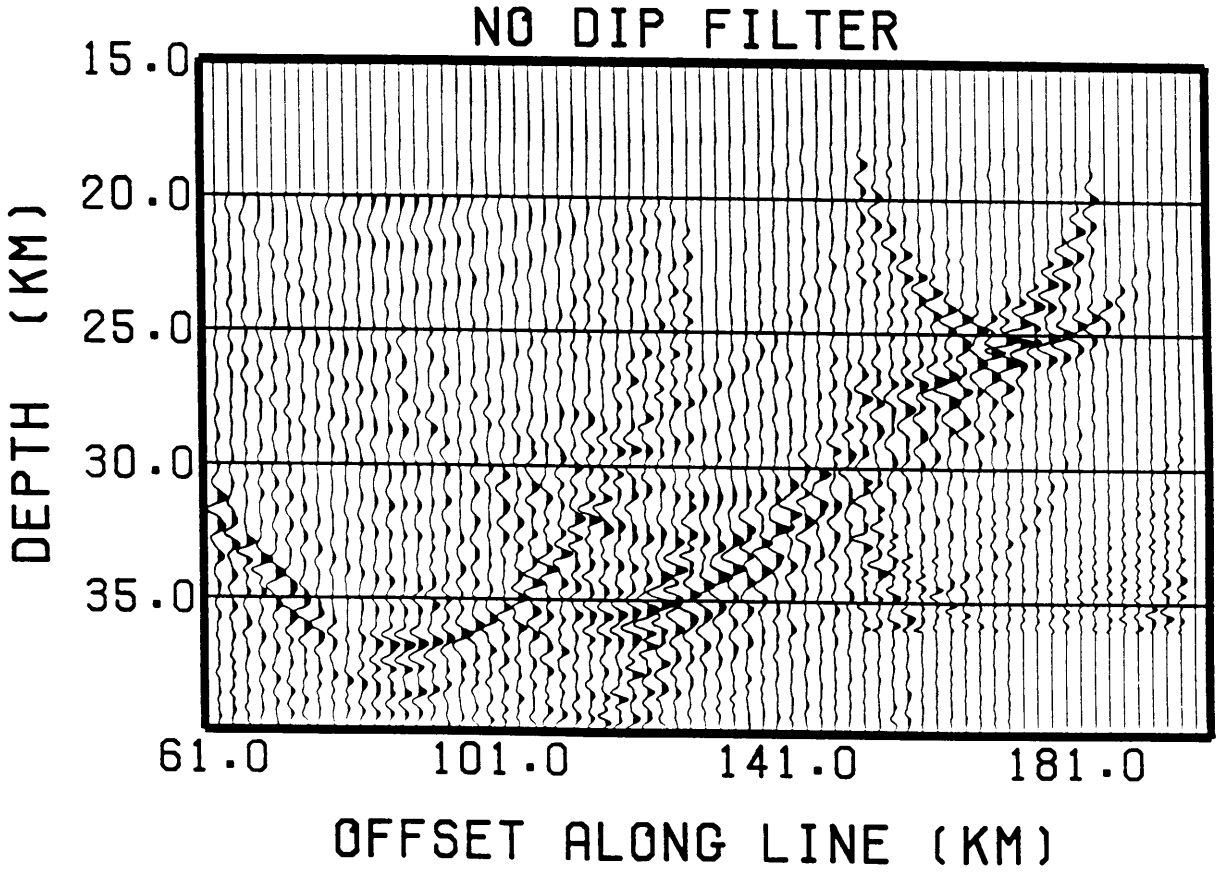

Figure 9. Composite image from summing the individual images from Figures 7 and 8. No dip filter has been applied and elliptical artifacts dominate the image. The image is sampled every 2 km in offset.

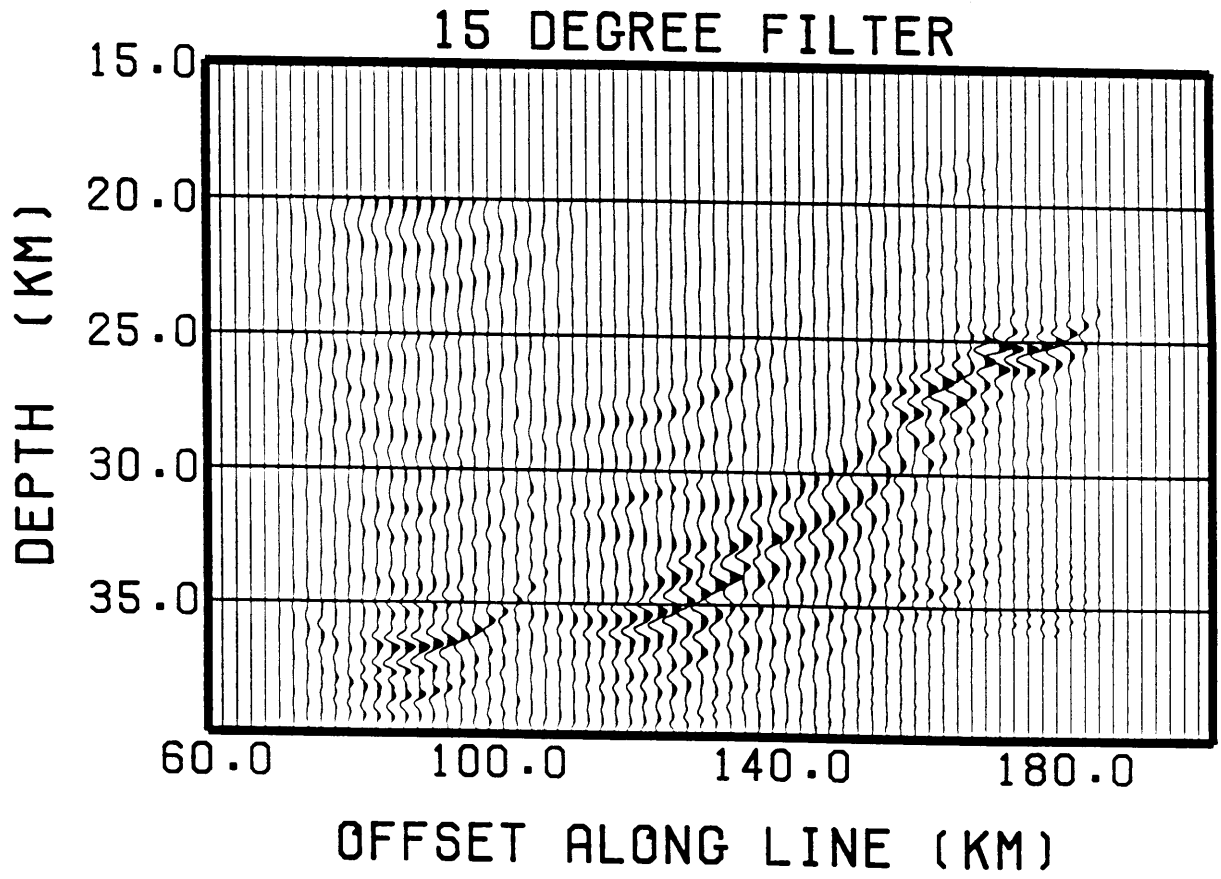

Figure 10. Composite image with a $\pm 15^{\circ}$ dip filter centered at dips between 2.5 and 7.5 degrees. See Table 2 for individual instrument's dip filter specifications.

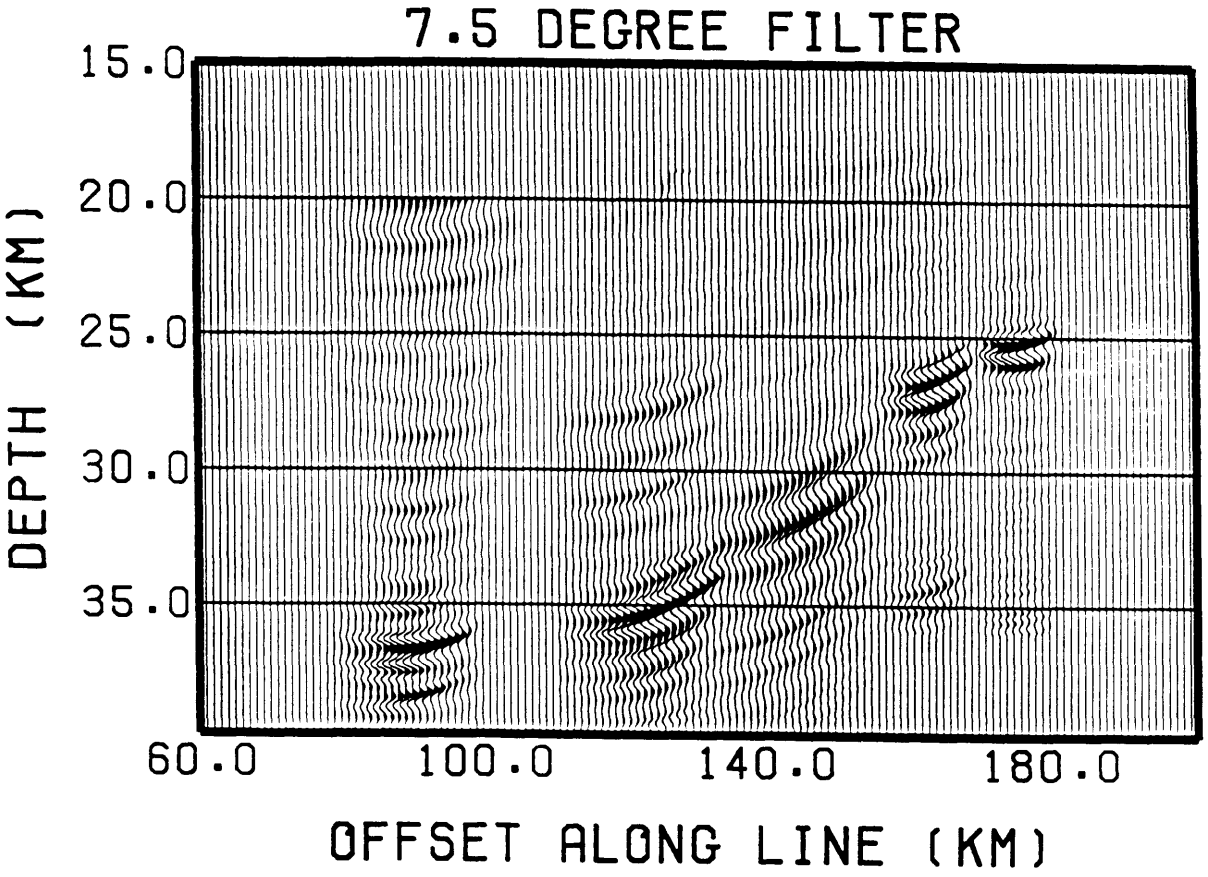

Figure 11. Composite image with a $\pm 7.5°$ dip filter centered at dips between 2.5 and 7.5 degrees. The image is sampled every 1 km in offset.

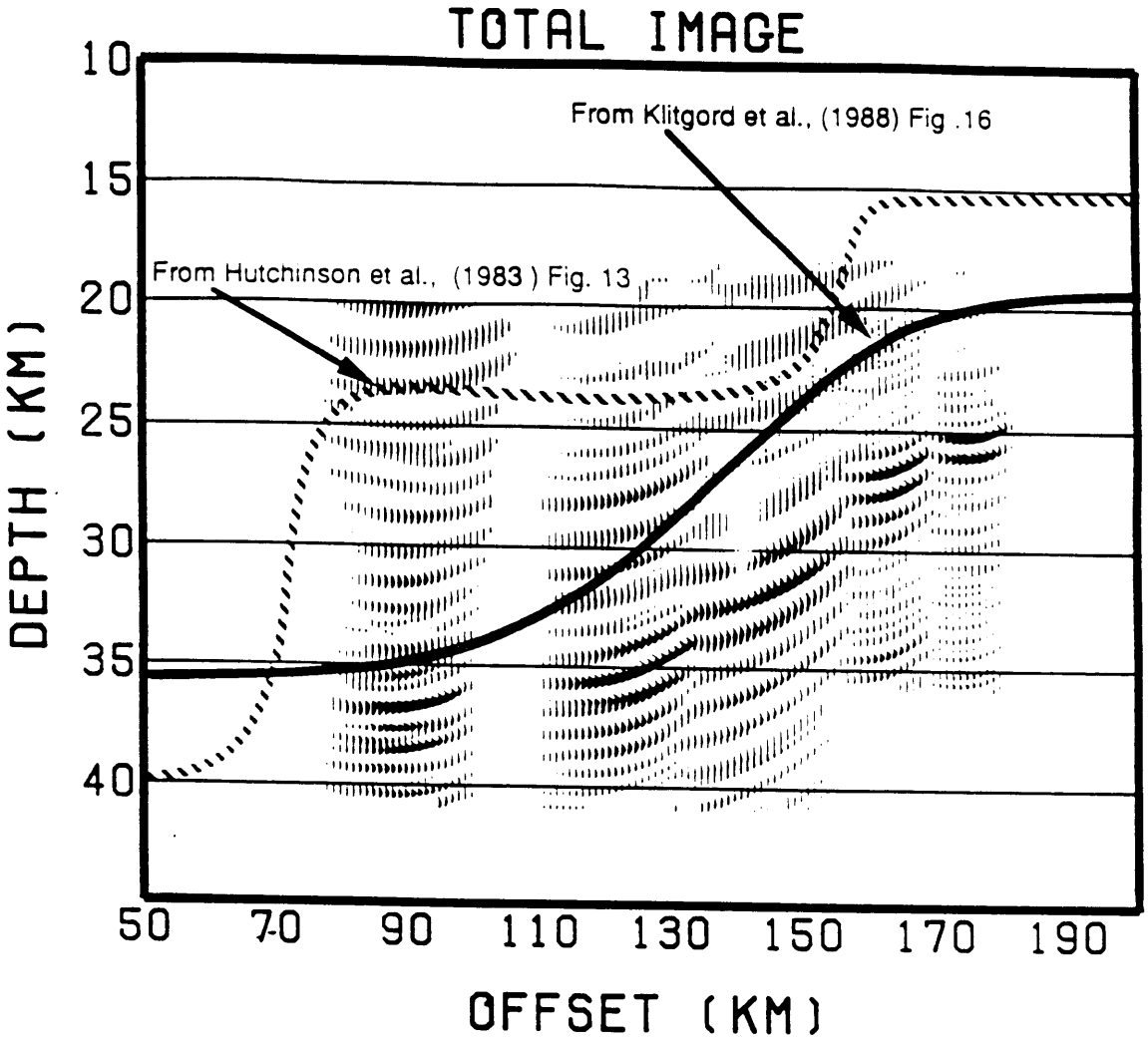

Figure 12. Wide angle Moho image versus published estimates from gravity and magnetic modeling. Our image indicates a Moho significantly smoother than that of Hutchinson et al. (1983) (dotted line).

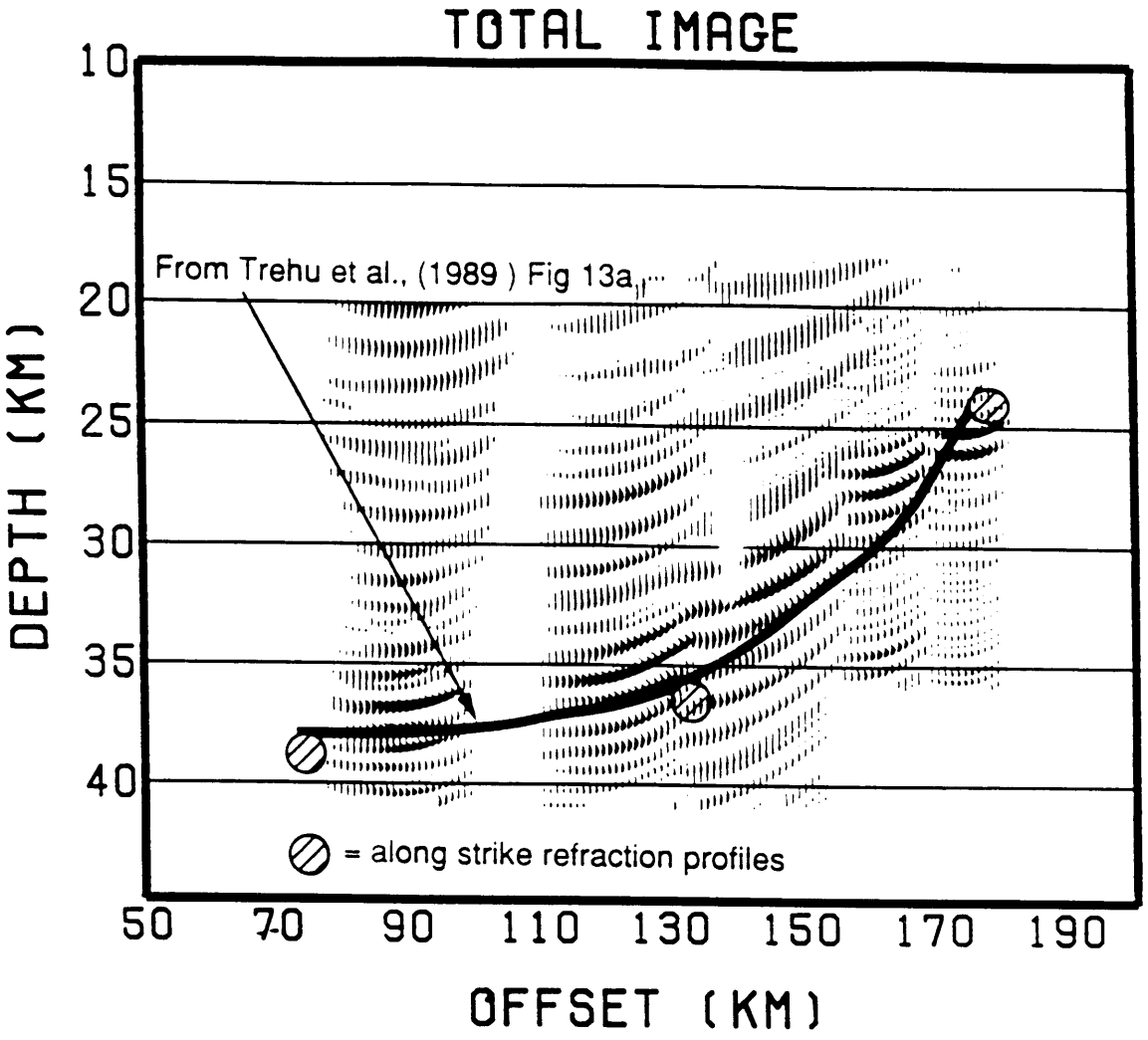

Figure 13. Wide angle Moho image versus results of three along strike refraction profiles of Trehu et al. (1989). Our results agree more closely with the refraction results than with models from gravity and magnetic modeling.

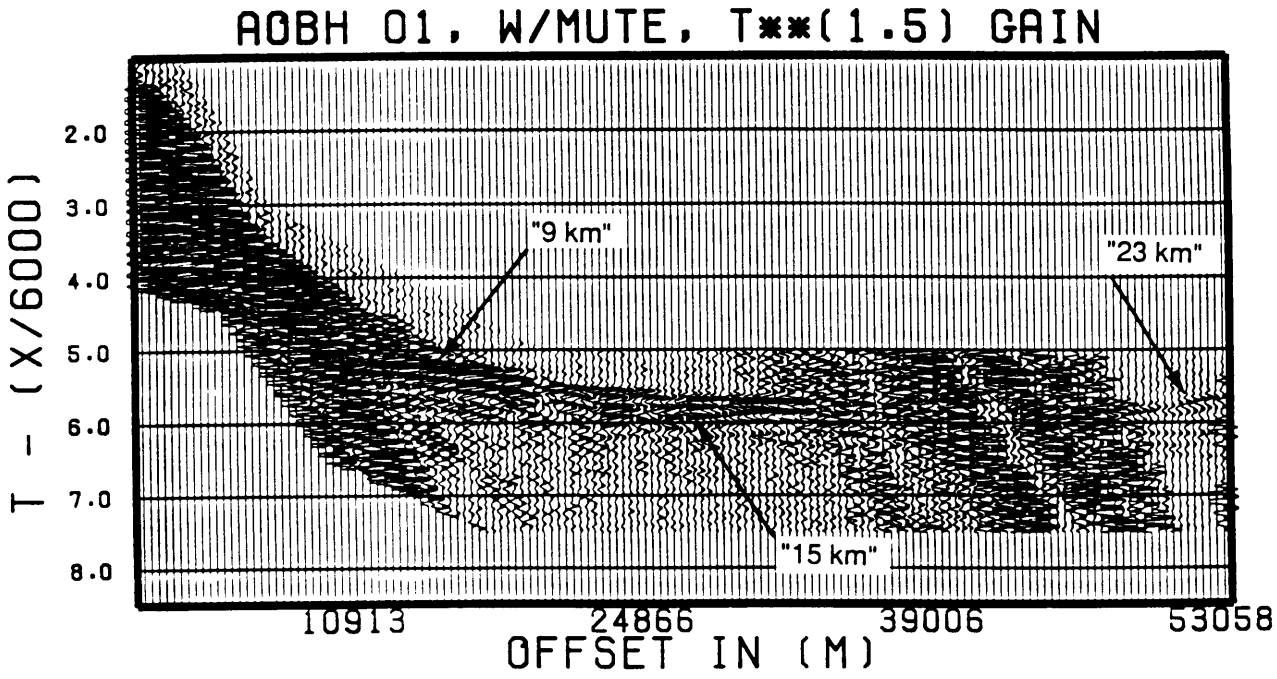

Figure 14a. a) A 53 km long receiver gather from Aobh01 presented in Chapter 2.

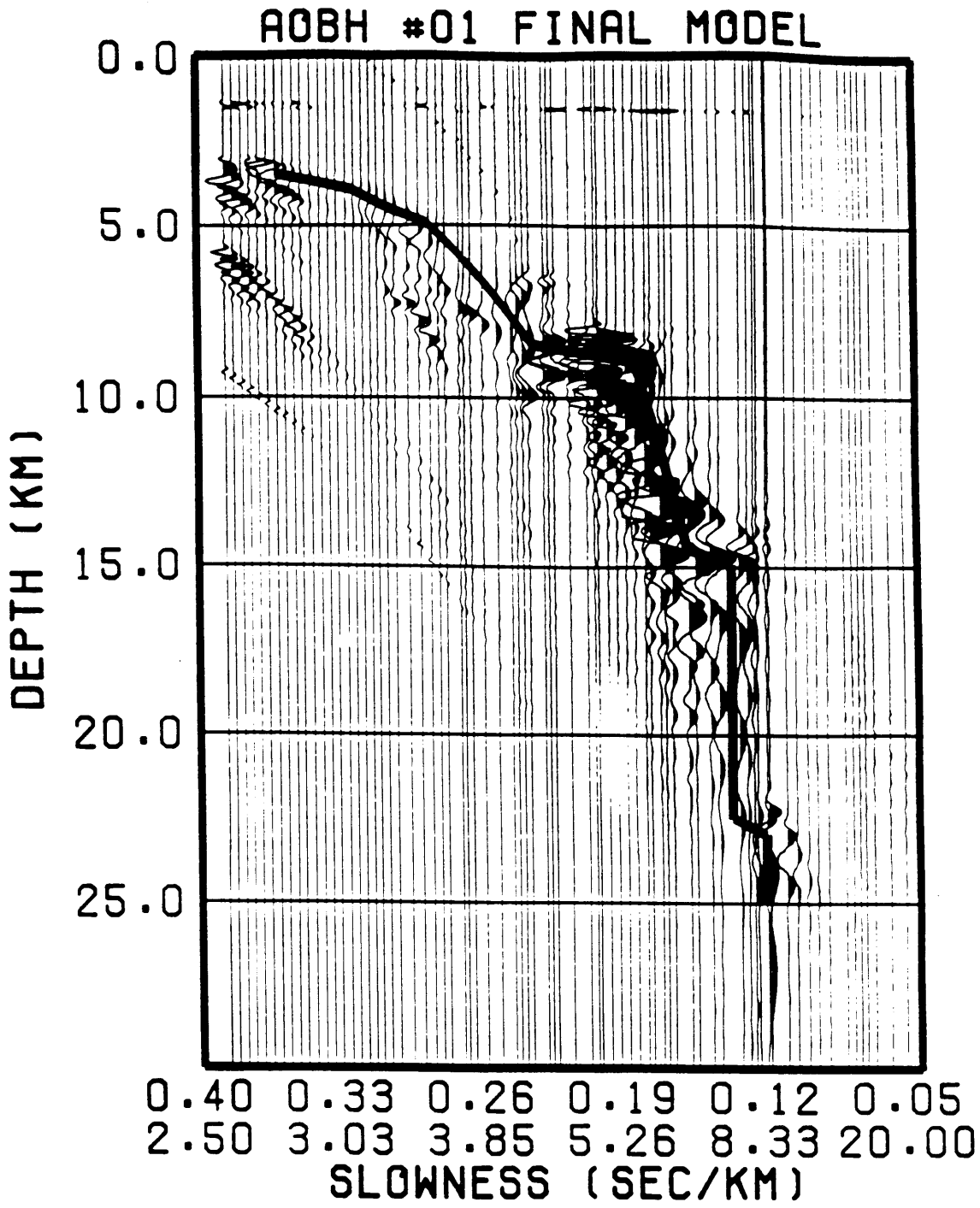

Figure 14b. b) An slowness-depth image from our 2-D $\tau - p$ method described in Chapter 2 from the data in Figure 14a.

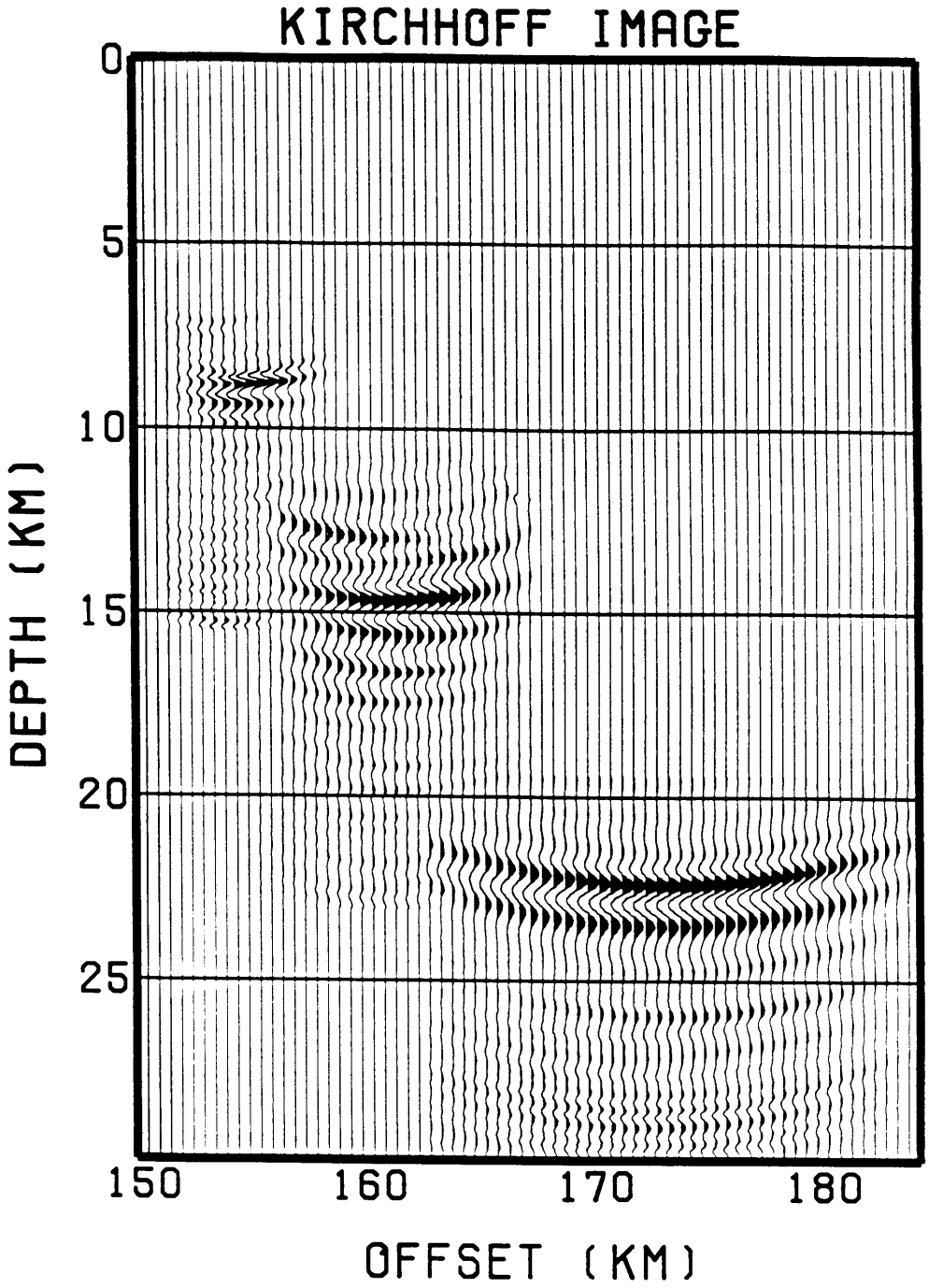

Figure 14c. c) Image from migrating (Kirchhoff) offsets 53-50 km and 30-12 km of the data in Figure 14a using the velocity model in Figure 14b for the migration. The three major velocity discontinuities in Figure 14b are now seen in a more traditional display of reflectivity.

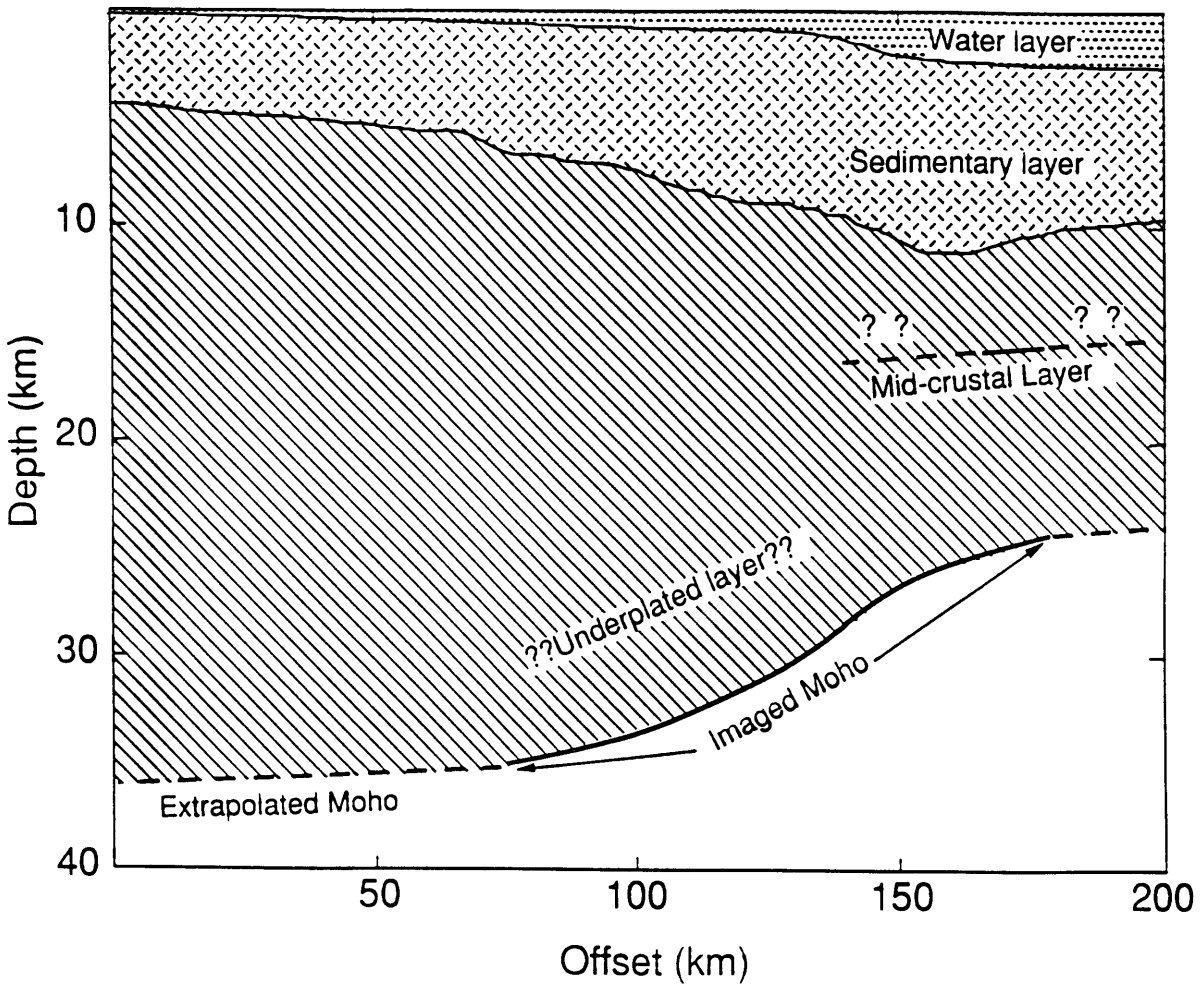

Figure 15. Composite model of the Moho across the Carolina Trough. The upper sedimentary layer was determined through forward modeling (Holbrook et al., 1990) and the Moho boundary from migration of wide angle PmP phases.

Chapter 5

Conclusions

In this thesis we have focused on techniques to image large offset ocean bottom seismic data. We have applied these techniques to OBH data acquired in the Carolina Trough. In an effort to more fully utilize the information contained in such data, we have developed several methods. A new method is presented to invert for and image a 2-D velocity function from post-critically reflected and refracted arrivals. These arrivals make up the vast majority of the large offset wavefield and thus our approach represents an efficient use of large offset data. In addition, we have shown that the first order water column multiple recorded by an on-bottom receiver may be used in 2-D imaging methods. This allows the volume of useful data to be essentially doubled, representing an even more complete use of ocean bottom seismic data. Both of these methods allow 2-D imaging of the observed data, making them useful to realistic seismic imaging targets.

The increase in large offset data volumes has caused a need for inversion/imaging approaches; this is apparent from a cursory examination of such experiments over the last decade. Modern large offset marine seismic experiments currently involve 5-20 receivers and 2000-4000 shotpoints, resulting in data volumes of between 10,000 and 80,000 source-receiver pairs (Austin et al., 1990; Ebeniro et al., 1988; Stoffa et al., 1988; Morel-a-l'Hussier et al., 1989). In contrast, large offset experiments less than

a decade ago involved data sets one to two orders of magnitude smaller in volume. For example, a state of the art United States Geological Survey refraction survey conducted in Maine in 1984 consisted of 120 instruments deployed over 100 km long. These recorded profiles yielded only approximately 480 source-receiver pairs. It is this increase in spatial sampling that both makes inversion/imaging possible, but at the same time requires inversion/imaging to handle the increased volumes of data and the demand for estimates of model confidence.

One benefit of simple imaging, such as computation of a reflectivity image with a Kirchhoff migration, is to provide an easy way to present an interpreter with a large volume of data. A forward modeler may present a 2-D line drawing of a best-fitting model which is accompanied by many record sections overlain by travel time curves as a final interpretation of large offset data. The sheer presentation of forward modeling is cumbersome, and becomes more so as data volumes increase. An image of reflectivity from a Kirchhoff migration, on the other hand, remains simple to present as data volumes increase. In fact, it provides a increasingly clear image of the subsurface as additional observations are migrated. However, migration does not provide a direct estimate of the confidence associated with the position of a given reflecting horizon. The position of the horizon is very dependent on the migration velocity model; the certainty associated with this velocity model is not directly displayed in the reflectivity image. Imaging solves the problem of how to display the data, but not how to express the reliability of that display.

The major advantages of inversion include providing some measure of confidence in the final model and determining in some sense a best-fitting model. Inversion approaches are similar to simple imaging in that they are amenable to large data volumes and are thus well-suited for modern large offset data sets. Inversion is different from simple imaging in that under ideal conditions a quantitative measure of confidence in the final model may be computed and displayed, allowing interpretation of the final model to proceed accordingly. Our 2-D velocity inversion/imaging approach

is an inversion scheme because it iteratively determines a best-fitting model, and an imaging scheme because it produces an image of that model. The final model is an image of 2-D velocity field which directly illustrates both the defined model and the quality of the data used. This presentation is helpful because it shows those portions of the model which are well-constrained and reliable, as well as those portions which are not resolvable with the observations. This approach has advantages of both imaging and inversion, making it well-suited as a tool to quantitatively examine suitable large offset seismic data.

However, forward modeling remains an effective method of extracting information from sparse large offset data. A major strength of forward modeling is the controlled manner in which sparse data may be fit. Large offset data are often too sparse to allow an inverse problem to converge. Also, if convergence can be achieved, it may be to a geologically unreasonable model. The forward modeler may choose geologically reasonable models which are consistent with the data from a wide variety of models which fit the data equally well. Thus the modeler may address the inherent non-uniqueness of large offset 2-D problems during the model-updating process. This stability in the presence of sparse data is a practical strength of forward modeling.

Summary

The major contribution of this thesis is the development and application of a new approach to invert for and directly image two- dimensional velocity fields. The first step of this procedure involves decomposition of the large offset wavefield into some function of slowness and either intercept time ($\tau - p$), offset ($X - p$) or total travel time ($T - p$). The most common slowness decomposition, $\tau - p$, is iteratively downward continued along numerically-computed ray paths to the domain of offset-depth-slowness. This work represents an extension to 2-D media of the pioneering 1-D wavefield continuation approach of Clayton and McMechan (1981). The dynamic nature of the ray parameter in 2-D media is corrected for by computing the difference between the

ray parameter observed at the receiver array and the ray parameter at the turning point. As in the work of Clayton and McMechan (1981), a trial velocity function is required for the downward continuation step. In our case a 2-D trial velocity field is required; convergence is assumed to be achieved when the downward continued data image onto the trial velocity field. Thus, our approach directly images a 2-D velocity field; this allows decisions about where the model is well or poorly constrained to be conveniently made. The velocity field is updated from the previous iteration's image much like the 1-D method, except in the 2-D case specific reflecting boundaries must be added during the inversion. Boundaries are required to allow the correct critical travel paths to be numerically computed with ray tracing. Each slowness observation is downward continued along a ray path which is found by searching for a ray which emerges with an angle corresponding to the observed slowness. We assume the velocity immediately beneath the receiving array is known, which allows an observed slowness to be related to the angle of incidence.

In Chapter 3 we present an approach to treating first order water columns as useful signal. We show that an on-bottom receiver records one of the two possible first order multiples with an amplitude very similar to the primary. The other possible first order multiple is reduced in amplitude by a factor dependent on the water-sediment reflection coefficient. This difference in amplitude allows the first order multiple to be utilized in 2-D imaging schemes. We use this property to image large offset ($>$ 80 km) reflections from a deep interface assumed to be the crust/mantle boundary. A 2-D Kirchhoff pre-stack depth migration is applied to deep water OBH recordings and used to image the data along both primary and water column multiple paths. Separate images obtained from the primary and water column multiple migrations are summed (after polarity correction) to produce an image with approximately twice the signal strength as the traditional image produced from the primary migration alone.

In Chapter 4 we apply both the 2-D velocity inversion/imaging method of Chapter 2 and the multiple migration approach of Chapter 3 to field data and illustrate how

these techniques may be used to successfully image deep crustal structure. We present an example in which the 2-D velocity inversion/imaging approach is used to invert for and image a velocity field in an area of known lateral heterogeneity. This velocity field is used as input into a Kirchhoff migration; the same data used in the velocity inversion scheme is then migrated to depth. The migrated image is shown to agree well with first order velocity discontinuities in the velocity image, demonstrating that large offset data may be used to image both velocity and reflectivity structure. We also demonstrate the utility of using migration to produce a high signal/noise ratio image of the deep crust from wide-angle reflections. Kirchhoff migration of several receiver gathers along both primary and water column multiple paths produces an image of the Moho over approximately 80 km. The effects of sparse receiver spacing are clearly evident in the raw migrated image and dip filtering is used to produce a more interpretable result. After dip filtering, we obtain a segmented but convincing image of the Moho shallowing from 37 to 25 km. This image indicates a gradual shallowing of Moho depth across the transition from purely continental crust to transition type crust (crust which has been significantly altered by the rifting process). Most significantly, we show that the large offset wavefield made up of post-critically reflected and refracted arrivals may be used to directly image deep crustal structure.

References

Austin, J. A., P. L. Stoffa, J. Oh, D. Sawyer, G. M. Purdy, and E. Reiter, Imaging a reactivated(?) crustal suture and a complex continent-ocean transition - A reflection profile across the Carolina Trough, *eos, 70,* 1347–1347, 1989.

Austin, J. A., P. L. Stoffa, J. D. Phillips, J. Oh, D. S. Sawyer, G. M. Purdy, E. Reiter, and J. Makris, Crustal Structure of the Southeast Georgia Embayment: A deep penetration MCS/OBH image of a continental suture(?) and a volcanic passive margin, *Geology, 18,* 1023–1027, 1990.

Bessanova, E. N., V. M. Fishman, V. Z. Ryaboyi, and G. A. Sitnikova, The Tau Method for Inversion of Travel Times–I. Deep Seismic Sounding Data, *Geophys. J. R. Astr. Soc., 36,* 377–398, 1974.

Beydoun, W. B., C. H. Cheng, and M. N. Toksoz, Detection of subsurface fractures and permeable zones by the analysis of tube waves, in *Vertical Seismic Profiling part B: Advanced Concepts,* edited by M. N. Toksoz and R. R. Stewart, Geophysical Press, London, 1984.

Bienvenu, G. and L. Knopp, Optimality of high resolution array processing using the eigensystem approach, *IEEE Trans. on Acoust., Speech Process.,, 31,* 1235–1247, 1983.

Biondi, B. and C. Kostov, High resolution velocity spectra using the eigenstructure methods, *Geophysics, 54,* 832–842, 1989.

Bisset, D. A. and T. S. Durrant, Radon transform migration below plane sloping layers, *Geophysics, 55,* 277–283, 1990.

Carrion, P. M. and J. T. Kuo, A method for computation of velocity profiles by inversion of large-offset records, *Geophysics, 49,* 1249–1258, 1985.

Cerveny, V., I. Molokov, and I. Psencik, *Ray methods in seismology,* Univerzita Karlova, Praha, 1977.

Chang, W. F. and G. A. McMechan, Wave Field Processing of Data from the 1986 Program for Array Studies of the Continental Lithosphere Ouachita Experiment, *J. Geophys. Res., 94,* 17,781–17,792, 1989.

Chang, W. F., G. A. McMechan, and G. R. Keller, Wave Field Processing of Data from a Large Aperture Experiment in Southwestern Oklahoma, *J. Geophys. Res., 94,* 1803–1816, 1989.

Chapman, C. H., Generalized radon transforms and slant stacks, *Geophys. J. R. Astr. Soc., 66,* 445–453, 1981.

Cicerone, R., J. Lee, M. Toksoz, and S. Alexander, Fracture detection and characterization from hydrophone VSP data, Kent Cliffs, New York, in *MIT-Reservoir Delineation Consortium Annual Meeting,* 1988.

Clayton, R. W. and G. A. McMechan, Inversion of refraction data by wavefield continuation, *Geophysics, 46,* 860–868, 1981.

Diebold, J. B. and P. L. Stoffa, The travel time equation, tau-p mapping, and inversion of common midpoint data, *Geophysics, 46,* 238–254, 1981.

Diebold, J. B., P. L. Stoffa, and T. L. study group, A large aperture seismic experiment in the Baltimore Canyon Trough, *The Geology of North America, Vol. 1-2 The Atlantic Continental Margin: U.S.,* 387–398, 1988.

Duckworth, G. L., *Processing and Inversion of Arctic Ocean refraction data,* PhD thesis, Massachusetts Institute of Technology, 1983.

Ebeniro, J. O., Y. Nakamura, D. S. Sawyer, and W. P. O'Brien, Sedimentary and Crustal structure of the Northwestern Gulf of Mexico, *J. Geophys. Res., 93,* 9075–9092, 1988.

Evans, J. R., Running median filters and a general despiker, *Bulletin Seis. Soc. of Am., 72,* 331–338, 1982.

Fowler, S. R., R. S. White, G. D. Spence, and G. K. Weatbrook, The Hatton Bank continental margin-II. Deep structure from two-ship expanding spread seismic profiles, *Geophys. J. R. Astr. Soc., 96,* 295–309, 1989.

Frieden, B. R., A new restoring algorithm for the preferential enhancement of edge gradients, *J. Opt. Soc. Amer., 66,* 280–283, 1976.

Gardner, L. W., An areal plan of mapping subsurface structure by refraction shooting, *Geophysics, 4,* 247–259, 1939.

Garmany, J., J. A. Orcutt, and R. L. Parker, Travel Time Inversion: a Geometrical Approach, *J. Geophys. Res., 84,* 3615–3622, 1979.

Gazdag, J., Wave equation migration with the phase shift method, *Geophysics, 43,* 1342–1351, 1978.

Grow, J. A., C. O. Bowen, and D. R. Hutchinson, The gravity field of the U.S. Atlantic Continental Margin, *Tectonophysics, 59,* 27–52, 1979.

Haldorsen, J. B. U. and P. A. Farmer, Suppression of high-energy noise using an alternative stacking procedure, *Geophysics, 54,* 181–190, 1989.

Hales, A. L., The travel times of P waves and their relevance to the upper mantle velocity distribution, *Tectonics, 13,* 447–482, 1972.

Hardage, B. A., *Verical Sesimic Profiling. Part A: Principles,* Geophysical Press, London, 1983.

Hardin, E., C. Cheng, F. Paillet, and J. Mendelson, Fracture characterization by means of attenuation and generation of tube waves in fractured crystalline rock at Mirror Lake, New Hampshire, *J. Geophys. Res., 92,* 7989–8006, 1987.

Hawman, R. B., R. H. Colburn, D. A. Walker, and S. B. Smithson, Processing and Inversion of Refraction and Wide-Angle Reflection Data from the 1986 Nevada PASSCAL Experiment, *J. Geophys. Res., 95,* 4657–4691, 1990.

Holbrook, W. S., G. M. Purdy, E. C. Reiter, M. N. Toksoz, J. A. Austin, P. L. Stoffa, and D. Sawyer, Crustal Structure of the Carolina Trough, U.S. East Coast Margin, From Coincident Multichannel Reflection and Ocean- Bottom Seismic Data, *Fall Am. Geophys. Union Abstracts, 73,* 1616, 1990.

Hsu, K. and A. B. Baggeroer, Application of the maximum-likelihood method (MLM) for sonic velocity logging, *Geophysics, 51,* 780–787, 1986.

Hu, L. Z. and G. A. McMechan, Migration of VSP data by ray equation extrapolation in 2D variable velocity media, *Geophysical Prospecting, 34,* 704–734, 1986.

Hutchinson, D. R., J. A. Grow, K. D. Klitgord, and B. A. Swift, Deep Structure and evolution of the Carolina Trough, *Studies in Continental Margin Geology: American Association of Petroleum Geologists, Memoir 34,* 129–152, 1983.

Johnson, L. E. and F. Gilbert, A New Datum for use in the Body Wave Travel Time Inverse Problem, *Geophys. J. R. Astr. Soc., 30,* 373–380, 1972.

Keho, T. H., *The Vertical Seismic Profile: Imaging Heterogeneous Media,* PhD thesis, Massachusetts Institute of Technology, 1986.

Key, S. C. and S. B. Smithson, New approach to seismic-reflection event detection and velocity determination, *Geophysics, 55,* 1057–1069, 1990.

Klitgord, K. D., D. R. Hutchinson, and H. Schouten, U.S. Atlantic continental margin; Structural and tectonic framework, *The Geology of North America, Vol. 1-2 The Atlantic Continental Margin: U.S.,* 19–55, 1988.

Koelsch, D. E., K. R. Peal, and G. M. Purdy, A digitally recording ocean bottom hydrophone, *Woods Hole Oceanographic Institution Technical Report,* 1982.

Kong, S. M., R. A. Phinney, and K. Roy-Chowdbury, A nonlinear signal detector for enhancement of noisy seismic record sections, *Geophysics, 50,* 539–550, 1985.

Leven, J. H. and K. Roy-Chowdbury, A semblance-weighted slowness-filter in the time domain, *SEG Expanded Abstracts, 54,* 432–436, 1984.

Lyslo, J. A. and R. L. Nowack, Slant stack velocity analysis of shot point 16 from the 1986 PASSCAL Ouachita Experiment, *J. Geophys. Res., 95,* 4647–4656, 1990.

McMechan, G. A., P-x imaging by localized slant stacks of t-x data, *Geophys. J. R. Astr. Soc., 72,* 213–221, 1983a.

McMechan, G. A., Wavefield inversion of sesimic refraction data via the p-x plane, *Geophys. J. R. Astr. Soc., 72,* 809–810, 1983b.

McMechan, G. A., Inversion of a refraction wavefield data by imaging in the p-x and v-z plane, *Geophys. J. R. Astr. Soc., 78,* 723–733, 1984.

McMechan, G. A. and G. S. Fuis, Ray Equation Migration of Wide-Angle Reflections from Southern Alaska, *J. Geophys. Res., 91,* 407–420, 1987.

McMechan, G. A. and R. Ottolini, Direct observation of a p-tau curve in a slant stacked wavefield, *Bulletin Seis. Soc. of Am., 70,* 775–789, 1980.

Milkereit, B., Migration of Noisy Crustal Seismic Data, *J. Geophys. Res., 92,* 7916–7930, 1987.

Milkereit, B., W. D. Mooney, and W. M. Kohler, Inversion of seismic refraction data in planar dipping structure, *Geophys. J. R. Astr. Soc., 82,* 81–103, 1985.

Morel-a-l'Hussier, P., Z. Hajnal, J. H. Karl, R. F. Mereu, R. P. Meyer, J. Sexton, A. Trehu, C. P. Ervin, D. R. Hutchinson, and A. G. Green, GLIMPCE 1986 seismic refraction experiment - An introduction to the data, *eos, 70,* 273–273, 1989.

Morse, P. M. and H. Feschback, *Methods of theoretical physics, Part I,* McGraw-Hill Book Co., Inc., New York, 1953.

Musgrave, A. W., *Seismic Refraction Prospecting,* Society of Exploration Geophysics, Tulsa, 1967.

Nakamura, Y., P. L. Donoho, P. H. Roper, and P. M. McPherson, Large-offset seismic surveying using ocean-bottom seismographs and air guns: Instrumentation and field technique, *Geophysics, 52,* 1601–1611, 1987.

Oh, J., P. Stoffa, J. A. Austin, J. D. Phillips, and D. S. Sawyer, Images of basin structures beneath the postrift unconformity - A deep reflection profile from the Blake Plateau Basin, *eos, 70,* 1347–1347, 1989.

Oh, J., P. Stoffa, J. A. Austin, J. D. Phillips, and D. S. Sawyer, Alternative interpretation for the Brunswick Magnetic Anomaly from deep penetration multichannel seismic reflection profiling: southeastern United States passive continental margin, *eos, 71,* 1617–1617, 1990.

Phinney, R. A., K. R. Chowdhury, and N. L. Frazer, Transformation and analysis of record sections, *J. Geophys. Res., 86,* 359–377, 1981.

Rabiner, L. R., M. R. Sambur, and C. E. Schmidt, Applications of a nonlinear smoothing algorithm to speech processing, *IEEE Trans. Acoustic, Speech and Signal Processing, ASSP-23,* 552–557, 1975.

Reiter, E. and M. N. Toksoz, Joint imaging with primary reflections and deep water multiples, *SEG Expanded abstracts, Vol II,* 1294–1296, 1990.

Reiter, E., G. M. Purdy, D. Sawyer, P. L. Stoffa, J. D. Phillips, J. A. Austin, and M. N. Toksoz, Ocean Bottom Hydrophone Results from a Multi-channel seismic survey in the Carolina Trough and Southeast Georgia Embayment, *eos, 69,* 1045 – 1045, 1988.

Reiter, E., M. N. Toksoz, G. M. Purdy, and T. H. Keho, Imaging with deep water multiples, *Geophysics, accepted,* , 1990.

Roller, J. C. and W. H. Jackson, Seismic wave propagation in the upper mantle: Lake Superior, Wisconsin to Central Arizona, *J. Geophys. Res., 71,* 5933–5941, 1966.

Schmidt, R. O., Multiple emitter location and signal parameter estimation, *IEEE Trans. on Antenna and Propagation, 34,* 276–280, 1986.

Sheridan, R. E., J. A. Grow, and K. D. Klitgord, Geophysical data, *The Geology of North America, Vol. 1-2 The Atlantic Continental Margin: U.S.*, 177–197, 1988.

Sheriff, R. E. and L. P. Geldart, *Exploration Seismology Volume I, History, theory and data acquisition,* Cambridge University Press, Cambridge, 1982.

Shuck, T., Personal communication, *MIT Reservoir Delineation Meeting, Annual Meeting,* , 1990.

Stark, P. B. and R. L. Parker, Velocity Bounds from Statistical Estimates of tau(p) and x(p), *J. Geophys. Res., 92,* 2713–2719, 1987.

Steinhart, J. S., Lake Superior seismic experiment: Shots and travel times, *J. Geophys. Res., 69,* 5335–5352, 1964.

Stoffa, P. L., P. Buhl, J. B. Diebold, and F. Wenzel, Direct mapping of seismic data to the domain of intercept time and ray parameter-A plane-wave decomposition, *Geophysics, 46,* 255–267, 1981.

Stoffa, P. L., J. Oh, J. Phillips, J. A. A. Jr., D. S. Sawyer, G. M. Purdy, J. Makris, M. Wietrechowski, E. Reiter, and M. N. Toksoz, A Deep Crustal MCS Study Offshore of the Carolina Trough and Southeast Georgia Embayment, *eos, 69,* 1045 - 1045, 1988.

Stolt, R. H. and A. K. Benson, *Seismic Migration Theory and Practice,* Geophysical Press, London, 1986.

Talwani, M., P. L. Stoffa, and W. D. Mooney, *Proceedings of: Workshop on Exploration of Deep Continental Margin Crust with Closely Spaced Shots and Receivers,* Houston Area Research Center, Houston, Texas, 1990.

Taner, M. T. and F. Koehler, Velocity spectra–digital computer derivation and applications of velocity functions, *Geophysics, 34,* 859–881, 1969.

Tang, R., A. Carswell, and W. Moon, Velocity analysis in the p-x plane from a slant stack wavefield, *Geophysical Prospecting, 32,* 1016–1032, 1984.

Trehu, A. M., A. Ballard, L. M. Dorman, J. F. Gettrust, K. D. Klitgord, and A. Schriner, Structure of the Lower Crust Beneath the Carolina Trough, U.S. Atlantic Continental Margin, *J. Geophys. Res., 94,* 10,585–10,600, 1989.

Treitel, S., P. R. Gutowski, and D. E. Wagner, Plane-wave decomposition of seismograms, *Geophysics, 47,* 1375–1401, 1982.

Verm, R. W., F. J. Hilterman, and L. C. Liang, Imaging vsp's 3 kilometers beyond the borehole receiver, *Offshore Technology Conference, OTC 5570,* 161–166, 1987.

Watt, T. and J. B. Bednar, Role of the alpha-trimmed mean in combining and analyzing seismic common depth-point gathers, *SEG Expanded Abstracts, 53,* 276–277, 1983.

Appendix A

1-D Tau-p,X-p and T-p Wavefield Continuation

Introduction

The original idea of inverting refraction data by wavefield continuation was first presented by Clayton and McMechan (1981). Their knowledge of migration by the phase shift method (Gazdag, 1978) was instrumental in the development of a standard and robust means of extracting 1-D velocity profiles from large offset data. Migrating or downward continuing pre-critical reflection data by means of a phase rotation was presented as a computationally efficient manner with which to migrate zero offset (stacked) seismic data (Gazdag, 1978). Clayton and McMechan (1981) realized that such a downward continuation approach could be applied to post-critically reflected and refracted data which had been transformed to the $\tau - p$ domain. They formulated the problem as a downward continuation of a single p vector at a time to the domain of slowness and depth $(p - z)$ using the same phase shift method as Gazdag (1978) used for zero offset data. Clayton and McMechan (1981) utilized the inverse relation between observed ray parameter p and interval velocity at the bottoming point to iteratively determine a best-fitting velocity model. Advantages of their approach

include elimination of travel time picking, direct illustration of model resolution and the ability to make decisions regarding the goodness of data observations directly in the model space. An often cited drawback is the uncertainty introduced by phase shifts caused by post-critically reflected branches of the travel time curve.

In the following Appendix, we first present the original 1-D wavefield continuation approach for $\tau - p$ data (Clayton and McMechan, 1981). We then summarize subsequent work of Duckworth (1983) and McMechan (1983a) which describe a similar wavefield continuation procedure for $X - p$ data. An additional continuation procedure for $T - p$ data is presented to complete our summary of 1-D velocity inversion schemes for slowness-decomposed data.

Consider the following scalar representation of the wave equation:

$$\left[\frac{\partial^2}{\partial^2 z} + \frac{\partial^2}{\partial^2 x} + 4\frac{w^2}{v^2(z)}\right] P(w,x,z) = 0 \tag{A.1}$$

$P(w,x,z)$ represents the wavefield as a function of frequency w, offset x and depth z. The quantity $v^2(z)$ is a 1-D representation of velocity. Using Equation 1, the wavefield recorded at the surface may be downward continued to any depth z in a 1-D medium by a simple phase rotation in the frequency domain (Gazdag, 1978).

$$P(w,k_x,z) = P(w,k_x,0)e^{-i2\int_0^z [\frac{w^2}{v^2(z)} - \frac{k_x^2}{4}]^{1/2} dz} \tag{A.2}$$

The slant stacked wavefield to be downward continued may be defined in the time domain as:

$$Q_\tau(\tau,p) = \int_{-\infty}^{+\infty} P(\tau + px, x)dx \tag{A.3}$$

or in the frequency domain as:

$$Q_\tau(w,p) = P(w,-wp) \tag{A.4}$$

In the time domain representation P is the recorded wavefield, while in the frequency domain expression the wavefield is assumed to have been doubly transformed over offset and time.

Equation 2 may be expressed in terms of slowness by substituting $k_h = -wp$.

$$P(w, -wp, z) = P(w, -wp, 0)e^{-iw\Psi_\tau(p,z)} \tag{A.5}$$

The phase term is now written as an operator $\Psi(p, z)$ expressed as:

$$\Psi_\tau(p, z) = 2\int_0^z [v^{-2} - p^2]^{1/2} dz \tag{A.6}$$

Using the frequency domain representation, the downward continuation of slant stacked wavefield may be written as:

$$Q_\tau(w, p, z) = Q_\tau(w, p, 0)e^{-iw[\Psi_\tau(p,z)]} \tag{A.7}$$

Taking the inverse Fourier transform, this may be written as:

$$Q_\tau(\tau, p, z) = \int Q_\tau(w, p, 0)e^{-iw[\Psi_\tau(p,z)-\tau]} dw \tag{A.8}$$

The imaging condition which expresses the desired bottoming point of post-critically reflected and refracted energy is found by setting $\tau = 0$ and simplifying to:

$$s(p, z) = \int Q_\tau(w, p, 0)e^{-iw\Psi_\tau(p,z)} dw \tag{A.9}$$

Now $s(p, z)$ represents the imaged $\tau - p$ data in the $p - z$ domain. The time domain representation emphasized in Chapter 2 may be written as:

$$s(p, z) = Q_\tau(\Psi_\tau(p, z), p) \tag{A.10}$$

Equation 10 is repeatedly evaluated with updated velocity functions picked from the previous iteration. When the data are downward continued with the correct velocity function, that velocity function is directly imaged in $s(p, z)$ space and the procedure is terminated. Convergence behavior is addressed extensively by Duckworth (1983); aside from some difficulties with quasi-stable states Clayton and McMechan (1981), the general approach is quite robust. Updated velocity models are typically picked from an interactive graphics device, as field data generally do not allow clean enough $\tau - p$ representations for effective automatic picking.

Figure 1a shows a simple velocity model consisting of gradients and velocity boundaries and the corresponding ray paths. Dashed lines depict reflections and solid lines show turning rays or refractions. A $\tau - p$ representation of these arrivals is shown in Figure 1b. The post-critical reflections map to concave-upward ellipses while the refractions map to concave-downward trajectories. A monotonically increasing velocity structure will produce a continuous τ curve (Bessanova et al., 1974), which is composed of both refracted and post-critically reflected energy. For example the largest slowness components of the τ curve in Figure 1b are found in the top right corner; they correspond to refracted arrivals in the uppermost layer of the model. The first layer refracted portion of the τ curve terminates at the slowness of the base of the first layer. The next portion of the τ curve is made up of post-critical reflections from the first interface. The post-critical reflection branch asymptotes (at large offsets) to the slowness of the deepest turning ray in the first layer. The next piece of the τ curve is a refraction from the 2nd layer. The smallest (fastest) observed post-critical reflection slowness from the first interface is followed by the shallowest refracted arrival from the 2nd layer along the τ curve. This alternating reflecting and refracting makeup of the τ curve defines velocity discontinuities and gradients respectively.

Figure 2 shows the relation between the τ curve from a monotonically increasing velocity profile and the bottoming points in (p, z) space of the constituent arrivals. Forward branches (refractions) of the travel time curve image the true slowness profile in a monotonically decreasing manner. Larger offsets record deeper refractions which arrive with faster apparent velocities or smaller slownesses. Reverse branches of the travel time curve such as post-critical reflections image the slowness profile in a decreasing manner. Larger offsets record smaller apparent velocities than shorter offsets and thus image larger slownesses. The significance of this difference is apparent when imaging field data recorded with finite apertures. The deepest interface being imaged may have the smallest slowness imaged well, while the larger slownesses constrained

by the reverse reflected branch are not adequately recorded.

Figure 3 shows a simple velocity model which we will use to demonstrate the 1-D wavefield continuation of Clayton and McMechan (1981). Synthetic data calculated with ray theory (Cerveny et al., 1977) are shown in Figure 4 and simulate a receiver gather 60 km long with receiver spacing of 0.20 km. A $\tau - p$ representation of the data shown in Figure 5 is generated with a simple time domain slant stack. Alternating portions of concave- downward and concave-upward energy are visible along the τ curve in Figure 5 representing refracted and reflected arrivals respectively. Linear events intersecting the τ axis at 5.25 and 7.25 seconds are artifacts from the slant stack. Figure 6 shows the result of repeatedly downward continuing the $\tau - p$ data in Figure 5 into $p - z$ space. The dashed line represents a trial velocity function and the solid line the correct velocity function. A trial velocity which is too slow will generally image the data at too shallow a depth. Figure 6a shows this behavior, and the updated velocity function will then be faster than the correct profile. This bracketing of the correct velocity function is observed throughout the convergence process. Figures 6a-e show the first 5 iterations, and illustrate the initial bracketing and convergence behavior commonly observed. Figure 6f shows the result of using the correct trial velocity model for the downward continuation. The data have imaged onto the trial velocity function which is barely visible at the bottom of the figure. The data were created with a non-causal zero phase 10 Hz wavelet and a peak amplitude picking criteria was applied for model updates. Clayton and McMechan (1981) discuss application of phase shifts to $\tau - p$ data in order to properly image true causal wavelets.

Data which has been decomposed to either offset-slowness (X-p) or total travel time-slowness (T-p) may also be iteratively downward continued to the $p - z$ domain in order to extract and image a 1-D velocity profile. Duckworth (1983), McMechan (1983b) and McMechan (1984) give expressions for imaging X-p data and we summarize their results in our notation.

$$\Psi_X(p,z) = 2\int_0^z p[v^{-2} - p^2]^{-1/2}dz \tag{A.11}$$

$$s(p,z) = Q_X(\Psi_X(p,z),p) \tag{A.12}$$

$Q_X(X,p)$ is a $X-p$ representation of the wavefield and may be computed with multiple overlapping slant stacks (McMechan, 1983a). $\Psi_X(p,z)$ is the downward continuation operator for $X-p$ data and $s(p,z)$ the downward continued image.

Additionally, data that have been decomposed into $T-p$ may also be imaged onto the $p-z$ plane. The following expressions are found in Chapter 2 for 2-D models and are repeated here in their 1-D form for the sake of completeness.

$$\Psi_T(p,z) = 2\int_0^z v^{-2}[v^{-2} - p^2]^{-1/2}dz \tag{A.13}$$

$$s(p,z) = Q_T(\Psi_T(p,z),p) \tag{A.14}$$

$Q_T(T,p)$ is a $T-p$ representation of the wavefield and may be computed with short overlapping velocity estimators in much the same manner as McMechan (1983a) computed $X-p$ data. For the case of $T-p$ data, we found by computing N short aperture $T-p$ semblance slant stacks and taking the maximum value of all N stacks, a reasonable $T-p$ image could be extracted.

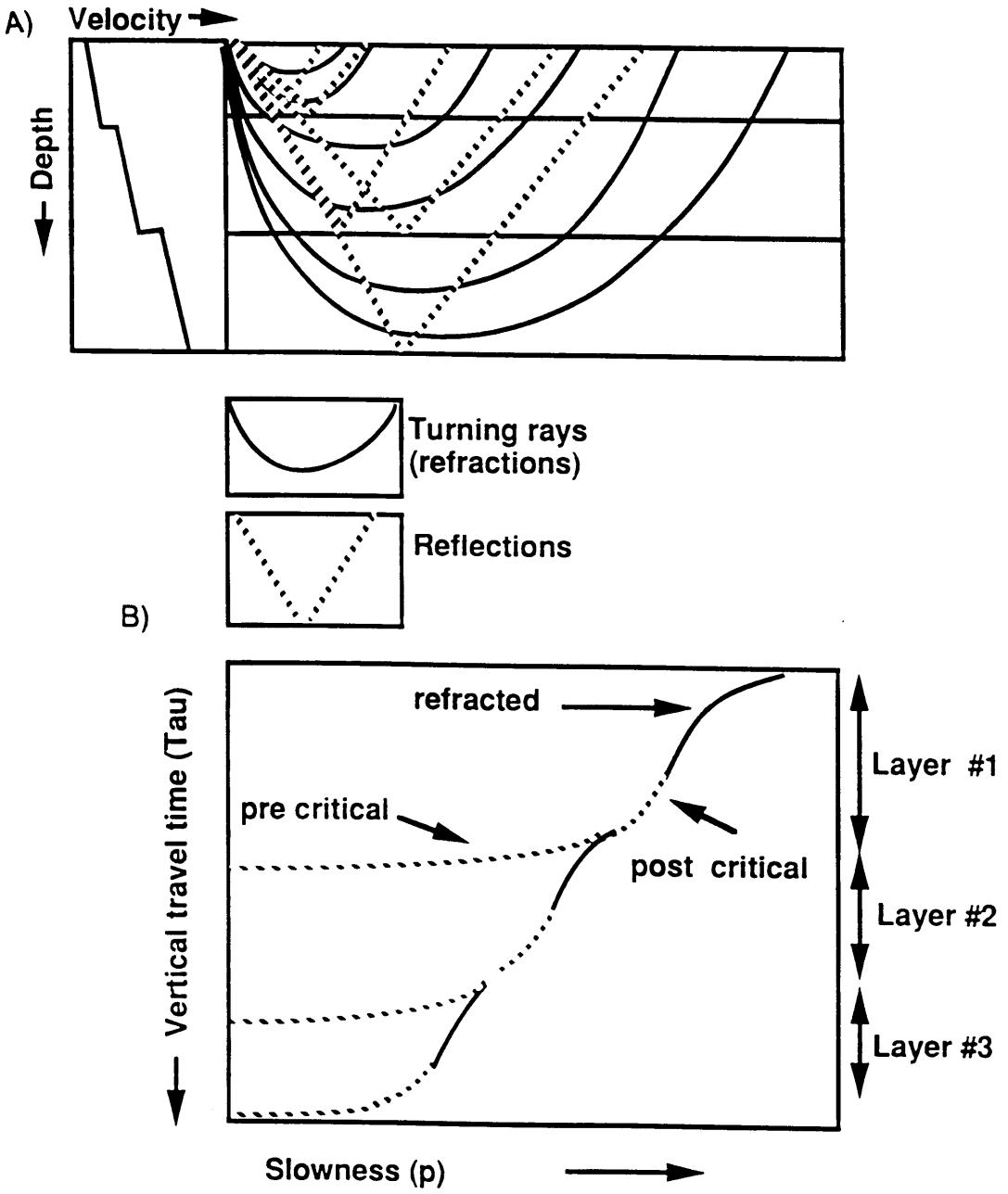

Figure 1. a) Velocity model and raypaths of turning rays (refractions) and post-critical reflections which make up the classic τ curve for a monotonically increasing velocity structure consisting of velocity discontinuities and gradients. b) $\tau - p$ representation of arrivals from the model in a). Refractions and post-critical reflections form a continuous trajectory while pre-critical reflections split off along elliptical trajectories.

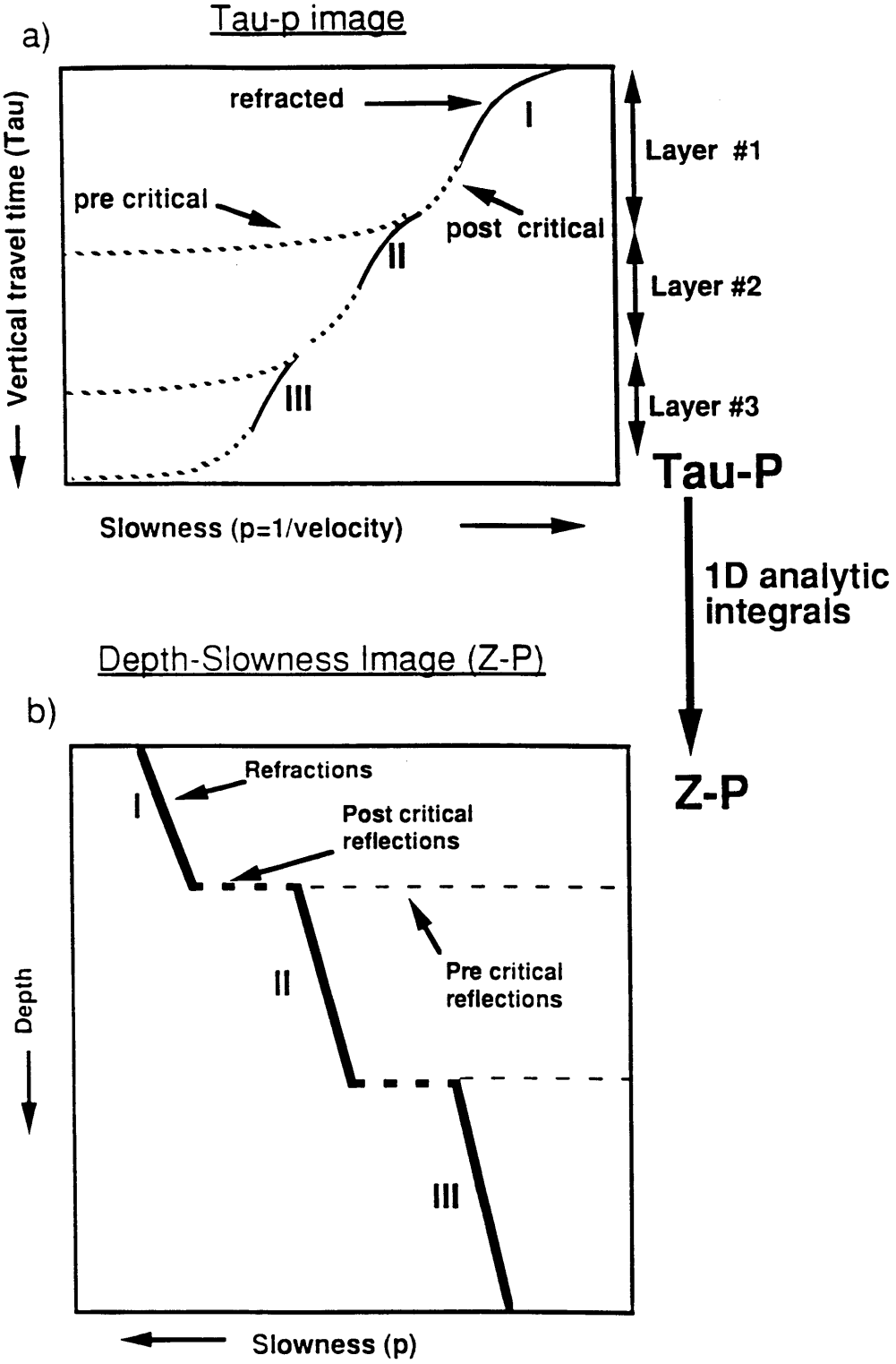

Figure 2. a) A $\tau - p$ representation from a monotonically increasing layered velocity structure. b) A depth-slowness $(Z - p)$ map of the classic $\tau - p$ curve. This shows the bottoming points of the post-critically reflected and refracted arrivals which make up classic τ curve.

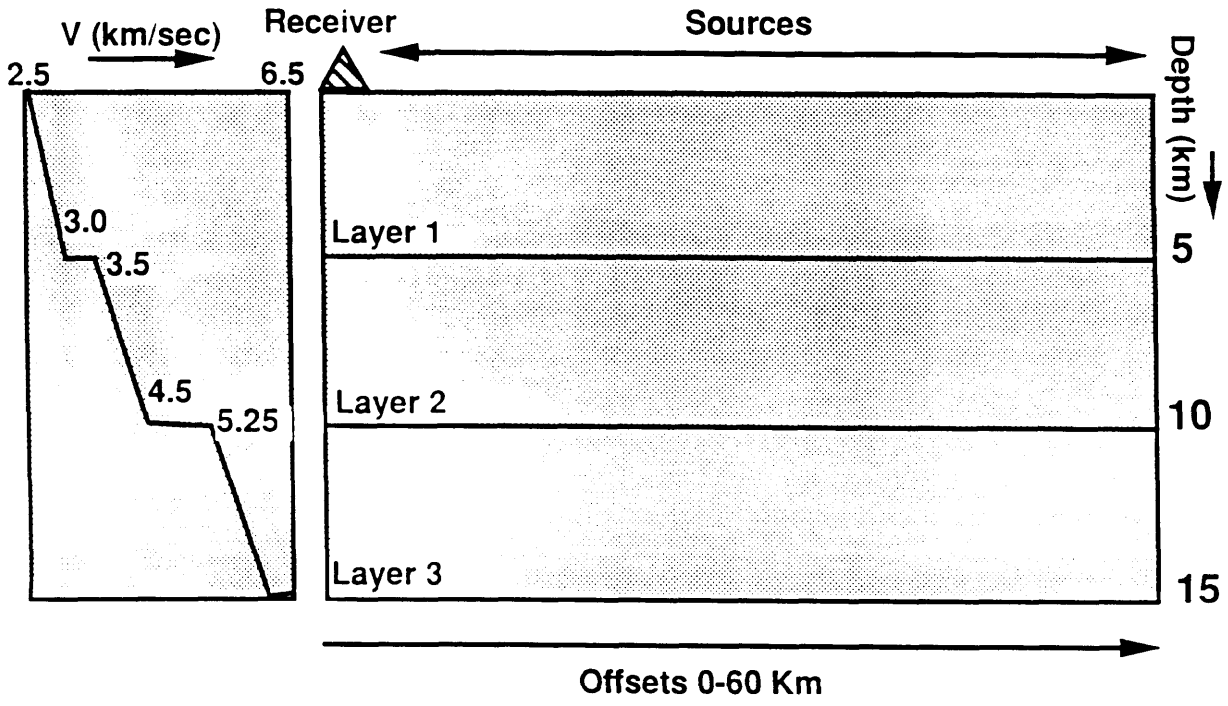

Figure 3. Model used to calculate the synthetic seismograms in Figure 4.

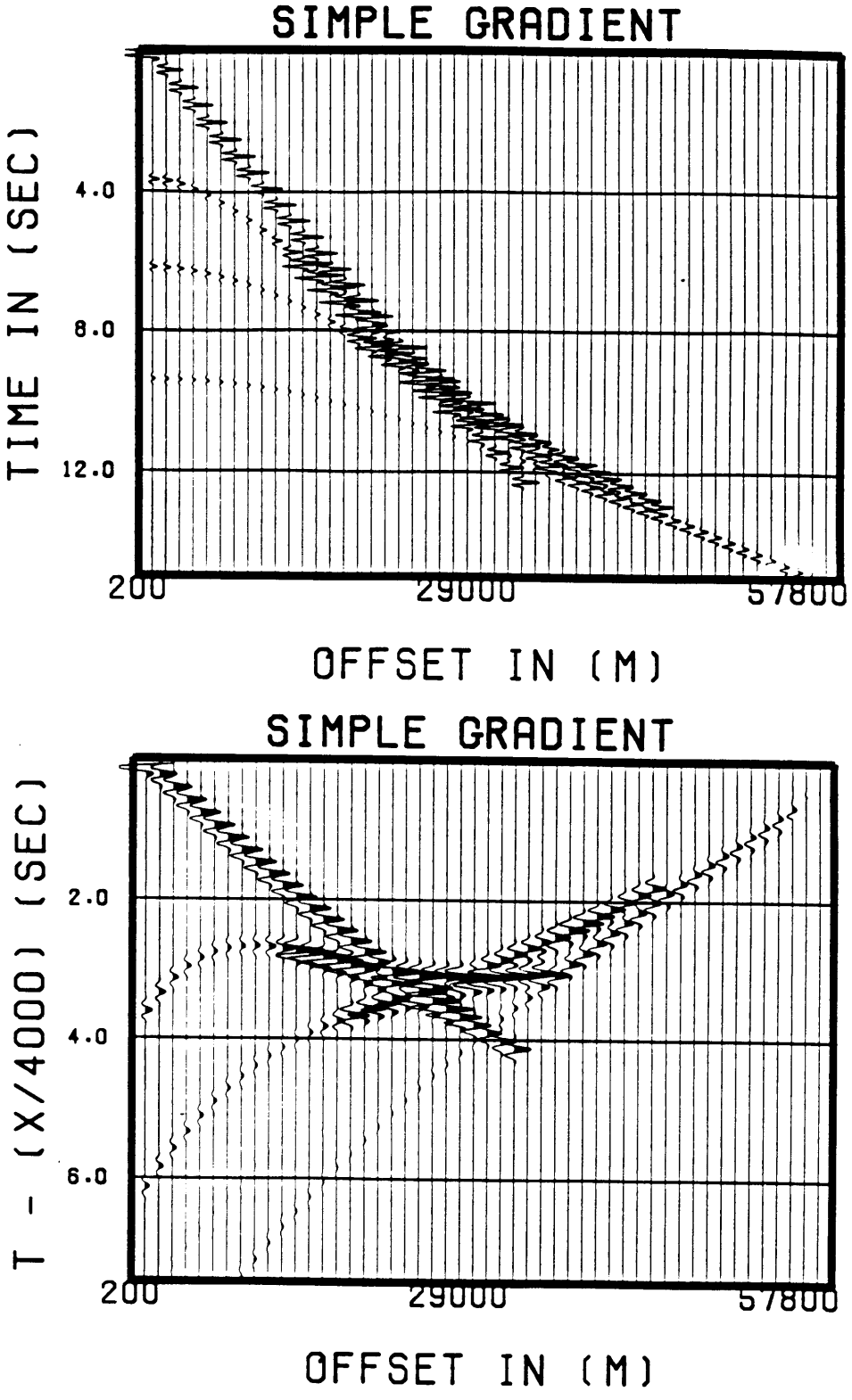

Figure 4. Ray-based synthetic seismograms computed for a single receiver recording a moving source from 0 to 60 km of offset. Top: Time versus offset plot. Bottom: Reduced time versus offset plot showing the details of the refracted and post-critically reflected arrivals.

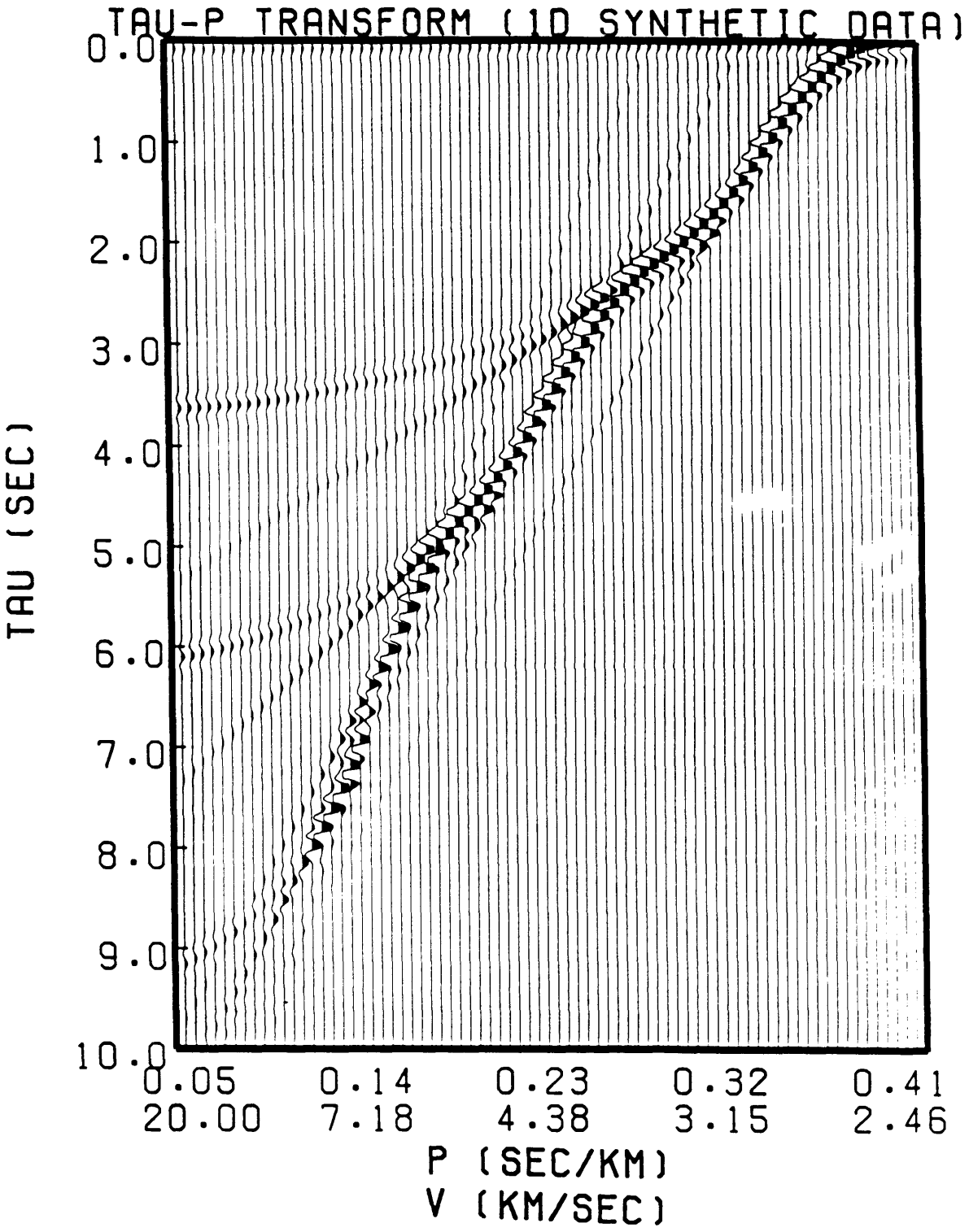

Figure 5. $\tau - p$ representation of the synthetic data shown in Figure 4. The classic $\tau - p$ curve shown schematically in Figure 1b can now be seen.

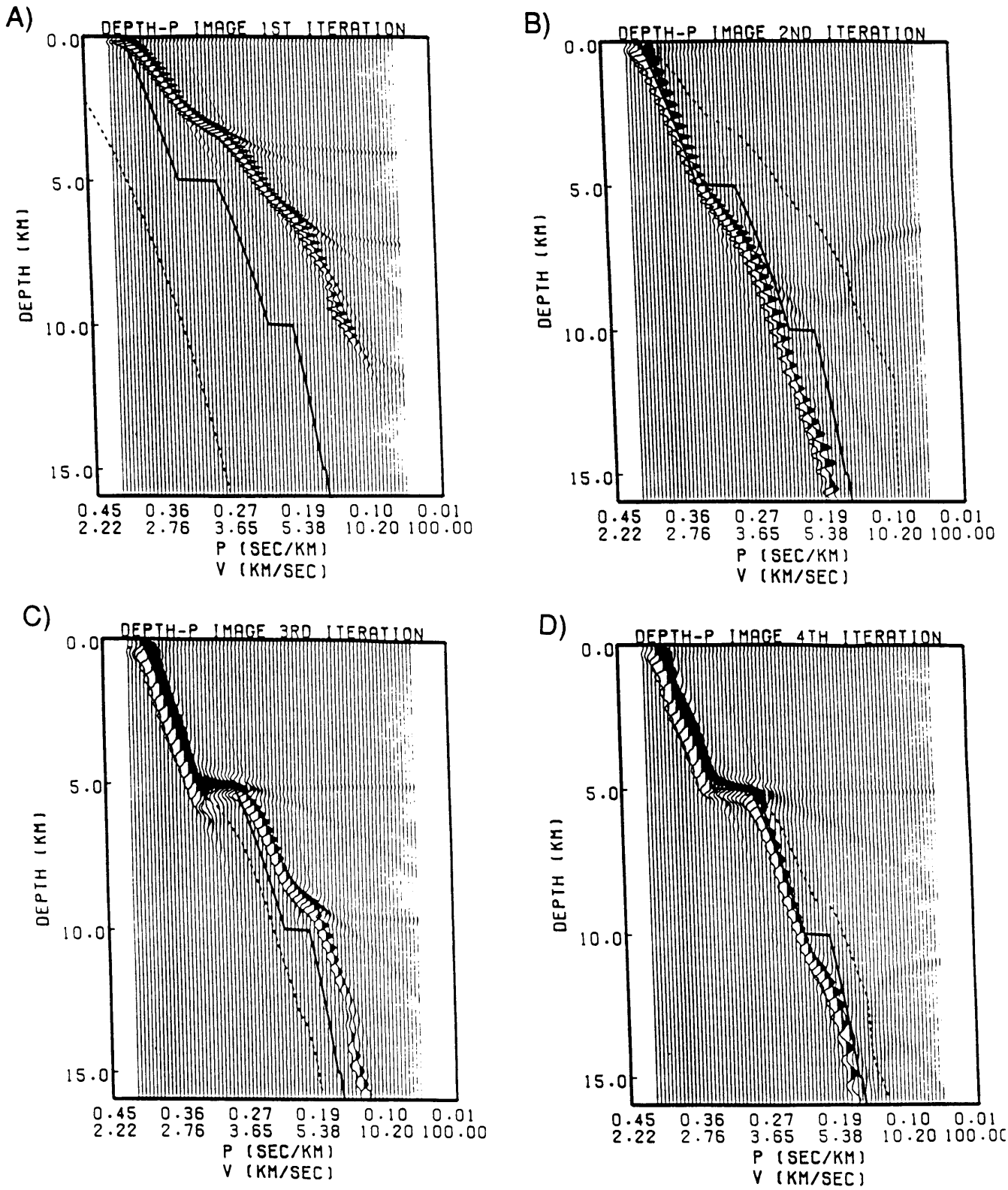

Figure 6a-d. a) Dashed line represents the velocity-depth profile used in the downward continuation and the solid line represents the correct model. In this first iteration, data have not imaged onto the velocity function used in the downward continuation and thus the procedure is repeated with an updated velocity model. b) Second iteration in which the trial velocity function is picked from the first iteration's image. c) Third iteration. d) Fourth iteration.

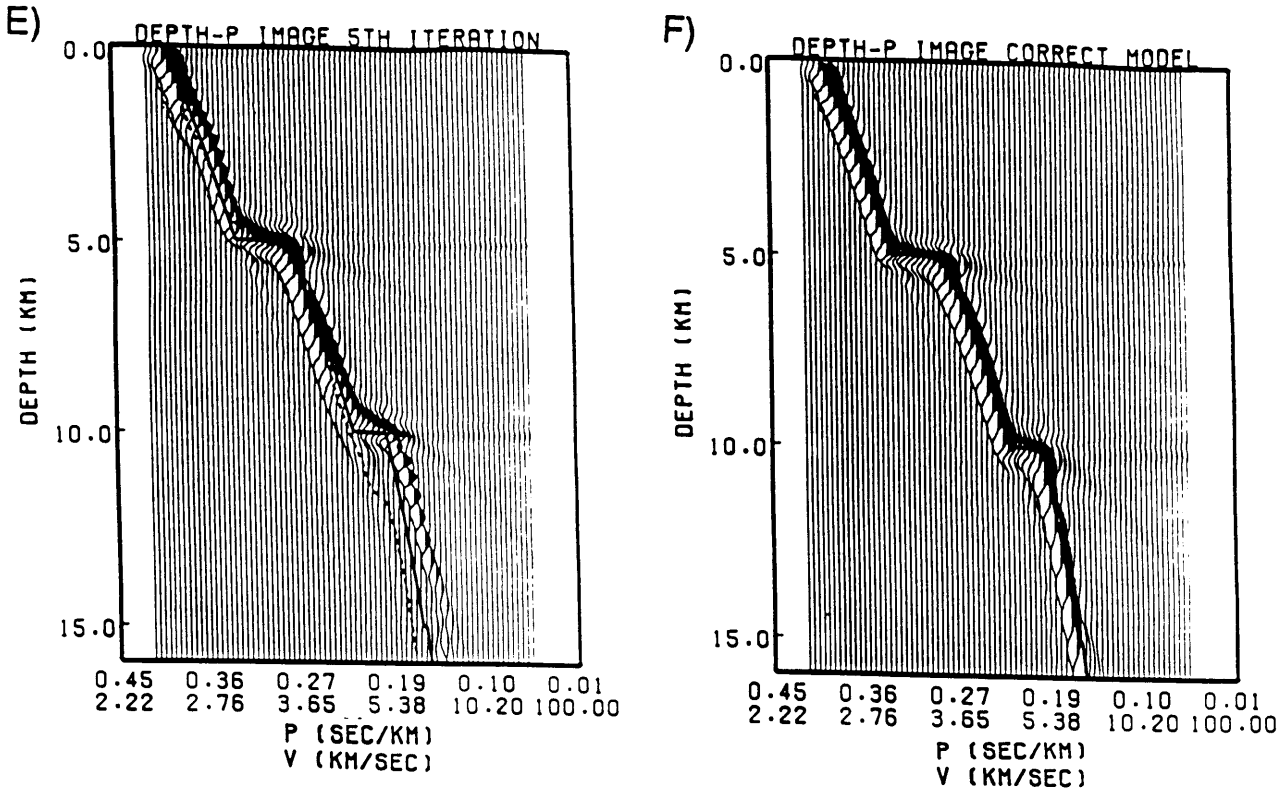

Figure 6e-f. e) Fifth iteration of the 1D downward continuation procedure. The data have nearly imaged onto the trial velocity function indicating the problem is close tom convergence. f) Slowness-depth image when using the correct velocity model in the downward continuation. The data have imaged the trial velocity function indicating convergence.

Appendix B

Two-Dimensional Kirchhoff Approximation

Non-planar Kirchhoff Derivation

Green's theorem relates observations of pressure and its derivative on a boundary to the pressure at some point enclosed by the boundary. This can be written as Equation 1 (Morse and Feschback, 1953).

$$P(r,t) = \frac{1}{4\pi}\int dt_0 \int_{S_0} dS_0 \left[G(r, r_0, t, t_0)\frac{\partial P(r_0, t_0)}{\partial n} - P(r_0, t_0)\frac{\partial G(r, r_0, t, t_0)}{\partial n}\right]. \quad \text{(B.1)}$$

In this equation, S_0 is the surface of integration where the pressure, $P(r_0, t_0)$ is measured. $\frac{\partial}{\partial n}$ is the derivative with respect to the normal of the surface S_0, r is the vector from the origin to the point at which the wavefield is to be calculated (the image point), r_0 is the vector from the origin to the observation point on S_0, and t_0 is the time at which the observations on S_0 are made. G is the Green's function for an acoustic medium with a point source located at r.

From Equation 1 it is apparent that both the pressure $P(r_0, t_0)$, and the derivative of the pressure $\partial P(r_0, t_0)/\partial n$, are required to calculate the pressure at some point enclosed by the surface S_0. Since $\partial P(r_0, t_0)/\partial n$ is not normally measured, a Green's

function is sought that is zero everywhere on the surface S_0. Such a Green's function would reduce the term involving $\partial P(r_0, t_0)/\partial n$ to zero. For a flat surface S_0, such a Green's function was given by Schneider (1978) and French (1975). They defined the Green's function to be the free space Green's function (G_{fs}) minus its reflection in the plane. Wiggins (1984) generalizes this to an arbitrary non-planar geometry where the Green's function (G_{np}) is required to have $G_{np} = 0$ at all points on the observing boundary S_0 with $\partial G_{np}/\partial n = 2\partial G_{fs}/\partial n$.

Defining $G_{fs} = \delta(t_0 - t - \frac{R}{c})/R$ with $R = r_0 - r$ and c being the velocity of the medium, Equation 1 can be written in a more useful form

$$P(r,t) = \frac{-1}{2\pi} \int dt_0 \int dS_0 \; P(r_0, t_0) \frac{\partial}{\partial n} \left[\frac{\delta(t_0 - t - \frac{R}{c})}{R} \right]. \tag{B.2}$$

Taking the Fourier transform of the observed pressure field $P(r_0, t_0)$ with respect to t_0 and substituting in Equation 2:

$$P(r,t) = \frac{-1}{2\pi} \int dt_0 dS_0 \frac{\partial}{\partial n} \left[\frac{\delta(t_0 - t - \frac{R}{c})}{R} \right] \cdot \int dw A(r_0, w) e^{iwt_0} \tag{B.3}$$

This may then be simplified to

$$P(r,t) = \frac{-1}{2\pi} \int dS_0 \int dw A(r_0, w) \frac{\partial}{\partial n} \left[\frac{e^{iw(t+R/c)}}{R} \right]. \tag{B.4}$$

The differentiation with respect to the normal to the boundary is then performed and higher order terms neglected. The inverse Fourier transform then yields

$$P(r,t) = \frac{-1}{c} \int dS_0 \frac{1}{R} \frac{\partial R}{\partial n} \frac{\partial P}{\partial t} \left(r_0, t + \frac{R}{c} \right) \tag{B.5}$$

In this form it is easily seen that the pressure field at any point in space enclosed by S_0 can be calculated from the time derivative of the pressure data recorded on an arbitrary non-planar boundary.

The application of Equation 5 to multiply-reflected energy involves calculation of the proper Green's function for the multiple path under consideration. A two-

dimensional ray trace scheme is used to calculate the necessary travel times for extrapolation and imaging conditions. In practice the surface of integration S_0 must intercept the scattered seismic energy. In our field data examples, the surface of integration was restricted to those offsets at which clear large amplitude reflected arrivals were observed.

Appendix C

Semblance-Guided Median Filtering

Introduction

Median filters, and the related alpha-trimmed mean filter (Watt and Bednar, 1983), describe a set of non-linear digital filters which have proven effective in a variety of geophysical applications. The median filter was first used in geophysics as a general data "despiker" to suppress unwanted noise spikes in seismic data (Evans, 1982) and later as a robust velocity filter (Hardage, 1983). Other applications of the median filter include the areas of speech processing (Rabiner et al., 1975) and image enhancement (Frieden, 1976). In this Appendix we describe an extension of the traditional median velocity filter commonly used in Vertical Seismic Profile (VSP) upgoing-downgoing wavefield separation. A one-dimensional median filter is applied at a slowness which is within a user-specified slowness passband. The slowness along which the median filter is applied is determined by a velocity estimator which in our implementation is the statistic of semblance (Taner and Koehler, 1969). The median filter is applied at the slowness at which a maximum value of semblance is computed. Thus our approach is composed of two distinct steps. First, a preferred slowness is computed with a

velocity estimator and then a median filter is applied at this slowness. Additional suppression of incoherent background noise may be accomplished by weighting the median filter output by the peak computed semblance.

This filter may be used both to enhance coherent signal from a background of incoherent energy, and as a highly non-linear velocity filter. The former use has been quite successful at improving signal to noise characteristics in densely-sampled large offset refraction/wide-angle reflection data. Field data from an Ocean Bottom Hydrophone (OBH) recording a near-surface airgun array demonstrates the effectiveness of this approach at increasing the signal-to-noise ratio of large offset seismic data. The highly repeatable airgun source allows the detection of weak signals with multi-channel velocity estimators and subsequent enhancement of these events with a median filter.

Velocity filtering represents the other possible use of this type of filter. The median filter first found widespread use in geophysics as a velocity filter in VSP wavefield separation problems (Hardage, 1983). In its original formulation, the median filter was designed as a local operator which was applied to an aligned wavefield. Alignment was usually achieved by manually or automatically picking downgoing first arrivals and shifting the data to vertically align the downgoing wavefield to some common time datum. The median filter was then applied to the moveout corrected data along vertical trajectories corresponding to the aligned downgoing pulse. The result was a robust estimate of the downgoing wavefield which could either be used by itself, or more commonly, subtracted from the original data to obtain an estimate of the weak upgoing wavefield. This procedure acted as a velocity filter by estimating the aligned downgoing wavefield while rejecting the upgoing wavefield. The major drawbacks with this approach are twofold: first, only the event which has been aligned by the interpreter may be estimated during each application of the median operator; secondly, the alignment of the data is a time consuming and tedious step. Our approach addresses both issues by allowing multiple events of differing slownesses

to be estimated provided they reside within a defined slowness passband, and by eliminating the need for a prior alignment of the data.

We demonstrate the ability of our filter to simultaneously pass events of differing slownesses on field data consisting of a hard rock short offset hydrophone VSP. Downgoing compressional (P) and shear (S) arrivals are enhanced in the presence of large amplitude tube wave arrivals generated at the intersection of fractures with the borehole. The downgoing P and S arrivals have significantly different moveouts corresponding to the in-situ hard rock velocity structure. Their *simultaneous* enhancement and corresponding tube wave rejection illustrates the successful application of our approach as a true velocity filter. Elimination of the traditional trace alignment step is demonstrated in a standard VSP upgoing wavefield separation procedure. We show that by defining a slowness passband which includes only upgoing arrivals, the semblance-guided median filter can directly track and estimate the upgoing wavefield. An additional step is taken to show how our approach may be used to estimate noise; for example, energy which is neither upgoing or downgoing arrivals in a VSP section. By separately estimating both the upgoing and downgoing wavefields and subtracting these from the original data, an estimate of this "noise" is obtained. This "noise" section will clearly show incoherent energy such as random background noise and poor geophone clamping, as well as coherent arrivals such as tube waves from outside the specified slowness passbands.

Semblance-Guided Median Filter Structure

Figure 1 illustrates the structure of a semblance-guided median filter. Input to the filter is a local set of M traces centered about the trace to be filtered. Provided M is an odd number, the local set of traces will be symmetric about the trace to be filtered. Choice of the filter aperture or width M depends on the spatial and temporal sampling of the input data and the specific noise characteristics to be suppressed. Larger filter widths generally provide increased velocity resolution but result in greater averaging

of the data along the offset or depth axis.

A range of velocities designating the slowness passband of the filter is selected and is defined as V_{min} and V_{max} in Figure 1. Semblance is calculated at Np equally spaced slownesses within the passband for a single sample window about the center trace and the inverse of the slowness where the peak semblance is found is designated as V_{event}. Data samples along the trajectory defined by V_{event} are input into a standard one-dimensional median filter which returns the statistical median of the input. As a result, coherent signals within this passband are enhanced, while those with slownesses outside the passband are suppressed. The filter is then moved to the next time sample of the same trace and the semblance values and median filter are computed once again. After filtering a single trace, the local trace gate is centered about the next trace to be filtered and reloaded with raw data.

Estimation of the signal's slowness or trajectory represents the first step of the filtering process. Semblance is one of many possible methods for velocity estimation. Other velocity estimation techniques such as the maximum-likelihood method (Duckworth, 1983; Hsu and Baggeroer, 1986) provide increased slowness resolution but involve a significantly greater computational burden. More recently, a group of methods which rely on decompositions of the wavefield into orthogonal signal and noise subspaces have been proposed. These methods have been applied in sonar array processing (Bienvenu and Knopp, 1983; Schmidt, 1986) to the problem of velocity/bearing angle estimation. Their extension to broadband seismic problems has been discussed by Biondi and Kostov (1989) and Key and Smithson (1990), with the latter citing an approach of considerable computational efficiency. Any of these approaches to the velocity estimation problem may be used in the first step of the filter.

Implementation of the velocity estimation step using the semblance statistic is

given in Equation A.1.

$$P_{preferred}(x_k, T_j) = MAX \sum_{i=1}^{Np} \frac{\left[\sum_{k=1}^{M} \phi(x_k, T_j + p_i x_k)\right]^2}{M \sum_{k=1}^{M} \phi^2(x_k, T_j + p_i x_k)}] \qquad \text{(C.1)}$$

The seismic data are represented by $\phi(x_k, T_j)$ with x_k being a discrete receiver location and T_j a discrete time sample. Equation 1 is evaluated for N_p slownesses p_i, and $P_{preferred}$ is selected as the slowness at which the maximum semblance was measured. Stoffa et al. (1981) discuss slowness resolution and its dependence on array length, receiver spacing and temporal sampling. The maximum slowness resolution and passband width determine the number of slownesses N_p over which to steer. After a preferred slowness has been determined, the median filter is applied along the appropriate trajectory. In practice, the data are sampled discretely in time, and interpolation between time samples is necessary to compute both the semblance values and input to the median filter. We perform a simple linear interpolation between the nearest two time samples. For data sampled coarsely in time, higher order interpolation methods may be justified.

A pure median filter acts as a non-linear filter whose input is a set of data points and whose output is the statistical median of that set. The median is defined as the midpoint of a reordered data set sorted from least to greatest value. In the case of an even number of input values the mean of the middle two values is used. This is allowable, although not desirable in our case, because an even number of input data requires a non-symmetric trace aperture in the offset or depth domain. The filter is termed non-linear because the output cannot be expressed as a linear combination of filter coefficients convolved with the input. A major consideration when applying non-linear filters to data is that the order of the processing steps makes a difference in the final output. Equation 2 represents the action of the median filter on an input data vector.

$$S_{median} = S((M-1)/2 + 1) \qquad \text{(C.2)}$$

with $S(1) < S(2) < S(3).....S(M)$ representing the sorted input data.

An intermediate step between the median operator of Equation 2 and the commonly used mean (average) operator is found in the alpha-trimmed mean (Watt and Bednar, 1983). The alpha-trimmed mean allows certain benefits of both pure median and pure mean estimators. The alpha-trim allows user specified rejection of outlying regions of a distribution while constructing a mean over the middle regions of the distribution. This procedure has been found useful in CDP stacking (Watt and Bednar, 1983; Haldorsen and Farmer, 1989) in the presence of noise bursts or coherent noise from neighboring seismic vessels.

Given the ordered sequence: $S(1) < S(2) < S(3).....S(M)$ the alpha-trimmed mean is defined by Watt and Bednar (1983):

$$Y_\alpha = \frac{1}{M-2l} \sum_{i=l}^{M-l+1} S(i) \tag{C.3}$$

The value l determines the amount of "trimming" and is controlled by α. $l = \begin{cases} \alpha \cdot M & M - odd \\ \alpha \cdot (M+1) & M - even \end{cases}$
where l represents the truncated integer value. From Equation 3 we see that for $\alpha = 0.0$ the α trimmed mean is a simple average and for $\alpha = 0.5$ it is a pure median.

Properties of Median Filters

Median filters are recognized to possess several advantages over more traditional linear filters. The ability to preserve sharp edges in data is one of the most desirable qualities of the median filter. Consider an input data set composed of a single step $D = 0,0,0,0,0,1,1,1,1,1$. Assume a five point median filter was applied to the single step defined by the previous sequence. To avoid interference with the edges, let the 3rd point of the sequence be the center of the first 5-point input window to the median filter. The input vector will be all 0's and the output will be 0. This procedure is repeated for the 4th and 5th data points and again the output of the median filter is

0. When the filter is centered around the 6th point of the input sequence, the values (0,0,1,1,1) are input to the median filter and the output is 1. Likewise, the median filter output is 1 for data points 7 and 8 of the input sequence. Thus the sharp step has been fully reproduced by the median operator with no smearing of the signal.

The other major advantage of the median filter is its robust behavior in the presence of large amplitude noise bursts. This characteristic led to the use of median filters as general data "despikers" to rid data of very large amplitude noise bursts (Evans, 1982). For applications of this type, a median filter of width M samples is applied to a 1-D time series contaminated by noise of length no longer than (M-1)/2. A simple example illustrating the robustness of a median filter is found by considering the simple data set $D = 1.6, 2.3, 2.1, 1.9, 1003.1$. Assume these 5 data points represented measurements from 5 separate runs of some physical experiment, for example, observations of pressure at some distance from a source. If one had the task of producing the best estimate of the pressure from the 5 observations, the median value would yield an acceptable estimate of 2.1, whereas the mean would yield 202.2. Thus we see that the median provides a better estimate in the presence of very large amplitude noise.

Synthetic Examples

We use synthetic data to test the ability of our semblance-guided median filter to suppress random bandlimited background noise and to perform as a velocity filter. Synthetic data are created with a 5 hz Ricker wavelet which is contaminated with bandlimited random noise whose spectrum is also centered about 5 hz. The ratio of the signal to background noise refers to the ratio of peak signal to peak noise amplitude over appropriate portions of the seismograms. Figure 2 shows synthetic data with 4 sets of crossing events having velocities of $\pm$2000 m/sec. The event sloping downward to the right will be arbitrarily referred to as the "downgoing" event (v=+2000 m/sec); this is the event we seek to enhance with our filter. The

event sloping upward (v=−2000 m/sec) will be referred to as the "upgoing" event. It is considered as noise for our purposes. The ratio of the background noise to the downgoing signal is 1. There are four sets of events in this synthetic section. In set 1, the ratio of the peak amplitudes of the upgoing event to the downgoing event is 1. In sets 2,3 and 4 the ratio of the upgoing to the downgoing is 4,8 and 16 respectively. Thus, the synthetic data have both a random background noise component and a coherent interfering event component; this represents in a gross manner a variety of types of seismic data. Figure 3 shows the synthetic data of Figure 2 after filtering with our semblance-guided median filter. A trace gate of 21 traces, and a slowness passband of 1000-3000 m/sec with 25 slowness steers was used to process the data in Figure 3. Figures 2 and 3 are plotted on the same scale, allowing a direct comparison of the input data with the filtered data. The random background noise has clearly been reduced significantly throughout the section. The first 0.25 seconds and last 0.25 seconds are left unfiltered for purposes of comparison. In set 1 the downgoing event shows little interference from the crossover of the upgoing event. In set 4 the downgoing event shows some interference in the crossover region, but it is still well estimated by the median operator. In sets 2 and 3 there is some interference at the crossover region but again the downgoing pulse is well estimated. The definition of the median filter explains why a linear increase in degradation of the estimated signal is not seen as the amplitude of the crossing event successively doubles. Data points in the crossover vicinity which are outliers in set 2 remain as outliers in sets 3 and 4, since they lie further out on the tails of their respective distributions.

Median filters provide an extremely effective method for noise removal, provided the noise may be manipulated to reside as an outlier in a distribution. In our case, by choosing a trace gate wide enough (see Figure 1), the noise is transformed from the original observation space to an outlier in a distribution. Once the noise is positioned as an outlier, the median operator effectively eliminates it from the data. The selection of an adequate trace gate is key to the relegation of noise to an outlier. Figure 4 is

identical to Figure 3 except the trace gate was narrowed to 11 traces. The ability to reject upgoing events especially in sets 3 and 4 has been significantly reduced. In this case the trace width is not adequate to ensure the noise will reside as an outlier. As a result, the median value is influenced by the noise and the resulting output is contaminated by an event well outside the slowness passband.

Figure 5 shows the same sets of crossing events as Figure 3, but with the level of background noise doubled; this lowers the ratio of the downgoing signal to the background noise to 0.5. Figures 5-7 are plotted on the same scale as Figures 2-4 allowing direct comparisons between filter results. Figure 6 is the result of filtering the data of Figure 5 with the same parameters as Figure 3 (21-trace gate). The major difference between Figures 3 and 6 lies in the level of background noise which passed through the filter. The doubling of the background noise level in the input data has resulted in increased levels of noise in the filtered data set. More importantly, the background noise is no longer random; it has been aligned at slownesses within the passband and appears as discontinuous segments of coherent signal. Figure 7 is the same as Figure 6, but an 11 trace gate is used in place of the 21-trace gate of Figure 6. The level of background noise which was passed is greater for the 11-trace gate (Figure 7) than for the 21-trace gate (Figure 6). Neither gate was sufficient to reduce the noise to the level seen in Figure 4.

Rejection of pure random background noise is achieved with similar degrees of success by either median or simple mean estimators. In the case of random noise, slownesses selected by the semblance step should equally represent all slowness within the passband. The resulting distributions will tend to be symmetric, in which case the median and mean will produce similar estimates. We examine this by processing the synthetic data of Figure 2 (downgoing signal to background noise ratio=1), but instead of using a median operator, we use a simple mean. This is represented in the alpha-trimmed mean terminology as $\alpha = 0.0$. Figure 8 shows the data of Figure 2 filtered with a 21-trace gate but with a mean instead of a median operator. Figure

8 (mean) may be compared with Figure 3 (median) to illustrate those types of noise better handled by the median filter. The background noise levels in Figures 3 and 8 are indistinguishable, clearly illustrating the effectiveness of either approach for symmetric distributions. However, the large tailed asymmetric distributions arising from the presence of large amplitude crossing events (or noise bursts) are handled quite differently by the median and mean. Figure 8 shows increasing interference as the amplitude of upgoing events increases. Sets 2-4 all show interference from the upgoing event in Figure 8 (mean), while Figure 3 (median) suppresses these events much better.

Vertical Seismic Profiling Applications

The ability to simultaneously pass arrivals of two distinct slownesses represents a significant improvement over previous median filter implementations (Hardage, 1983). We illustrate this using a VSP field data set acquired in Kent Cliffs, New York. The well drilled crystalline rock to a depth of 3300 ft and the data acquired used a weight drop source at 37 m offset, and a hydrophone array. Figure 9a shows data from a short offset (37 m) hydrophone VSP. Prominent arrivals include a first arrival downgoing P wave and numerous tube waves generated at the intersection of fractures with the borehole (Beydoun et al., 1984; Hardin et al., 1987; Cicerone et al., 1988). A faint downgoing S wave is also observed, but it is often masked by the large amplitude tube waves. The coupling of source-generated Rayleigh waves with the borehole generates additional very large amplitude tube wave energy evident in the upper right hand portion of Figure 9a. Figure 9b is the data of Figure 9a plotted at 0.25 the amplitude scale; it more clearly illustrates the large amplitude tube waves. Figure 10 shows the data after semblance-guided median filtering with a passband of 7.62 km/sec (25,000 ft/sec) to 3.10 km/sec (11,000 ft/sec). This passband includes both the P wave velocity which averages about 6 km/sec and the S wave velocity averaging about 3.35 km/sec. A 31-trace gate (centered) with 25 slowness steers was used to define

the filter. The filtered data in Figure 10 show clear downgoing S and P arrivals, and greatly diminished tube wave amplitudes. Figure 10 is plotted at the same scale as Figure 9a. The tube wave generated at the free surface by ground roll is not effectively eliminated. Although reduced in amplitude, this energy persists over 20 or more traces (in depth), because the median filter is not wide enough to properly characterize it as an outlier. The fracture-generated tube waves seen at depths of 232, 286 and 512 m (761, 938 and 1680 ft) are effectively reduced in amplitude, while both downgoing P and S arrivals are enhanced. Figure 11 illustrates the detrimental effect of specifying a filter width which is not adequate to suppress the targeted noise. Figure 11 uses the same filter parameters as Figure 10 but uses a 21-trace gate in place of the 31-trace gate of Figure 10. In this case, more fracture-generated tube wave energy is passed, especially between 457 and 609 m (1500 and 2000 ft), indicating that a 31-trace gate is more appropriate. In this case, the drawback of increasing the filter width is a loss of spatial resolution in depth; this is manifested in the filtered section as a smearing of energy. Although a median filter will preserve a noiseless monotonically increasing or decreasing sequence, in the presence of noise some smearing of signal will occur. Shorter windows will result in less smearing but poorer estimations of the signal. An additional benefit of a wide trace gate is found in the initial velocity estimation step. Wider trace gates result in more accurate velocity estimates because of the increased array aperture. The better velocity estimation in turn allows better statistics; this results in an overall increase in signal estimation ability.

We now compare our method of directly estimating the upgoing VSP wavefield to the traditional indirect method (Hardage, 1983). Traditional methods involve a temporal alignment of the downgoing arrivals, followed by an estimate of the downgoing wavefield by a median operator (Shuck, 1990). The upgoing wavefield is obtained by subtracting the downgoing estimate from the original unfiltered data. We refer to this method as the "predict and subtract" approach. Our method involves a single step in which our semblance-guided median filter is applied to the original (without move-

out correction) data, with a passband corresponding to the minimum and maximum upgoing arrival velocity. The drawback with the traditional "predict and subtract" method is that anything not predicted by the downgoing estimator, e.g. tube waves, noise bursts, ringing from poor clamping, will remain in the final estimate of the upgoing wavefield. In our approach, the upgoing wavefield is directly predicted, and the tube waves, noise bursts etc. will not appear as coherent arrivals within the upgoing passband. Thus they will be rejected by our filter and will not appear in the final upgoing wavefield estimate.

We compare the traditional "predict and subtract" method to our approach in Figure 12. Figure 12a shows raw field data from a zero offset vertical component VSP at MIT's Burch Well. An estimate of the downgoing wavefield obtained with the semblance-guided median filter is shown in Figure 12b. A strict comparison to the "predict and subtract" method would achieve the downgoing wavefield estimate by a single directional median filter applied to moveout corrected data. We predict the downgoing wavefield in a single step by applying our filter with a passband of 4.5-7.6 km/sec (15,000-25,000 ft/sec) and 21 slowness steers. Subtraction of the downgoing estimates in Figure 12b from the original data in Figure 12a gives the "predict and subtract" estimate of the upgoing wavefield in Figure 12c. As expected, Figure 12c shows no downgoing arrivals; several upgoing events are more visible, including a clear reflection originating at about 4600 ft (1533 m). However, large amplitude tube waves and noise from poor geophone clamping remain in what ideally would be an estimate of pure upgoing energy. An additional median filtering step would help in eliminating the remnant energy, but in its present form the upgoing wavefield estimate is not optimal. Current industry practice (Shuck, 1990) involves this additional median filtering step, where the upgoing wavefield is aligned by travel time picking and another median filter is applied. This additional step assumes that the upgoing wavefield is sufficiently obvious to allow travel time picking and alignment.

Figure 12d shows the upgoing wavefield estimate from our semblance-guided median filter with a passband of 4.5-7.5km/sec and a 21-trace gate. In this case, tube wave noise and ringing has been eliminated because it was not predicted by the upgoing wavefield estimator. Comparison of Figure 12c and 12d shows the superior result obtained with direct estimation of the upgoing wavefield with the semblance-guided median filter. Our approach eliminates the need for data alignment, and provides an direct and improved estimate of the wavefield. Figure 12e shows the total wavefield (Figure 12a) minus the sum of the estimated upgoing (Figure 12d) and downgoing (Figure 12b) wavefields. This wavefield represents all energy which was not predicted as upgoing or downgoing, i.e. pure noise. Clear tube waves and poor geophone coupling are seen in this estimate of the noise (Figure 12e). Conversely, the estimated upgoing (Figure 12d) and downgoing wavefields (Figure 12b) may be combined to yield an estimate of pure coherent signal as shown in Figure 12f. In this case no tube waves or geophone ringing is present, and the section is much easier to interpret than the original data in Figure 12a.

Ocean Bottom Hydrophone Applications

Large offset refraction/wide-angle reflection data often consist of a fairly simple wavefield characterized by linear moveouts and low signal-to-noise levels. For data of this type, a semblance-guided median filter may be used as a general pre-processing step to increase signal-to-noise levels by enhancing linearly coherent signals. The general simplicity of the large offset wavefield allows us to tailor our filter to enhance coherent energy from an incoherent or random background. This is in contrast to the VSP case, where the background contained strongly coherent noise (e.g. tube waves or downgoing wavefields). The specialization of our filter to deal more effectively with low signal-to-noise random background problems involves an additional weighting of the non-linear median filter output by some measure of the semblance. Leven and Roy-Chowdbury (1984) present a time domain semblance-weighted slowness filter

which weights input points by the square of the arithmetic mean of semblance values calculated in some specified range of slownesses. For our filter, we weight the output of our median operator by either the peak semblance value or some average of the highest semblance values found within the slowness passband. Equation 4 describes the weighting of the output of the median filter defined by Equations 1-3.

$$W = \frac{1}{Np - aNp} \sum_{j=aNp}^{Np} Semb(j) \tag{C.4}$$

for a greater than 1/Np.

The array $Semb(j)$ represents sorted values of semblance computed at each of the Np slownesses. The constant a controls the extent of averaging. An a of 0 specifies a pure averaging of all the computed semblances. As a approaches 1, the weighting value W consists of the peak measured semblance only. We obtained the best results with values of a around $0.8 - 0.9$; these values provided a measure of stability through averaging. Also, values of a between $0.8 - 0.9$ still retain dynamic range, which can be suppressed by excessive averaging over large slowness bands.

Figure 13a shows raw large offset seismic data acquired by an OBH recording an airgun array. The airgun array fired every 50 m allowing acquisition of a densely sampled refraction/wide-angle reflection data set. In Figure 7, data between approximately 52 and 57 km are shown reduced at a velocity of 6 km/sec (eg., $t = t_o - offset/6$). Data after bandpass filtering with a smoothed trapezoid defined at 1, 4, 20, 25, hz is shown in Figure 13b. The signal is enhanced somewhat by suppression of high frequency noise, and varies from a signal-to-noise ratio of around 2 at 52 km and 4.0 seconds to less than 0.5 at 57 km and 4.0 seconds. The event at 4.0 seconds is thought to be a refraction through the mid-crust and the event at 7.0 seconds is the corresponding water column multiple. Very large amplitude noise after 8 seconds in Figure 13 is caused by energy reverberating throughout the water column from the previous shot. A relatively high degree of background noise coupled with portions of signal which appear discontinuous are common problems with such

data. The primary event at 4.0 seconds grows very weak at the far right of Figure 13a. After elimination of higher frequency noise in Figure 13b, the signal is slightly more visible. While such discontinuities in arrivals may contain valuable structural information, they may also be the result of local interference by background noise or temporary receiver or source malfunction. In this case, the event is more clearly seen in the water column multiple arriving at around 7.0 seconds; it is continuous in this arrival. A filter which smooths over such discontinuities in a controllable manner may therefore be a useful tool in enhancing this type of data.

The number of input traces M (Figure 1) is one of the most important parameters to be selected by the user. The proper number of input traces to use depends on the quality of the input data and the amount of lateral smearing acceptable in the subsequent processing flow. In subsequent discussions, all record sections are scaled by the rms amplitude value found from 2.0-4.0 seconds; thus they may not be directly compared. Figure 14 is an 11-trace input, filtered version of the field data in Figure 13b. A passband of 6-15 km/sec with 21 slowness steers has been used, and a median filter with no semblance weighting has been applied. Figures 15 and 16 are also filtered versions of Figure 13b, but with 21- and 31-trace input gates, respectively. A comparison of Figures 14, 15 and 16 clearly illustrates the smearing effect of increasing the filter width. Figure 16, which used a 31-trace gate, shows a continuous arrival across the entire 5 km. The 11-trace gate in Figure 14 shows the same arrival, but it is broken at 53 and 56.5 km. In addition to the increase in event continuity, the level of background noise is further reduced as the trace gate widens. This is the result of zero-mean noise being more effectively estimated as the sampling increases.

Application of a semblance weighting term has the beneficial effect of further suppressing background noise, but it will also distort coherent signal in the passband in the case of crossing events. Distortion of coherent energy occurs because the semblance value drops when the desired signal undergoes interference from the crossing event. For the VSP geometry where crossing events are common, semblance weight-

ing results in generally undesirable distortion at all crossing points. Large offset data such as shown in Figure 13 are well-suited to semblance weighting because of the relative simplicity of the signal. Figures 17, 18 and 19 show the data of Figure 13 filtered with a semblance weighting term only. Input trace gates of 11, 21 and 31 were used for Figures 17, 18 and 19, respectively. Comparison of Figures 17 and 19 demonstrates the tendency of larger trace gates to suppress background noise more effectively. While a noise burst may appear coherent over 11 traces and produce a high semblance value, a longer trace gate could reduce the semblance value and more effective suppression would result.

Stoffa et al. (1981) pointed out that when weighting data by semblance, care must be taken to avoid distortion of the wavelet at regions of zero crossings. At zero crossings, the semblance value drops near zero, and multiplication by a raw semblance estimate will distort the pulse in these regions. Stoffa et al. (1981) propose a low-pass filtered version of the semblance estimate to eliminate the high frequency notch which causes pulse distortion. This approach, coupled with a threshold operator, was used to weight $\tau - p$ data to reduce aliasing effects. Kong et al. (1985) also use a similar $\tau - p$ domain approach to enhance and velocity-filter noisy seismic data. In Figures 17-19 a low-pass filter with cuts at 5 and 7 hz were applied to the semblance estimate before weighting. Comparison of the pulse shape in Figures 17-19 with the pulse shape in the raw data (Figure 15a and 15b) reveals good reproduction of the original wavelet.

Having examined the effects of median filtering and semblance weighting separately, we now demonstrate their concurrent application to OBH data. Figures 20, 21 and 22 show data that have been median filtered and semblance weighted with trace gates of 11, 21 and 31, respectively. As we have seen in the previous examples, the 31-trace gate produces the greatest noise reduction and trace-to-trace repeatability. The 11-trace gate passes signal coherent over shorter distances and results in a greater level of background noise. The 21-trace gate generally produces results more

similar to the 31-trace gate than the 11-trace examples. Concurrent application of median filtering and semblance weighting enforce a significant degree of trace-to-trace similarity. Care must be taken not to interpret signal which is nothing more than an artifact induced by the various non-linear operations. Figure 22 (for example) shows coherent signals over offsets up to twice the filter width in a region where the data is presumably incoherent. All arrivals later than 8 seconds are from very high amplitude water-born energy that did not appear coherent in the original data of Figure 13. This energy which now appears coherent has undergone a tremendous reduction in amplitude relative to its unfiltered state in Figure 13. Artifacts such as these should appear as laterally discontinuous arrivals of widths on the order of the filter width. Events which persist over many filter widths such as the event at 4.0 seconds in Figure 13 may be reliably interpreted as signal.

Conclusions

The extension of traditional single-direction median filters to velocity (semblance)-guided median filters greatly expands the utility of this proven and effective filtering method. We have demonstrated the effectiveness of this approach as both a signal enhancer on large offset refraction data and a velocity filter on VSP data. Marine refraction data acquired with fixed ocean bottom hydrophones (eg., Figure 13) is especially suited for this type of filter. Travel time picking of such data is difficult due to the low signal-to-noise ratios characteristic of large offset pre-stack data. Excellent source repeatability of large airgun arrays and dense shot spacing combine to allow velocity estimators to perform well. This in turn enables the median filter to enhance the estimated signal, resulting in high signal to ratios. Travel time picking of the filtered data (eg., Figures 14-21) is far more reliable. Wavefield imaging techniques such as migration and $\tau - p$ inversions also benefit by using the enhanced data.

VSP wavefield separation may be achieved more conveniently with a semblance-guided median filter than with the traditional method of travel time picking, wavefield

alignment and fixed slowness median filtering. Some error is incurred during the velocity estimation step of our approach and therefore the traditional method should perform better for perfectly picked and aligned data. However, our field data examples show that our approach performs quite well with a simple semblance velocity estimator, indicating that the velocity estimator works well for realistic conditions. Offset VSP data is often not composed of the linear arrivals we assume when we steer over linear trajectories. This may be accomodated in our approach by steering over parabolic or hyperbolic trajectories which better approximate the kinematics of the events which are estimated. Events which are too weak to pick and align can not be directly enhanced with traditional methods of median filtering. Our method allows the enhancement of such events by letting the velocity estimator track weak arrivals and the median filter operate along the appropriate trajectories.

We could improve our implementation by replacing our semblance velocity estimator with a higher resolution estimator. Velocity estimators which are designed to perform well on short arrays should prove especially useful, since efforts to control lateral smearing enforce limited array apertures. Although we found a pure median filter to yield satisfactory results on large offset OBH data, use of the alpha-trimmed mean may be more appropriate for some very low signal-to-noise data.

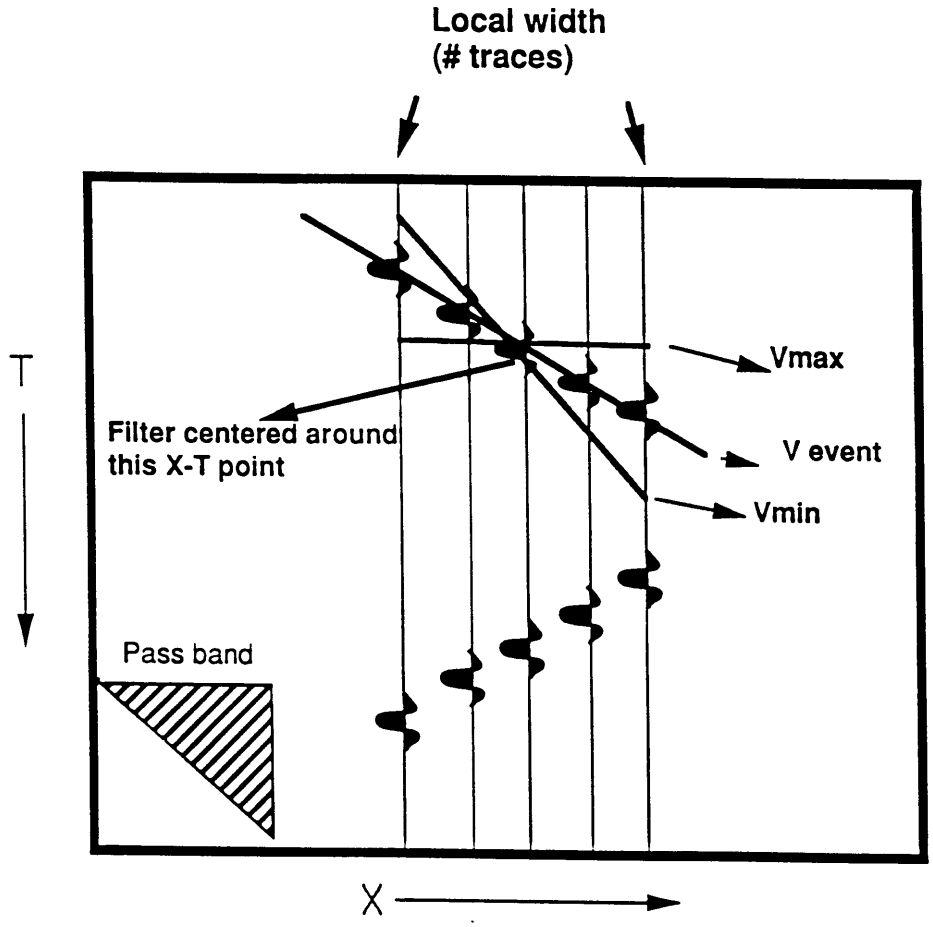

Step 1:

Estimate slowness (trajectory) of signal. We use semblance although a variety of techniques are available.

Step2:

Replace central data point with the median value (or trimmed mean) of the data set collected along the preferred trajectory.

Figure 1. Diagram illustrating structure of semblance guided median filter. Input to the filter consists of a local set of traces centered about the trace to be filtered. A slowness passband is selected and semblance computed over linear moveouts within the slowness passband. A median filter is applied at the slowness at which the peak semblance was computed.

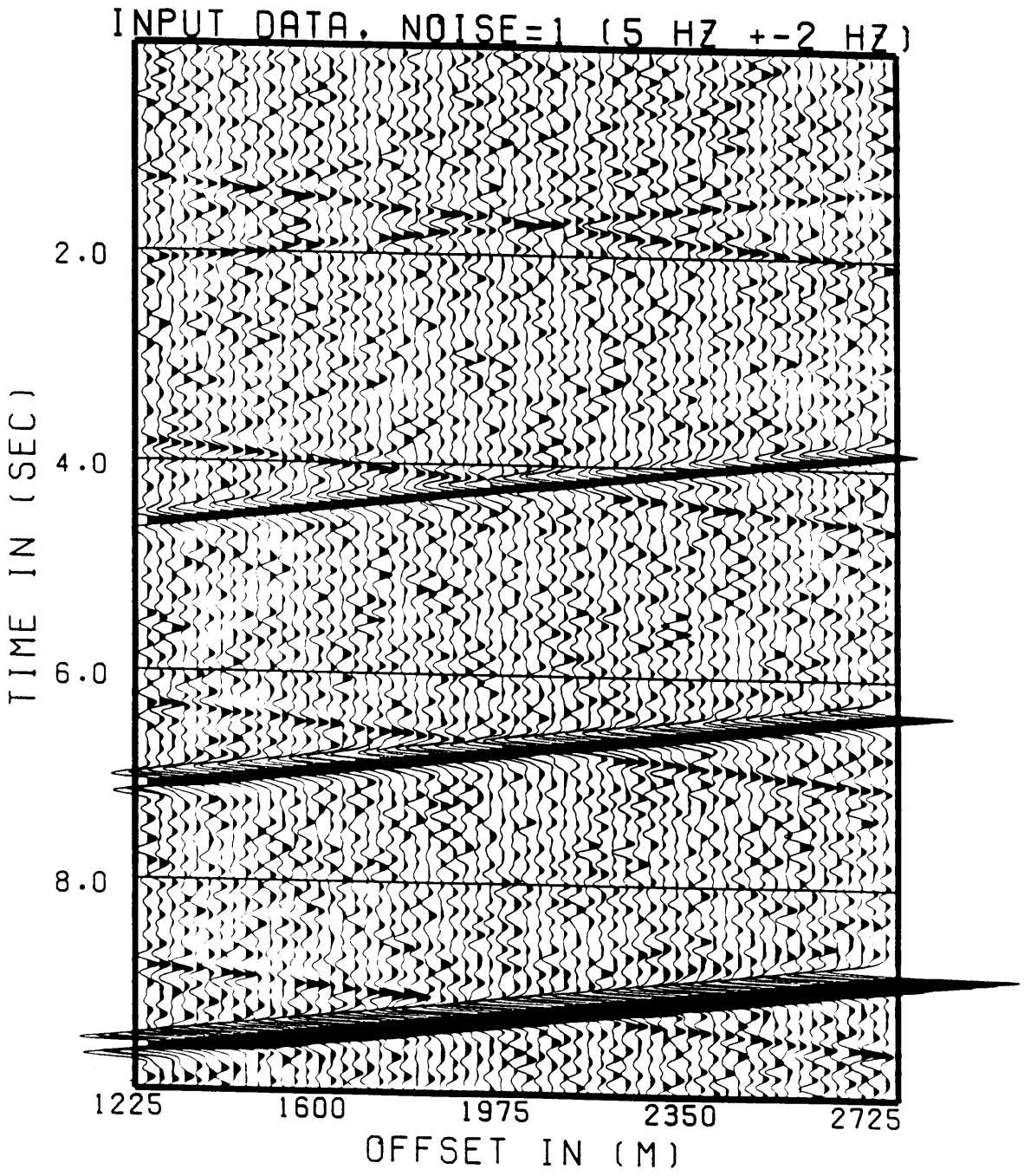

Figure 2. Synthetic data used to evaluate the semblance guided median filter. The data consist of four sets of linear intersecting events having apparent velocities of $\pm 2000 m/sec$. The ratio of the amplitudes of the downgoing event to the upgoing event are 1:1 in the first set, 4:1 in the second set, 8:1 in the third set and 16:1 in the fourth set. The signal is a 5 hz Ricker wavelet and random bandlimited background noise also centered about 5 hz is added to the data. The ratio of this background noise to the downgoing arrival is 1:1.

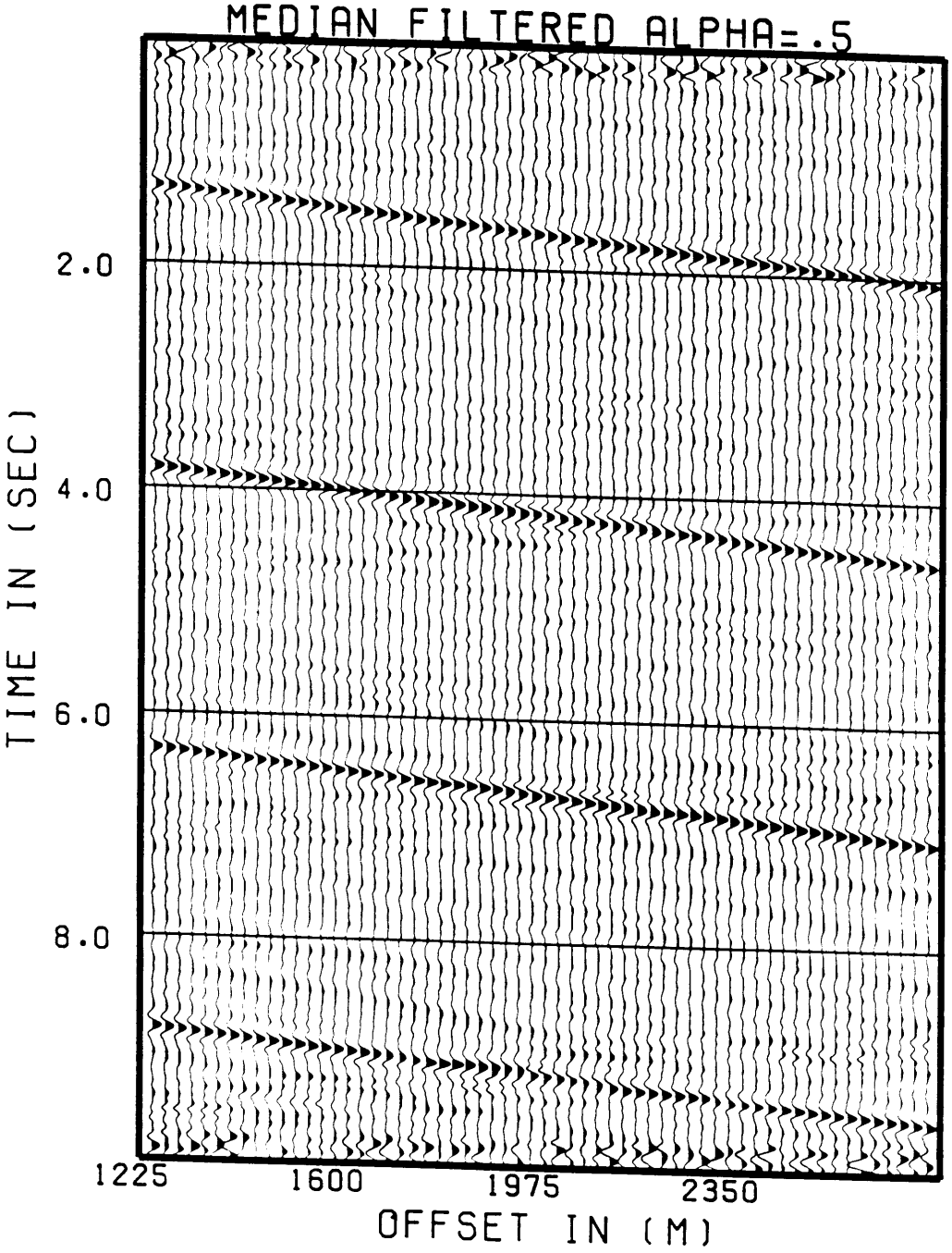

Figure 3. Filtered version of the data in Figure 2 with a 21 trace gate, a 1000 to 3000 m/sec passband, 21 slowness steers and a pure median operator. The slowness passband is centered (in velocity) about the downgoing arrival and results in both rejection of background noise and rejection of the upgoing arrival.

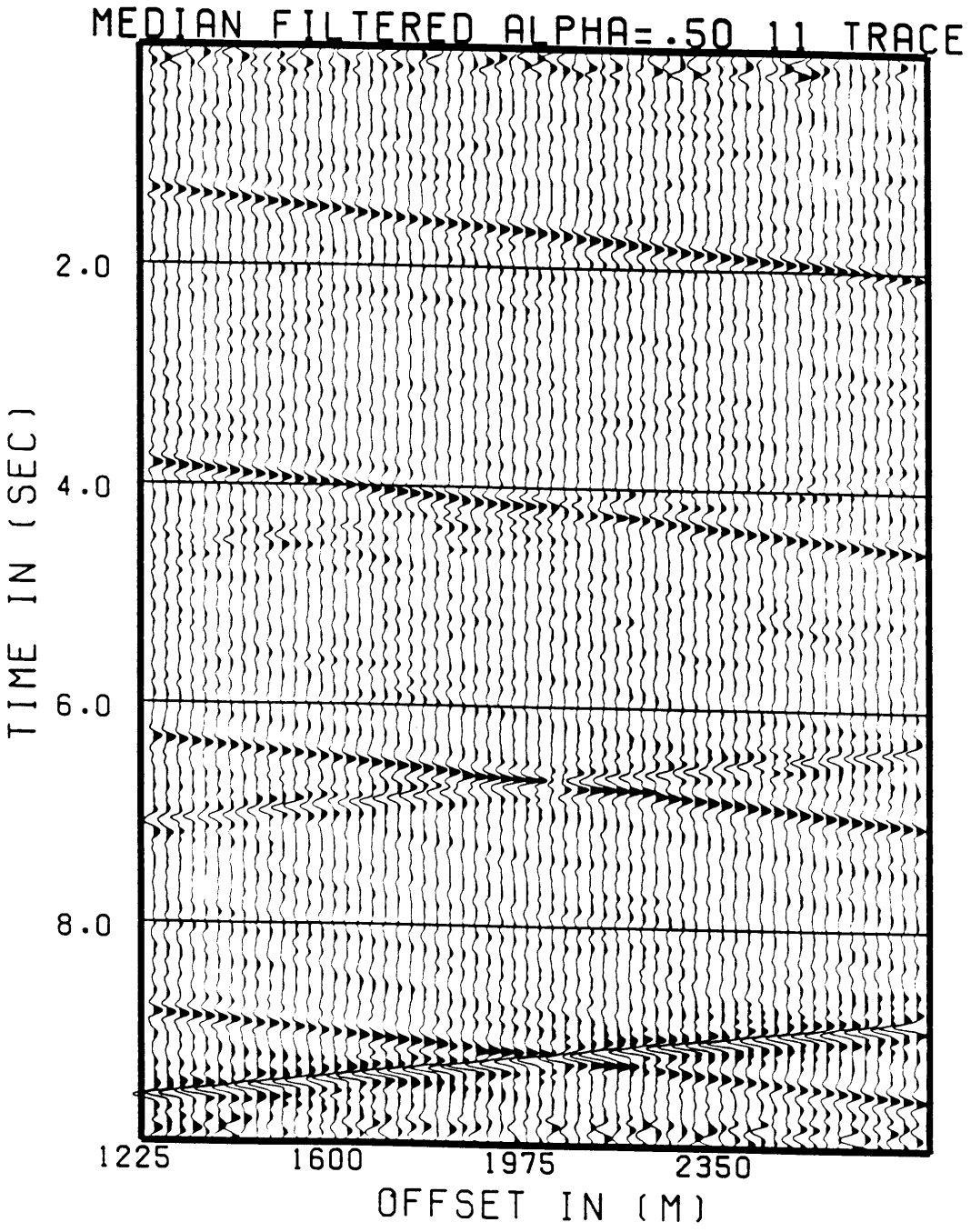

Figure 4. Same as Figure 3 but with an 11 trace gate instead of a 21 trace gate. The smaller trace gate results in both increased levels of background noise and poor rejection of the upgoing event for sets three and four.

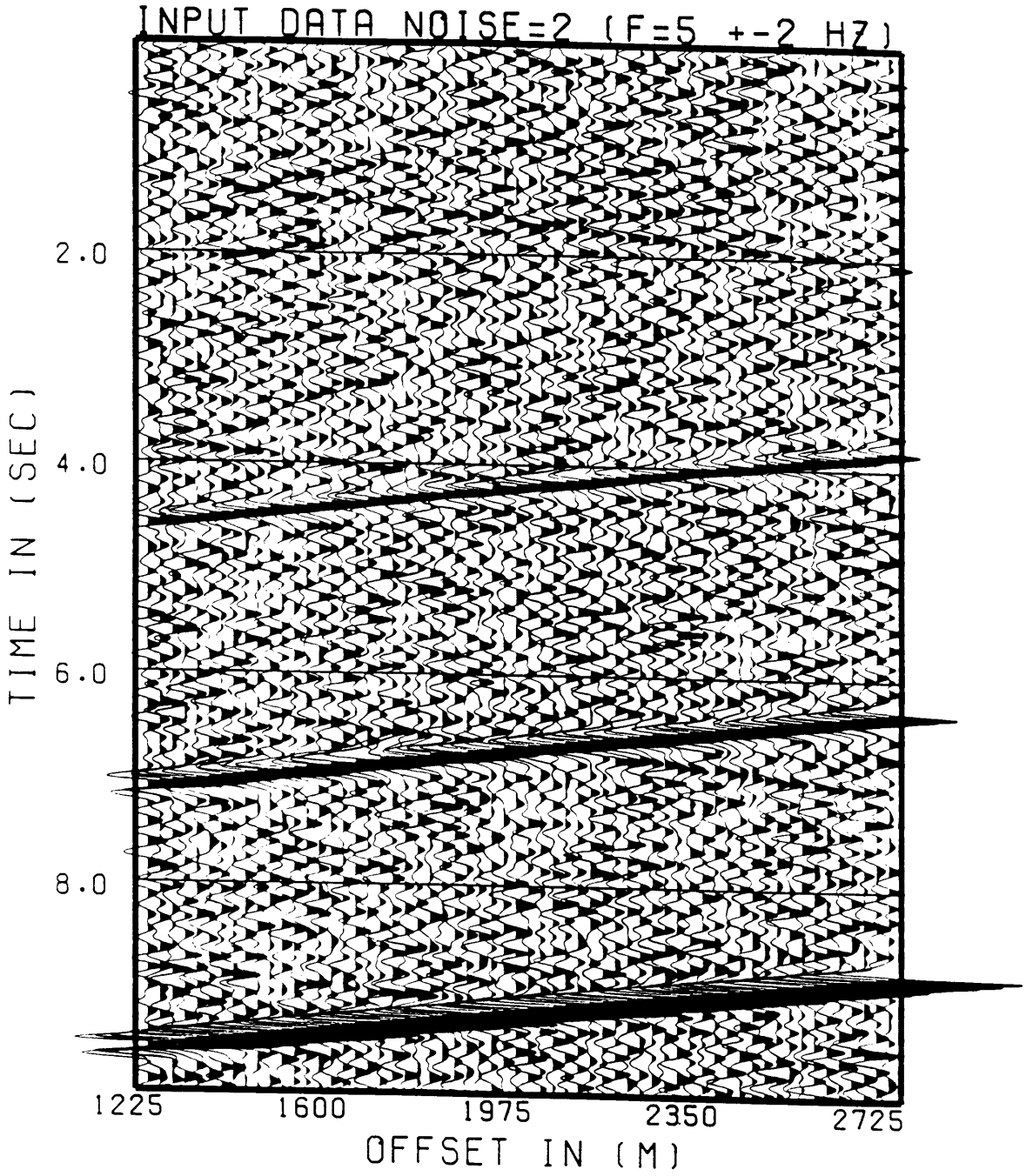

Figure 5. Synthetic data of Figure 2 but with double the level of background noise. The ratio of the downgoing arrival to background noise is 1:2 (signal/noise = 0.5).

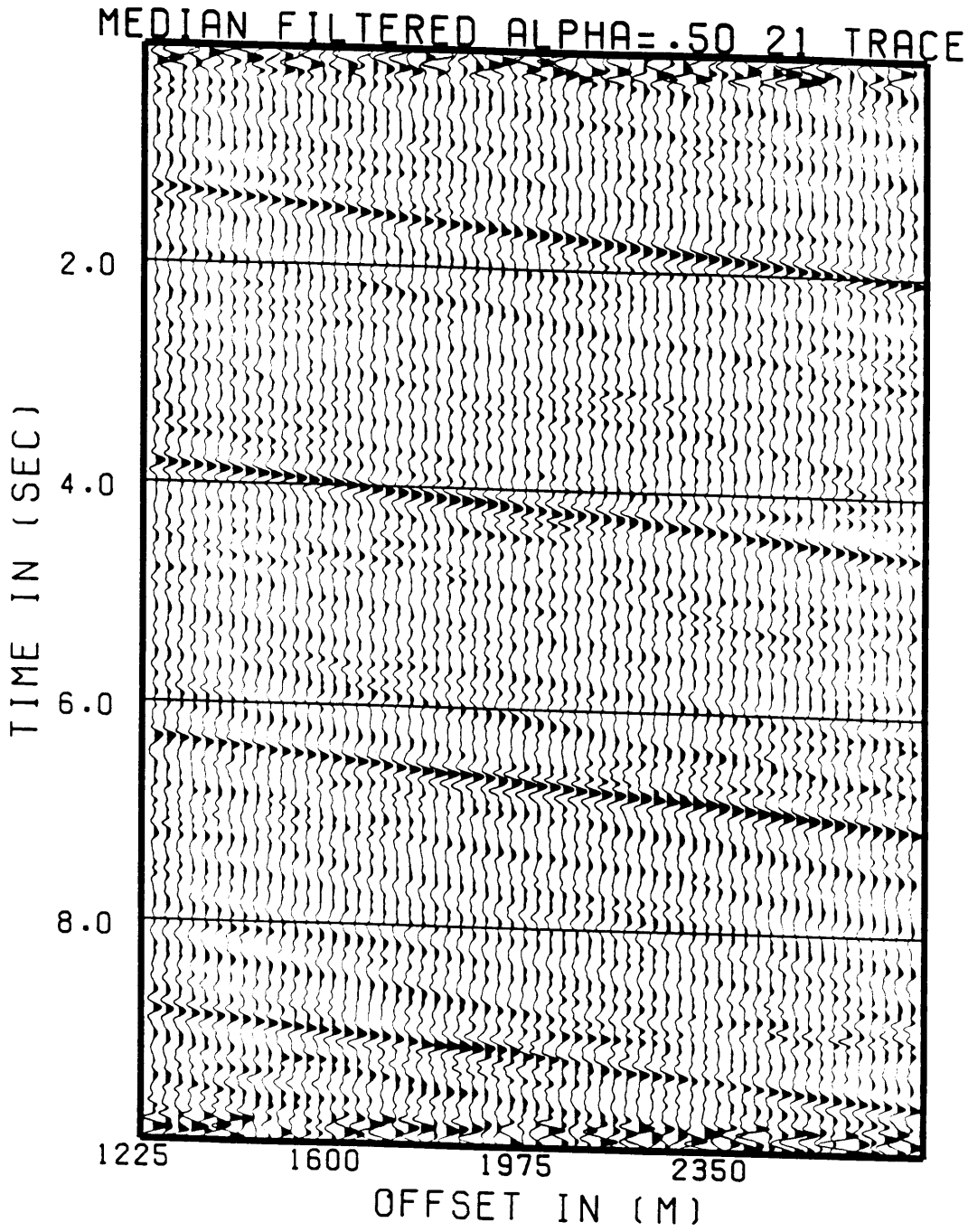

Figure 6. Filtered version of the data in Figure 5 (signal/noise=0.5) with a 21 trace gate, 1000-3000 m/sec passband, 21 slowness steers and a pure median operator. The increase in random background noise results in increased levels of this noise being passed by the filter when compared to data with half the background noise level filtered with identical parameters (Figure 3).

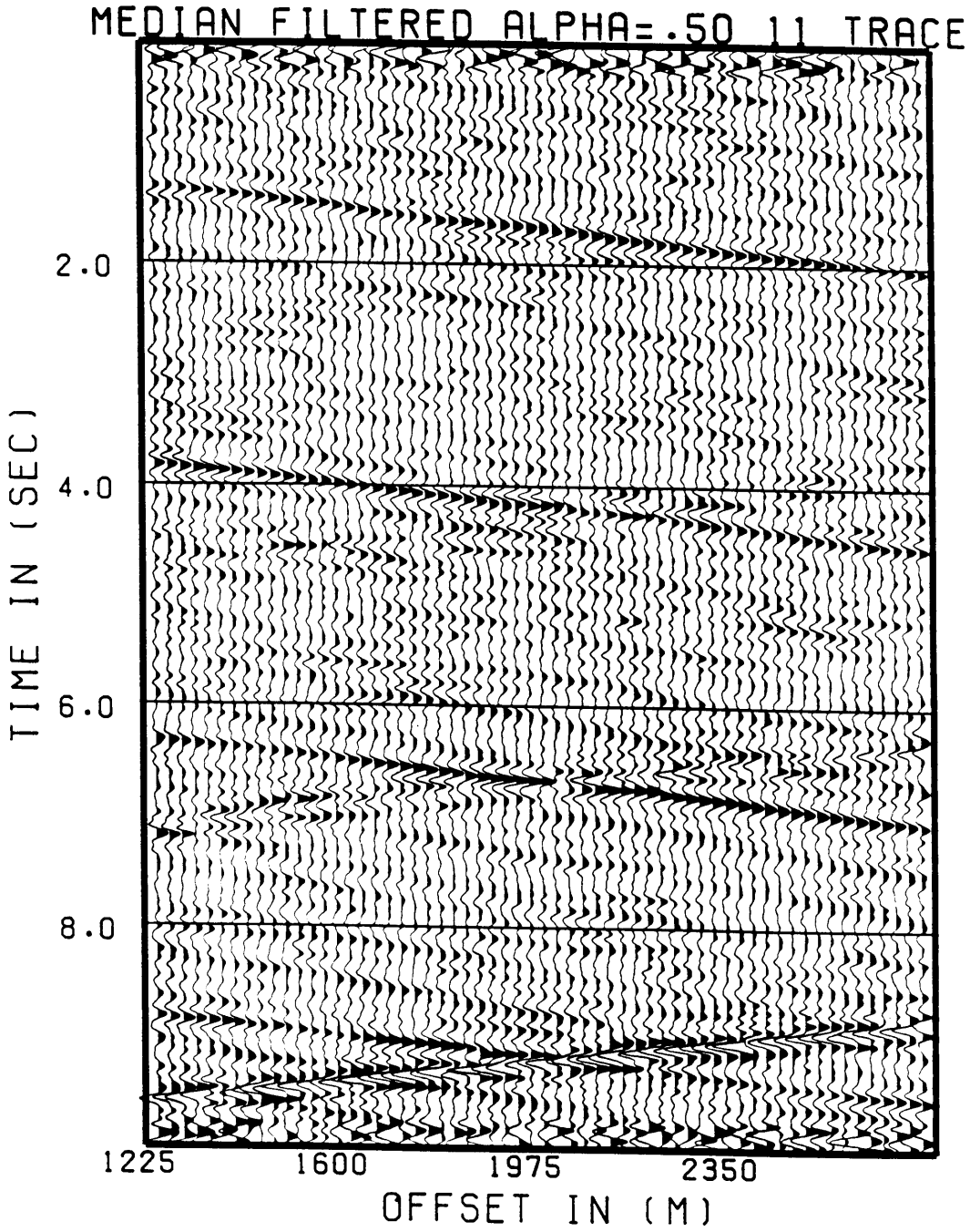

Figure 7. Same as Figure 6 but with an 11 trace gate instead of a 21 trace gate. Poorer signal estimation and increased levels of background noise result from reduction in gate size.

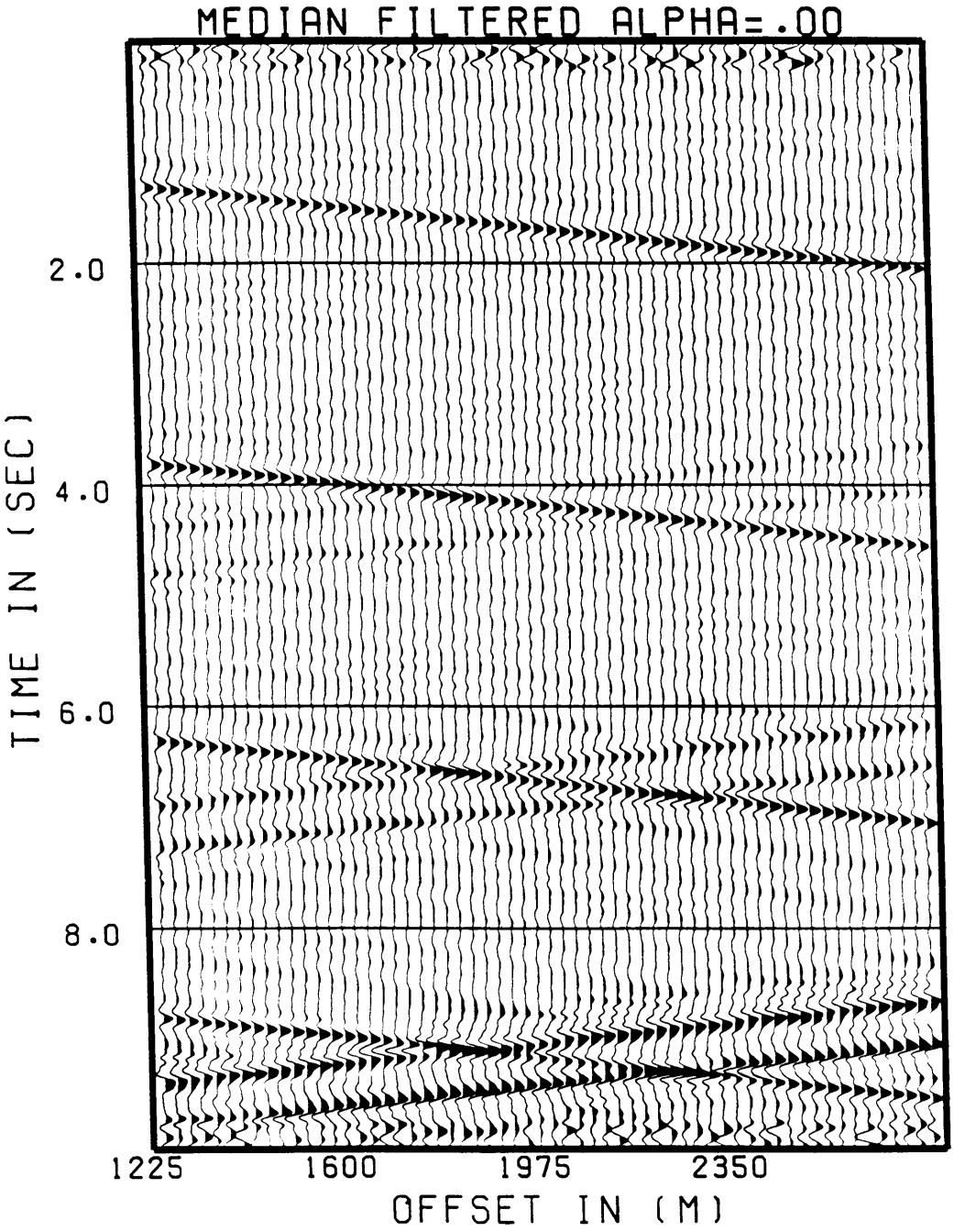

Figure 8. Same as Figure 3 but with a simple mean used in place of the median operator. Little difference is seen in the background noise levels between the median (Figure 3) and the mean (this Figure) but poor rejection of the upgoing event is achieved with the mean.

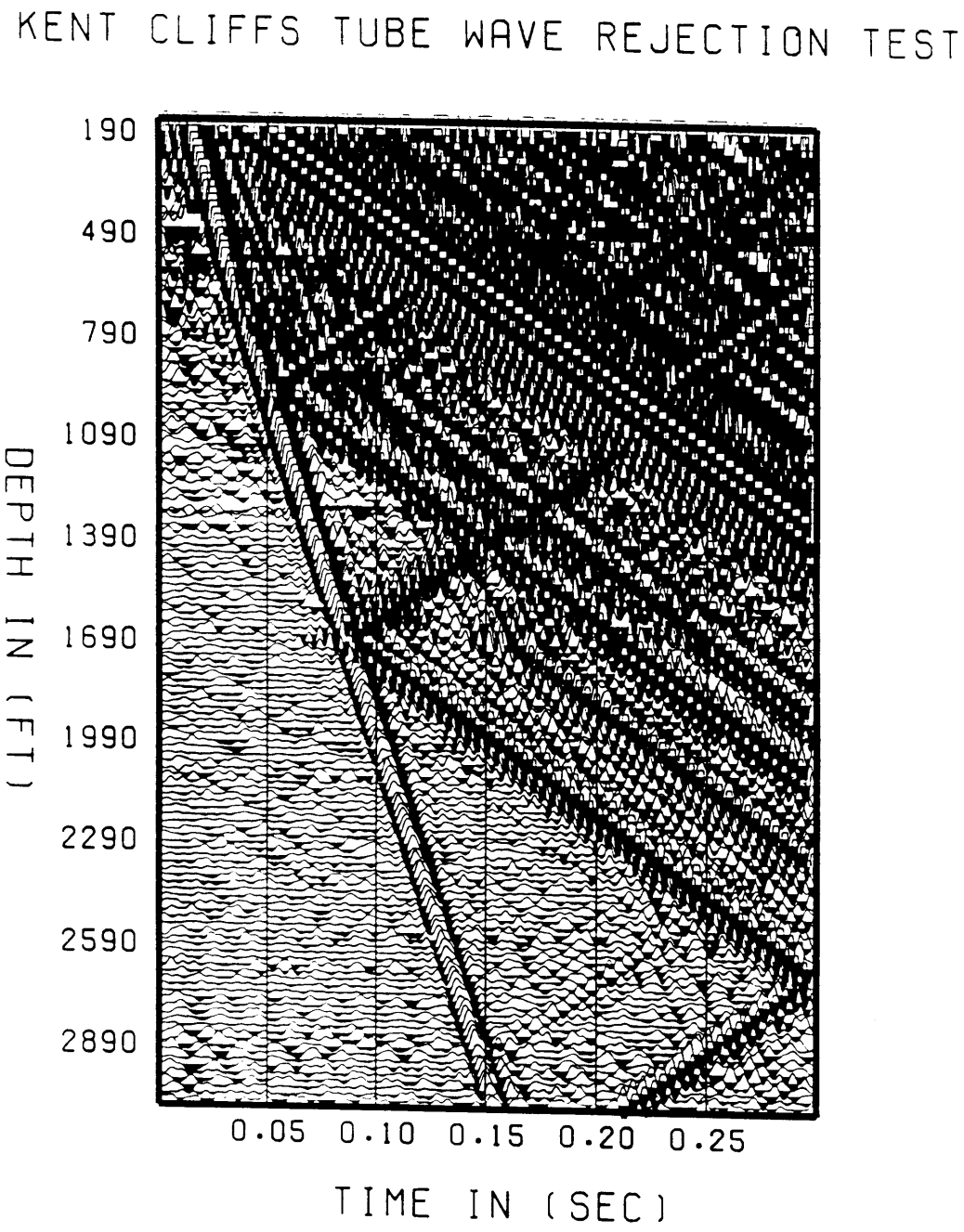

Figure 9a. Short offset hydrophone VSP data from Kent Cliffs , New York. The data show very large amplitude tube waves originating at the intersection of fractures with the borehole. We seek to suppress the tube waves and enhance the downgoing compressional and shear arrivals with the semblance guided median filter.

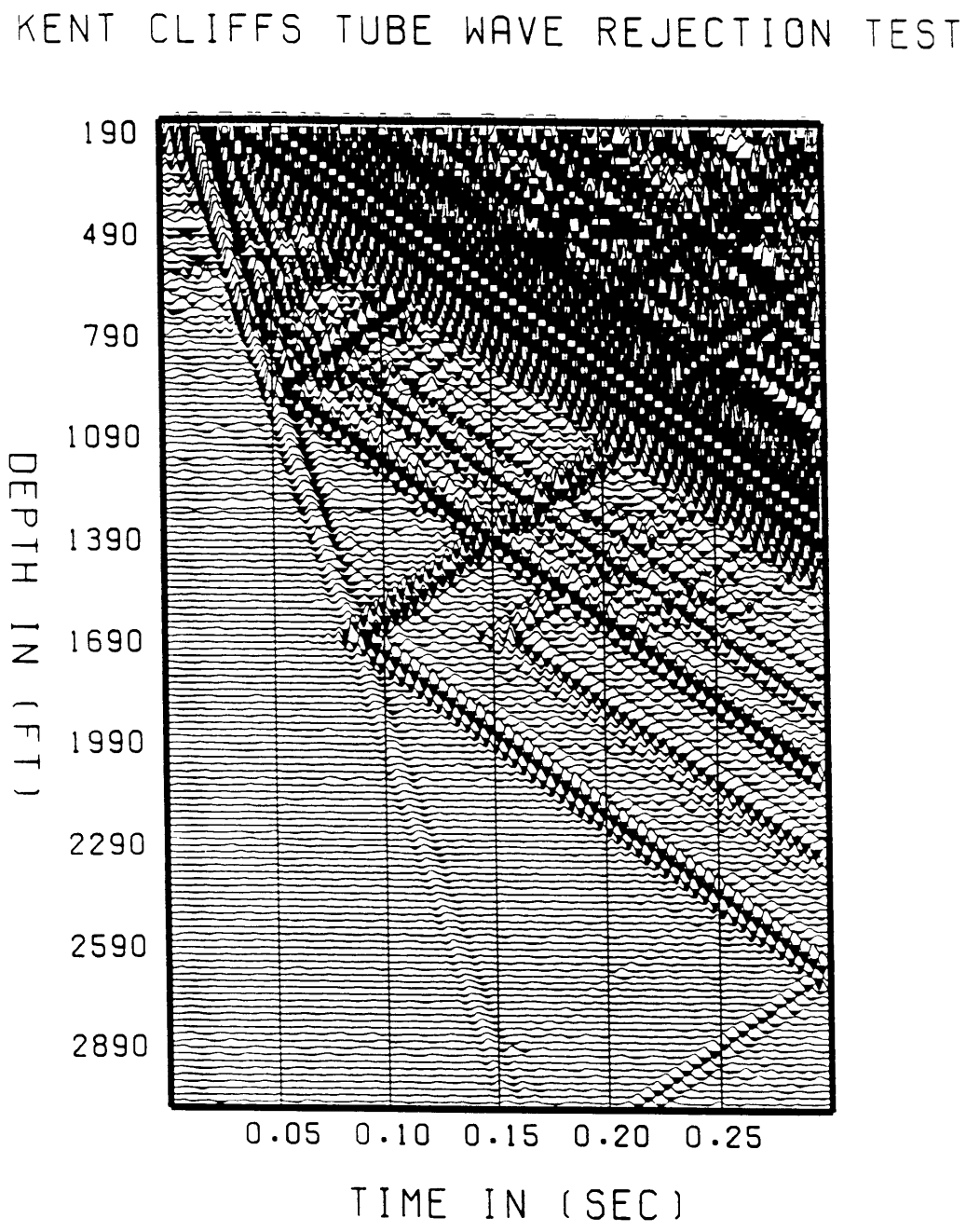

Figure 9b. Same as 9a but plotted with 0.25 the scale factor to illustrate the true amplitude of the tube waves.

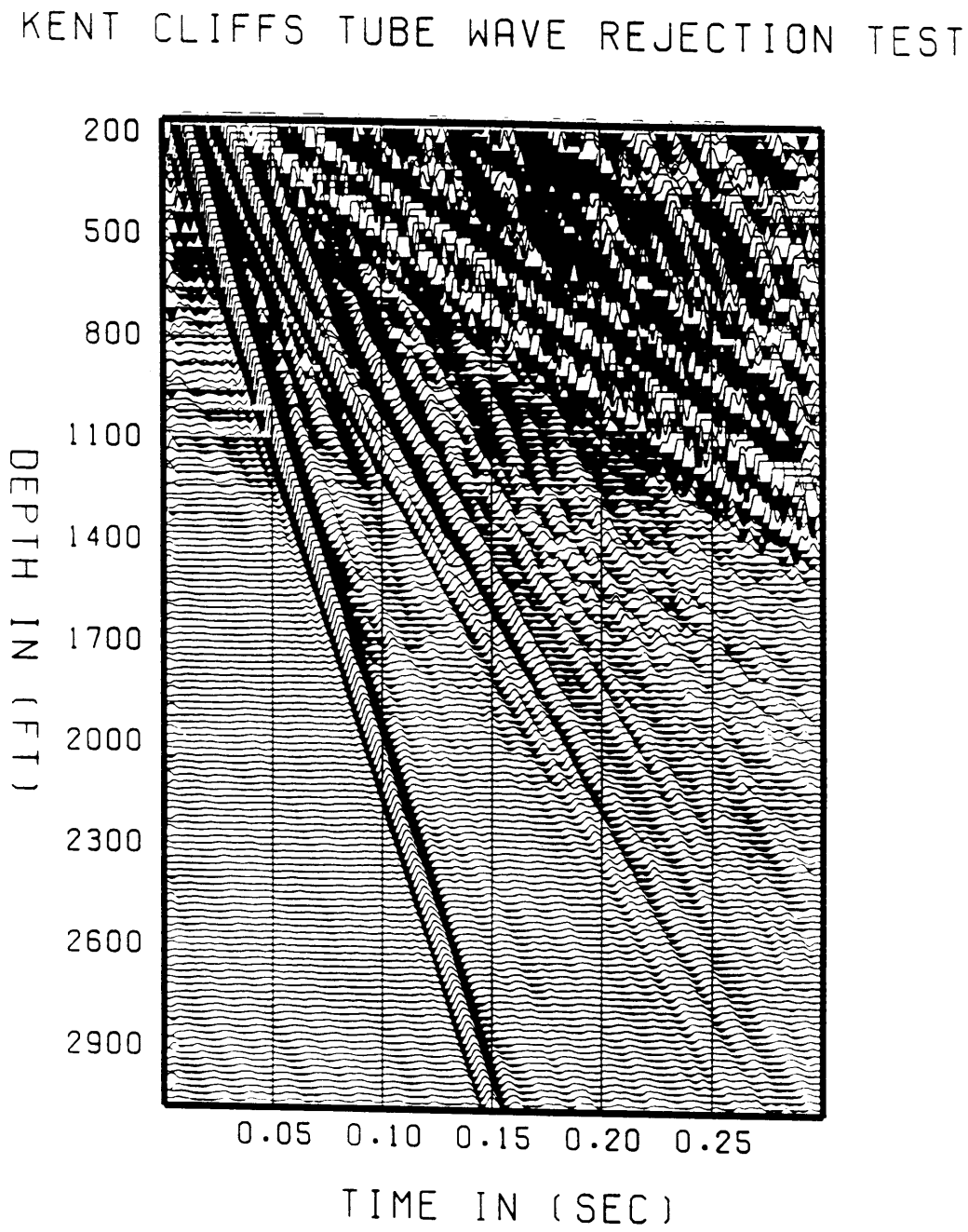

Figure 10. Filtered version of the data in Figure 9 with a 31 trace gate, 7.62-3.35 km/sec passband, 25 slowness steers and a pure median operator. A clear shear arrival is now visible and the fracture generated tube waves are eliminated and the tube waves originating at the wellhead are reduced in amplitude.

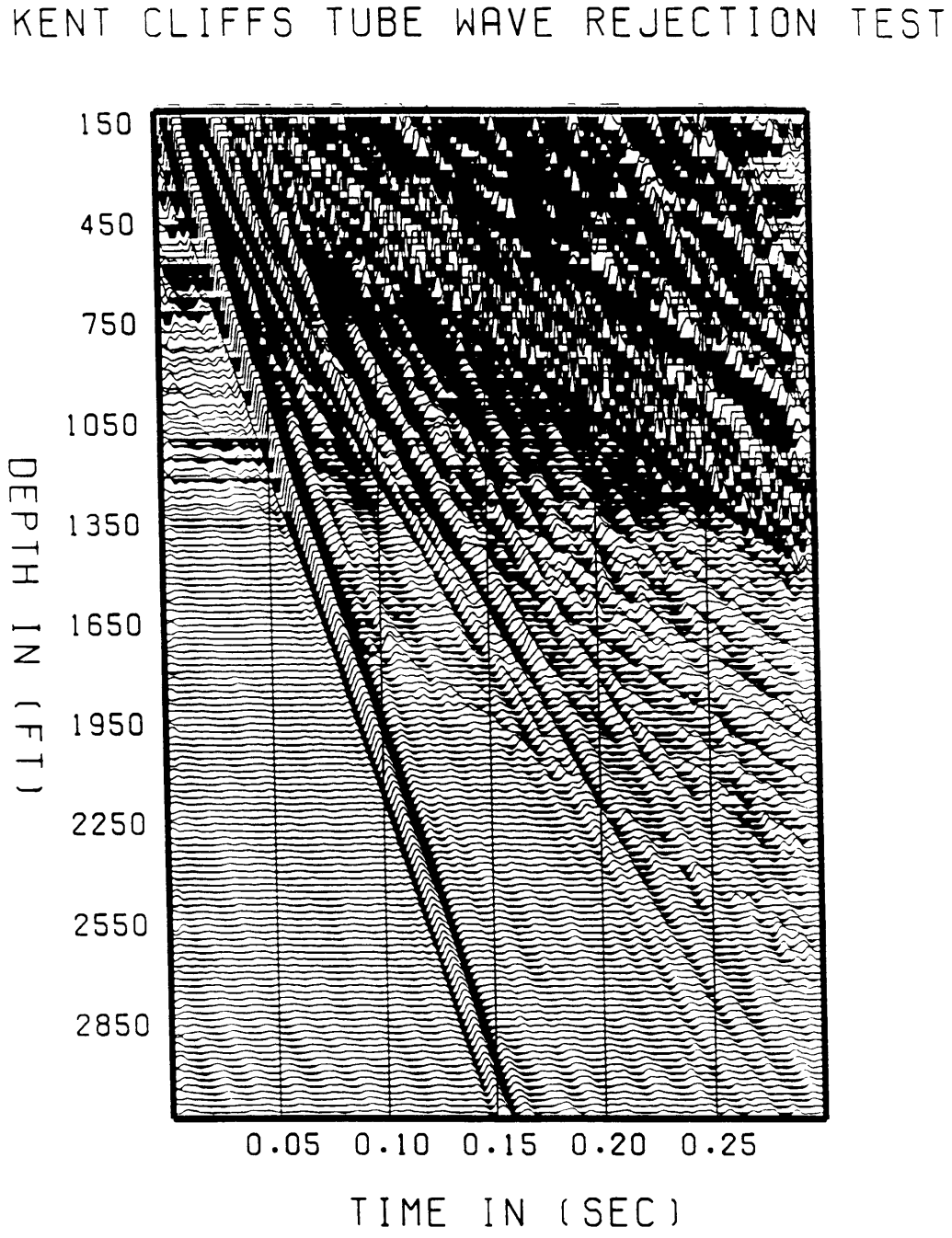

Figure 11. Same as Figure 10 but with a 21 trace gate. The reduction in gate size results in more tube wave energy leaking into the filtered section.

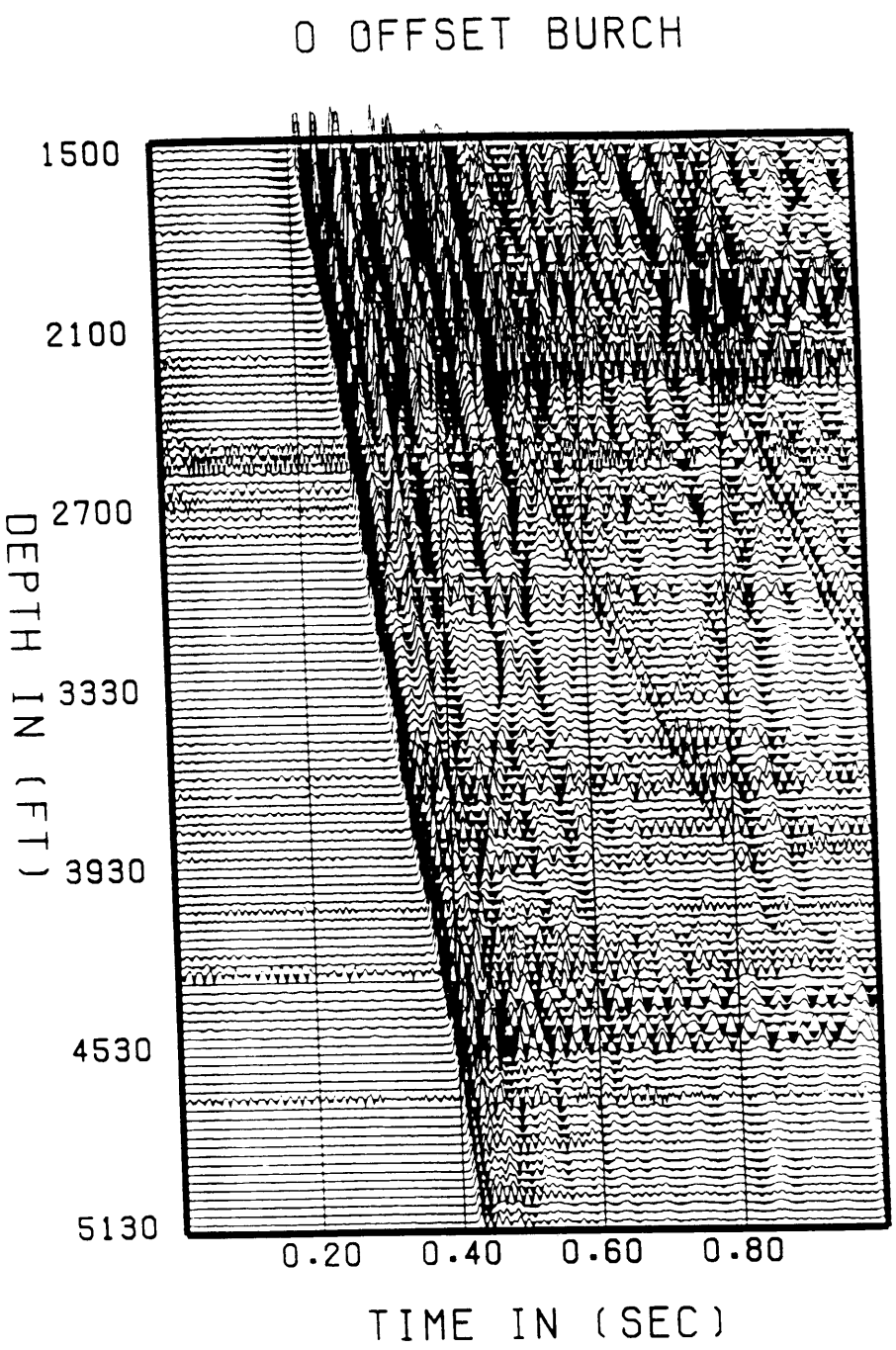

Figure 12a. Zero offset vertical component VSP from Traverse City, Michigan. The data contain reflected upgoing arrivals and tube waves as well as background and receiver generated noise such as ringing from geophone clamping difficulties.

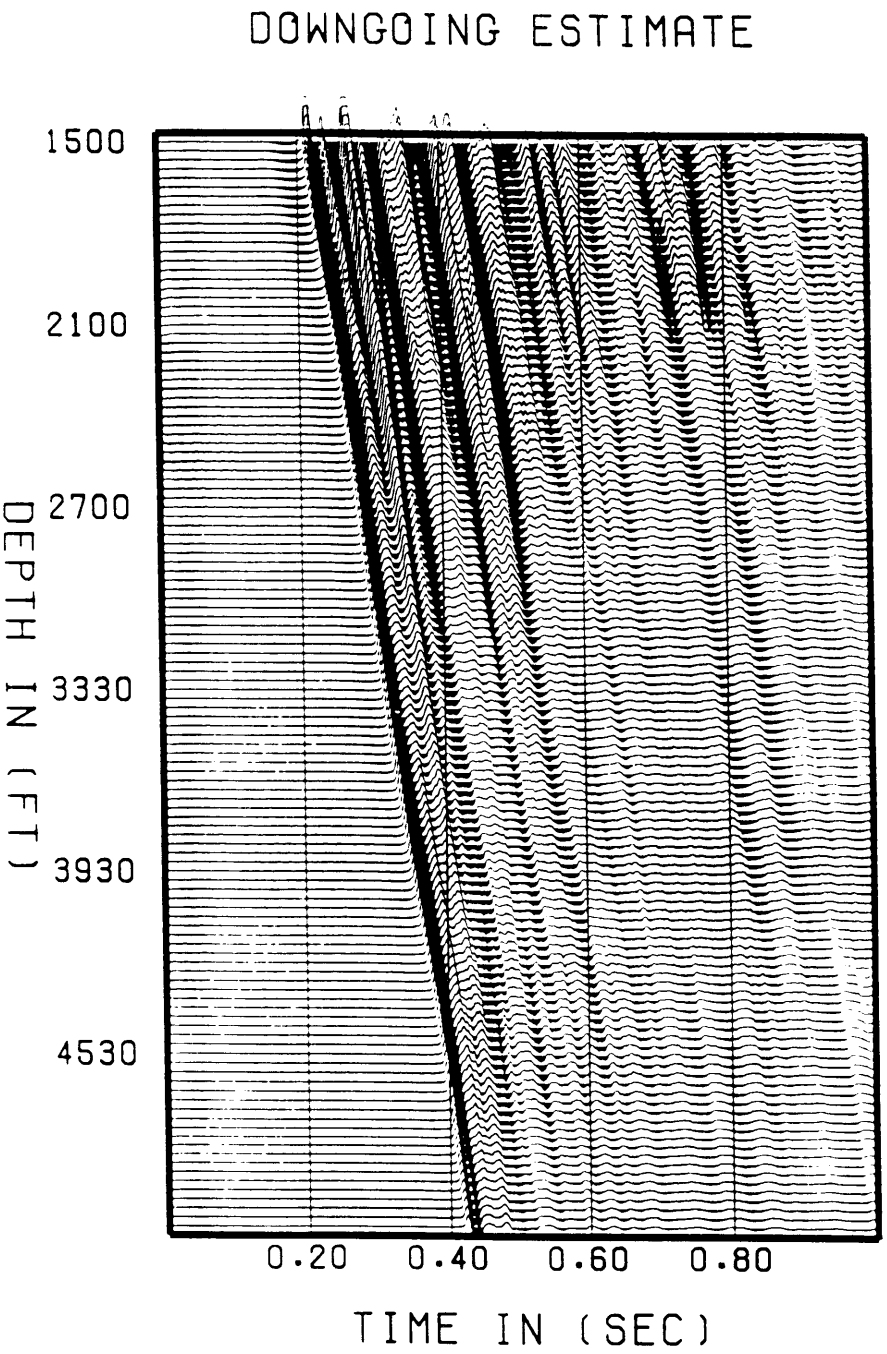

Figure 12b. Estimate of the downgoing wavefield from the semblance guided median filter. Filter parameters include a 21 trace gate, 4.5 to 7.6 km/sec passband, 21 slowness steers and a pure median operator.

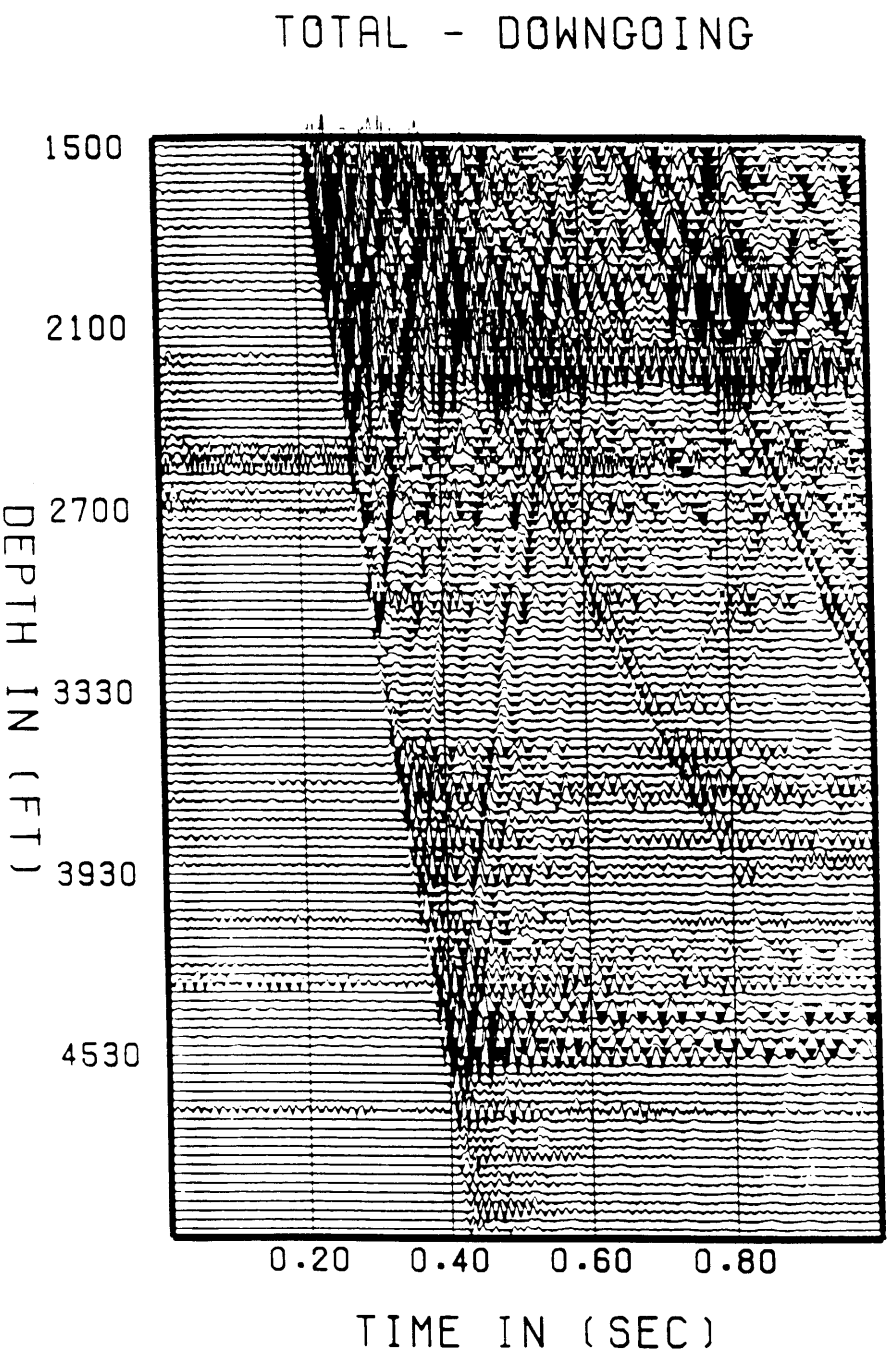

Figure 12c. Upgoing wavefield estimate from subtracting the downgoing estimate (Figure 12b) from the original data (Figure 12a). Note the large amplitude upgoing event at 1533 m (4600 ft). Tube waves and background noise remain in the section when only the downgoing arrivals are subtracted.

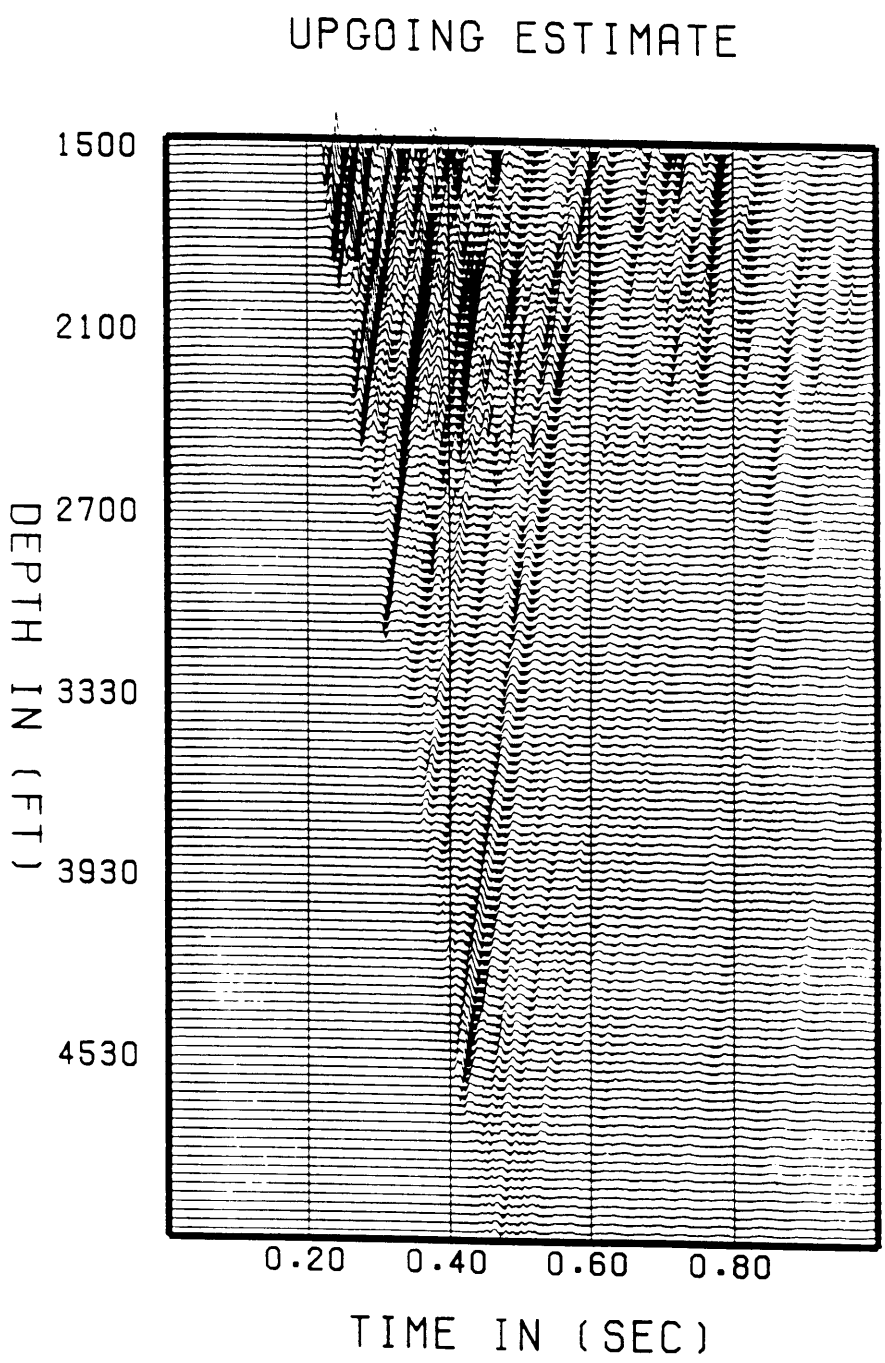

Figure 12d. Upgoing wavefield estimate from the semblance guided median filter using parameters of a 21 trace gate, -4.5to -7.5 km/sec passband, 21 slowness steers and a pure median operator. Note the elimination of tube waves and background noise when compared to a simple subtraction of the downgoing wavefield (Figure 12c).

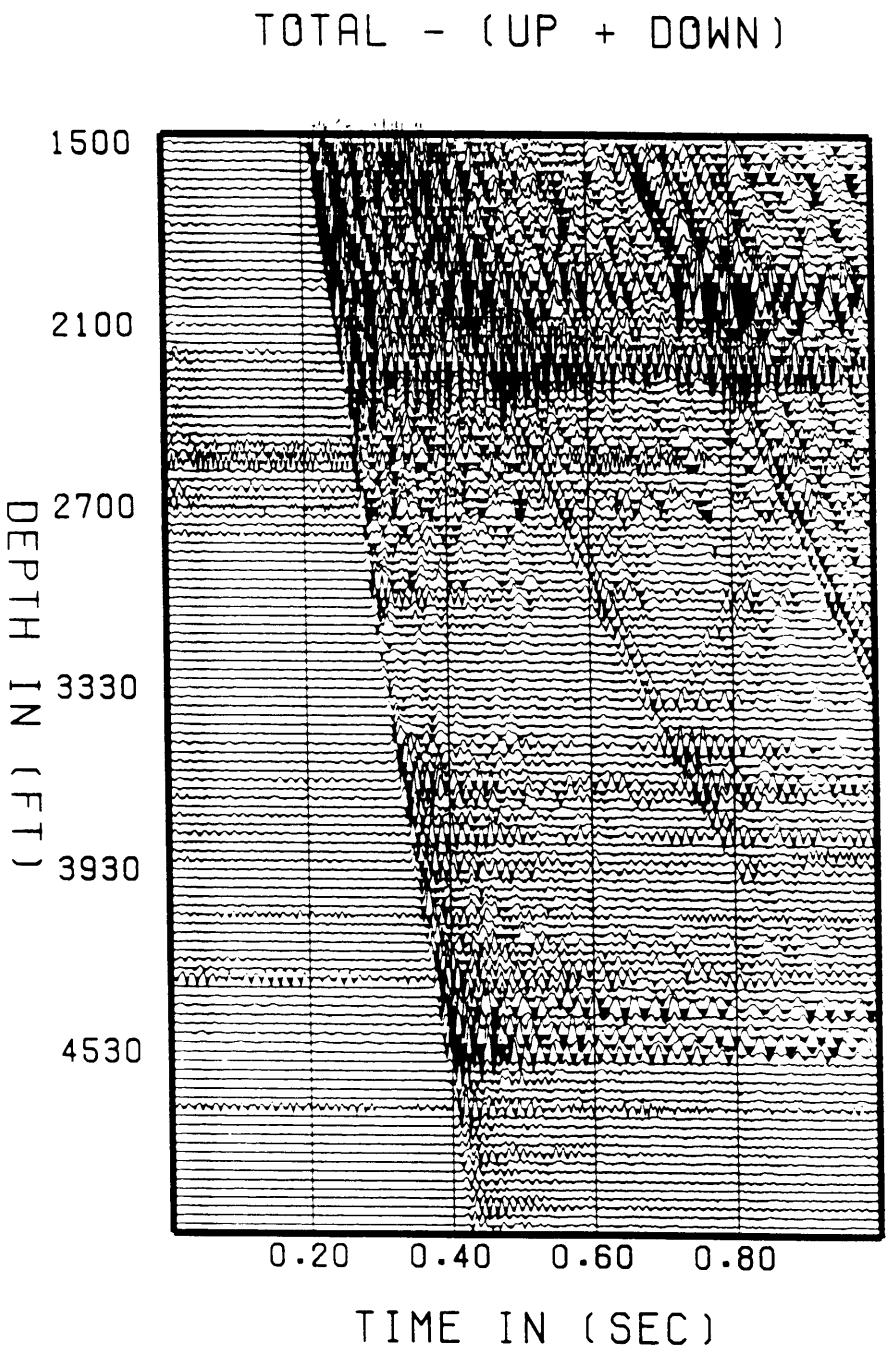

Figure 12e. A section of "pure noise" obtained by subtracting our downgoing (Figure 12b) and upgoing (Figure 12d) wavefield estimates. The "noise" encompasses all energy which does not correspond to coherent arrivals within the passbands. In this case the noise consists primarily of tube waves and ringing from geophone clamping problems.

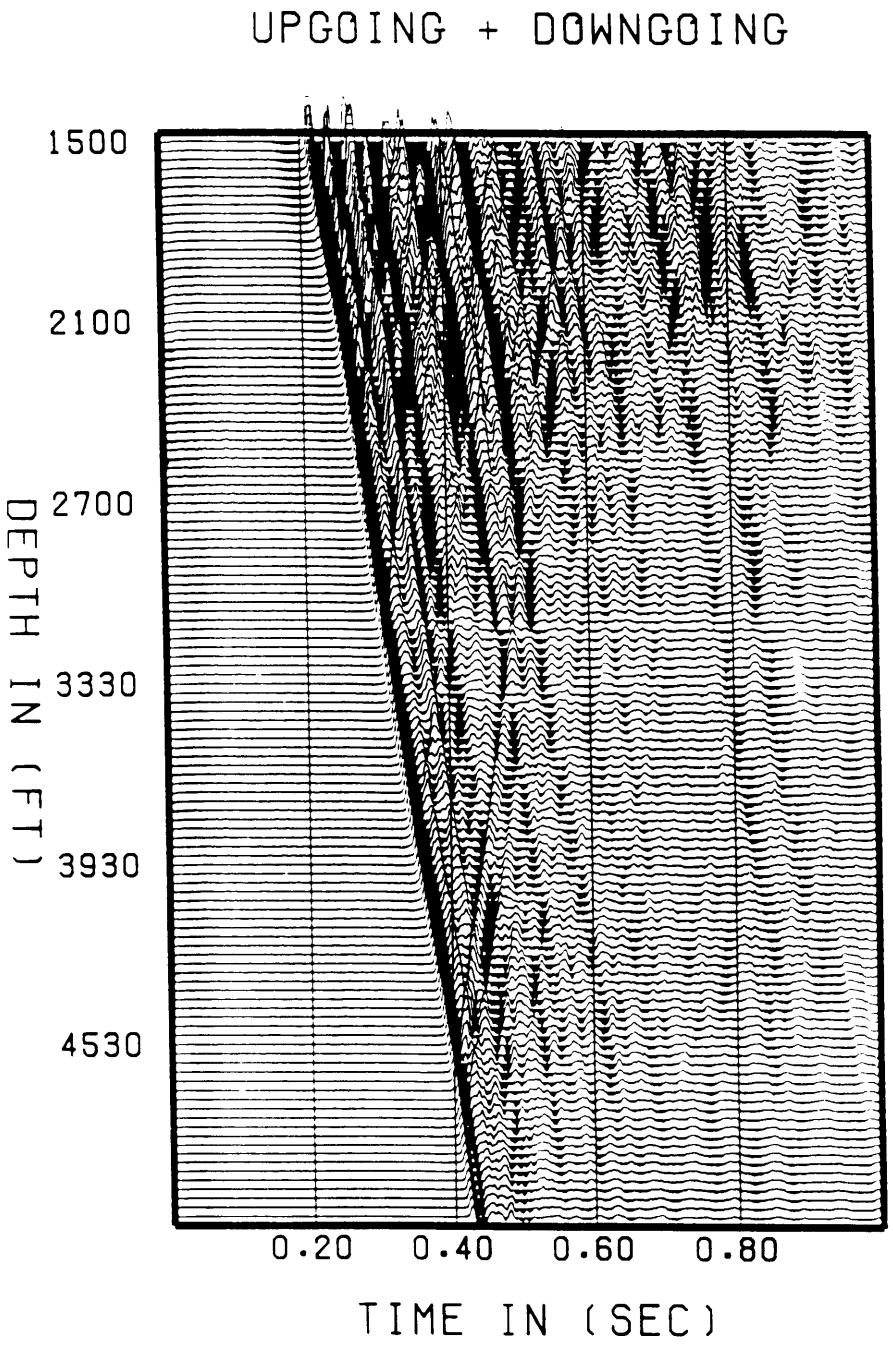

Figure 12f. A section of "pure signal" from summing our separate estimates of the downgoing (Figure 12b) and upgoing (Figure 12d) wavefields. Note the clarity of this section when compared to the raw data in Figure 12a.

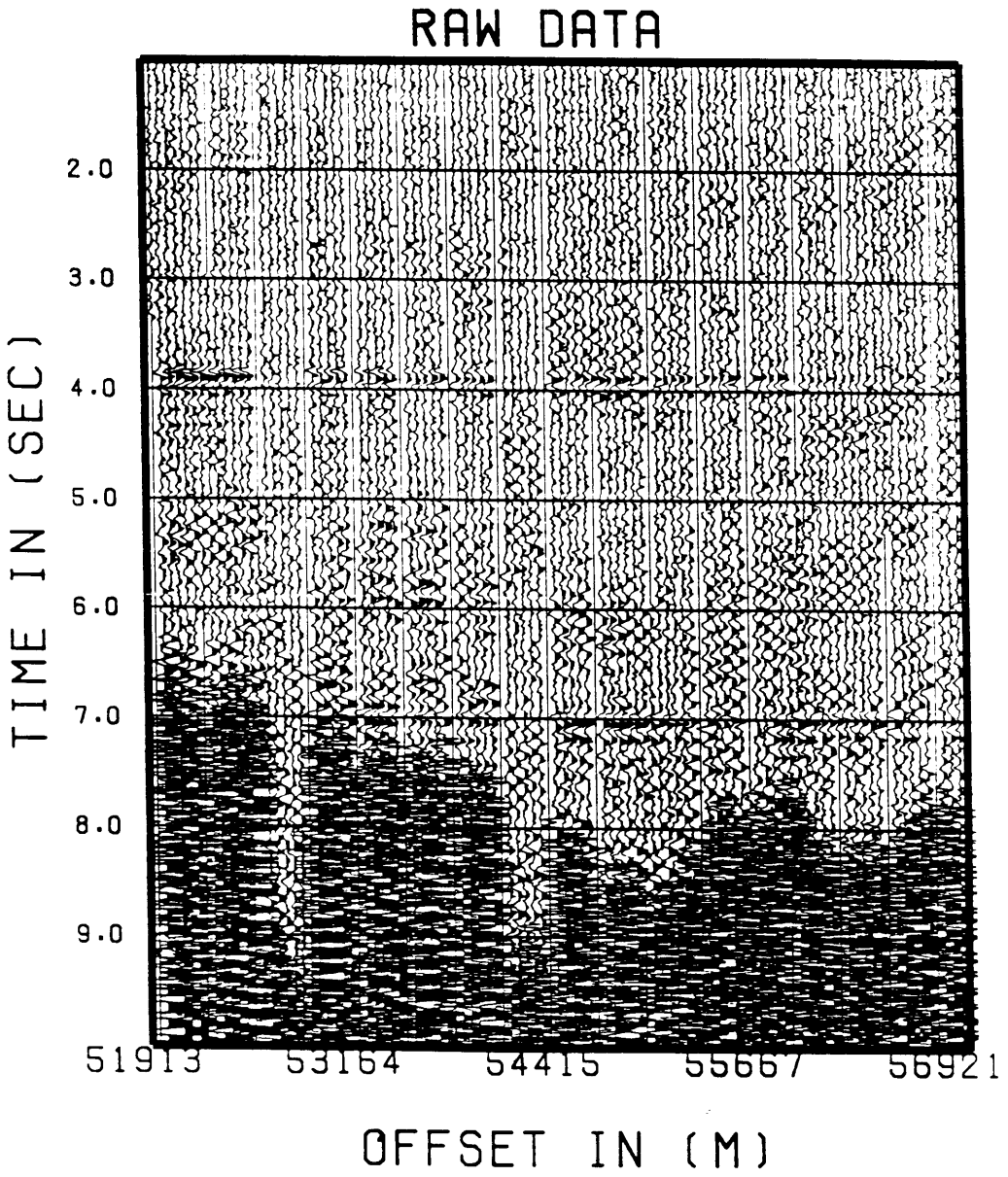

Figure 13a. Five kilometers of raw large offset data acquired by an Ocean Bottom Hydrophone recording the airgun array of a seismic vessel firing every 0.05 km. The primary event arrives at approximately 4 seconds and a water column multiple at around 7 seconds. The large amplitude incoherent energy below 8 seconds is energy from the previous shot reverberating throughout the water column.

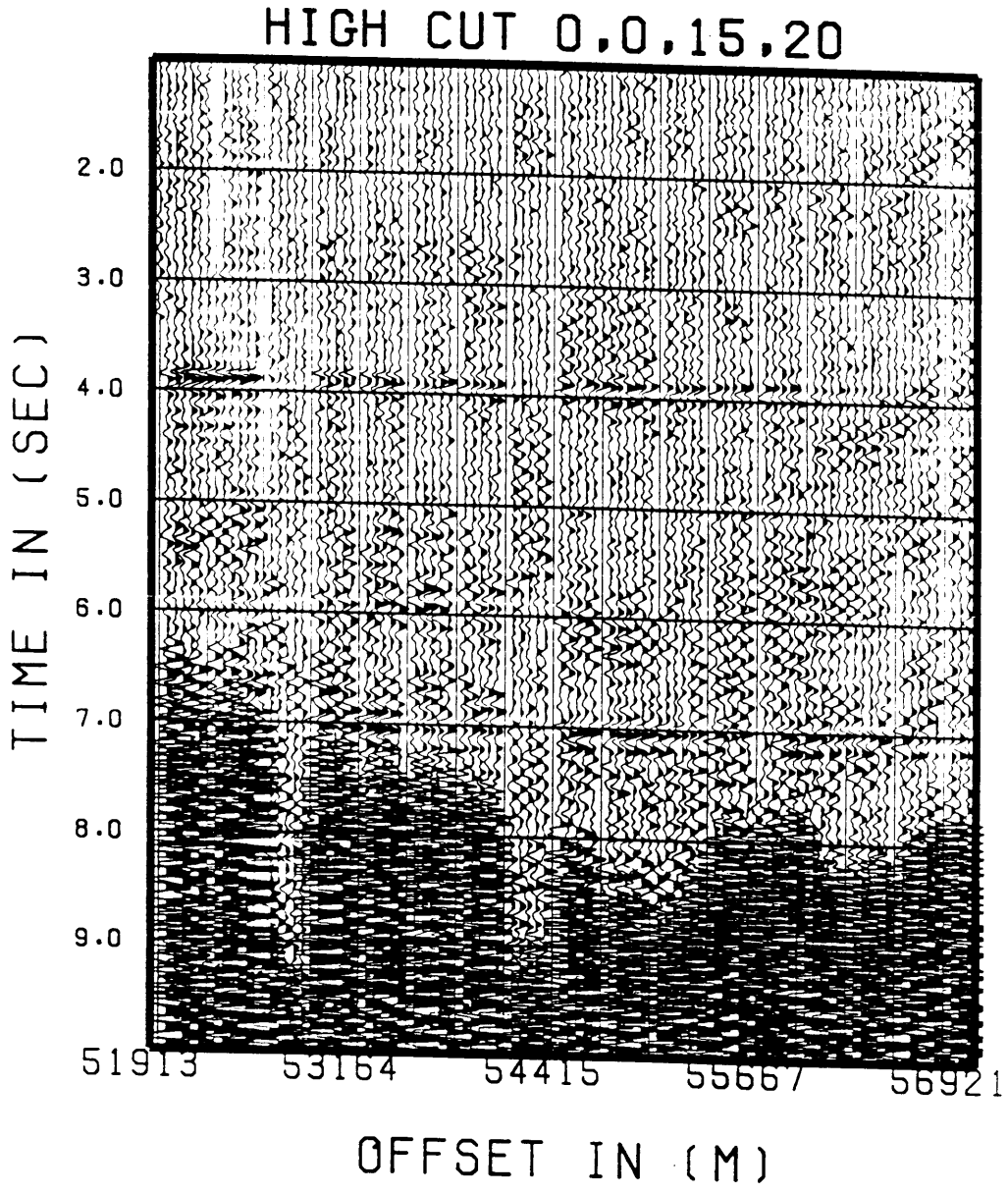

Figure 13b. Same as Figure 13a but filtered with a smoothed trapezoidal bandpass filter defined at 1, 4, 20, 25 hz.

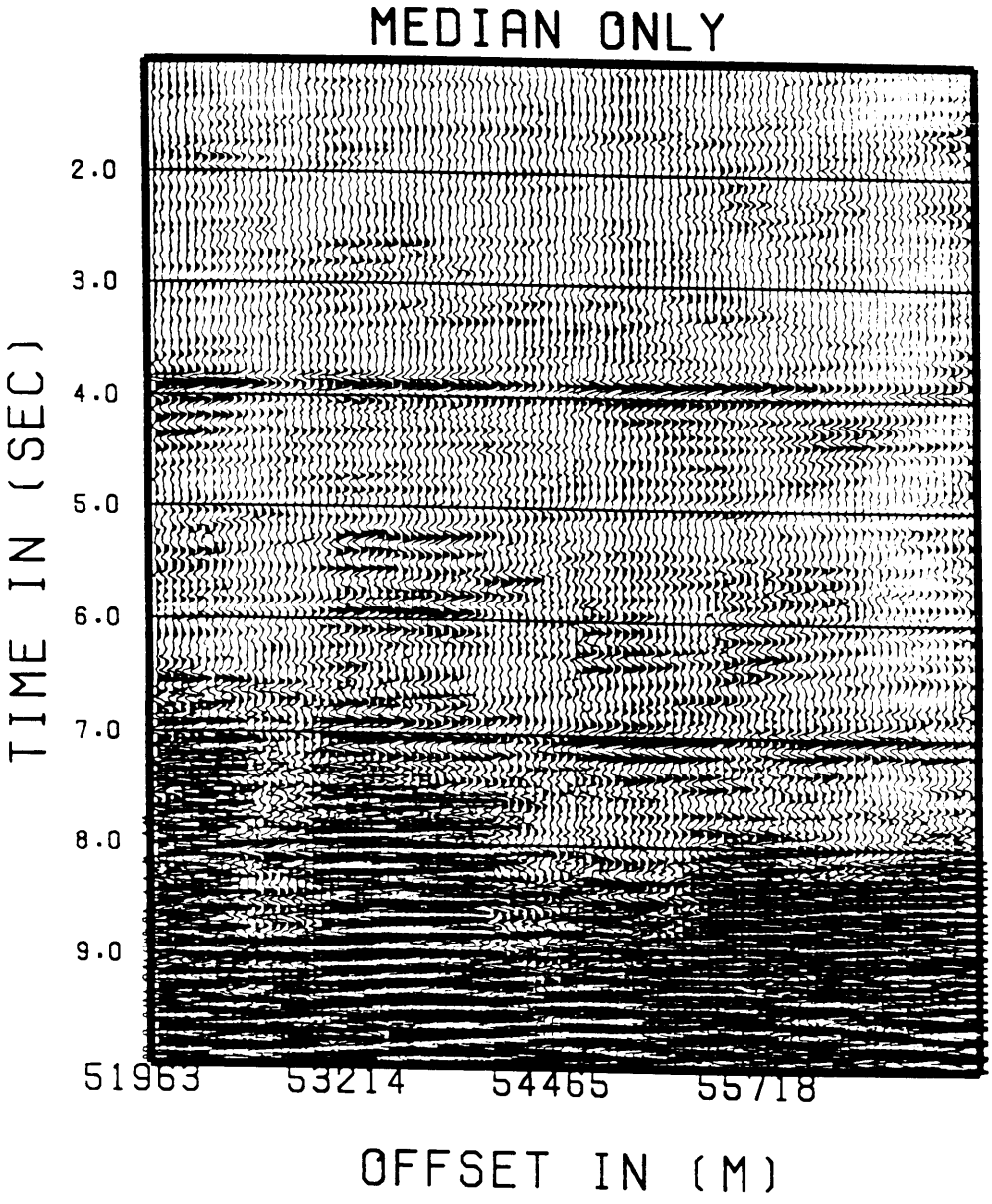

Figure 14. Data of Figure 13b filtered with an 11 trace gate, 6 to 15 km/sec passband, 21 slowness steers, a pure median filter with no semblance weighting.

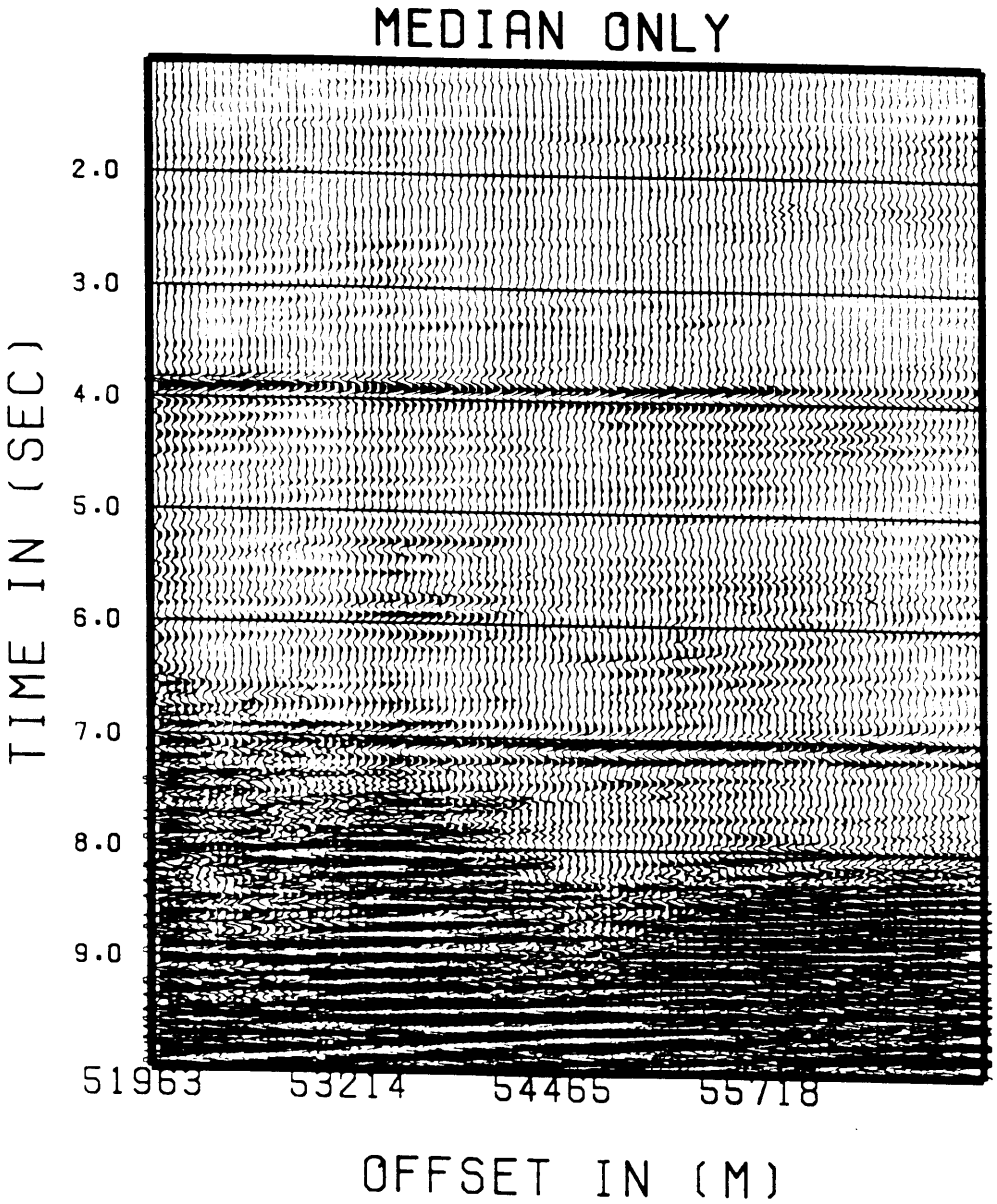

Figure 15. Data of Figure 13b filtered with a 21 trace gate, 6 to 15 km/sec passband, 21 slowness steers, a pure median filter with no semblance weighting.

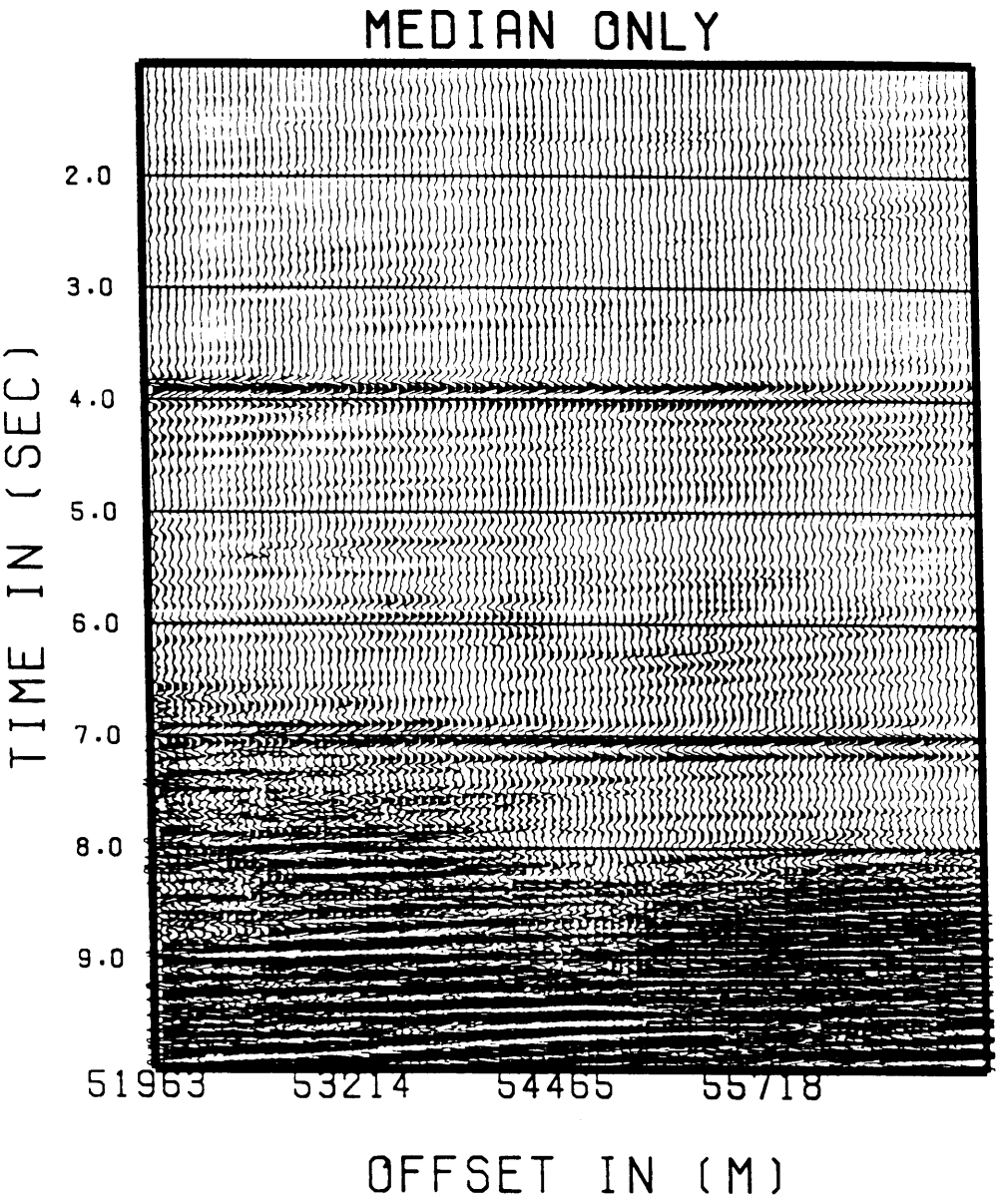

Figure 16. Data of Figure 13b filtered with a 31 trace gate, 6 to 15 km/sec passband, 21 slowness steers, a pure median filter with no semblance weighting.

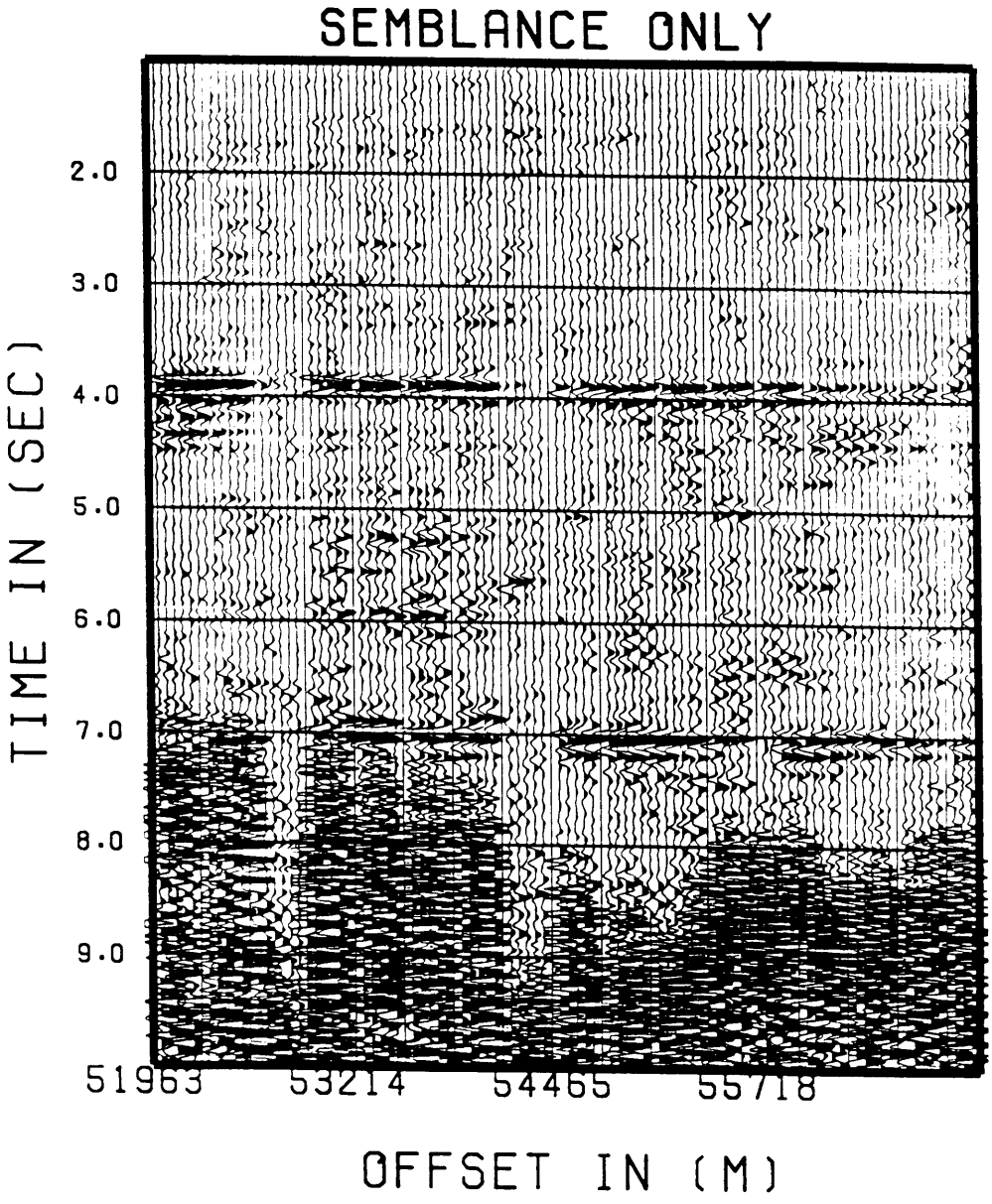

Figure 17. Data of Figure 13b filtered with an 11 trace gate, 6 to 15 km/sec passband, 21 slowness steers, no median operator and with semblance weighting.

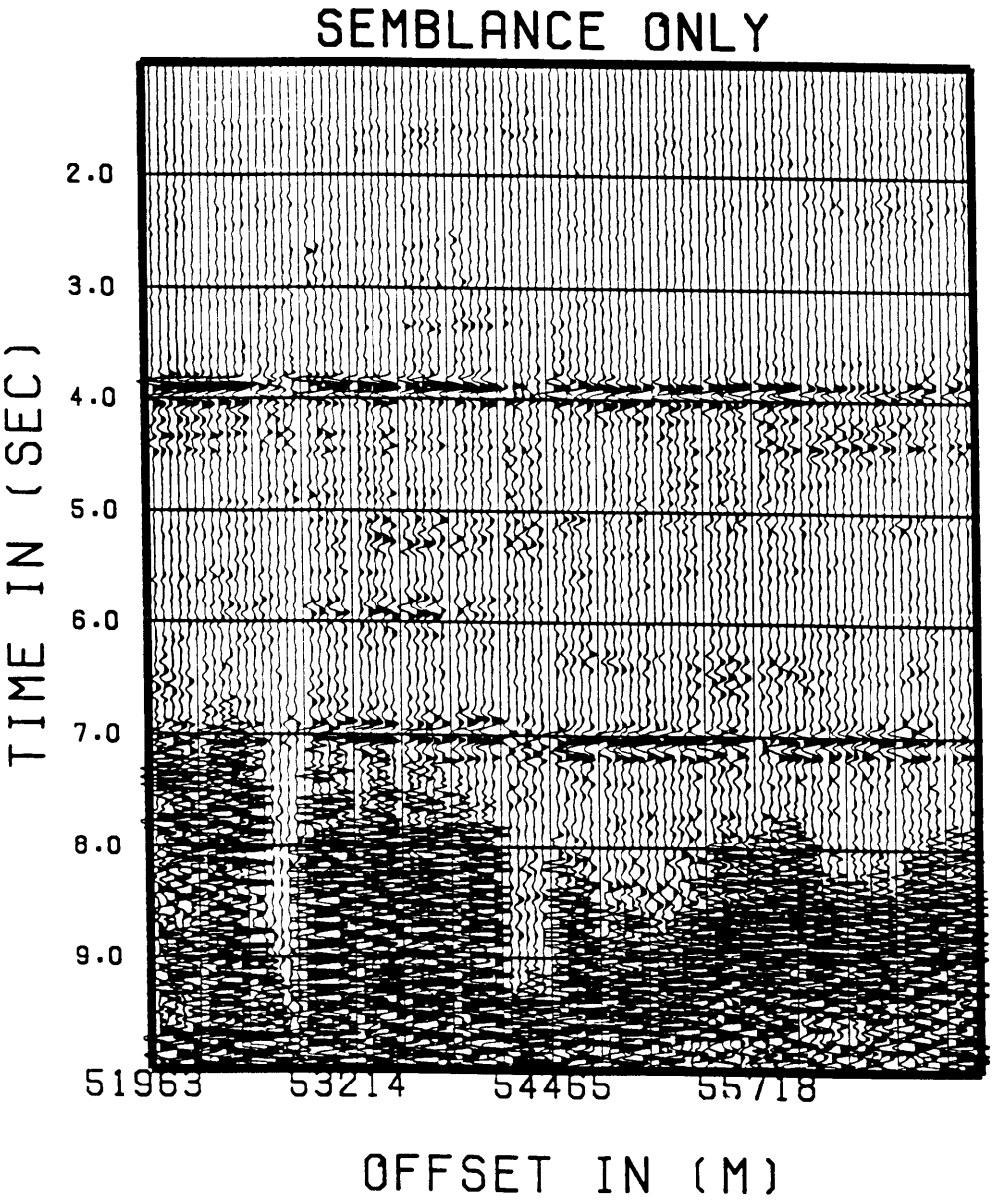

Figure 18. Data of Figure 13b filtered with a 21 trace gate, 6 to 15 km/sec passband, 21 slowness steers, no median operator and with semblance weighting.

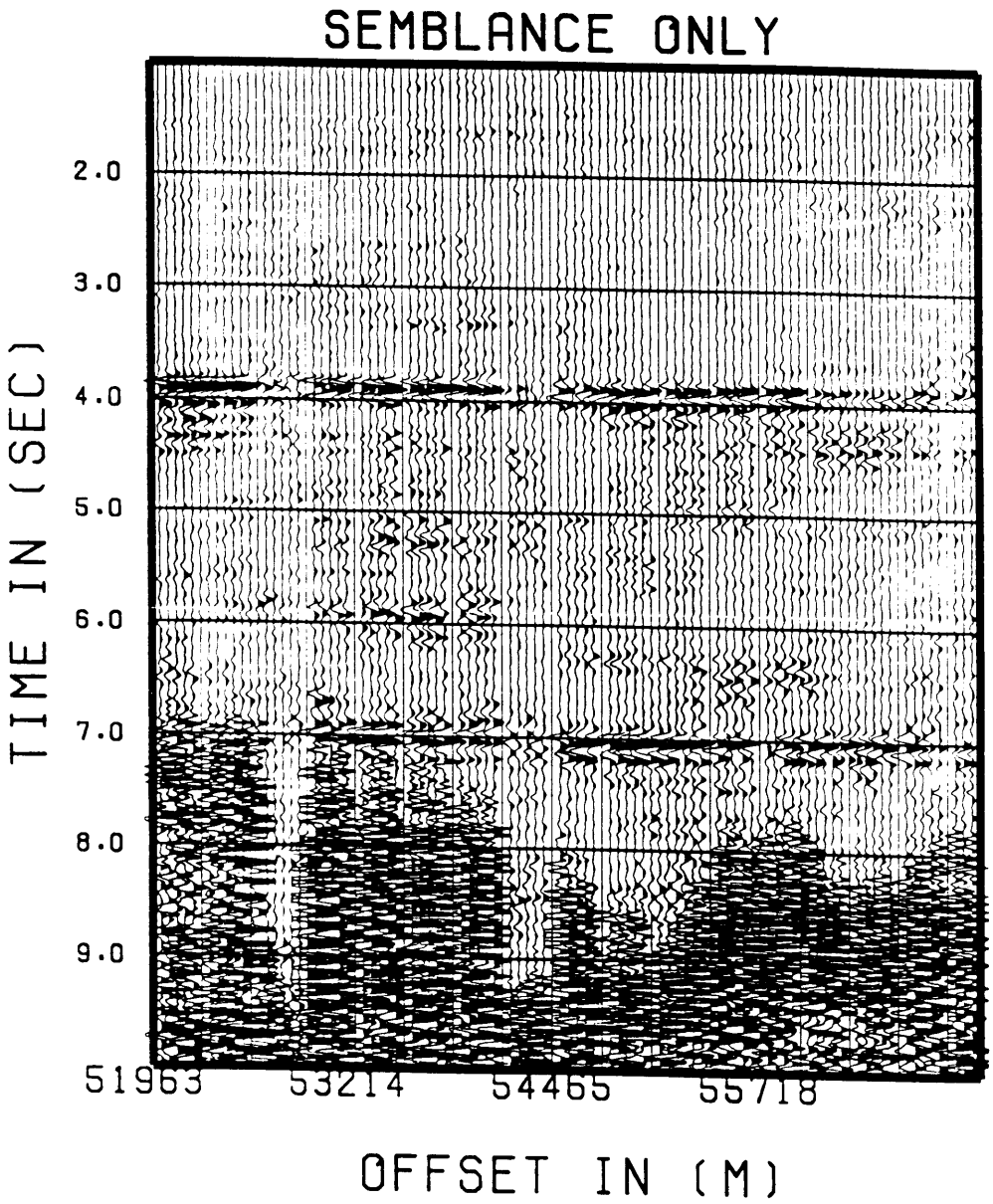

Figure 19. Data of Figure 13b filtered with a 31 trace gate, 6 to 15 km/sec passband, 21 slowness steers, no median operator and with semblance weighting.

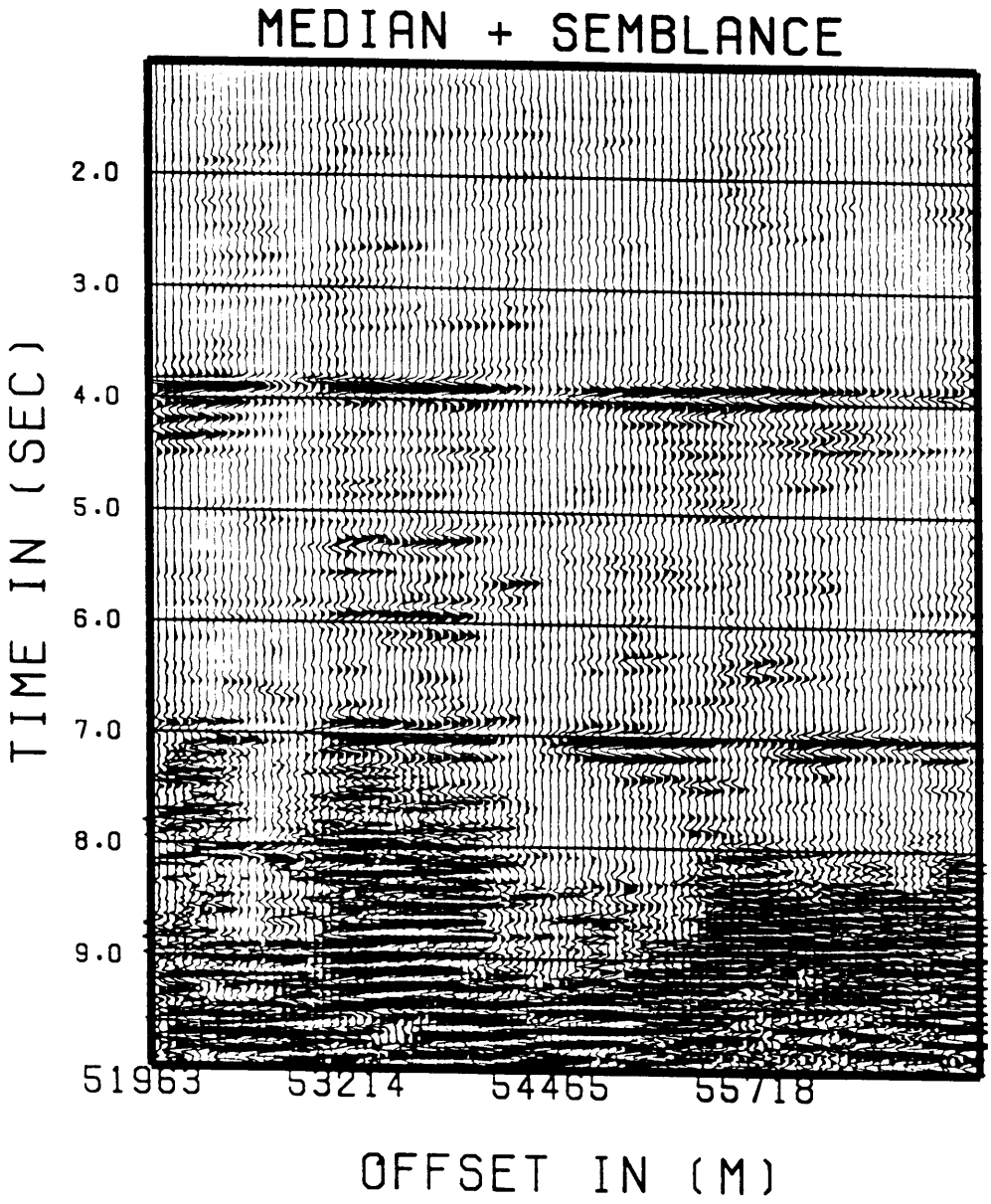

Figure 20. Data of Figure 13b filtered with an 11 trace gate, 6 to 15 km/sec passband, 21 slowness steers, pure median operator and with semblance weighting.

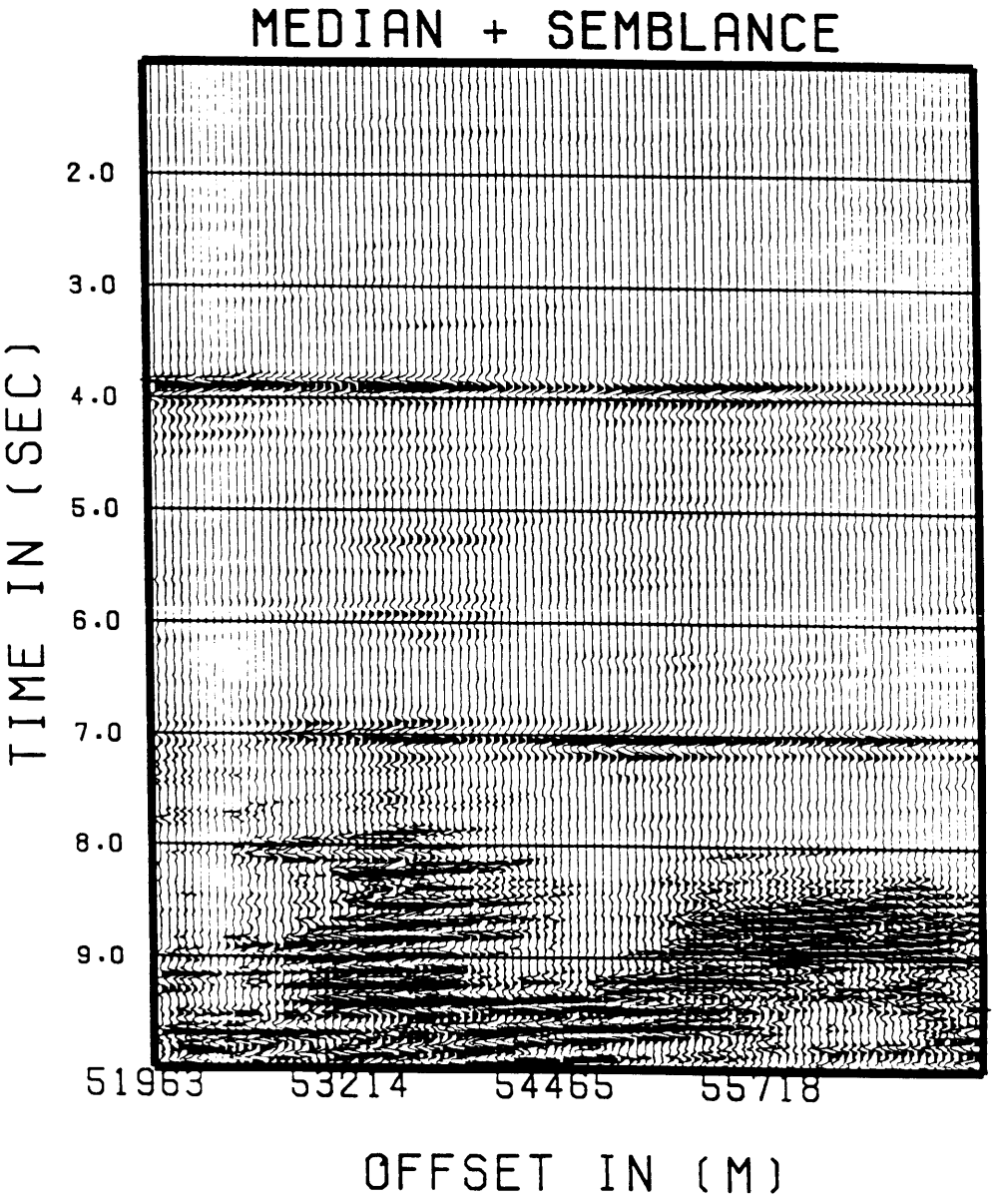

Figure 21. Data of Figure 13b filtered with a 21 trace gate, 6 to 15 km/sec passband, 21 slowness steers, pure median operator and with semblance weighting.

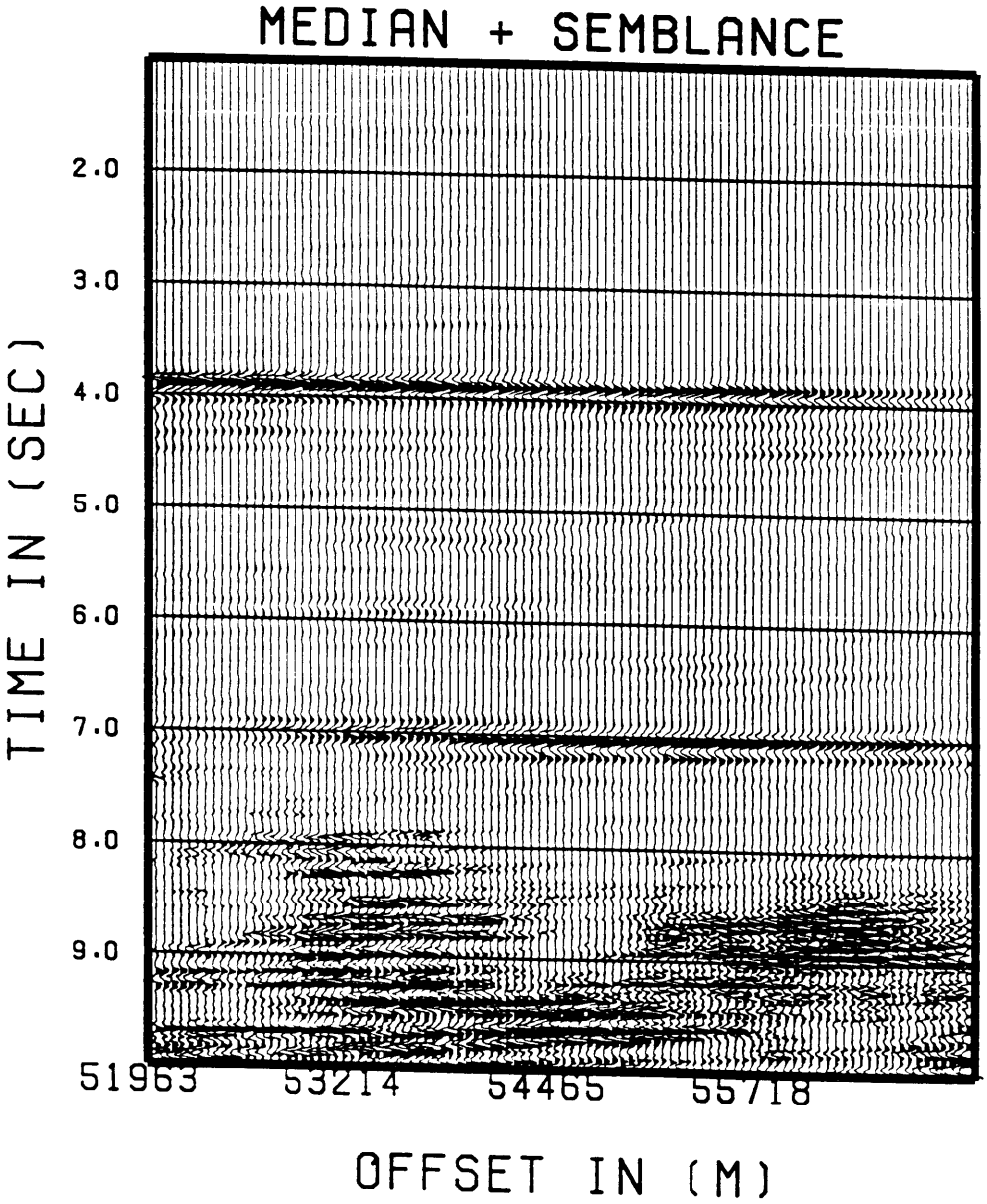

Figure 22. Data of Figure 13b filtered with an 31 trace gate, 6 to 15 km/sec passband, 21 slowness steers, pure median operator and with semblance weighting.